FRACTURE CHARACTERISTICS AND MECHANISMS IN CAST STEEL

NIGEL HOWARD CROFT M.A. (Cantab.)

Thesis submitted in fulfilment
of the requirements for the
degree of Doctor of Philosophy,
at the Department of Metallurgy,
University of Sheffield.

DECEMBER, 1981.

For Joe

FRACTURE CHARACTERISTICS AND MECHANISMS IN CAST STEEL

By Nigel Howard Croft, M.A. (Cantab.)

SYNOPSIS

The current practices of the UK steel foundry industry have been described and a review has been made of the fracture characteristics and mechanisms which commonly occur in steel castings. Emphasis has been placed on intergranular embrittlement phenomena caused by segregation and precipitation effects, and in particular the role of aluminium nitride has been considered.

The problem of AlN-induced intergranular fracture (I.F.) has been examined using experimental 0.30C-1.50Mn castings with varying Al and N contents, and commercially-produced material. The mechanism of fracture has been studied using various optical and electron optical techniques and the existence of two forms of AlN (a plate-like form and a dendritic form) has been confirmed. Directional solidification work has shown that the dendritic AlN forms in the residual liquid at a late stage of solidification. The plates are precipitated at a later stage when the casting is fully solidified. The plates nucleate at the grain boundaries and grow into the adjacent austenite grains with an orientation relationship of the form

$(0001)_{AlN} // \{111\}_{\gamma}$; $\langle 10\bar{1}0\rangle_{AlN} // \langle 1\bar{1}0\rangle_{\gamma}$

The effects of some processing variables on the susceptibility to IF have been examined. IF is favoured by a high Al and N content and a slow cooling rate. The state of heat treatment was also found

to be important, with quenched and lightly-tempered samples being more susceptible to IF. A model has been proposed which is based on a comparison of the relative yield strength, cleavage strength and intergranular strength of a casting. This can be used to explain the variation in fracture behaviour with testing temperature.

A programme of mechanical testing has shown that different testing techniques and conditions can influence the severity of IF observed quite significantly. Although there maybe a considerable decrease in Charpy impact energy as a result of intergranular embrittlement, there is little effect on the initiation value of the crack opening displacement (δ_i). The C.O.D. at maximum load, (δ_{max}), however, is decreased and the implications with regard to engineering design practices are considered.

CONTENTS

TEXT

Chapter 1

Introduction

The casting route continues to provide a uniquely versatile and economic method of producing certain engineering components in spite of many recent developments in the fields of metal forming and fabrication. Steel castings in particular have a number of applications in the mechanical engineering industry. They are widely used in chemical plant, earth moving equipment, mining and mineral processing, iron and steel plant and the power generating industry (Reynolds, 1979).

Complex geometry and difficulties in hot working often dictate that some components can only be made by casting, but very often there is direct competition from a forging route. Although on purely economic grounds casting directly to final shape is usually the more favourable, doubt is often expressed about the quality of the cast product with regard to internal integrity and surface quality.

Reynolds (1979) suggests that there is nothing inherently wrong with a correctly heat-treated cast structure. Indeed, a wide range of mechanical properties can be achieved simply by varying the carbon and alloy content of the steel, and the heat treatment of the casting. These properties tend to be more isotropic than in comparable wrought materials (Nakajima et al, 1977). The main problem is the incidence and detection of random defects. Alloy compositions are available to cater for most physical and mechanical requirements, but it is necessary to ensure that the

castings will perform as specified, having due regard for the imperfections which often arise during the casting process.

In recent years, the techniques of linear elastic fracture mechanics and general yielding fracture mechanics have been increasingly used as a design and inspection tool in the manufacture of pressure vessels and welded assemblies. Such techniques are now being applied to large steel castings, making it possible to assess the significance of any discontinuities with greater confidence, and to ignore any defects which are unimportant (Selby, 1979). Whilst this can result in the adoption of more realistic design criteria and the avoidance of over-specification, it is imperative that the mode of failure under service conditions can be predicted. Clearly it would be totally inappropriate to design a component using room temperature toughness data if it were to be used at temperatures below the ductile-brittle transition. Equally important, however, is the need to avoid other embrittlement phenomena which may change the fracture mechanism at a given temperature, and result in a lowering of the toughness.

One such problem which is occasionally encountered in carbon and low alloy steel castings is intergranular fracture (I.F.) which is often referred to more pictorially as "Rock Candy" fracture. This has been responsible for a number of premature failures in service and the rejection of large tonnages from within the foundry as a result of cracking in the mould. Intergranular fracture is usually encountered at temperatures above the ductile to

brittle (cleavage) transition, resulting in a dramatic reduction of the upper shelf toughness. Although there are many contributory causes, investigations in the past have shown a major factor to be the precipitation of aluminium nitride on the prior austenite grain boundaries of the steel. Preferential failure can occur around these precipitates, and even though a new system of grains may have been established by subsequent heat treatment, the fracture still appears to follow the original as-cast boundaries. This behaviour is characterised by the presence of coarse, shiny facets on the fracture surface.

Previous work by Woodfine and Quarrell (1960) and Wright and Quarrell (1962) has identified the presence of two morphologies of aluminium nitride on the fracture surface, a dendritic and a plate-like form. Since this time, however, there has been little fundamental research on the phenomenon, and despite numerous ad-hoc investigations of commercial failures, intergranular fracture is still a cause of serious concern among foundrymen.

The aim of this research is therefore to adopt a more basic approach to the problem by examining the precipitation behaviour of aluminium nitride in experimentally and commercially melted steels, and relating this to the fracture mechanisms observed. A steel of nominal composition 0.30%C, 1.50%Mn (BS 3100 A5/6) has been used as a basis for the experimental work, since previous investigations have shown this to be particularly susceptible to intergranular fracture. Initially, experimental castings were

made with varying aluminium and nitrogen contents, and were subjected to different heat treatments to obtain a range of hardness levels. Fracture surfaces from bend specimens were examined optically and in the scanning and transmission electron microscopes. In parallel with this work, examinations were made of commercially produced castings which had failed in an intergranular manner.

Subsequent work was aimed at defining more clearly the crystallography of the aluminium nitride precipitates and the details of the precipitation temperature of the two morphologies observed. Directional solidification techniques were used to exert greater control over processing parameters.

In order to quantify the effects of I.F. on mechanical properties impact tests were carried out, and the results compared to information obtained by fracture toughness (C.O.D.) testing. In this way, the practical implications of intergranular fracture could be assessed.

Chapter 2 gives a general outline of the steelmaking methods in use in the UK steel foundry industry today with particular emphasis on the gas content associated with each. This is intended to place the current research in its industrial context.

Chapter 3 is a review of the various fracture mechanisms by which a steel can fail under normal service conditions. The current theories of ductile and brittle (cleavage) fracture are discussed briefly, and the conditions under which intergranular

fracture can occur are considered. Several particular causes of I.F. are described in more detail.

The role of aluminium nitride in causing I.F. is discussed in Chapter 4 which also gives details of the solubility and precipitation of AlN. Other phenomena which are attributable to AlN are mentioned.

Chapter 5 describes the experimental techniques used in the current research, most of which are well established and are only considered briefly. These include electron metallography, mechanical testing (tensile, impact and fracture toughness) and directional solidification.

Chapters 6, 7 and 8 give the results, discussion and conclusions, respectively.

Chapter 2

The Steel Foundry Industry - Current Practices

2.1 Introduction

Before embarking on a review of the scientific literature relevant to the fracture of cast steel, it is pertinent to survey briefly the various methods employed to produce steel castings in the UK. This will place the current research in context, and will highlight some of the technological and economic limitations which often dictate that the ideal solution to a scientific problem cannot be implemented in practice.

The business of the steel foundry industry is the production of plain carbon, low alloy and high alloy steel castings. General areas of application are shown in Fig . 2.1. Casting processes are available which are suited to the production of virtually any size component from a few grams to over two hundred tonnes, and in any quantity, from a "one-off" to many millions.

In 1978, British foundries produced approximately 250,000 tonnes of castings worth over £225m before finish machining, and employed over 20,000 people. This compares with a total world production of 13M tonnes p.a., of which the USSR produces almost 7M tonnes, the USA 1.6M tonnes and Japan 0.6M tonnes. (Jackson, 1979).

2.2 Steelmaking

In the UK, liquid steel for making castings is melted mainly by electric arc and induction furnaces, although techniques such as AOD are currently being introduced for special applications.

Figures for 1977 (Jackson, 1979) show that in British foundries 369,500 tonnes of liquid steel were produced by the arc furnace route, 109,500 tonnes by induction furnaces and 20,500 tonnes by other techniques (mainly cupolas and convertors). Although this means that almost 75% by weight of all castings produced are made using arc furnace practice, it should not be concluded that the use of electric arc steelmaking is more widespread than induction practice, since the latter is used extensively for producing small quantities. This is highlighted by a summary of UK furnace useage for 1978. (Table 2.1).

Table 2.1 Number of furnaces of different capacities currently in use.

Arc furnaces

<5t	5-10t	10-20t	20-30t	>30t	TOTAL
61	20	15	4	3	103

Induction furnaces

<0.5t	0.5-1t	1-2t	>2t	TOTAL
67	96	26	20	209

In addition, 13 converter-type furnaces were also in operation.

These figures have remained fairly constant for the last few years, but will no doubt be affected by recent closures in the industry.

It is apparent from these data that not every foundry will be equipped to accept orders for castings of all weights. For example, there are only seven furnaces in operation in the UK having a capacity of 20 tonnes or more. A customer requiring a 30 tonne casting would therefore be limited in his choice of

approach to a foundry, but it should be emphasised that most foundries can produce large castings by utilising the combined melting capacity of a number of smaller furnaces.

2.2.1 Induction Practice

Despite the relatively small tonnages of steel produced by this route, the induction furnace is widely used throughout the foundry industry, and there are currently more than twice as many induction furnaces as arc furnaces in operation. Induction furnaces are less expensive than arc furnaces to buy and install, and their smaller sizes (usually less than 2 tonnes) are ideally suited for service where casting is to occur at short, but regular intervals. One large advantage is that for a foundry producing many grades of alloy steels, it is possible to have several furnace bodies, each one reserved for specific steels, all switched into one generator. This avoids contamination from the lining in successive melts and obviates the need to make a "wash heat" to remove traces of unwanted alloying elements from the furnace. This is particularly important, since the induction furnace is normally considered to be a dead melting unit, with most of the alloys or impurities contained in the initial charge being retained in the final melt. Careful selection of scrap for the furnace charge is therefore crucial, to avoid exceeding the alloy specifications.

For example, in a series of experiments reported by Holt and Hubbard (1975) a small induction furnace was used to remelt the same charge three times in succession. The absence of a carbon boil meant that the nitrogen content of the steel increased from 0.010% in the initial charge material to 0.017% after the third

remelting. This resulted in porosity in the finished casting, which highlights one of the many problems which may be encountered by the continuous recycling of internal foundry scrap with induction furnace practice.

Induction furnaces may be used with either an acid (SiO_2) or basic (MgO) lining, each practice having its associated advantages and disadvantages. The main advantage of a silica lining is its low cost, which for a comparable life is about half that of a basic lining. However, other considerations such as the necessity to use scrap low in sulphur and phosphorus have meant that basic induction steelmaking practice is more common in the UK.

In preparing the charge for a basic furnace, the scrap is usually shot blasted to remove any adherent sand, which will otherwise form a slag and attack the furnace lining. In acid practice, however, sand is left intact so that it will react with any iron oxide present in the charge and lessen the attack of the siliceous lining. Some foundries employing an acid practice are actually known to add a quantity of sand to the charge when highly oxidised or sand-free scrap is used.

Once a molten heel has formed in the bottom of the furnace, the induction furnace becomes an ideal unit for melting small pieces of scrap such as swarf. This is carried out almost immediately under the surface of the melt and there is no preheating in the atmosphere where oxidation can occur. This results in high yields compared to other air melting furnaces. (Hubbard, 1972).

In dead melting practice, the scrap is charged into the furnace

together with all the other non-oxidisable alloying additions, and when these have melted out, the oxidisable additions are made to bring the steel into specification. The melt is then superheated to the required temperature and tapped as quickly as possible. Final deoxidation (usually with aluminium) is carried out either in the furnace, in the ladle, or both.

If for some reason the melt has to be held at elevated temperature for any length of time, the gas content of the steel will increase rapidly (see Section 2.3), and because the induction furnace normally has to retain a molten heel for efficient power utilisation, there is a tendency for gas pick-up to occur during each successive tapping. To overcome this problem, the temperature of the melt is kept as low as possible at all times, and immediately after tapping one cast, the cold charge for the next melt is added to the furnace.

Although it has so far been assumed that the induction furnace is a dead melting unit, this is not entirely correct. Holt and Hubbard (1971) report that it is possible to promote a controlled carbon boil by the addition of small quantities of ore to the melt. This is advantageous in that the scrap in the base charge does not need to be so carefully selected, since carbon, manganese and silicon removal can now be achieved. The boil also serves to flush out unwanted gases, and promotes much lower nitrogen and hydrogen levels. (Fig. 2.2).

Hubbard (1972) does not consider the use of vacuum induction furnaces to be a feasible proposition for general foundry melting, but there have recently been introduced several new furnace designs

which allow for operation under reduced pressure, further lowering the gas content. However, these are not in widespread use.

2.2.2 Electric Arc Practice

The design and operation of the modern electric arc furnace is well documented, and in the context of steel castings production has been reviewed by Holt, Hubbard and Jackson (1973). The main advantage as far as the steelmaker is concerned is the ability to refine the composition of the liquid metal by using appropriate slags, thereby obviating the need for stringent selection of charge materials.

The most versatile unit available is the basic lined electric arc furnace which, with the use of suitably composed slags (oxidising or reducing), makes it possible to remove phosphorus and sulphur to very low levels. Hence the steelmaker can use poor quality scrap and still produce a casting with the required chemical composition. It is the necessity to remove phosphorus and sulphur which has restricted the use of an acid practice in Britain, although acid lined furnaces are widely used in the USA, where low phosphorus, low sulphur charges are more readily available.

The charge to the arc furnace is normally made up from a suitable mix of light scrap (turnings, etc)., heavy scrap (feeder heads, runners), and in some cases, ore. Prior to charging, it is usual to add some form of recarburiser such as anthracite, coke or crushed electrodes to the furnace bottom to ensure a sufficiently high carbon content at melt-out. This allows an adequate carbon boil to proceed.

It has long been recognised that a vigorous carbon boil is the prime factor in controlling the hydrogen and nitrogen content of steel, and it is generally agreed that a carbon drop of 0.30% is sufficient to remove these harmful dissolved gases to acceptable levels (Holt, Stephenson and Jackson, 1971). There are, however, two schools of thought as to when the boil should be terminated. Some foundries prefer to oxidise the bath to give a carbon content of about 0.10%, and then recarburise to the required level. Others prefer to "catch" the carbon at, or just below the level required by the specification. The first method requires little control to be exercised over the decarburisation period, but can give rise to problems due to overoxidation of the bath (see Section 2.3.1). The second technique is less easily controlled, but results in more predictable oxygen contents, making subsequent deoxidation easier. The recent introduction of rapid techniques for analysing the carbon content of the melt (the "checkpoint" type liquidus arrest apparatus) has resulted in greater popularity for the "catch-carbon" technique.

2.3 Control of Gas Content

The presence of dissolved gases in liquid steel can have extremely deleterious effects on the mechanical properties and structural integrity of the solidified casting. This is a consequence of the fact that the high solubility of many gases in the liquid state decreases steadily with decreasing temperature, and drops very sharply at the liquidus. Any gases present in the melt will therefore be rejected during solidification, and unless preventative measures are taken, will give rise to porosity in the casting. For this reason, numerous investigations have been carried out

over many years regarding the control and effects of the gases commonly encountered during steelmaking.

Jackson (1975) found it convenient to divide the more important gases into four groups:

i) The monatomic (inert) gases.

ii) The elemental diatomic gases (e.g. O_2, N_2, H_2).

iii) The compound diatomic gases (e.g. CO).

iv) The triatomic gases.

Of these, the most crucial with regard to steelmaking are the diatomic gases, and in particular oxygen, nitrogen and hydrogen. The monatomic gases are, however, useful since their virtual insolubility at all temperatures allows them to be used to flush out undesirable gases from the melt (Fast, 1965). A typical example of this is the ladle degassing of steel using argon, which can reduce the hydrogen and nitrogen contents quite significantly, and also promote greater homogeneity of temperature and composition by its stirring effect.

The solution of diatomic gases in liquid steel was first proposed by Sievert (1929), who took into account the fact that such gases have to dissociate before they can dissolve in the melt to form monatomic solutions.

For the reaction $G_2 \rightleftharpoons 2\,G$ (metal)

$$K = \frac{[G]^2}{[G_2]}$$

where K is the equilibrium constant

$[G]$ is the activity of gas atoms in the melt.

$[G_2]$ is the activity of the diatomic gas above the melt.

Assuming ideal gas behaviour, and that Henry's law holds, then Sievert's law follows directly:

$[\%G] = K' \sqrt{P_{G_2}}$ where P_{G_2} is the partial pressure of gas above the melt.

Because of this square root relation, it is extremely difficult to remove completely gases such as oxygen and nitrogen during steelmaking. It has already been noted (Section 2.2.1) that vacuum steelmaking facilities are not widely available in the steel foundry industry, and so it has to be accepted that some dissolved gas will always be present in the liquid steel, and will be evolved during solidification. Clearly, the aim of the foundryman is to ensure that the presence of any such gases does not result in the formation of blowholes or porosity in the casting. This is best effected by the addition of alloying elements which will combine with any excess gas to produce solid inclusions, such as oxides or nitrides, in a suitably innocuous form.

2.3.1 Oxygen

Oxygen plays a very important role during the manufacture of steel, and can influence the quality of the cast product quite significantly (Jackson, 1975). Although the reaction between oxygen and carbon is vital during the steelmaking process, it is a positive disadvantage during the solidification of steel castings and the evolution of carbon monoxide gas is often manifest as blowholes in the finished product. For this reason, steel castings are always fully killed before pouring, and rimming or semi-killed steels are never produced.

Although Carney (1953) has shown oxygen to have quite high

solubility in liquid iron, the solubility in steel prior to deoxidation is controlled mainly by the carbon content of the melt. Figure 2.3 shows the carbon/oxygen equilibrium at 1540°C and various partial pressures of carbon monoxide. This has a particular relevance to the control of the carbon boil in electric arc practice and subsequent deoxidation of the melt. If the boil is allowed to progress too far, then excessive amounts of oxygen will become dissolved as the carbon content decreases, and the final oxygen content will be high and variable. This can give rise to erratic yields of deoxidants, and leads to a tendency for the foundryman to "over-kill" the steel in an attempt to avoid blowhole formation at all costs. (Wilson, 1981).

Jackson (1975) advocates the use of the "catch-carbon" technique to overcome this problem. By terminating the carbon boil at a carbon content just below the specified level, the oxygen content of the melt will be lower, and subsequent deoxidation behaviour more predictable. The use of this technique generally means that an excess of carbon has to be added to the furnace charge to allow an adequate boil to proceed.

Deoxidation of the steel is normally achieved by the addition of weak deoxidants to the furnace (silicon and manganese, as Fe-Si or Fe-Mn), augmented by the use of a stronger deoxidant in the ladle, to prevent pinhole porosity. Aluminium is widely used for this latter purpose in the form of 99% pure Al rods or bars, because of its relatively low cost and availability compared to elements such as titanium and zirconium. Many steel foundries are reluctant to use titanium for deoxidation on the grounds that

it produces a "dirty" steel with an associated loss of impact strength. The use of aluminium is generally satisfactory, although variable levels of recovery can sometimes result in the formation of deleterious type II manganese sulphide inclusions, or even pin-hole porosity when yields are particularly low. The usual morphology of sulphide inclusions in steel castings is type III (angular) which are associated with a low oxygen content.

A major problem may, however, be encountered when excessive quantities of the deoxidant are used. Under these circumstances, the aluminium which is added beyond the level for stoichiometric combination with the oxygen is free to combine with any nitrogen present in the steel to form aluminium nitride. Under certain circumstances this will precipitate on the as-cast grain boundaries during the initial cooling of the casting, and can cause severe intergranular embrittlement. The conditions under which this occurs will be considered in greater depth in Chapters 3 and 4.

It has been noted that in recent years, the amount of aluminium used for deoxidation has been rising, and aluminium contents in excess of 0.10% are not uncommon. The reason for this is thought to lie in the uncertainty of prediction of oxygen content in the furnace, and the unilateral addition of a fixed amount of aluminium regardless of the state of oxidation of the bath. Clearly a dead-melted induction furnace heat will require less aluminium for deoxidation than a heavily blown electric-arc melt.

2.3.2 Nitrogen

The absorption of nitrogen by iron and its alloys during melting and refining operations has been recognised as important for many years, and has been the subject of intensive investigation. The presence of nitrogen in steel was first demonstrated in the late nineteenth century, when Allen (1879) determined contents of 0.005% to 0.015%N by chemical methods. Indeed this is the range of nitrogen contents which is frequently observed for most air melted steels in use today. The actual nitrogen content does vary slightly with the different steelmaking methods in use and Speith and Vom Ende (1959) and Kuhn and Detrez (1962) have made surveys of the nitrogen levels expected from each method. Table 2.2 shows that the highest nitrogen contents are normally associated with processes where there is extensive contact between the molten metal and the atmosphere. Any nitrogen introduced into the melt from scrap additions, pig iron and ferro-alloys is usually quite small in comparison (Jackson, 1975).

Pehlke and Elliott (1960) quote a solubility of 0.045 wt%N in pure iron at 1600°C and one atmosphere pressure and the way in which this solubility varies with temperature is shown in Fig. 2.4.

In liquid steel, the presence of alloying elements also influences the solubility of nitrogen. Strong nitride forming elements such as vanadium and niobium increase the solubility quite markedly (Fig. 2.5) while carbon and silicon reduce it slightly.

In practice, the amount of nitrogen commonly found in liquid steel

is much less than the solubility limit. (Wright, 1962). The reason for this is kinetic, since it is necessary for nitrogen in the atmosphere to dissociate before it can be incorporated into the melt. In the arc furnace, the liquid metal is usually protected from the atmosphere by a slag cover, making nitrogen absorption difficult. Induction melted casts rarely benefit from slag cover in this way and together with the absence of a carbon boil, this can often lead to very high nitrogen levels being encountered.

In certain grades of steel where the nitrogen content is deliberately increased (Cottrell, 1975a), nitrogen additions are made using cracked ammonia, calcium cyanamide, or manganese nitride, which overcomes the kinetic problems associated with the dissociation of molecular nitrogen. Indeed it has been reported (Blake and Jordan, 1971) that under some circumstances during the arc melting of iron, the absorption of nitrogen can exceed that predicted by Sievert's law. The authors suggest that this is a result of the high local temperatures near the arc (5000-6000K) dissociating the nitrogen and eliminating the kinetic barrier.

Nitrogen is well known to form a number of nitrides with iron at temperatures within the ferrite range. Paranjpe et al, (1950) determined the phase diagram for the iron-nitrogen system below 900°C and found the existence of five distinct phases. In steels, however, it is unusual to find evidence of these phases since nitrogen usually combines with other alloying elements present to form a more stable nitride.

Pearson and Ende (1953) collected the thermodynamic data for most metal nitrides and their results are summarised in Figure 2.6. The order of decreasing stability of the nitrides is: ZrN, TiN, AlN, BN, Si_3N_4, VN, Cr_2N, CrN and Fe_4N. The nitrides formed by zirconium and titanium are the most stable, and because of their very low solubility in austenite and ferrite, it can be assumed that if a sufficient quantity of these two elements is present, no other metal nitrides will be formed (Wright, 1962). Under normal circumstances, however, aluminium is the most stable nitride former present in a steel casting, since it is used extensively for deoxidation. Thus most of the nitrogen rejected from the melt during solidification will combine with excess aluminium to form solid precipitates. The morphology and distribution of these precipitates can have a profound effect on the properties of the casting as will be discussed in subsequent Chapters.

2.3.3 Hydrogen

The major effect of hydrogen in steel castings is its tendency to form gaseous pores during solidification as a result of the decrease in solubility on transition to the solid state. These pores can often be formed in conjunction with nitrogen but, as Svensson and Fredriksson (1981) point out, hydrogen is the more dangerous of the two gases because of its high mobility even at moderate temperatures. This mobility can also result in the diffusion of hydrogen to grain boundaries of the solidified casting and the formation of hairline cracks. In steelmaking, the major source of hydrogen is from water vapour present in the atmosphere, although contributions from the moisture content of

refractories and alloying elements cannot be discounted (Jackson, 1975).

With the exception of dead melted induction heats, the hydrogen content of a bath of steel is determined by the balance between the rate at which the water vapour dissociates and the rate at which hydrogen is purged from the bath by the action of the carbon boil. During the boil, the hydrogen level generally falls to approximately 2-3ppm, but in air melted casts it is impossible to prevent a subsequent increase during the reducing period. Hence double-slag melts tend to have higher hydrogen levels than single slag heats because of the longer time spent under reducing conditions. Figure 2.7 shows typical variations in hydrogen content for a 3½ tonne arc furnace heat (Stephenson, 1974).

Air-melted casts usually contain 3-6ppm of hydrogen which rarely gives rise to problems in smaller castings where diffusion to the surface is possible. In heavy sections, however, most of the hydrogen is retained inside the casting and can only be removed by lengthy and costly diffusion annealing. Since it is not possible to combine the hydrogen chemically with other alloying elements, it is often necessary to use vacuum treatment for large, critical components. In this way, it is possible to reduce the hydrogen level of the melt to approximately 1ppm and problems with porosity and hairline cracking are largely eliminated. (Jackson, 1975).

2.4 Solidification Behaviour

2.4.1 Grain Structure

The classical representation of the grain structure of a casting is shown in Fig. 2.8 which depicts the outer chill zone, the intermediate columnar zone and the central equiaxed zone. The grain size and relative proportions of these zones are determined largely by material and processing variables such as alloy composition, pouring temperature and mould properties, (Davies and Garland, 1975).

a) The chill zone arises from the copious nucleation of dendrites at the mould wall as a result of thermal undercooling, and the size of this zone depends on turbulence in the melt caused by pouring and convection. (Bower and Flemings, 1967).

b) The columnar zone is produced by a competitive growth mechanism of the chill crystals at the solid/liquid interface. This region exhibits strong anisotropy of mechanical properties since the columnar crystals show a preferred orientation along the <100> directions, which are the directions of dendritic growth (Hellawell and Herbert, 1962). The columnar region normally extends until the growth of the columnar crystals has become obstructed by the presence of equiaxed crystals in the centre of the casting.

c) The equiaxed zone There are three major mechanisms for producing equiaxed crystals:

i) isolated heterogeneous nucleation events in the melt (Chalmers, 1963).

ii) fragmentation of the growing columnar zone (Jackson et al, 1966).

iii) nucleation at the free surface of the casting (Southin, 1967).

All three sources normally contribute to the origin of equiaxed crystals to varying degrees, and it is the manipulation of processing variables to influence these mechanisms that facilitates control of the final cast structure. For example, equiaxed grain formation is often enhanced by the introduction of heterogeneous nucleants such as TiC or FeTi in steel, or by encouraging dynamic fragmentation of the growing dendrites.

2.4.2 Solute Redistribution During Solidification

It is well known that as steels solidify there is always some concurrent redistribution of solute elements on a microscopic and macroscopic scale. There have been several theoretical models proposed over a number of years to describe the variation of alloy composition as solidification proceeds. These vary in complexity from assuming equilibrium freezing conditions to models where complete solute mixing in the liquid is incorporated. (Flemings, 1974). All are derived assuming that the solid/liquid interface is macroscopically planar and moves at constant speed. A schematic representation of the solute distribution predicted by each model is shown in Fig. 2.9.

It is not intended to describe each model in detail, but the simplest approximation to the solidification of a steel casting is obtained by assuming complete mixing of solute in the liquid and that no diffusion takes place in the solid. The latter is not strictly true of course, but solid state diffusion coefficients for most substitutional alloying elements are several orders of

magnitude smaller than in the liquid and the effects of solute redistribution in the solid can usually be ignored. The exceptions are carbon and nitrogen, which are interstitial elements and where back diffusion in the solid may be significant.

For the unidirectional solidification of a bar of initial composition C_o, the composition of the solid (C_s) at the solid/liquid interface is given by

$$C_s = C_o k (1 - f_s)^{k-1} \qquad (2.1)$$

where f_s is the fraction solid

k is the equilibrium partition coefficient.

This can alternatively be rewritten in terms of the liquid composition (C_L) and the fraction liquid (f_L)

$$C_L = C_o f_L^{k-1} \qquad (2.2)$$

since $C_s = kC_L$ and $f_s + f_L = 1$

These equations have been derived by Scheil (1942) and Pfann (1952) and are referred to as the Scheil Equations, corresponding to curve (c) in Fig. 2.9. Initially, when the volume of liquid is large, there is little overall change in composition, but as solidification proceeds, so the liquid becomes solute enriched and providing the partition coefficient k is constant, some liquid will remain until an invariant temperature (e.g. a eutectic) is reached. In practice this extreme is rarely achieved in steel castings, but considerable microsegregation of alloying elements such as P and S can and does occur. Perhaps the closest approximation to the situation described above would be the

formation of an interdendritic Fe-FeS eutectic in a steel containing grossly inadequate amounts of manganese.

Not only can microsegregation result in high local solute concentrations, but the effect can be compounded with the influence of macrosegregation in the casting. There are several contributory causes of macrosegregation, including density differences which lead to differential movements of solute enriched liquid and interdendritic fluid flow. (Flemings et al, 1968; Flemings and Nereo, 1968; Mehrebian et al, 1970; Bridge and Beech, 1980).

In large castings this macrosegregation is not inconsiderable. In the extreme case of a 200 tonne anvil block casting which took over 80 hours to solidify completely, Table 2.3 shows the variation of liquid analysis in the feeder head from the start of pouring to just before final solidification (Wilson, 1981).

Table 2.3

Variation in liquid metal analysis from start to finish pouring of a 200 tonne casting.

Liquid Composition	C*	Si	Mn	S	P	Al	Ti	N
Initial	0.12	0.40	1.16	0.016	0.012	0.020	0.042	0.012
Final	0.37	0.56	1.17	0.060	0.032	0.003	0.018	0.021

* exacerbated by the effects of arc feeding.

Thus it can be concluded that although the nominal base composition of a casting may be in accordance with a specification, inhomogeneities in the structure arising from micro- and macro-segregation can mean that material properties vary significantly through the casting section.

Chapter 3

Fracture Mechanisms in Cast Steel

3.1 Introduction

The aim of a Fracture Mechanics based design philosophy is to replace the degree of uncertainty inherent in conventional design factors by a quantitative parameter which is a direct measure of the material's fracture resistance (Knott, 1973a). Using this parameter, it is possible to assess the significance of any defects present in the material with greater confidence, and to avoid the use of excessive factors of safety (Jackson and Wright, 1977). However, this can only be achieved satisfactorily if the mechanism of failure under service conditions can be predicted, and the fracture toughness data used for the design must be representative of this mechanism.

The single most important parameter which determines the fracture mode of steels is temperature, although strain rate and state of triaxiality also play a part. In mild steels, there is usually a sharp transition from low- to high-energy fracture over a narrow temperature range, and this is associated with a change in mechanism from bright crystalline cleavage to dull fibrous fracture. A schematic representation of the effect on impact energy is shown in Fig. 3.1.a.

For most applications it is desirable to operate under conditions of high impact energy, and many specifications for steel castings now include the requirement for a minimum impact energy at a specified temperature (BS 3100, 1976: BS 1504, 1976). This can usually be achieved quite readily by the addition of alloying elements such as manganese to the

steel which lower the impact transition temperature, (Reed-Hill, 1972), or by modification of the heat treatment to produce an inherently tougher microstructure.

Although temperature has an overall effect on the fracture mechanism, other embrittling phenomena can occur in steel castings which result in a lowering of the fracture toughness at temperatures where the steel would otherwise be ductile and tough. These are particularly important, since they can completely invalidate any design calculations based on the expected mode of failure. An example, taken from the work of Wright and Quarrell (1962) is shown in Fig. 3.1.b.

The aim of this Chapter is to review briefly the mechanisms of ductile and brittle fracture in steel and to examine in greater detail some of the factors which can give rise to intergranular embrittlement in steel castings.

3.2 Ductile Fracture

The generally accepted mechanism for ductile fracture is one of void nucleation at inclusions or second phase particles followed by the growth and coalescence of these voids to give final failure (Thompson and Weihrauch, 1976). This results in the typical dull fibrous appearance of the fracture surface, on which the voids are manifest as dimples.

The concept of void nucleation by inclusions was first proposed by Tipper (1949) and Puttick (1950). By unloading tensile samples prior to final failure and examining longitudinal sections in the light microscope, they were able to observe the close

association of voids and inclusions. Further indirect support for this mechanism came from Crussard et al (1956), who reported that an increase in the inclusion content of steel resulted in inferior Charpy upper shelf energies without changing the impact transition temperature.

Later, more quantitative work by Kunio et al (1977) investigated the effects of inclusion size and distribution in electrolytically pure iron containing only FeO inclusions. By examining fracture surfaces in the scanning electron microscope (S.E.M.) they found a minimum inclusion diameter of 0.1μm to be capable of nucleating a void, and determined a linear relationship between the inclusion diameter and the dimple size observed (Fig. 3.2).

It was noted that voids were initiated by the separation of the FeO/matrix boundary. In general, however, void nucleation depends very much on the nature of the bonding at a matrix-particle interface. For inclusions such as oxides and sulphides in steel, this bonding is weak and voids can be initiated and will grow at very low plastic strains (Knott, 1973). In contrast to this, precipitates such as carbides and nitrides are relatively strongly bonded to the matrix, and Ashby (1966) showed that under such circumstances voids can only be initiated by the high localised stresses formed by vacancy loops at the "poles" of the particles. It is therefore clear that the ductile fracture of cast steels will be dominated by the presence of relatively large sulphides and oxides, and it is these inclusions which are most frequently observed on fibrous fracture surfaces (Figs. 3.3 to 3.5). Control of the size and distribution of these inclusions can have a considerable

effect on the tensile ductility of steel, as shown by the work of Gladman, Holmes and McIvor (1971). Fig. 3.6 demonstrates the improvements which can be achieved by reducing the volume fraction of inclusions, and also shows the effect of inclusion/matrix bonding discussed earlier, by comparing results for sulphides and carbides.

Although macro inclusions play an important role in determining the fracture strain, they do not generally control details of the fracture process (Broek, 1973). In particular they cannot account for the spacing and size of the small voids or dimples which are frequently observed on the fracture surface, and which may not contain inclusions at all. (Crussard et al, 1956). Rogers (1960) first recognised that voids at macro inclusions need not coalesce, but that they can be linked by sheets of very small voids which form in the shear bands between the macro inclusions. This essentially represents the intervention of shear on a microscopic scale and photographic evidence of the process is presented in Fig. 3.7 (Cox, 1973).

The intervention of a ductile shearing mechanism at a macroscopic level usually prevents the formation of a fully fibrous fracture, and is manifest as shear lips on a "cup and cone" type fracture, or as slant fracture on bend specimens. The reason for this is that as void coalescence occurs, the sample geometry changes to that of an internally cracked specimen, and a shearing mechanism is favoured near the surface. As a result, the fracture surface may show elongated dimples in this region, and areas with relatively few surface markings are observed.

3.3 Brittle Cleavage Fracture

3.3.1 Theoretical Treatments

In steels, the mechanism of cleavage involves the transgranular fracture of the b.c.c. matrix along {100} planes, and is usually associated with low ductilities. The tendency for this mode of failure is increased not only by a decrease in temperature, but also by a high strain rate and a triaxial stress state. As a result, cleavage fracture is only encountered in slowly strained uniaxial tensile specimens of mild steel during deformation at very low temperatures (~100K), whereas in notched impact specimens it may become apparent near room temperature (Armstrong, 1977).

Several models have been proposed to account for the nucleation of a brittle cleavage crack, and whilst they differ slightly in detail, they have essentially the same foundations. On the basis of Low's work of 1954 on mild steel it became clear that some yielding always precedes fracture (since yield is necessary to produce a cleavage crack nucleus), and the models proposed by Stroh (1957), Cottrell (1958), Petch (1958) and Smith (1966) all involve the blocking of a slip band or twin by an obstacle such as a second phase particle or a grain boundary. A typical representation of this process is shown in Fig. 3.8, where a pile-up of dislocations in a grain of diameter d produces a highly concentrated stress at each end of the slip band. An applied tensile stress σ will give rise to a shear stress τ acting on the slip band, where $\tau \sim \sigma/2$. Since slip proceeds by dislocation movement, this shear stress is opposed by a friction stress τ_i which includes contributions from the inherent resistance of the lattice to slip (the Peierls-Nabarro force),

from small precipitates and from clusters of solute atoms. By treating the slip band as a freely slipping crack under Mode II deformation, and considering fracture to occur when a critical value of stress is attained in the adjacent grain, Stroh (1957) derived a relationship between the stress required to nucleate a cleavage crack (σ_F) and the grain size (d):

$$\sigma_F = \sigma_i + k_F d^{-\frac{1}{2}} \qquad (3.1)$$

where k_F is related to the local tensile stress required to fracture the second grain.

The similarity of this equation to the Petch relation between grain size and yield stress will be noted, since the two derivations are based on the same principles. Smith and Barnby (1967), however, extended the Stroh analysis by considering the conditions under which a crack, once nucleated, would spread. Their results indicated that any increase in length of the nucleus would result in a decrease in total energy of the system, thereby implying that cleavage fracture is nucleation-controlled.

It was predicted that the important stress in causing cleavage fractures is the effective shear stress (τ_{eff}), where

$$\tau_{eff} = \tau_y - \tau_i = K_y^s d^{-\frac{1}{2}} \qquad (3.2)$$

τ_y is the applied shear stress required to spread yield from grain to grain.

τ_i represents the resistance of the grain to slip.

K_y^s is a constant which is related to the shear stress state.

However, this analysis fails to explain why cleavage fractures predominate at low temperatures where, although the yield stress is high, the value of $(\tau_y - \tau_i)$ is not significantly

different from its room temperature value. The experimental results of Hahn et al (1959) suggest that cleavage fracture must be growth controlled within a certain temperature regime because of the presence of a significant number of grains containing micro-cracks after fracture. This implies that nucleation is not the rate controlling step. There is also a strong dependence on the applied tensile stress, which is not accounted for in the Stroh analysis.

The Cottrell theory of brittle fracture is based on a dislocation mechanism which allows for growth of the crack to be the controlling factor by providing an easy nucleation process. (Cottrell, 1958).

In this theory, the cleavage crack is nucleated by the interaction of two partial dislocations on intersecting {101} slip planes in iron to form a sessile edge dislocation, according to the reaction

$$\frac{a}{2}[\bar{1}\bar{1}1]_{(101)} + \frac{a}{2}[111]_{(\bar{1}01)} \rightarrow a[001]_{(001)}$$

This therefore provides the first stage of crack nucleation, (see Fig. 3.9) and Knott (1973b) likens the model to the driving of a wedge into the cleavage plane.

By energy considerations, Cottrell (1958) determined the criterion for the propagation of this crack nucleus to be

$$\sigma_F \geq \frac{2\mu\gamma}{K_y^s} d^{-\frac{1}{2}} \qquad (3.3)$$

where σ_F is the stress required for fracture

μ is the shear modulus

γ is a surface energy term

Hence this model emphasises the role of tensile stress, and explains the effect of grain size ($d^{-\frac{1}{2}}$) in a similar way to the Stroh analysis.

It is also predicted that hardening, other than by decreasing the grain size, will promote cleavage fracture by raising the value of the tensile stress at the yield point.

Hence the Cottrell model appears satisfactory for homogeneous polycrystalline samples of iron, for example. However, most steels contain carbides in one form or another which, being very brittle, can provide easy sites for cleavage crack nucleation. An example of cracking nucleated at pearlitic cementite is presented in Fig. 3.10. Smith (1966) therefore proposed a model which takes into account the effect of carbides, and predicts low fracture stresses to be associated with the presence of coarse carbides. This is in good agreement with the experimental results of McMahon and Cohen (1965).

3.3.2 Fractographic Aspects of Cleavage

Cleavage fractures, once nucleated, propagate very rapidly and the resulting fracture surface exhibits highly reflecting facets (Fig. 3.11). Microscopically, the surface of the facets may show a series of ridges or steps which are often arranged in the form of "river markings". Low (1959) considered these markings to represent a difference in height between the steps on the cleavage facet, and subsequent fractographic work has confirmed this. The steps result from the fact that instead of following a single crystallographic plane, the cleavage crack can be broken up by the presence of discontinuities in the crystal structure

and may proceed along several parallel planes (Gilman, 1956). These eventually merge to form fewer larger steps as the crack front proceeds, and it is generally agreed from fractographic evidence that the crack propagates in the direction of "flow" of the river markings (Herzberg, 1976). An example of the appearance of river markings is given in Fig. 3.12, which shows the effects of a high angle grain boundary. As the largely planar crack has advanced from right to left across the boundary, the crack plane has been forced to splinter in an accommodation process as the crack front searches out suitable cleavage planes in the new grain.

Other discontinuities which may also contribute to the formation of river markings include interphase interfaces, inclusions and screw dislocations which cut across the cleavage plane (Gilman, 1956).

Although most cleavage fractures exhibit the same general appearance, details on the fracture surface are often influenced by the microstructure and composition of the steel, and the features observed may be quite complex. A good example of this is the fracture of an untempered or lightly tempered martensitic structure, in which few well defined cleavage facets can be identified, and the failure mode is best described as quasi-cleavage. (Fig. 3.13).

3.4 Brittle Intergranular Fracture

The two most common failure mechanisms in cast steels, namely fibrous and cleavage fractures which occur in a transgranular manner, suggest that under normal circumstances, grain boundaries

are not an inherent source of weakness. However, numerous observations dating from the nineteenth century bear witness to the fact that grain boundaries are easily susceptible to serious embrittlement, principally by the presence of elements or precipitate particles that alter the localised grain boundary chemistry. (Hondros and McLean, 1976).

The reduced performance of engineering alloys through intergranular failure has been observed in a wide range of metallurgical situations, and in the case of steels some of the factors which give rise to intergranular fracture have been reviewed by Briant and Banerji (1978). These are presented in Fig. 3.14, and can be classified into four general categories:

i) The presence of certain elements which have segregated to the grain boundary without any detectable phase precipitation.

ii) The presence of discrete grain boundary phases or precipitates.

iii) The action of certain corrosive environments.

iv) The action of stresses applied at high temperatures.

These factors may act alone or in combination, (in which case the embrittling effect can be more severe), but only categories (i) and (ii) will be reviewed here.

It is generally accepted that the intergranular fracture path in steels will be along the highest angle grain boundaries present, (Briant and Banerji, 1978). These may be the austenite boundaries, or in their absence, martensite packet or ferrite

boundaries. In some circumstances even a particle/matrix boundary which may be coincident with a previously existing grain boundary can provide a favourable route for crack propagation, and this situation will be discussed later.

Hondros and McLean (1976) have examined the susceptibility of metals to intergranular fracture in terms of the grain boundary cohesion, and a summary of their approach is given here.

By considering a schematic stress/separation curve for the atoms on two surfaces formed in a fracture process (Fig. 3.15), it can be seen that the cohesion is measured by the maximum stress σ_m beyond which fracture should occur.

Because, to a first approximation, both γ (the surface energy) and σ_m are proportional to E (the Youngs Modulus), then

$\sigma_m \propto \gamma$

This facilitates a comparison of grain boundary cohesions by examination of the appropriate macroscopic surface energies.

For an intergranular fracture along a high angle grain boundary, the work done in forming two new surfaces (the surface energy of fracture γ_b^*) is given by

$$\gamma_b^* = 2\gamma_s - \gamma_b \qquad (3.4)$$

where γ_s is the surface energy of the exposed boundary

γ_b is the surface energy of the pre-existing boundary

By comparing the cohesive strength of the grain boundary σ_b with the cleavage strength of the matrix, σ_{cl}, it is possible to obtain a measure of susceptibility for intergranular fracture.

Since cleavage usually proceeds by the parting of two low index crystallographic planes {hkl}, then

$$\sigma_{Cl} \propto \gamma_{Cl}^* = 2\gamma_{hkl} \qquad (3.5)$$

where γ_{Cl}^* is the surface energy of cleavage fracture

γ_{hkl} is energy of the freshly created surfaces.

Hence the relative cohesion at a grain boundary compared with that at any other cleavage plane is

$$\frac{\gamma_b^*}{\gamma_{Cl}^*} = \frac{2\gamma_s - \gamma_b}{2\gamma_{hkl}} \qquad (3.6)$$

Using the data of Mills et al (1973) and Hondros and Stuart (1968) for a Fe-3%Si alloy (the only ferrous system for which experimental data are available) Hondros and McLean (1976) compiled a table of cohesive energies (Table 3.1).

Table 3.1

Cohesive Energies for Intergranular and Cleavage Fracture in Fe-3%Si (Hondros and McLean, 1976)

Fracture Path Energy (mJ/m^2)	Intergranular (Average Plane)	Cleavage (100)	(110)	(111)
$\gamma_{(hkl)}$	1754(average)	1670	1745	1848
γ_{Cl}^*		3340	3490	3696
γ_b	462			
γ_b^*	3047			
$\frac{\gamma_b^*}{\gamma_{Cl}^*}$	0.87	0.91	0.87	0.82

Since cleavage normally occurs by the separation of {100} planes, it is clear that although intergranular cohesion is less than the lattice cohesion for these planes $\left(\frac{\gamma_b^*}{\gamma_{Cl}^*} = 0.91\right)$, the difference is so marginal it does not normally have any

effect on the fracture process. It is usually only in the presence of segregated species or discrete precipitate particles that the relative energies of cohesion become appreciably different.

These two situations will now be discussed in greater detail.

3.4.1 Segregation Effects

In comparison with the situation described for Fe-3%Si, where there is theoretically only a marginal expectation for intergranular failure in preference to {100} type cleavage, it is well known that the presence of small amounts of residual elements can promote unequivocal intergranular fracture, (Briant and Banerji, 1978). Some of the specific phenomena related to cast steels will be considered later, but first it is pertinent to consider the mechanism by which embrittlement occurs.

There have been numerous observations on the relationship between the segregation of residual elements and grain boundary embrittlement, and a quantitative model was proposed by Seah and Hondros (1973). They considered the effects of segregation on interfacial energies, and were able to obtain some idea of the corresponding changes in grain boundary cohesion. Although it would be inappropriate to use the grain boundary cohesion as a measure of fracture stress in absolute terms, this model gives a useful indication of the tendency for intergranular failure when compared to the cohesion of a suitable set of cleavage planes.

The change in interfacial energy for a dilute binary alloy is given by the Gibbs adsorption isotherm, which takes the form

$$d\gamma = - RT\Gamma d\ (\log_e X) \qquad (3.7)$$

where $d\gamma$ is the energy change corresponding to a bulk composition interval dX, and Γ is the associated interfacial enrichment.

The effect of small bulk solute concentrations on the surface energy (which is of the same order of magnitude as the grain boundary energy) is shown in Fig. 3.16 for a number of alloy systems. This again can be used only as a guide to the effects of the residual elements, since an absolute value of the surface energy will depend on the segregation inherent in the system, which in turn is a function of prior heat treatment.

By assuming equal partitioning of the segregant on the two intergranular fracture surfaces, Hondros and McLean (1976) were able to obtain a ratio between the cohesion of a boundary with segregation ($\sigma_{b(s)}^*$) and that of a clean boundary (σ_b^*).

$$\frac{\sigma_{b(s)}^*}{\sigma_b^*} \approx \frac{\gamma_{b(s)}^*}{\gamma_b^*} = \frac{2\gamma_s^{m-x} - \gamma_b^{m-x}}{2\gamma_s - \gamma_b} \qquad (3.8)$$

where the suffix m-x refers to the alloy (metal-solute X). The experimental data of Hondros and McLean (1970) suggest that the minimum value of the surface energy is given by $\gamma_s^{m-x}(\min) \approx \frac{1}{2}\gamma_s$, and in general, the same situation applies for grain boundary energies, i.e. $\gamma_b^{m-x}(\min) \approx \frac{1}{2}\gamma_b$. Using these approximations in equation (3.8) the relative cohesion becomes $\frac{\gamma_{b(s)}^*}{\gamma_b^*} \approx 0.5$.

Despite the crude approximations used in this model, the result agrees well with the experimental observations of Seah and Hondros (1973), who used Auger spectroscopy to obtain a direct measurement of the segregation, and obtained a similar value of the cohesion ratio using the Gibbs equation.

Compared with lattice cohesion for <u>cleavage</u> fracture, the cohesion at a segregated boundary will be even lower than the value predicted above, since $\frac{\gamma_{b(s)}^*}{\gamma_{c_l}^*} = \frac{\gamma_{b(s)}^*}{\gamma_b^*} \times \frac{\gamma_b^*}{\gamma_{c_l}^*}$ and typical values of $\frac{\gamma_b^*}{\gamma_{c_l}^*}$ are 0.8-0.9 (see Table 3.1).

This gives $\frac{\gamma_{b(s)}^*}{\gamma_{c_l}^*} \simeq 0.4$

Under these circumstances, an intergranular mode of failure would be expected.

3.4.1.1 <u>Temper Embrittlement (T.E.)</u>

This phenomenon has been studied extensively in both wrought and cast low alloy steels, but only a brief resumé of the work relating to steel castings will be presented here.

The segregation of residual impurities to the grain boundaries in steel can occur at any stage of the heat treatment cycle to which the steel is subjected (Banerji and Briant, 1980) and although the embrittlements resulting from segregation at various stages of thermal exposure are manifest in slightly different ways, they all lead to intergranular cracking and the associated loss of ductility.

The most common grain boundary embrittlers are from groups IV-VI of the periodic table (see Table 3.2) which are often found as trace impurities in steels. (Briant and Banerji, 1978).

Table 3.2

Common Grain Boundary Embrittlers

Group	IVa	Va	VIa
	Si	P	S
	Ge	As	Se
	Sn	Sb	Te

Historically, research into the problem of temper embrittlement has been divided into two regimes.

a) One-step Temper Embrittlement (O.S.T.E.), or 350°C embrittlement as it is often known, occurs mainly in high strength quenched and tempered steels, where the martensite has been tempered for short times at low temperatures (<400°C). The hardness of such steels decreases monotonically as the tempering temperature increases, yet the steel exhibits an anomalous decrease in fracture energy when tempered in the range 250°-350°C.

Although the characteristics of this type of embrittlement have been known for many years, the actual mechanism responsible has, until recently, remained speculative. Work by Briant and Banerji (1979 a, b, c) has shown that in low alloy steels substantial segregation of P, S and N can occur during austenitisation. In most cases, however, alloying elements such as manganese and aluminium are present in the steel and form stable compounds with sulphur and nitrogen respectively, but phosphorus is usually in

SHEFFIELD UNIVERSITY LIBRARY

solution in the austenite and is free to segregate to the grain boundaries in its elemental form. For this reason, phosphorus is the most deleterious impurity element with respect to O.S.T.E. However, phosphorus segregation alone is not sufficient to cause temper embrittlement - a crack nucleating site is first required.

At tempering temperatures of around 350°C, the ε-carbide in the structure transforms to give a thin plate-like cementite (Lement et al, 1954). Those plates which are coincident with the prior austenite grain boundaries (which are already weakened by the segregated phosphorus) can provide effective additional slip barriers to nucleate a brittle intergranular crack. Moreover, McMahon (1975) has shown that the formation of cementite can exacerbate the effects of phosphorus segregation by solute rejection along the grain boundaries.

Thus there are two factors which combine to give O.S.T.E., neither of which is sufficient to promote intergranular fracture in isolation. For example Banerji et al (1978) examined a high purity steel which exhibited little segregation during austenitisation, and even after tempering in the susceptible region, no embrittlement was observed.

At higher tempering temperatures (>400°C) the steel will no longer be vulnerable to one-step temper embrittlement, since the carbides coarsen and lose their effectiveness as crack nucleating sites.

b) Two-step Temper Embrittlement (T.S.T.E.) refers to the decrease in toughness and increase in the ductile-brittle transition temperature that is often observed when tempered low-alloy steels are isothermally aged in the temperature range 375°-560°C (McMahon, 1975). The same effect may also be observed when a steel is cooled slowly after tempering at relatively high temperatures. This is particularly important in practice since large castings cannot be rapidly quenched and their cores may take days to cool to room temperature.

As in O.S.T.E., phosphorus is again the main contributory cause since it segregates readily to the grain boundaries unless its diffusion is retarded by the addition of alloying elements such as molybdenum, titanium or boron.

However, after prolonged exposure to the ageing temperature, other more potent embrittlers such as Sb and Sn may also segregate to the grain boundaries and within 100-200hrs. sufficient segregation can occur to induce intergranular brittle fracture (Mulford et al, 1976).

The actual mechanism of crack nucleation in T.S.T.E. is not yet fully understood. Kameda and McMahon (1980) observed a crack which appeared to have nucleated at the interface between the matrix and a non-metallic inclusion, but recent work by Wirth and Clarke (1981) suggests that fine needle-like precipitates of an unidentified compound may be responsible. Although these precipitates have been observed at the prior austenite grain boundaries of embrittled En30A, the results are by no means conclusive, and further investigations are warranted.

It is, therefore, clear that both one-step and two-step temper embrittlement processes are liable to occur during the heat treatment of large steel castings. In order to minimise this possibility, the first obvious approach is to produce the cleanest possible steels with minimum impurity contents. However, there are practical and economic limits to which this can be achieved, and so the other approach is to attempt to minimise the segregation of impurity elements to the grain boundaries. It has already been noted that Mo additions can retard phosphorus segregation, but the effect relies on the presence of the large Mo atoms in solution, not precipitated as carbides. Consequently, the effectiveness of Mo in suppressing phosphorus induced intergranular fracture depends not only on the Mo:P ratio, but also on the carbon content of the steel which determines the solubility of the Mo. A similar problem is also encountered with Ti, which readily forms carbides and nitrides, thus negating its effect. Seah et al (1979) showed beneficial effects of rare-earth elements in controlling T.S.T.E., but additional problems were encountered owing to the formation of RE-oxysulphides which reduced the upper shelf energies.

3.4.1.2 Hot Tearing

Although hot tearing is, strictly speaking, an interdendritic rather than an intergranular embrittlement phenomenon, it is included here since it represents one of the most common and serious defects encountered in steel castings (Middleton, 1966).

The nature of the fracture arising from a hot tear is shown in Figs. 3.17 and 3.18.

It is now generally accepted that hot tearing occurs within the solidification range before the steel is completely solid. Certain characteristic features of the tearing process have been known for some time, and are relevant to the hot cracking of other cast metals besides steel (Clyne, 1976).

These are:

i) The stresses which lead to crack formation originate mainly from the freezing contraction of the metal, which can be assumed to be constant within the normal range of steel compositions. (Kondic, 1968).

ii) Cracking occurs in the solid/liquid two-phase region when the fraction solidified is large. (Bishop, Ackerlind and Pellini, 1958).

iii) The interdendritic cohesion and liquid distribution in the cracking region are extremely important in determining the ability of a casting to withstand the thermal contraction stresses (Metz and Flemings, 1970).

Details of the processes available for strain accommodation may be found in Clyne (1976).

From the considerations above, it is clear that two of the main factors which promote hot tearing are

a) Mould restraints (cores, inserts or the inherent casting design) which accentuate the contraction stresses.

b) The presence of a temperature gradient along the casting which generates a "hot spot". This region will still contain a film of interdendritic liquid after solidification of the remainder of the casting is complete.

An example combining (a) and (b) would be a casting containing thick members which are restrained by already solidified, quicker cooling areas.

Various experimental techniques have been employed to study the hot tearing susceptibility, but the most quantitative method involves the use of a "dog-bone" shaped casting (Fig. 3.19). This was initially devised by Clyne and Davies (1975) to study solidification cracking in aluminium alloys, but has been adapted by Shin (1981) to evaluate the effects of compositional variables in steel. Using the electrical resistance method of Clyne and Davies (1975) it is possible to calculate a quantitative measure of the area of cracking (X_{cr}) such that $X_{cr} = 0$ for an uncracked casting, and $X_{cr} = 1$ for a completely broken sample.

In addition to examining commercial low C steels, Shin (1981) studied binary alloys of Fe with S, Mn, P, Si and C and also the ternary Fe-Mn-S and Fe-Mn-Si systems. The most pronounced effects on hot tearing were shown to be from sulphur and phosphorus which segregate strongly to the interdendritic regions during solidification. Silicon also proved to be deleterious, but both sulphur and silicon were rendered harmless by the addition of manganese to the melt. This is in agreement with previous observations by Middleton (1966). However, it is recognised that in commercial steels, the effects of a combination of alloying elements on cracking susceptibility is by no means clear, since there may well be solute interactions which influence the potency of each element.

3.4.2 Precipitation Effects

There are many examples of intergranular failure being initiated by the presence of grain boundary precipitates, some of which will be discussed later in this section.

Plateau et al (1960) proposed a mechanism for brittle inter-granular fractures which propagate in a semi-ductile manner due to the presence of precipitates. He suggested that micro-cracks are nucleated either by fracture of the precipitates or by decohesion at their interface with the matrix. Crack propagation by the linking of these microcracks results in the fracture having the dimpled appearance characteristic of ductile failure on a microscopic scale, while at the same time being confined to the immediate vicinity of the grain boundary.

Hondros and McLean (1976) have considered the way in which grain boundary cohesion is affected by the presence of hard particles. Schematically, the situation is shown in Fig. 3.20, where γ_b and γ_{m-p} are the energies of the metal/metal and metal/particle interfaces and γ_s and γ_p are the average surface energies of the metal and the particle.

The cohesion at the particle/matrix interface compared to the grain boundary cohesion is given by

$$\frac{\gamma_{m-p}^*}{\gamma_{b}^*} = \frac{\gamma_s + \gamma_b - \gamma_{m-p}}{2\gamma_s - \gamma_b} \qquad (3.9)$$

The term γ_{m-p}^* is referred to as the work of adhesion. Although values of the interfacial energy have been measured experimentally

for only a few systems, Navara and Easterling (1971) measured the work of adhesion for alumina particles in iron by examining the contact angle between a decohered particle and the matrix after an equilibrium anneal.

Using their data, Hondros and McLean (1976) calculated $\frac{\gamma^*_{Fe\text{-}Al_2O_3}}{\gamma_b^*}$ = 0.22, which shows the extremely low strength of the $Fe\text{-}Al_2O_3$ interface compared to that of the original grain boundary, and therefore fracture is likely to proceed by the separation of this interface. In general, the tendency of a precipitate to promote an intergranular failure will depend on both the nature of its bonding to the matrix and the morphology of the precipitate.

Once again, it must be emphasised that the strength of cohesion of the interface is only used as a comparative measure of the fracture strength. It is well known that most materials can fail at stresses up to several orders of magnitude below those predicted theoretically as a result of localised stress concentrations.

The concept of a slip band intersecting a hard non-deformable particle to produce a crack nucleus has been introduced by Smith (1966). The high stresses which build up at the head of a slip band may either result in the decohesion of the particle/matrix interface or may be sufficient to generate a shear crack through the particle. Such a crack, once nucleated, will follow the most energetically favourable route, which is likely to be along the already weakened grain boundaries.

Some specific instances of intergranular fracture in steel castings caused by precipitation phenomena will now be discussed.

3.4.2.1 Aluminium Nitride Precipitation

This is considered by many to be the single most important cause of intergranular fracture in steel castings and there have been many investigations into the phenomenon over a number of years. Despite the abundance of work, however, details of the mechanism by which embrittlement occurs and realistic ways of avoiding it have not been unequivocally established. Consequently intergranular failures continue to occur and the topic will be discussed in greater detail in Chapter 4.

Macroscopically, the fracture morphology is characterised by the presence of coarse angular facets which are closely related to the as-cast grain boundaries of the casting, despite the fact that these boundaries may have been replaced by a new system of grain boundaries during heat treatment. Unlike the case of temper-embrittled samples (Fig. 3.14) the facets show some relief and often appear dull, with occasional bright reflections from features on the surface.

After the initial observations by Jolivet (1942) that intergranular fracture could be caused by the "deposition of metallographic constituents such as cementite or some other non-metallic phase" and frequently occurred in aluminium-killed steels, the first positive evidence that aluminium nitride could be a cause came from Lorig and Elsea (1947). These authors varied the aluminium and nitrogen contents of a 0.30%C, 1.60%Mn steel and showed that a high level of these elements in conjunction

with a slow cooling rate increased the susceptibility to intergranular fracture.

AlN was identified as the cause by X-ray analysis of residues separated from the steel electrolytically. In the steels containing high aluminium and nitrogen it was possible to observe a grain boundary network of precipitates in the optical microscope. These appeared as needles growing into the austenite grains adjacent to the boundary.

Lorig (1952) proposed a mechanism for intergranular failure whereby the crack propagates between these needles in a transgranular manner near to the grain boundary. Macroscopically, this results in the fracture having an intergranular appearance, though microscopically crack propagation has occurred by a series of steps between the AlN needles adjacent to the grain boundary. A schematic representation is shown in Fig. 3.21.

More detailed investigation of the fracture process was made possible by the development of microfractographic techniques in the transmission electron microscope (TEM). Wright and Quarrell (1962) observed two idiomorphic forms of AlN on replicas extracted from the fracture surface. These were plates and dendrites, both of which could be positively identified as AlN by electron diffraction, although no attempts were made to explain the reasons for the two different morphologies. It was found that the plates were associated with flat, featureless facets on the fracture surface which gave rise to the occasional bright reflections when viewed optically. The dendritic form resulted in microductile failure occurring round the precipitate

near to the grain boundary. This observation was supported by the later work of Altmann et al (1965).

Although Lorig (1952) described the fracture as occurring round "needles" of AlN, it should be remembered that the dendrite arm spacing observed by Wright and Quarrell was extremely fine (~2μm) and these precipitates would therefore appear as needles in the optical microscope. The important concept revealed by these investigations is that although grain boundary AlN gives rise to a fracture which appears intergranular, the micro-mechanisms of crack propagation depend to a large extent on the properties of the matrix, since the fracture path is not exactly coincident with the boundary.

3.4.2.2 Sulphide Precipitation

After aluminium nitride precipitation, this is the second most common cause of IF in steel castings, and may contribute to the embrittlement in several ways.

a) Type II MnS Precipitates

It is well known that the morphology of MnS inclusions in steel is determined mainly by the oxygen content (Baker and Charles 1972, 1973). Under normal circumstances steel castings which have been deoxidised thoroughly with aluminium contain Type III (angular) MnS inclusions. If, however, insufficient Al is added or segregation of aluminium has given rise to high local oxygen contents, then the dendritic Type II MnS inclusions may be encountered (Jackson 1977). Since they occur in sheets, these can initiate pseudo-intergranular fracture in a casting and reduce the upper shelf energy quite significantly.

In order to avoid the formation of type II MnS, it is necessary to ensure that sufficient Al is added to promote type III sulphides. This provides yet another motive for the tendency to add excessive amounts of aluminium, which may in turn result in intergranular fracture from AlN embrittlement.

b) Overheating

This phenomenon occurs in both cast and wrought steels and is associated with the secondary precipitation of MnS at the austenite grain boundaries during cooling from high temperature. In wrought steels, this normally occurs after the dissolution of the primary sulphides by a high temperature austenitising treatment, but Brammar et al (1959) and Baker and Harrison (1975) have shown that a similar effect can take place during the slow cooling of large steel castings after solidification is complete. Examination of a 0.15%C, 3%Ni investment casting containing 0.02%S and 0.009%P revealed a matt intergranular fracture surface with extensive arrays of fine equiaxed dimples nucleated by very small (0.5μm) particles of MnS (Baker and Harrison, 1975). Additionally, towards the centre of the casting smooth facets were observed which were found to be associated with intergranular films of iron phosphide (FeP not Fe_3P).

A mechanism was proposed for the precipitation process (as shown in Fig. 3.22) wherein the solute-rich interdendritic regions give rise to a film of iron phosphide at the intersections with the austenite grain boundaries. On subsequent cooling through the austenite region, those areas on the grain boundary which do not contain the phosphide act as sites for the precipitation of the secondary sulphides. Thus, as Fig. 3.22 shows, there is a

transition from MnS-induced IF at the surface of the casting to FeP-induced IF at the centre.

c) Other Sulphides

Leger and Guillaume (1979) have identified large intergranular precipitates of AlS and Al-rich MnS in a steel casting containing 0.10%Al together with an abnormally low Mn content of 0.31%. These sulphides were much coarser than AlN precipitates and could be seen clearly on a polished micro section, but the resulting fractures were similar in appearance to AlN-induced IF, though slightly more "shiny". However, most commercial steel castings contain much higher manganese contents than 0.31%, and for this reason the sulphides are almost exclusively MnS. Therefore under normal circumstances the precipitation of AlS is unlikely to be a problem.

3.4.2.3 Niobium Carbide Precipitation

Hannerz et al (1968) and Gibson (1979) have reported instances of intergranular failure in large steel castings which were attributed to the presence of niobium carbide precipitates at the as-cast grain boundaries.

The casting examined by Hannerz et al was a crankshaft for a naval diesel engine with an as-cast weight of 20 tonnes, and a nominal composition of 0.22%C, 0.76%Mn and 0.068%Nb. Fractographic examination revealed features similar to those observed on AlN-embrittled surfaces (a dull background interspersed with shiny facets) and large plates of NbC were identified by electron diffraction (Fig. 3.23). By considering the precipitation process to be controlled by the rate of diffusion of niobium, and knowing the cooling rate of the casting the authors

calculated the thickness of the precipitate to be ~2000Å. It was found that the precipitate could be redissolved only by solution treatment at temperatures of 1400°C or above which is clearly impractical on a commercial scale.

Gibson (1979) reported the presence of coarse filamentary NbC precipitates on the partially intergranular fracture surface of a large node steel casting containing 0.13%C, 1.30%Mn, 0.055%V and 0.025%Nb.

In both these instances, fracture appears to have been caused by the separation of the particle/matrix interface as suggested in Section 3.4.2, rather than by the fracture of the precipitates.

3.4.2.4 Vanadium Carbide Precipitation

This has been identified as a possible cause of IF by Barnard and Brook (1976) who observed dendritic vanadium carbide precipitates on the fracture surface of a 2%Ni-Cr-Mo-V ingot, and by Naumann and Spiess (1973) in a 42 tonne Cr-Mo-V casting. In the latter case, the precipitate was present in a massive plate-like form. In neither case were the mechanical properties impaired as seriously as with other forms of intergranular embrittlement. Nevertheless, the effect was significant. This was particularly so for the investigation reported by Barnard and Brook, where other precipitates, namely aluminium nitride and manganese sulphide were also present to exacerbate the problem.

3.4.2.5 Boride and Carboboride Precipitation

A minor cause of intergranular fracture was investigated by Mahmoud (1974), who reported the presence of small globular carboboride precipitates and a massive semi-continuous boride

film at the prior austenite grain boundaries of steel castings containing 0.002-0.006% boron. The former promoted a dimpled intergranular fracture with voids initiated by the carboboride while the latter resulted in a much smoother fracture appearance similar to that associated with temper embrittlement.

Ion microprobe analysis showed both forms of precipitate to have a complex chemistry, the carboboride having a composition of approximately $(Fe_{0.9}, M_{0.1})_{20-22}$ $(C_{0.1}, B_{0.9})_{5-6}$ and the boride being based on Fe_2B, with other elements replacing Fe in solution.

In order to minimise the effects of these two constituents, it was suggested that since optimum boron contents for hardenability purposes are in the range 0.001-0.003% (the hardenability effect relies on soluble boron) excessive additions have little beneficial effect and should be avoided.

Chapter 4

Aluminium Nitride in Cast Steels

4.1 Introduction

The influence of aluminium nitride on the structure and properties of steel has only been fully appreciated since a method for its chemical determination was developed by Beeghly (1949). Since that time, a considerable amount of work has been carried out to determine the effect of this precipitate on the mechanisms of phenomena such as intergranular fracture, grain size control, forging break-up and ingot panel cracking, and a correlation between AlN and these features is now generally accepted.

This chapter examines the techniques available for the observation and detection of AlN and discusses some of the consequences of AlN precipitation with respect to the structure and properties of cast steels.

4.2 Detection, Observation and Identification of AlN

The structure of aluminium nitride is close packed hexagonal (similar to ZnO) with lattice parameters $a = b = 3.11\text{Å}$, $c = 4.99\text{Å}$. It melts at 2200°C and 4 atmospheres pressure, but dissociates at pressures below this. AlN is hydrolised slowly by water and more rapidly by mineral acids to form alumina and ammonia as decomposition products. This means that during the extraction of AlN from the matrix (either for chemical analysis or for metallographic purposes) care must be taken to ensure the reagents used are anhydrous.

4.2.1 Chemical Methods of Detection

The most widely used method for determining the aluminium nitride content of steel has been that developed by Beeghly in 1949.

This involves the dissolution of the matrix in an anhydrous ester/halogen mixture (typically bromine/methyl acetate) followed by filtration and the determination of nitrogen in the residue by a distillation procedure. The original claims by Beeghly that the method was unaffected by the presence of other alloying elements in steel resulted in this technique being used extensively to determine the "%N as AlN". Several authors including Woodfine and Quarrell (1960) and Jackson and Bradshaw (1970) attempted to define minimum "%N as AlN" values below which intergranular fracture could be avoided. However, not only do many other factors have an influence on the susceptibility to IF, but as Swinburn and Melia (1970) have pointed out, the Beeghly method cannot be assumed to separate AlN alone from the matrix. Other nitrides such as Si_3N_4 and SiN are also insoluble in the ester-halogen solution, and may be included in the analysis. As a consequence, the validity of some predictions based on this criterion is seriously in question. Swinburn and Melia suggest that a more accurate description of the Beeghly method would be to say that it determines the nitrides which are insoluble in the ester/halogen solution, but soluble in sodium hydroxide (used for the determination of nitrogen in the residue).

More recently, a hydrogen extraction method has been developed by Baker et al (1979) to determine the mobile nitrogen content of a sample of steel at different temperatures. Knowing the dissociation temperature of the various nitrides present and the total nitrogen content of the steel, it is then possible to calculate the amount of nitrogen present as each individual nitride. This work has further emphasised the inadequacies of

the Beeghly method, since it was found that manganese-silicon nitride may also remain undissolved in the bromine/methyl acetate solution.

However, in a great number of instances where there is no interference from other nitrides, the Beeghly method is valid, and it would be wrong to cast doubt on all correlations based on this technique.

4.2.2 Metallographic Techniques

Grain boundary precipitates of AlN can be extremely fine when viewed in a metallographic section, and as Woodfine and Quarrell (1960) pointed out, the inability to detect a grain boundary phase in the optical microscope cannot be taken to imply its absence. For example, in one sample whose fracture was 80% intergranular, no metallographic evidence of AlN could be found, even though the Beeghly method of analysis indicated 0.005%N as AlN. It is usually only when the aluminium and nitrogen contents of the steel are high (~0.15%Al, ~0.015%N) that AlN can be resolved optically.

When viewed unetched and in reflected light aluminium nitride appears dark grey in colour, but it can be seen more easily using polarised light, under which it is strongly anisotropic. Lorig and Elsea (1947) and Woodfine and Quarrell (1960) found that an etchant of picric acid in alcohol highlighted the grain boundary AlN, particularly when a wetting reagent such as zephiran chloride was also used.

It was not until 1962 that direct observation and identification of AlN was made by Wright (1962) using microfractographic

techniques in the T.E.M. This involved the deposition onto the fracture surface of a thin carbon film which was subsequently removed using a solution of 5% bromine in ethyl alcohol. Intergranular fracture surfaces were found to be covered by AlN precipitates, which had been extracted onto the carbon during replication. Selected area electron diffraction techniques were used to identify the AlN, and the measured spacings agreed moderately well with published ASTM data. Baker (1962) suggested that the slight deviations (5%) from the published spacings may have resulted from the presence of other elements in solution in the AlN.

The development of the SEM with energy dispersive analysis has also been useful for the examination of intergranular fractures, and IF caused by AlN precipitation can be identified by its characteristic appearance in the SEM (see Chapter 6).

4.2.3 Other Techniques

Techniques such as electron probe microanalysis (e.p.m.a.) have limited use as tools for examining AlN precipitates, since it is necessary to use polished microsections for quantitative analysis and the precipitates are not readily visible.

Mahmoud (1974) used ion microprobe analysis on intergranular fracture surfaces to identify a complex form of AlN which contained small amounts of Fe, Mn, Si, Cr, Ca and Ti in solid solution. However, the limited availability of this technique and the complex experimental requirements mean that the method is little used.

A novel technique for detecting AlN in steel castings was devised

by Steck (1969) who claimed to be able to differentiate between embrittled and good castings by ultrasonic testing. It was found that if the ultrasonic probe was positioned perpendicular to the columnar grains of the casting, there would be an additional attenuation of the beam due to the presence of AlN at the prior austenite grain boundaries. This of course would be true for any grain boundary network, and not just for AlN. Steck suggests the technique may also be able to detect the presence of large amounts of Type II MnS inclusions.

4.3 AlN as a Cause of Intergranular Fracture

The term "Rock Candy" fracture is widely used within the steel foundry industry to imply intergranular embrittlement caused by the precipitation of aluminium nitride. However, because of the ambiguities involved in a descriptive term of this kind, the term will be avoided in the remainder of this work and inter-granular fracture caused by AlN precipitation at the prior austenite grain boundaries will be designated "IF". Lorig and Elsea (1947) identified AlN as a possible cause of intergranular fracture when they examined a defective commercial casting which had an unusually high aluminium and nitrogen content. At high magnifications in the optical microscope (>1000x) they were able to observe chains of non-metallic particles which appeared to follow the original columnar grain boundaries around which fracture had occurred.

Using experimentally melted casts of base composition 0.30%C, 1.60%Mn, 0.50%Cr, 0.35%Mo, they varied the aluminium and nitrogen contents and after heat treatment (quench and temper) samples were broken by slow three point bending. Although it was not possible

to analyse individual castings for Al and N, a clear correlation between the amount of Al added during deoxidation (varied from 0-28lb/ton*) and the degree of intergranular fracture was noted. Increasing the amount of Al added resulted in an increased tendency for IF up to about 8lb/ton (0.40%). With Al additions greater than 20lb/ton (0.89%), however, the percentage IF on the fractures decreased. Later work by Woodfine and Quarrell (1960) attributed this to the precipitation of AlN in the melt. This was in a coarse, random form which acted as a nucleus for subsequent solid state precipitation and prevented the formation of a grain boundary network.

Lorig and Elsea also noted a correlation of %IF with the nitrogen content and the cooling rate of the casting. For a given Al content, the amount of IF observed increased with increasing nitrogen content and decreasing cooling rate, both of which tend to promote AlN precipitation.

Fig. 4.1 presents a summary of the effects of these three important variables (%Al, %N and cooling rate). Compositions corresponding to points above and to the right of each curve are likely to be susceptible to IF at the cooling rate represented.

* Since the actual Al contents were not analysed, this nomenclature will be retained: as a guide, 1lb/ton ≈0.05%Al, assuming 100% recovery.

Lorig and Elsea stressed, however, that the curves were obtained from single test results and showed only trends. They cannot be used to predict "safe" Al and N levels to be sure of avoiding IF. Hannerz (1968) used a theoretical model to predict similar curves and despite the questionable nature of some of his approximations the agreement with Lorig and Elsea's measurements was quite good. The model was based on IF occurring when a continuous layer of AlN of critical thickness is precipitated at the grain boundaries. This required an integration of the precipitation rate over a range of temperatures to estimate the total AlN thickness for different Al and N levels.

4.3.1 Effect of Heat Treatment

It was noted by Lorig and Elsea (1947) that castings which had been hardened and tempered were more likely to fail in an intergranular manner than those which had been normalised or were as-cast. Wright and Quarrell (1962) explained this in terms of the relative strength of the matrix and the grain boundary (see Chapter 3.4). When the matrix strength is increased by heat treatment the grain boundaries provide a relatively more favourable route than they do when the matrix strength is low. Wright (1962) tempered a 0.27%C, 1.06%Mn steel at various temperatures between 150°C and 650°C to obtain different strength levels, and performed mechanical tests at room temperature. A transition was observed from ductile failure at high tempering temperatures (lower matrix strength) to an intergranular mode corresponding to the lower tempering temperatures (higher matrix strength). At the lowest tempering temperatures a point was reached where cleavage became the predominant fracture mechanism in the

martensitic steels.

The concept of removing IF by a high temperature solution treatment was considered by Lorig and Elsea (1947). They homogenised samples containing 1½lb/ton (0.07%) and 3lb/ton (0.15%) of aluminium for 2 hours at 1260°C and found that by rapid cooling in oil, IF was eliminated in the first case, and reduced in the second. Woodfine and Quarrell (1960) repeated some of this work on a steel containing 0.06%Al and 0.016%N, and found that solution treatment at 1260°C followed by water quenching was sufficient to eliminate IF, and that slow cooling from the solution temperature resulted in fracture occurring round the newly established austenite grains. This implied that the AlN was being dissolved from the prior austenite grain boundaries. Rapid cooling resulted in its retention in solid solution, whilst slow cooling allowed precipitation to occur at the new austenite boundaries. Harris and Chandley (1962) came to the same general conclusions, but all these authors can be criticised for assuming that IF can be universally removed by such a heat treatment. Clearly the success in dissolving the AlN grain boundary network will depend on the Al and N contents of the steel in question, which in turn dictate the solubility temperature. This will be discussed further in Section 4.4 of this Chapter.

4.3.2 Effect of Chemical Composition

The effects of aluminium and nitrogen contents on the susceptibility for IF have already been discussed in Section 4.3.

Wright and Quarrell (1962) examined the influence of carbon, manganese, sulphur and phosphorus on mechanical properties. A low carbon content (0.12%) was found to favour a fibrous fracture mechanism, whilst high carbon contents were associated with cleavage failure. It was only at intermediate levels of carbon that intergranular fracture was encountered.

This is in some ways analogous to the effects of tempering temperature (Section 4.3.1), in that a relatively low strength matrix (low carbon cf high tempering temperature) favours ductile failure and a higher strength matrix (higher C, lower tempering temperature) tends to promote IF. In cases where the matrix is hard and brittle (high C, or untempered) cleavage fracture predominates.

Manganese was also found to have an effect on the susceptibility to IF, and this can again be interpreted in terms of its effect on matrix properties. Wright and Quarrell (1962) found that by increasing the manganese content of a 0.30%C steel from 0.50% to 2.14%Mn, the fracture mode changed from fibrous to a mixed fibrous/intergranular mode. A corresponding increase in tensile strength and reduction of ductility was noted.

Although little effect of phosphorus content was observed, sulphur had a marked influence on fracture behaviour, and Wright and Quarrell's work resolved a paradox which had confused researchers for a number of years. This was the fact that Bessemer steels (often high in nitrogen) rarely exhibited IF, whereas in high quality armour plate steels the phenomenon was frequently observed. Wright and Quarrell's results showed that

a high sulphur content could promote a premature ductile failure because of the ease of void nucleation at the sulphide inclusions present. This was the case with Bessemer steels. In contrast, the armour plate steels were invariably low in sulphur and very clean, making intragranular void nucleation more difficult and grain boundary failure correspondingly more favourable.

The use of more powerful nitride forming elements such as titanium and zirconium to combine with nitrogen and avoid aluminium nitride formation has been considered by several workers. Woodfine and Quarrell (1960) showed that both titanium and zirconium could be used successfully to replace aluminium for deoxidation without giving rise to IF, since both form stable nitrides which do not precipitate on the grain boundaries. However, whereas titanium additions were found to prevent IF even in the presence of aluminium, this was not the case for zirconium. The explanation given by Woodfine and Quarrell was that since the stability of the oxides and nitrides decreases in the order ZrO_2, Al_2O_3, TiO_2, ZrN, TiN, AlN, combined titanium and aluminium additions tend to give Al_2O_3 and TiN, whereas combined zirconium and aluminium additions result in the formation of ZrO_2, leaving the aluminium free to form AlN.

Baliktay (1976) and Höner and Baliktay (1978c) have pointed out that provided the deoxidants are added in the correct sequence (i.e. Al added before Ti or Zr) a combined addition of these elements can be beneficial. Indeed this practice is adopted in several large foundries in the UK and has been successful in reducing the occurrences of IF (Wilson, 1981). However, many

smaller foundries without access to vacuum degassing facilities have found that the use of titanium for deoxidation results in a 'dirty' steel with poor upper shelf toughness properties, and are therefore reluctant to change their practice. (Jackson, 1980).

Lorig and Elsea (1947) and Fremunt (1962) found a beneficial effect of molybdenum on the susceptibility to IF, which they attributed to the retardation of nitrogen and aluminium diffusion by the large Mo atoms in the matrix, thus hindering AlN precipitation.

The effect of other alloying elements is not clearly defined in the literature, although it is to be expected that elements which refine the primary grain structure will reduce the susceptibility to IF by increasing the grain boundary area. For example Fremunt (1962) noted a suppression of IF by the addition of small quantities (unspecified) of niobium, which gave a fine grain size because of the formation of NbC precipitates.

It can also be anticipated that elements which increase the matrix strength will promote IF by decreasing the grain boundary: matrix strength ratio, although other factors may outweigh this contribution. An example is boron which, despite increasing the matrix strength, also forms a stable nitride and can have a beneficial effect on properties (Lorig and Elsea, 1947).

Alloying elements can also influence the precipitation temperature of aluminium nitride by their effect on the solubility product. Solute element interactions of this nature will be considered in Section 4.4.

4.4 The Solubility of AlN in Steel

4.4.1 In Austenite

Although several investigations of the solubility of nitrogen in γ-iron have been reported (Sieverts 1931 and 1938, Iwase and Fukusima 1939), the first extension of the work to determine the solubility of AlN in steel was by Darken et al (1951). These workers determined the nitrogen contents of aluminium-killed steels equilibrated with nitrogen gas at temperatures above 1000°C. For a given temperature, the equilibrium nitrogen content was found to be independent of the aluminium level up to a critical amount, whereupon the nitrogen content rose abruptly. (See Fig. 4.2). This rise was explained as being due to the formation of AlN, and the solubility product (K_s) could be determined from the position of the break in the curve. The values of K_s thus found were plotted against the reciprocal of the absolute temperature and gave the following empirical relationship:

$$\log_{10} [Al] [N] = - \frac{7400}{T} + 1.95 \qquad (4.1)$$

Numerous subsequent investigations* have predicted equations with similar slopes, but with lower values of the constant term. Thus,

* See, for example, Leslie et al (1954), Pearson and Ende (1953), Pehlke and Elliot (1960), Erasmus and Mech (1964), Irvine, Pickering and Gladman (1967), Höner and Baliktay (1978a), and König et al (1961).

equation (4.1) represents an upper limit to the solubility of AlN which can be expected. The reasons for the differences have been interpreted by Leslie et al (1954) in terms of segregation and the slow attainment of equilibrium conditions. To take these factors into account, they predicted an "apparent solubility product" (Kapp), given by

$$\log_{10} \text{Kapp} = \frac{-6770}{T} + 1.03 \qquad (4.2)$$

Inadequacies in the analysis technique were discounted by Leslie et al as a reason for the discrepancies in measured solubility product, since it was considered that the Beeghly technique would tend to underestimate the amount of nitrogen present as AlN. This, they reasoned, would result in an apparent increase in solubility product, since $N_{sol} = N_{total} - N_{AlN}$.

However, it is interesting to note that unlike all subsequent investigations, the work of Darken et al did not utilise the Beeghly method for the solubility determinations, and it has since been shown that in certain circumstances the Beeghly method can result in <u>overestimations</u> of the %N as AlN (see Section 4.2.1). Therefore it could be that equation (4.1) describes the solubility product more closely than has previously been assumed.

Gladman and Pickering (1967) collated the solubility data available and using this, together with their own results for a 0.1%C steel, derived a "mean" solubility product given by

$$\log_{10} [Al][N] = \frac{-7500}{T} + 1.48 \qquad (4.3)$$

Table 4.1 presents some of the empirical equations together with

the relative solution temperature predicted for a steel containing 0.1%Al and 0.01%N. It can be seen that this temperature can vary by as much as 200°C, which is by no means obvious when the data are presented graphically as in Fig. 4.3.

A more satisfactory method of presenting the solubility data is that used by Gladman and McIvor (1972). This relates the aluminium and nitrogen contents of a steel which are soluble at a given temperature. Fig. 4.4 shows an example of this solubility diagram extended to take into account the higher aluminium contents frequently encountered in cast steels.

4.4.2 In Liquid Steel

The solubility of AlN in the liquid state has not been thoroughly investigated, but Höner and Baliktay (1978a) found a similar temperature dependence to that obtained for the solubility in austenite (see Fig. 4.3). For a GS-60 steel containing 0.40%C, 0.8%Mn they obtained the following relation in the range 1550-1750°C

$$\log_{10}[Al][N] = \frac{-8490}{T} + 2.37 \qquad (4.4)$$

4.4.3 Solute Interactions

The presence of alloying elements in austenite or liquid steel can alter the solubility of AlN quite significantly by solute interactions. The effects on the solubility of nitrogen in liquid steel have been shown schematically in Fig. 2.5, and interaction

coefficients have been evaluated by a number of workers.*

The effects of alloying elements on the solubility of Al have not been determined extensively, but what data are available are listed in Tables 4.2 and 4.3. These give values of $e_N^{\times}$ and $e_{Al}^{\times}$ in liquid steel and in austenite, where $e_N^{\times} = \frac{\log f_N}{\%\times}$ for $\%\times \rightarrow 0$

f_N is the activity coefficient for N. Elements with a positive interaction coefficient thus tend to decrease the solubility.

A useful correlation has been established by Mori and Ichise (1968) for nitrogen in situations where the interaction coefficient in austenite is not known. This makes use of the fact that there is an empirical relation between interaction parameters of nitrogen in liquid iron and in austenite, which can be represented thus:

$$e_N^{\times}\ (1200^{o}C) = 1.9\ e_N^{\times}\ (1600^{o}C) - 0.005 \qquad (4.5)$$

$$e_N^{\times}\ (1000^{o}C) = 3.1\ e_N^{\times}\ (1600^{o}C) - 0.016 \qquad (4.6)$$

4.5 Precipitation of AlN

4.5.1 Temperature of Precipitation

Under isothermal conditions, the precipitation of AlN is typical of precipitation from supersaturated solid solutions in that the rate is slow at high temperatures, reaches a maximum at intermediate temperatures and decreases again at lower temperatures (C-curve behaviour). Leslie et al (1954) determined the maximum

* For example, Pehlke and Elliott (1960), Schenck et al (1958), Schurmann and Kunze (1967), Uda and Pehlke (1974), Maekawa and Nakagawa (1959), Evans and Pehlke (1964), Gomersall et al (1968), Leewis and Maclean (1979), Wada and Pehlke (1978).

precipitation rate to be at about 800°C, and this has since been confirmed by other workers (Wiester et al (1957), Takei et al (1964), Wertebach and Hoff (1958)).

However, it would be inappropriate to apply such results to explain precipitation phenomena in cast steels for two reasons. Firstly, precipitation does not take place under isothermal conditions, since castings usually cool slowly over several hours or even days. Secondly, the results of Leslie et al can only be applied to steels with similar (low) aluminium and nitrogen contents to the ones examined by them. Clearly any increase in the amounts of these elements present will increase the solubility temperature, and hence the AlN will begin to precipitate at a correspondingly higher temperature during cooling.

Reference to Fig. 4.4 shows that for the aluminium and nitrogen contents likely to be encountered in a casting (typically up to 0.10%Al, 0.010%N) the temperature at which a component becomes insoluble may be in excess of 1350°C. This also ignores the effects of any micro- or macro-segregation of Al and N which may exist, which would tend to increase the precipitation temperature in enriched areas.

Therefore it can be expected that precipitation of AlN may take place in the upper range of the austenite region, if the cooling rate is slow enough. Indeed, Barron (1974) and Chojecki and Kowalowka (1978) suggest that for high Al and N contents precipitation may take place in the liquid during solidification. As described earlier, the precipitation of AlN in a <u>random</u> form in the liquid has been cited by Woodfine and Quarrell (1960) to

explain why castings with very high Al contents often do not show IF.

4.5.2 Precipitate Morphology

Lorig and Elsea (1947) were the first to suggest that AlN could occur in two idiomorphic forms, although the low resolving power of the optical microscope they used meant that they were unable to distinguish clearly between the two. Wright and Quarrell (1962) resolved the problem by using microfractographic techniques when they identified AlN on fracture surfaces in the form of plates and dendrites, (Figs. 4.5 and 4.6). However, no attempt was made to distinguish between the precipitation conditions under which each of these had occurred. It was found that the majority of the precipitates were of the dendritic kind, and appeared to have nucleated at the original austenitic grain boundaries, growing into the grains with a crystallographic relationship between the arms. In most cases, the dendrites appeared asymmetric, with secondary arms growing from only one side of the primary arm. Thus it was implied that dendritic precipitation was taking place in the solid state. Although this has been shown to be possible in certain Cu and Ti alloys during isothermal annealing (Bainbridge, 1972) and for some carbides in steel (Stickler and Vinckier, 1961 and Wilson, 1971) these systems resulted in the formation of small, ill-defined dendrites and not the extensive arrays typical of the AlN precipitate.

It is, therefore, unclear at what stage of primary cooling the dendritic precipitates form. Most workers seem to have assumed that precipitation occurs in the solid state, because this is the

experience from steels where only small amounts of Al are added for grain refinement. It has already been shown, however, that solution temperatures for the amounts of AlN likely to be found in cast steels are considerably higher, and together with the effects of microsegregation, this may be sufficient to promote precipitation during solidification, (Stachura, 1969, 1971, 1977). The dendrites of AlN are much finer than the solidification structure, and measurement of the dendrite arm spacing on the fracture surfaces of Wright and Quarrell (1962) gives λ ~1μm (Fig. 4.5). This compares to typical solidification dendrite arm spacings of 20-200μm (Edvardson et al, 1976).

Altmann et al (1965) were of the opinion that the morphology of the AlN precipitates is determined by the substructure and orientation of the austenite grain boundary on which the particles grow. Some of their fractographs show regions where it is difficult to distinguish clearly between dendritic and plate-like particles. Indeed Stachura (1980) considers the plate-like form of the nitride merely to result from growth and coarsening of the arms of certain favourably orientated dendritic precipitates and it may be that there is no clear distinction between the two forms.

4.6 Other Phenomena Attributable to AlN Precipitation

4.6.1 Grain Growth Inhibition

In a pure metal, grain growth is a thermally activated process where the grain size developed is a function of time and temperature. Grain boundary mobility may be reduced significantly by the presence of a fine, randomly dispersed precipitate. Halley (1946) noted that the additon of 0.03%Al to steel increased

the temperature at which grain coarsening occurred (G.C.T.), and this was attributed to the precipitation of AlN.

A similar effect is found with titanium and zirconium (Fig. 4.7), but whereas further additions of these elements beyond 0.03% continued to increase the GCT, with aluminium a subsequent decrease was noted. Rickett and Leslie (1957) suggested that this was because at higher Al contents AlN precipitates at higher temperatures and in a coarser dispersion, making it less effective at pinning the grain boundaries.

Thus Al is frequently added to wrought steels in amounts $\leq$0.04%Al to form a fine dispersion of AlN during cooling. This then promotes a fine grain size by pinning the austenite grain boundaries effectively.

4.6.2 Impaired Hot Ductility

This is normally manifest in two different ways, and AlN precipitation has been cited as a cause of both. (Reynolds and Gladman, 1979).

4.6.2.1 Ingot Panel Cracking

These longitudinal cracks all too frequently appear in Al-treated steel ingots during cooling or on charging to the soaking pits, and steels in the range 0.4-0.7%C are particularly susceptible (Hagger, 1975). Irvine and Pickering (1957) showed that the crack path is intergranular, following the prior austenite grain boundaries, and it is thought that cracking occurs as a result of internal thermal stresses set up during the cooling of the ingot in the range 600-800^{o}C. These may be sufficient to nucleate a crack at AlN precipitates in the prior austenite grain

boundaries. This crack can then readily propagate through the pro-eutectoid ferrite network.

Desai (1959) found that the hot tensile ductility of uncracked ingots was greater at 600-700°C than for cracked ingots, and that the latter were associated with higher Al and N contents.

Control of ingot panel cracking can be achieved by the addition of titanium to ingots which are to be cooled through the susceptible temperature range, and by ensuring that ingots which are to be rolled at once are charged to the reheating furnace before the temperature falls within this range (Jackson, 1978).

4.6.2.2 Surface Break-up During Hot Working

This can occur during either forging or rolling operations and has been associated with a lowering of hot ductility caused by AlN precipitation (Erasmus, 1964 and Funnell, 1979). In each case identification of the mechanism by which AlN affects hot ductility has been hindered by difficulties in making direct observations of the high temperature structure which transforms during cooling. However, recent work by Funnell and Davies (1978) on an austenitic alloy has shown the mobility of the grain boundaries to play an important role since the boundaries must be able to migrate away from developing cavities to promote good ductility. There will obviously be a critical AlN particle size above which grain boundary migration can occur and this is likely to be a function of the volume fraction of precipitate, the initial grain size and the stored energy of deformation.

Chapter 5

Experimental Work

5.1 Introduction

The aims of the experimental programme were to obtain more detailed information regarding the mechanism of AlN-induced I.F., to study the AlN precipitation phenomena responsible for the two forms of precipitate observed by Wright and Quarrell (1962) and to examine the effects of I.F. on mechanical properties.

The steel chosen for the experimental work was BS 3100 A5/6 (1976) containing 0.30%C, 1.50%Mn. This alloy is widely used in industry for general applications where shock resistance, strength and wear resistance are important in thin section castings such as track assembly items, mine car wheels and earth moving equipment. It has also been shown to be particularly susceptible to cracking problems associated with I.F. (Lorig and Elsea, 1947; Wright and Quarrell, 1962).

Initially, 10kg induction melted castings which were high in Al and N were used to study the mechanism of I.F. in samples which were broken by slow three-point bending. The effects of some processing variables such as pouring temperature and heat treatment were also determined. Subsequently, directional solidification work was undertaken. This facilitated closer control of solidification parameters and the samples produced were used to examine the AlN precipitation phenomenon in more detail.

Quantitative information regarding the effects of I.F. on

mechanical properties was obtained using tensile, Charpy impact and fracture toughness (C.O.D.) data for embrittled and non-embrittled steels.

The techniques used throughout this work are already well-developed, and therefore have been described only briefly.

5.2 Production of Experimental Melts

All the steels used in this work were air-induction melted using one of the three practices outlined below.

Practice A

Melting unit: 12kg Radyne variable frequency induction furnace.

Lining: MgO

Base charge: 'Armco' iron punchings

Alloying additions: white iron (4.2%C)

Si metal

Mn flake

5% N/Mn flake

Al rod (99% purity)

Moulds: 75mm square CO_2/sand moulds, nominal capacity 10kg

Exothermic powder: Foseco 'Feedex 3'

Melting details: The base charge was melted at 28kW power, and when fully molten, the additions of white iron, silicon and manganese were made in that order. When the desired casting temperature was achieved (measured using a Pt/Pt-13%Rh thermocouple) the additions of N_2/Mn and Al were made by immersion into the bath. The melt was poured directly into the mould and after adding the exothermic powder was transferred to a sand pit and buried immediately after casting. This gave a slower cooling rate than

would otherwise have been attainable, thereby promoting the formation of AlN. The cooling rate at the centre of a typical casting was monitored using a Pt/Pt-13%Rh thermocouple connected to a 'Servoscribe' chart recorder and was found to have a mean value of 0.1°C sec^{-1} in the range 1100°C-800°C. Castings were allowed to cool to room temperature over a period of ~24hrs before being removed from the moulds.

Practice B

Melting unit: 70kg Birlec medium frequency induction furnace.

Lining: MgO

Base Charge: 'Armco' iron billet and punchings

Alloying additions: As for Practice 'A'

Moulds: 12.5kg CO_2/sand keel blocks

Exothermic powder: Foseco 'Feedex 3'

Melting details: As for Practice 'A', except that the melt was poured into a preheated ladle containing the Al additions. An allowance of 30°C was made for the temperature drop between bath and ladle. Each 55kg melt produced sufficient molten steel for four keel blocks.

Practice C

Melting unit: 180kg APV Paralec medium frequency induction furnace located at SCRATA.

Lining: MgO

Base charge: Low carbon 'coffin' scrap

Alloying additions: White iron, FeSi, High C-FeMn, 5%N-FeMn, Al bar (98% Al)

Moulds: 100mm square CO_2/sand moulds

Exothermic powder: Foseco 'Ferrux 16'

Melting details: As for Practice 'B'.

5.3 Chemical Analysis

Full spectrographic analysis of each cast was carried out on samples taken from the body of the casting (i.e. not from the feeder head). Carbon and sulphur levels were determined by oxygen combustion techniques (LECO). The total nitrogen content was measured either by the Feichtinger vacuum fusion technique or using a LECO gas analyser. Drillings for analysis were taken at various positions across the section of the casting to minimise the effects of segregation.

Full details of each casting used in this work can be found in Table 5.1.

5.4 Heat Treatment

a) The castings were subjected to typical commercial heat treatments in a muffle furnace after removal of the feeder heads and sectioning, where necessary. Care was taken to ensure that samples were water quenched after tempering treatments to avoid temper embrittlement.

b) High temperature heat treatments were performed in platinum-wound vacuum resistance furnaces to avoid excessive decarburisation or oxidation of the surface. Samples from selected casts were solution treated for times between 1hr and 24hrs at 1250°C and 1350°C before being either water quenched or furnace cooled. The aim of this part of the work was to determine whether the AlN present in embrittled castings could be re-dissolved as reported by Lorig and Elsea (1947) and Woodfine and Quarrell (1960).

5.5 Mechanical Testing

5.5.1 Hardness Measurements

Vickers pyramidal diamond hardness measurements were made on samples whose surface had been freshly ground on 600-grade emery paper. In all cases, the hardness recorded was the average of three separate impressions.

5.5.2 Three-point Bend Testing

In the preliminary work and on some subsequent occasions it was necessary to determine the fracture mode without the requirement for extensive sample preparation. Samples of approximately 25mm x 25mm x 150mm were cold sawn from the appropriate castings and heat treated as necessary. After removing any surface oxide layers by a linishing operation, the samples were saw-notched to a depth of ~5mm and broken by slow three point bending in a Denison hydraulic testing machine. Immediately after fracture, they were placed in a desiccator to await fractographic examination.

5.5.3 Tensile Testing

Room temperature tensile tests were carried out in accordance with BS 18 Part 2 (1971) using cylindrical samples of 150mm^2 cross sectional area and gauge length $5.65\sqrt{So}$ on a Dartec servo-hydraulic testing machine under displacement control. In the case of the square castings, the tensile samples were machined from the columnar regions to minimise the effects of porosity.

Low temperature tests were performed on the same equipment fitted with an environmental chamber. Cooling was effected using a

fine spray of liquid nitrogen, circulated within the chamber by an electric fan. In this way, the temperature was held constant to within $\pm 3^{o}C$ for 20 minutes prior to testing.

High temperature tensile testing was carried out in accordance with BS 3688 Part 1 (1963) using samples with a cross sectional area of $100mm^2$. These were soaked for 30 minutes in a resistance-heated environmental chamber at temperature (measured to within $\pm 2^{o}C$) prior to testing. Load/extension curves were plotted automatically using the read-out from a Baldwin high temperature extensometer.

5.5.4 Impact Testing

The main programme of mechanical testing employed the Charpy V-notch impact test. Samples were cold sawn from the columnar regions of test castings prior to heat treatment. The orientation of the samples is shown in Fig. 5.1 and it can be seen that the notches were positioned to allow fracture to proceed parallel to the long axis of the columnar grains. In this way any orientation effects were minimised.

After finish machining the samples were tested in accordance with BS 131 Part 2 (1972). The soaking temperatures were attained using the techniques shown in Table 5.2 and a soaking time of 15 minutes at temperature was used throughout.

Table 5.2

The media used to obtain soaking temperatures for Charpy samples.

Temperature Range	Medium
-196°C	Liquid Nitrogen
-164°C to -60°C	Isopentane/liquid nitrogen
-60°C to 20°C	Methyl alcohol/solid CO_2
20°C to 150°C	Thermostatically controlled oil bath
>150°C	Air muffle furnace

Clearly the method used for the high temperature tests was the least accurate in terms of temperature control, but in this regime it was the fracture mechanism and not the absolute value of impact energy which was of importance. Hence the variations in temperature arising during the transfer of the sample from the furnace to the Charpy machine could be tolerated.

Because of the complex nature of some of the fracture surfaces, measurements of the % I.F. were made by photographing the broken specimens, cutting out the appropriate areas and weighing on an accurate balance. The effects of density differences of the photographic paper were measured and were found to be negligible. It should be noted, however, that this technique measures the % I.F. projected onto a two dimensional surface and does not take into account the effects of surface relief. The inaccuracies introduced because of this are considered to be small.

5.5.5 Fracture Toughness Testing

Samples of the 0.30C-1.50Mn steel were tested in an embrittled and an unembrittled condition. For each case, steels were tested in the quenched and tempered state (950°C for 1½hrs, W.Q.; 600°C for 1hr, W.Q.) and the normalised state (950°C for 1hr, air cooled). Because of the excessive size requirements necessary to obtain valid K_{IC} results for this material, (Appendix 1a), the fracture toughness parameter measured was the crack opening displacement (C.O.D.).

Initially, it was intended to use small keel block castings made by Practice 'B' (Section 5.2) throughout this work, but because of the relatively fast cooling rates in the body of these small keels, it was not possible to produce a fully intergranular fracture, even with high aluminium and nitrogen contents (Casts 46/5-7). Consequently, four 100mm square ingots high in Al and N were produced using Practice 'C'. Because of the significantly slower cooling rate, these exhibited fully intergranular fracture surfaces at room temperature in the heat treated condition.

The position of the samples taken from the castings is shown in Fig. 5.2. Note that the square castings were sampled from the columnar regions to minimise the effects of porosity.

Pre-fatiguing of the test specimens was carried out in accordance with BS 5762 (1979) using an Amsler vibrophore machine fitted with a 2t dynamometer. Testing took place at SCRATA using the Dartec servo-hydraulic testing machine fitted with an environmental chamber. (Fig. 5.3). This utilised a fine thermostatically

controlled spray of liquid nitrogen circulated by a fan for the low temperature testing, and a heating element (again assisted by the fan) for high temperature testing. In this way the temperature could be varied from -190°C to +150°C, calibrated to an accuracy of $\pm$3°C.

During the tests, the machine was operated automatically in displacement control at a ram speed of 0.033mms^{-1}. Crack opening was monitored using the double clip gauge (DCG) technique which has been described by Veerman and Muller (1972), Selby and Danson (1977) and El-Soudani (1980). This is shown schematically in Fig. 5.4.

Two simultaneous plots of

(a) load vs clip gauge displacement (as required by BS 5447) and

(b) clip gauge displacement (V_1) vs clip gauge displacement (V_2) were obtained for each test.

By considering the geometry of the system (Fig. 5.4) it can be seen that if the crack front moves forward at a constant COD, then the apparent centre of rotation of the specimen must also move forward. The result is a change in the relative magnitudes of the two clip gauge signals, since the displacement at each set of knife-edges depends on the distance between the apparent centre of rotation and the knife edges. In the initial elastically loaded regime, the centre of rotation is stationary and a straight line plot of V_1 vs V_2 is obtained. However, the development of a plastic zone or a crack tip opening displacement constitutes a change in the effective crack length which gives rise to a movement of the apparent centre of rotation. This is manifest on the V_1/V_2 plot as a

displacement towards the V_1 axis, since the displacement V_1 becomes a larger fraction of V_2 as a result of the crack movement. Significant events in the fracture process were determined on the DCG plot and related to the relative position on the load/displacement curve. By correlating these points with features on the fracture surface it was possible to calculate appropriate COD values. An example of the complete procedure for obtaining the COD data is presented in Appendix 1b.

5.6 Metallographic Techniques

5.6.1 Macroscopic

In order to reveal the cast structure, samples were machined flat by grinding, and etching was carried out in acidic copper ammonium chloride solution. After depositing a layer of copper using a neutral solution, the sample was transferred into baths containing progressively higher concentrations of HCl, up to 15%HCl, where it remained for up to 8 hours. In this way, the dendritic structure of the casting is revealed by the differential etching characteristics of microsegregated regions.

5.6.2 Optical Microscopy

Samples were prepared in the usual way, by polishing on successively finer grades of emery papers and diamond wheels to a finish of 0.25μm. In cases where the metallographic work was to check the effects of heat treatment on the microstructure, a solution of 2% Nital was used as the etchant.

However, when the object was to observe the precipitates of AlN at the prior austenite grain boundaries it was found that none of the commonly available etchants nor those suggested by Lorig

and Elsea (1947), Woodfine and Quarrell (1960) and Mahmoud (1974) was suitable, since they merely highlighted the microstructural features present at the time of examination. Indeed, the tendency was to hinder observations of the AlN. The most satisfactory technique for cases where the AlN was thick enough to be resolved optically was to polish to a 0.05μm finish with a suspension of γ-Al_2O_3 in water and to examine unetched at high magnification. The initial observation of AlN on each sample was often difficult, but once a line of precipitates had been observed, the whole of the sample could readily be traversed merely by following the network of grain boundary particles.

5.6.3 Scanning Electron Microscopy

The instrument used throughout this work was a Philips PSEM 500 fitted with a LINK energy dispersive analysis system. This was used primarily at 25kV in the secondary electron mode for the examination of fracture surfaces, but other techniques such as backscattered electron imaging and contrast enhancement were employed to observe polished microsections.

Of particular value was the eucentric goniometer specimen stage, which was used extensively to examine the angular relationships between some of the features observed on the fracture surfaces. Details of the technique adopted will be presented in Section 6.2.1.

5.6.4 Transmission Electron Microscopy

Examination of extraction replicas taken from intergranular fracture surfaces was used to supplement the SEM work because of the improved resolution of this technique, and the ability to identify AlN precipitates by electron diffraction.

The instrument used for the majority of the work was a Philips EM301 TEM operated at 100kV, but at a late stage of the project a Philips EM400T fitted with a STEM attachment and EDAX analysis facilities became available. A limited amount of work was carried out using this equipment.

Samples were prepared for examination by two methods

(a) Two-stage extraction replicas.

This technique was used in situations where severe degradation of the fracture surface was to be avoided. A piece of 100μm thick 'Formvar' sheet was cut to an appropriate size and softened in acetone. After wetting the fracture surface with acetone, the Formvar was placed on the fracture and allowed to assume its topography. After 2-3 hours, the film had hardened sufficiently to be stripped away from the fracture surface and coated with a thin layer of carbon (~20nm thick) in an Edwards carbon evaporation unit.

The plastic replica was then cut into small squares, ~2mm x 2mm in size which were placed on 200-mesh copper grids with the carbon layer uppermost. By suspending these grids just above the surface of a bath of acetone, the plastic was dissolved away slowly over a period of several hours leaving behind the carbon replica on the copper grid.

(b) Direct carbon extraction.

Although the technique of direct extraction was found to produce good quality replicas with the efficient extraction of precipitates, it does result in a degradation of the fracture surface due to attack by the acid.

Within thirty minutes of fracturing, a layer of carbon approximately 20nm thick was evaporated directly onto the fracture surface in an Edwards carbon evaporation unit operated at a pressure of 5×10^{-5} Torr.

With the exception of the area of interest, the sample was coated with 'Lacomit' stopping-off compound to prevent any unwanted extraction. It was then marked into small squares with a scalpel. The matrix of the sample was etched away through the carbon layer using a solution of 5% bromine in anhydrous ethyl alcohol for 2-10 minutes. The carbon was floated off the sample in distilled water and washed in methylated spirit before being caught on a 200-mesh copper grid for examination in the microscope.

In addition to the examination of fracture surfaces, attempts were made to observe the AlN precipitates in thin foils taken from the grain boundary regions of as-cast samples. Slices ~1-2mm thick were cut from an embrittled casting using a diamond cutting wheel. Etching in 2% Nital solution revealed the position of the prior austenite grain boundaries which were delineated by a ferrite network, and disks ~3mm in diameter were spark machined from these areas. These were thinned by mechanically polishing on emery paper followed by electro-polishing in a solution of 10% perchloric acid in ethyl alcohol in a Struers 'Tenupol' unit.

5.6.5 Electron Probe Microanalysis (EPMA)

5.6.5.1 Specimen Preparation

Samples were mounted in a conducting bakelite resin and subjected to the procedures outlined in Section 5.6.2 to observe the required features. Regions of interest within the specimens were selected

and marked by indentation on a Leitz microhardness tester using a 400g load.

The samples were then repolished to remove all signs of the etchant and the finish necessary for microanalysis was reached by polishing on 0.05μm γ-Al_2O_3.

5.6.5.2 Analysis

The experiments were carried out on a Cambridge Microscan Mk 5, using standard techniques and an accelerating potential of 15kV.

In order to measure the extent of microsegregation of Al in the experimentally melted 75mm square castings, a scan speed of 0.16μms^{-1} was used and the output from the ratemeter was recorded on a three-pen chart recorder. Prior to and after each specimen was analysed, 20-second counts were taken on an aluminium standard, and at the end of each scan a background Al count was made.

The count rates of each scan were converted to weight percent aluminium using a 'Sheffield Frame Three' computer program, which corrects for atomic number, absorption and fluorescence effects.

The instrument was also used in the 'spot' mode for the qualitative analysis of AlN precipitates found in some of the heat treated samples. Using a low atomic number detector it was possible to analyse for nitrogen, which is not detected by the energy dispersive SEM facility because of atomic number limitations. Because of the low peak/background ratios encountered, counting times of 200s were used.

5.7 Directional Solidification (D.S.) Technique

The technique of directional solidification was used in order to exercise closer control of solidification parameters and to facilitate a more detailed investigation of the AlN precipitation mechanism. Small samples of material were remelted under an inert atmosphere of argon and could be quenched from high temperatures. In this way it was possible to obtain in one sample structures originating from the fully liquid, partially solid and fully resolidified regions of the steel.

The two compositions selected for this part of the work were cast 4282 (0.08%Al, 0.014%N) which was not susceptible to I.F., and cast 4283 (0.17%Al, 0.017%N) which was susceptible. Cylindrical samples approximately 200mm long and 5mm in diameter were prepared by the progressive extrusion, cold swageing and grinding of the 75mm square castings.

5.7.1 Details of the specimen assembly

Each sample was ground on a linishing wheel until it could be inserted into a 400mm long Degussit Alumina tube of 8mm o.d., 5mm i.d. which was closed at one end. This tube was then fixed with 'Autostik' cement to a 360mm length of 6mm o.d., 5mm i.d. stainless steel tubing which had one end reduced to 4.9mm o.d. to accommodate the tube. The top end of the tube was screwed into a brass holder which was connected by a flexible steel wire to the driving unit. This was capable of speeds between $0.005 mms^{-1}$ and $5 mms^{-1}$. By means of a port in the stainless steel tube an atmosphere of argon was maintained over the specimen during each experiment. A schematic view of the specimen assembly is shown in Fig. 5.5.

5.7.2 The Solidification Apparatus

The apparatus used in the present work was originally designed by Eruslu (1976) to study the solidification sequence of austenitic stainless steel, and was later modified by Pereira (1979) and Bridge (1981). Fig. 5.6 gives a general view of the equipment.

A Radyne 10kW high frequency power unit with a voltage stabiliser was used to provide the heat necessary for melting. In order to keep oxidation to a minimum, a silica tube was secured around the specimen assembly with service heads providing coolant and an inert atmosphere of argon. A graphite susceptor of length 200mm, 25mm o.d., 16mm i.d. was placed inside the cast alumina insulator (see Fig. 5.5) and aligned with the work coil.

To facilitate easy quenching the vertical method of growth was chosen which allowed specimens to be dropped under gravity into an agitated quench tank of water. At an appropriate time, the bottom service head was opened and the specimen was quenched by releasing the supporting wire for the specimen assembly.

5.7.3 Measurement of the Temperature Gradient

Experiments were carried out using a dummy specimen which had been partially slit along its length to incorporate a thermocouple. A 0.2mm Pt/Pt-13%Rh thermocouple threaded through 1.2mm o.d. twin bore recrystallised alumina tubing was used for this purpose. The thermocouple bead was protected by inserting it into a 5mm length, 1.8mm o.d. single bore recrystallised alumina tube which was sealed using CC60 alumina cement fired at 1500°C. It was found, however, that even with these precautions, the life of the thermocouples at temperatures in excess of 1550°C was very short

owing to attack by the molten metal. Several attempts were made to evaluate the temperature gradients directly but these were unsuccessful owing to the premature failure of the thermocouples. The technique which was finally used was to determine the position of the hot zone of the induction coil at a temperature where the thermocouple was stable, and to measure the temperature at that point for the power inputs used in the actual quenching experiments. The thermocouple life was sufficient for this to be carried out satisfactorily. In this way the maximum temperature attained during the tests was measured, and an approximate temperature gradient could be calculated on the basis of subsequent metallographic examinations of the test piece.

5.7.4 A Typical Procedure

Having placed the specimen assembly into the silica tube, the system was sealed and dried high purity argon was allowed to flow through the furnace for twenty minutes in order to replace the air within the system. Before the power was supplied, the specimen drive unit was switched on and the specimen assembly positioned so that at least 50mm of the sample would be below the solid/liquid interface.

The furnace was switched on and the specimen allowed to heat up slowly to avoid refractory cracking. This heating process to a final power input of 0.89kW normally lasted about an hour. Before starting the run, the specimen was held steady for ten minutes at temperature after which it was driven downwards through the furnace at a rate of $0.033 mm s^{-1}$. After the sample had moved by 70-100mm, the wire was cut and the sample quenched.

5.7.5 Specimen Examination

In order to obtain fracture surfaces from the directionally solidified material, samples were saw-notched lightly at intervals of 10mm along their length, and were broken with a single hammer blow at each notch in turn. The resulting fractures were examined in the SEM for any evidence of AlN precipitation. It was necessary to adopt this approach because of the difficulties of observing AlN in microsections.

5.8 Industrial Examinations

During the course of this work, several foundries have encountered problems with I.F. and short term investigations have been carried out under the auspices of S.C.R.A.T.A. These investigations involved visits to the foundries concerned for discussions with technical personnel, the sampling of embrittled castings, and metallographic examinations in the laboratory. Two typical reports are included in Appendices 2 and 3.

Chapter 6

Results

6.1 The Mechanism of AlN-induced Intergranular Fracture

A macroscopic view of a typical room temperature intergranular fracture surface is shown in Fig. 6.1. This was obtained by the slow three-point bend testing of a quenched and tempered sample taken from cast 4176 which contained 0.18%Al and 0.015%N. Fracture had taken place around the large as-cast grain boundaries of the sample and on a macroscopic scale appeared brittle. When viewed under a binocular microscope, however, the intergranular facets exhibited some relief and occasional bright reflections could be seen arising from features on the surface. Fig. 6.2 is an optical fractograph showing one such intergranular facet. In addition to the reflective areas numerous dark linear features can be seen. These are, however, similar to the bright areas and also reflect strongly when suitably oriented with respect to the light source. For certain specific orientations of the fracture surface, whole 'families' of parallel reflecting features were observed which were evenly distributed over each intergranular facet. This suggests some crystallographic orientation relationship between the features, an observation which will be discussed in Section 6.2.1.

SEM examination of the fracture surface revealed similar features to those seen optically. Fig. 6.3 is a low magnification micrograph showing the presence of several large grains, each with the crystallographically oriented surface markings. At higher magnifications (Fig. 6.4) these markings can be seen to correspond to flat plate-like features which lie at specific angles to each

other in the grain boundary surface. Energy dispersive analysis (Fig. 6.5) showed that these plates were enriched in aluminium, but because of atomic number limitations it was not possible to analyse for nitrogen. However, extraction replicas taken from the fracture surface contained large plate-like precipitates (Fig. 6.6). These were identified as AlN by selected area electron diffraction, and were found to correspond to {0001} basal planes of the hexagonal AlN structure. The agreement with calculated spacings based on the AlN lattice parameters was excellent, generally to within 0.5% (Table 6.1). Similar features have also been identified in commercial failures (see Appendix 2, Fig. 4).

Although the room temperature fracture surface was macroscopically brittle, Fig. 6.4 does show the presence of considerable micro-ductility. This is manifest as the background of fine dendritic shaped dimples on which the larger plate-like features are superimposed.

It was impossible to see any detectable precipitate responsible for the formation of these dimples in the SEM, although, as with the plates, they were associated with an increased count rate of Al. However, examination of extraction replicas in the TEM revealed the presence of extensive arrays of dendritic AlN precipitates (Fig. 6.7 and Appendix 2, Fig. 8). These were identified by electron diffraction, and the observed lattice spacings agreed well with calculated values (Table 6.2). The fact that these precipitates were responsible for initiating the micro-voids observed in the SEM is beyond doubt. Fig. 6.8 shows a scanning electron micrograph of a dendritic feature on the fracture surface

of cast 4176 (as-cast) together with a TEM dark field image of an AlN dendrite extracted from the same sample. The dendrite arm spacing is of the order of 1μm, which is considerably smaller than the solidification dendrite arm spacings (typically 20-200μm).

The mechanism of AlN-induced I.F. is therefore two-fold. The dendritic form of the nitride which is present in the as-cast grain boundaries acts as a void-initiating inclusion at room temperatures. The AlN plates which lie at an angle to the grain boundaries result in the crack front occasionally deviating from the exact position of the boundaries. This occurs by a mechanism of precipitate/matrix decohesion, as shown in Figs. 6.9 and 6.10. These are scanning electron micrographs of mating halves of an intergranular fracture surface and show that aluminium nitride is present on only one side of each plate-like feature.

It will be noted from Fig. 6.5 that associated with the plate-like features on some fracture surfaces were 'spines' of globular or occasionally rod-like inclusions. These were found to be MnS and were manifest either as inclusions or as holes left by the inclusions on the fracture surface (Fig. 6.11). T.E.M. examinations showed the sulphides to be heavily faulted (Fig. 6.12), which is consistent with their having been precipitated in the solid state. This occurs as a result of the decreasing solubility product of MnS during cooling which often produces fine dispersions of secondary inclusions at the austenite grain boundaries (see Section 3.4.2.2). The fact that the MnS inclusions are in such close proximity to the AlN suggests that the two precipitates may have formed at a similar stage of primary cooling in the austenite region. However,

numerous AlN plates were present on the fracture surface which did not contain the MnS 'spine' and for this reason the sulphides cannot be considered to contribute significantly to the fracture process.

6.2 AlN Precipitation

Both forms of AlN are extremely thin under normal circumstances and could not be resolved optically when viewed in a metallographic section. By examining several extraction replicas of intergranular fracture surfaces in the TEM, however, it was possible to estimate the thickness of the precipitates. This was done by searching for a suitably prominent precipitate in a 'plateau' region of the replica and tilting the specimen stage until the precipitate could be seen 'edge-on'. This position was identified when the apparent thickness of the precipitate when viewed on the screen was a minimum (Fig. 6.13). In this way, the thickness was measured directly to be 65nm (650Å). This represents an upper limit, since any inadequacies in the technique would result in overestimates of the thickness. Because of the presence of the supporting carbon film which was approximately 20nm thick it is therefore reasonable to assume a typical AlN thickness of ~50nm (0.05μm). All the precipitates observed were estimated to be of a comparable thickness, since they exhibited similar contrast.

6.2.1 Plate-like AlN

The crystallographic nature of the plate-like form of AlN was examined using the eucentric goniometer stage of the SEM. Since it was known from the TEM studies that the plane of the AlN plates was parallel to $\{0001\}_{AlN}$ the approach taken was to measure the angular relationships between the 'families' of plates observed

on a single grain boundary surface, and to relate these to the interplanar angles of the austenite matrix. In this way it was possible to establish the habit plane of the precipitate. It was necessary to adopt this indirect method because the precipitation takes place at high temperatures, and therefore any orientation relationship developed with the austenite cannot be observed at room temperature when the structure has transformed.

Preliminary experiments were carried out using the broken half of a Charpy impact specimen taken from cast 4210. This was mounted in 'Plasticine' on a goniometer head and examined optically under a binocular microscope (Fig. 6.15). Illumination was provided by a point souce of light ~2m away in an otherwise darkened room. The sample was tilted and rotated until a family of plates was in a reflecting position and the goniometer readings were noted. By repeating this procedure for several families of plates the relative angular positions were plotted on a stereogram, and it was noted that a commonly occurring angle between families of plates was approximately 70^{o}. (The angles between {111} planes in austenite are 70.53^{o} and 109.47^{o}).

More accurate measurements were made using the goniometer stage of the SEM. In this case the sample was mounted in an auxiliary tilt holder (Fig. 6.16) and viewed in the normal secondary electron mode. The fracture surface was then rotated until one family of plates was parallel to the horizontal axis of the viewing screen and tilted until the flat surfaces of the plates were on the point of disappearing (Fig. 6.17 and 6.18). This uniquely defined the direction of the plate normal and the angular readings of the goniometer

drive unit were recorded. Occasionally, because of the limited range of tilt on the specimen stage, it was not possible to achieve 'extinction' of the plates. In this situation, the direction of the plate normal was calculated by the method shown in Appendix 4.

The position of the normals to five individual families of plates on one grain boundary surface are plotted on a stereographic projection in Fig. 6.19, and the angles between them are presented in Table 6.3. At first sight, it is apparent that there are several angles of approximately 70^{o} or 110^{o}, but that other arbitrary angles are also present. However, it is important to remember that the grain boundary surface originally comprised two austenite grains, one of which is on the mating half of the fracture surface, and that both have contributed to the features observed.

This is shown quite clearly in Figs. 6.20 and 6.21. In each case the linear discontinuity in the morphology of the fracture surface represents the line of intersection of three columnar grains. The fact that the surface being viewed is convex in nature means that this is a single prior austenite grain which has been in contact with two other grains. These are now on the mating half of the fracture surface. In Fig. 6.20, the platelet observed is continuous across the line of intersection of the grains, indicating that in this case, the feature has arisen from an AlN plate growing into the austenite grain which is present on the fracture surface. Fig. 6.21, however, shows platelets on either side of the line of intersection terminating at the discontinuity. It can be concluded that these platelets have grown into the two adjacent austenite grains

which are on the mating half of the fracture surface.

Therefore there are two sets of angular relationships in Table 6.1 corresponding to the growth of AlN into the two austenite grains which are at some arbitrary angle to each other. By dividing the five families of plates into two groups (Table 6.3a) it is seen that the angles between plates 1, 3 and 4 are 108^{o}, 68^{o} and 76^{o} and the corresponding angles for plates 2, 3 and 5 are 109^{o}, 74^{o} and 70^{o}. Comparing these angles with the angles between {111} planes in austenite (70.53^{o} and 109.47^{o}) it can be concluded that the $\{0001\}_{AlN}$ plates grow into the austenite grains parallel to the $\{111\}_{\gamma}$ planes. The errors involved in the measurement of the angles in the SEM are estimated to be $\pm 3^{o}$ when a direct measurement was made, and $\pm 5^{o}$ when the angle was calculated as in Appendix 4.

By choosing two plates which intersected on the fracture surface, it was possible to obtain a more accurate measurement of the angle between them. This was done by tilting and rotating the sample until <u>both</u> were on the point of disappearing simultaneously (Fig. 6.22). The plate normals were then perpendicular to their traces and in the plane of the photograph. Measurement of the angle between the normals shows it to be $71^{o} \pm 1^{o}$. Similar measurements on numerous other grains and other fracture surfaces confirmed the frequent occurrence of this angular relationship.

It was not possible to confirm the atomic orientations within the $\{0001\}_{AlN}$ // $\{111\}_{\gamma}$ planes by the use of thin foil TEM specimens for the reasons noted earlier. However, the examination of foils taken from the grain boundary region of an as-cast sample did show the AlN plates growing into the austenite grains on each side of the

boundary, (Fig. 6.24). The austenite had of course transformed to pro-eutectoid ferrite during cooling and no orientation relationship could be inferred.

6.2.2 Dendritic AlN

6.2.2.1 Results of the Directional Solidification Work

With the power inputs employed during the solidification process, the maximum temperature attained in a dummy specimen was found to be 1610°C, and subsequent metallographic observations revealed the two phase (solid/liquid) region to extend for a distance of approximately 30mm behind the liquidus. Fig. 6.25 shows how the position of the liquidus was determined from a longitudinal section in the optical microscope. The dendrites arising from the directional solidification process had a considerably larger arm spacing than the dendrites which had formed from the liquid during quenching of the sample (Fig. 6.26), so the interface between the two was quite clearly recognisable.

Fig. 6.27 shows how the fracture morphology varied with position along the casting for both the high Al and N (4383) and low Al and N (4382) casts. At low magnifications, the fractures were similar in both cases. In the areas which had been quenched from above the solidus, an interdendritic morphology was encountered (Fig. 6.27). Some central porosity was also evident. In areas which had been fully solid prior to quenching, the fracture was fibrous, and finally areas which had partially transformed to ferrite (Fig. 6.28) gave an intergranular fracture around ferrite networks at the prior austenite grain boundaries.

The main areas of interest were the interdendritic fractures from the partially solid region and these were examined in more detail for evidence of AlN precipitation. The samples from cast 4382 (low Al and N) exhibited numerous type II MnS precipitates in the interdendritic regions (Fig. 6.29) but with no evidence to suggest any AlN precipitation. The D.S. samples made from cast 4383 (high Al and N), however, contained fine dendritic inclusions superimposed on the interdendritic fracture surfaces (Fig. 6.30) and these were found to be rich in Al. The dendrite arm spacing of the precipitates was 1-2μm, which is at least an order of magnitude smaller than the solidification dendrite arm spacing and is in reasonable agreement with that of AlN dendrites observed on intergranular fracture surfaces (see, for example, Fig. 6.8).

6.2.2.2 Metallographic Observations

The examination of extraction replicas taken from the intergranular fracture surface of cast 4176 revealed evidence to suggest that in some cases the dendritic AlN present in the grain boundaries may act as a nucleus for subsequent solid state precipitation of AlN plates. Fig. 6.31 shows areas where the plates and dendrites are continuous, with the plates appearing to be merely extensions of the dendrite arms.

6.3 Effects of Processing Variables

6.3.1 Aluminium and Nitrogen Contents

Table 6.4 gives details of the room temperature fracture morphology of the 0.30C-1.50Mn steels used in this investigation, showing that the mode of failure of castings in the quenched and tempered condition depends on the aluminium and nitrogen contents of the steel.

For a given steelmaking practice (in this instance corresponding to a constant cooling rate) the amount of I.F. observed increases with increasing $\left[\%Al\right] \times \left[\%N\right]$. For the 75mm square castings which were cooled at a rate of $0.1^{o}C\ sec^{-1}$, (Practice 'A'), the critical level below which I.F. will not occur corresponds to a value of $\left[\%Al\right] \times \left[\%N\right]$ $\sim 1.5 \times 10^{-3}$ (comparing casts 4211 and 4351).

Table 6.4 also shows how the susceptibility to I.F. decreases with increased cooling rate. The small keel block castings made by Practice 'B' which were cooled at $0.23^{o}C\ sec^{-1}$ contained only 50% I.F. with a $\left[\%Al\right] \times \left[\%N\right]$ value as high as 3.7×10^{-3}.

Comparing these values with the critical cooling rate curves obtained by Lorig and Elsea (1947) (Fig. 4.1) it can be seen that they lie well within the susceptible region for each cooling rate. This suggests that the results of Lorig and Elsea err on the side of safety, and can therefore be used with some confidence. It should further be remembered that their aluminium levels refer to the Al added, and a recovery rate of approximately 50% will be expected. This has the effect of halving the values on the horizontal axis of their graph.

The effects of Al micro-segregation were measured by EPMA techniques on cast 4210 which had a nominal Al content of 0.17%. Fig. 6.32 shows the micro-hardness indents which identified the scan path for the probe. The maximum concentration detected was 0.19%Al in the interdendritic region compared to 0.16%Al in the dendrite core. This corresponds to a segregation ratio of Cmax/Cmin = 1.19.

6.3.2 Carbon Content

Increasing the carbon content of three 75mm square castings to 0.42%, 0.56% and 0.65%C (casts 4353, 4354 and 4355 respectively) resulted in a marked change in the quench and tempered fracture morphology. At a level of 0.42%C, the fracture was fully intergranular and similar to that of a 0.30%C steel. The 0.56%C and 0.65%C steels still exhibited a fully intergranular fracture surface, but in this case the size of the grain boundary facets was much smaller, (see Fig. 6.33). This corresponds to a change in the solidification behaviour from the peritectic transformation at carbon contents ≤0.50%C to solidification directly to austenite at higher carbon levels.

It can, however, be concluded that the $\gamma \rightarrow \alpha$ transition (which results in the formation of a ferrite network at the prior austenite grain boundaries for hypoeutectoid steels) is not influencing the precipitation process, since the 0.65%C, 1.50%Mn steel was fully pearlitic and still contained I.F.

6.3.3 Pouring Temperature

The pouring temperature of the casting was found to have little effect on the fracture mechanism. Three keel block castings of embrittled 0.30C-1.50Mn steel were produced with pouring temperatures of 1550°C, 1620°C and 1700°C corresponding to superheats of 50°C, 120°C and 200°C respectively. After heat treatment, the fracture was fully intergranular in each case, and the examination of macro-etched sections through the castings revealed no discernable differences in as-cast grain structure.

6.3.4 Heat Treatment

(a) Cast 4176 was initially used to examine the effect of matrix hardness and microstructure on the susceptibility for I.F. Results of the slow three point bend tests carried out after various heat treatments are presented in Table 6.5. The fracture surfaces were used to 'reconstruct' a full cross section of the casting, which is shown in Fig. 6.34. The close association between the fracture facets and the cast structure can clearly be seen.

In the as-cast state, failure occurred by a cleavage mechanism, but after various hardening heat treatments such as quenching and tempering or normalising, the fractures became intergranular. It was only after annealing in the furnace from 900°C that the amount of I.F. was reduced to approximately 40%, the remainder of the fracture being ductile.

The effect of different hardness levels on impact properties was also examined by tempering Charpy samples for various times at 600°C. The results will be presented in Section 6.4.2.3.

(b) Casts 4210 (0.17Al, 0.017N) and 4351 (0.12Al, 0.014N) were subjected to the high temperature solution treatments shown in Fig. 6.35 to attempt to reduce the levels of I.F. by redissolving AlN as reported by Lorig and Elsea (1947).

However, there was no marked difference between the macroscopic fracture appearance before and after heat treatment of either cast. In both cases the amount of intergranular fracture remained constant, but after heat treatment the fracture surface did not exhibit the shiny facets which have been attributed to the AlN plates and the

appearance was altogether more dull. Examination of the fracture surfaces in the SEM revealed the reason for this difference. Although the high temperature heat treatments had been unsuccessful in dissolving the AlN, some considerable coarsening of the precipitates had taken place. The dendritic features associated with the ductile dimples on normal I.F. surfaces had coarsened and assumed a rod-like morphology (Fig. 6.36), whilst the plate-like features had begun to spheroidise (Fig. 6.37) and also induced failure by void nucleation.

Hence although the macroscopic features of the fracture surface had not changed, on a microscopic scale the mechanism of failure had been modified.

The coarsening of the AlN meant that the precipitates could now be seen in the optical microscope at high magnifications (Fig. 6.38) and could be analysed in the E.P.M.A. Using this technique, both aluminium and nitrogen were detected and had an approximate weight ratio of 2:1. The corresponding ratio for pure AlN is 27:14 (1.93:1). No other major element such as sulphur, manganese, silicon or phosphorus was found in the nitride.

Using the SEM to observe polished microsections, it was also possible to view the precipitates in some detail, as shown in Fig. 6.39. The use of backscattered electron imaging and contrast enhancement techniques highlighted the coarsened precipitate, and energy dispersive analysis was able to detect an increased Al count rate in the region of the precipitate.

6.4 The Results of Mechanical Testing

6.4.1 Tensile Testing

The room temperature tensile properties of an embrittled steel (cast 46/89) and an unembrittled steel (casts 46/1 and 46/4) in two states of heat treatment are presented in Table 6.6. The effect of I.F. on the tensile properties can be seen most clearly in the quenched and tempered condition, with the tensile ductility falling from 57% reduction of area (16% elongation) in the base material to 12% reduction of area (3% elongation) in the embrittled steel. The specification for this grade of steel (BS 3100 A5, 1976) requires a minimum of 13% elongation.

It will further be noted that cast 46/89 had a higher 0.2% P.S. and UTS than casts 46/1 and 46/4 after identical heat treatments. This is thought to arise from the variations in manganese contents of the castings, which were made from different heats (see Table 5.1). The higher Mn content of cast 46/89 has contributed to its higher tensile strength. In the quenched and tempered condition both sets of results were, however, within the 0.2% P.S. and UTS specifications of BS 3100 A5 (1976).

Table 6.7 and Fig. 6.40 show the variation in tensile strength and ductility of cast 46/89 with temperature. The temperature dependence is similar to that which would be expected for normal fibrous failures, in that both the 0.2% P.S. and the UTS decrease significantly with increasing temperature. This is in agreement with the earlier observations (Section 6.1) that intergranular fracture proceeds by a mechanism of void nucleation and growth at AlN inclusions which are localised at the position of the prior

austenite grain boundaries. Hence the fracture path is transgranular with respect to the microstructure present at the time of testing, and the 'intergranular' strength will depend to some extent on the yield strength of the matrix.

The increased values of the UTS at temperatures in excess of 200°C can be attributed to a partial transition to fibrous modes of failure. Typical fracture surfaces are shown in Fig. 6.41.

6.4.2 Impact Testing

6.4.2.1 The Effect of I.F. on Impact Properties

The effect of I.F. on impact properties can clearly be seen in Figs. 6.42 and 6.43, which give the Charpy impact transition curves for unembrittled and embrittled castings respectively in the quenched and tempered condition (950°C for 1½hrs, WQ; 600°C for 1hr, WQ). Cast 4231, which had a low Al and N content (Fig. 6.42) showed the usual transition from ductile fibrous failures at high temperatures to cleavage failures at lower temperatures. The impact transition temperature was -60°C, and the upper shelf energy was 83J.

Cast 4210, however, which contained 0.17%Al and 0.017%N exhibited significantly different behaviour, (Fig. 6.43). At low temperatures (-196°C) the failure mode was by cleavage, but instead of promoting a transition to fibrous failures, increasing the temperature resulted firstly in a fully intergranular fracture, then a mixed I.F./ fibrous mechanism. This gave a significantly lower energy fracture than the unembrittled material at the same temperature and agreed well with the observations of Wright (1962) which were presented

in Fig. 3.1. However, by increasing the testing temperature still further, a second transition was observed at ~200°C. In excess of this temperature, the fracture mode became fully fibrous and an upper shelf energy similar to that of cast 4231 was attained.

The effect of the presence of I.F. on the impact energy is shown quite markedly in Fig. 6.44 which is a least squares plot of the results obtained from the mixed intergranular/fibrous region of Fig. 6.43. However, it will be noted that only in fractures where the %I.F. was greater than ~85% did the impact energy fall below the specified minimum of 25J (BS 3100 A5, 1976).

6.4.2.2 Effect of Testing Temperature

In order to investigate the transitions between the various fracture mechanisms more fully without having to use high temperatures, a less severely embrittled casting (cast 4351) was used to produce further Charpy specimens. At room temperature and in the quenched and tempered condition this failed in a ductile manner with an impact energy of 82J, (Fig. 6.45). This is similar to the upper shelf energy of the unembrittled material. By reducing the temperature below 0°C, however, an intergranular regime was encountered down to a temperature of -164°C when the failure mechanism became one of cleavage. The fracture morphology at each testing temperature is also shown in Fig. 6.45.

Examination of the fracture surfaces in the SEM revealed a complete and continuous transition with decreasing temperature from fully fibrous failures, through mixed fibrous/I.F. to almost fully I.F. (-90°C) and then through mixed I.F./cleavage to fully cleavage.

SEM examinations of the broken test pieces revealed the following characteristics.

i) In the fibrous fracture region, occasional coarse dendritic features were observed (Fig. 6.46a). These were on a much larger scale than the voids nucleated by AlN (Fig. 6.4) and appeared to be associated with the dendritic structure of the casting. The fracture could not be described as interdendritic per se, as shown at higher magnification (Fig. 6.46b). Failure had occurred by the usual mechanism of void nucleation at MnS inclusions, but the reason for the dendritic appearance is considered to be the greater density of MnS in the interdendritic regions of the casting. Thus the micromechanism of failure is identical to that of normal fibrous failures, and it is only the distribution of inclusions which results in the dendritic appearance in certain areas. This phenomenon was also observed in cast 4231 but no adverse effects on the impact energy were noted in either instance.

ii) As the testing temperature was decreased, not only did the macromechanism of failure change, but the micromechanisms of the intergranular fracture process also changed. Figs. 6.47a and b show scanning electron micrographs of intergranular facets from samples broken at -30°C and -164°C, respectively. At the higher temperature there is evidence of ductile dimples around the AlN dendrites (Fig. 6.47a) which is the mechanism normally associated with I.F. At the lower temperature however, the overall fracture appearance of the intergranular facet is one of cleavage (Fig. 6.47b). The AlN appears to have taken the role of cleavage crack initiator, with fracture proceeding for short distances along the prior austenite grain boundaries. Although less clearly defined, some of the

plate-like features typical of room temperature failures can still be resolved.

iii) At temperatures below -164°C, the fracture mode was predominantly transgranular cleavage, and Fig. 6.48 shows a typical fracture surface.

6.4.2.3 The Effect of Matrix Hardness

The effect of matrix hardness on the impact strength was also examined. Samples from casts 46/6 and 46/7 were solution treated at 950°C and water quenched, followed by tempering at 600°C for ½hr, 1hr, 2hrs, 4hrs and 8hrs, respectively. The impact transition curves obtained are shown in Fig. 6.49, and optical photographs of the fracture surfaces are presented in Fig. 6.50. It is apparent that the samples with the higher matrix hardness (shorter tempering times) were not only more susceptible to fail by I.F. at room temperature, but also exhibited the phenomenon over a wider range of testing temperatures. In the samples which had been tempered for 8hrs to give a matrix hardness of 186 HV30 there was very little evidence of any I.F. This is concordant with the observations of Wright and Quarrell (1962) who used isochronal tempering treatments to show the dependence of the susceptibility for I.F. on matrix hardness.

6.4.3 Fracture Toughness Testing

The method of calculating COD values from the test data and the significance of δ_c, δ_i, δ_u and δ_{max} are discussed in Appendix 1.b.

The results of the COD tests carried out at different temperatures are given in Tables 6.8 to 6.11. Values of δ_c, δ_i, δ_u and δ_{max}

are given where appropriate. The material codes assigned to each of the four series of tests were as follows:

HHQT : High aluminium, High nitrogen, Quenched and Tempered.

LLQT : Low aluminium, Low nitrogen, Quenched and Tempered.

HHN : High aluminium, High nitrogen, Normalised.

LLN : Low aluminium, Low nitrogen, Normalised.

For the quenched and tempered material, sufficient samples were tested to allow the full transition behaviour to be examined. A smaller number of normalised samples were tested for comparison purposes.

Comparison of Tables 6.8 and 6.9 reveals an interesting difference in behaviour between the HHQT (susceptible to I.F.) and LLQT (non-susceptible) samples. Despite the difference in overall fracture behaviour, the initiation value of the COD (δ_i) does not vary signficantly between the two sets of samples, and is in the range δ_i = 0.06 - 0.09mm. However, comparing the values of the COD at the point of maximum load (δ_{max}) it can be seen that the values for the HHQT steel are in general much lower than for the LLQT steel. The criteria for the selection of a 'critical' value of the COD (δ_i vs δ_{max}) have been considered in Appendix 1b. Figs. 6.51 and 6.52 give transition curves based on δ_i and δ_{max} respectively. At low temperatures there is no ambiguity in determining the critical event, and the value of COD used is δ_c.

The difference between the two kinds of fracture behaviour can be seen more clearly with reference to the schematic load vs displacement curves and typical fracture surfaces shown in Figs. 6.53 to 6.55.

Fig. 6.53 shows the behaviour exhibited by all the samples (both quenched and tempered and normalised) at temperatures of -100°C and below. Fracture is macroscopically brittle, with no evidence to suggest slow crack growth prior to failure.

Fig. 6.54 is the behaviour associated with the LLQT (unembrittled) steel. After a small amount of plastic deformation, a slow crack is initiated and continues to grow in a uniform way. Since the test is carried out under displacement control, a maximum force plateau is reached and the load decreases steadily as the crack front progresses.

Fig. 6.55 shows that for the HHQT material, the load vs displacement curve is almost identical to that shown in Fig. 6.54 up to the initiation of slow crack growth. Subsequently, however, after a limited amount of crack propagation, fracture proceeds in sharp bursts along the embrittled grain boundaries. This gives rise to the discontinuous decreases in load observed after the attainment of maximum load.

At first sight, therefore, it seems strange to find that the initiation value of the COD (δ_i) is not sensitive to the presence of I.F. However, examination of the fracture surfaces of embrittled samples (Fig. 6.56) shows that in all cases, fracture has been initiated in a fibrous manner at the root of the fatigue crack. The reason for this was thought to be due to the highly localised position of the fatigue crack tip with respect to the large prior austenite grain boundaries in the castings. Because of this, the fatigue crack tip is unlikely to end exactly at a favourably oriented embrittled grain boundary, and some fibrous crack growth

has to take place before failure can proceed in an intergranular manner. Fig. 6.57 is a scanning electron micrograph showing a region of ductile fibrous crack growth immediately ahead of the fatigue crack tip. In order to propagate in an intergranular manner, the crack had to cross over to a plane 1.5mm away from the original crack plane. This corresponds to a change in the focussing conditions on the SEM shown in Fig. 6.57.

Chapter 7

Discussion

7.1 Introduction

The results of this work have provided a considerable amount of information for cast steels on the nature of the intergranular fracture surface and the role played by AlN in the fracture process. This has been supported by the observation of effects caused by variations in heat treatment, composition and testing conditions.

This chapter considers the mechanism by which AlN-induced intergranular fracture proceeds, and the way in which the AlN precipitates form. The effects of some processing variables are discussed in Section 7.4, and finally the influence of I.F. on mechanical properties is considered in Section 7.5.

Although most of the work has been carried out in a laboratory environment, the industrial significance of some of the results is highlighted.

7.2 The Mechanism of I.F.

The results have confirmed that the precipitation of AlN on the primary grain boundaries can be a major cause of intergranular fracture. However, in order to understand the mechanism by which I.F. occurs, it is important to remember that in most cases the crack propagation is actually transgranular with respect to the microstructure which exists at the time of testing. The crack front merely follows the network of AlN precipitates which continue to delineate the original boundaries on which they formed. Hence

it is not surprising to find that the micromechanisms of I.F. depend to a certain extent on the mechanical properties of the matrix.

The mechanism proposed by Lorig (1952) was shown in Fig. 3.21 and in broad terms is correct. It was suggested that fracture occurred in the region of the grain boundary, but deviated from the precise location of the boundary to follow the AlN 'needles' (*sic*) which projected into the austenite grains at either side. Wright (1962) provided some experimental justification for such a theory when he observed jagged steps in a longitudinal section through the fracture surface. These he attributed to the dendritic form of AlN which he considered to lie in the grain at a 'fairly constant' angle to the grain boundary.

The results of the present work have enabled this proposed mechanism to be extended and modified. The use of scanning electron microscopy (unavailable to these earlier workers) has shown that the steps observed by Wright are indeed at several well-defined angles to the grain boundary (Section 6.2.1). However, as Figs. 6.4 and 6.6 reveal, the features arise not from the dendritic AlN, but from the plate-like form of the precipitate which has nucleated in the boundary and grown into the adjacent austenite grains with a specific orientation relationship.

The general mechanism of I.F. is, therefore, one in which the crack front broadly follows the position of the prior austenite grain boundaries which are defined by the dendritic form of AlN, but occasionally deviates from the boundary when it encounters

plate-like precipitates of AlN. The exact mechanism has, however, been shown to depend on the temperature of testing and the overall fracture mechanism of the matrix. At temperatures above the ductile/brittle transition temperature (DBTT) the unembrittled steel fails by void nucleation and growth at appropriate second phase particles, usually sulphides or oxides.

In embrittled steel, however, in the same temperature regime, I.F. occurs as a result of preferential void nucleation and growth at the dendritic AlN precipitates (Fig. 6.4). Deviations from the exact position of the prior grain boundaries occurs as a result of decohesion at the interface of the plate-like AlN precipitate and the matrix (Figs. 6.9 and 6.10). This situation was considered in Section 3.4.2.

Below the DBTT the fracture mechanism of the unembrittled matrix is one of cleavage and this is reflected in the nature of the intergranular fracture surface of embrittled material at similar temperatures. The AlN dendrites now appear to be linked by areas of cleavage which are confined to the region of the as-cast grain boundary (Fig. 6.47b) and the plate-like features are much less clearly defined. This is probably because deviations from the plane of the cleavage crack are energetically unfavourable.

In both the high temperature and low temperature regions, therefore, the fracture process appears to be dominated by the dendritic form of the nitride, with the plate-like form being responsible for the characteristic spangled appearance of the fracture surface.

Wright (1962) has already emphasised the importance of relative

grain boundary and matrix strengths in determining the susceptibility to I.F. (Section 4.3.1). Since both of these vary with temperature, it is possible to explain the change in fracture mode from fibrous to I.F. to cleavage with decreasing temperature. This has been observed in Figs. 6.43 and 6.45. If we consider the classic Orowan (1945) model used to explain normal ductile to brittle transitions, it can be seen that by comparing the yield strength and the cleavage strength at any temperature the mode of failure may be predicted. This model can now be extended to include a conceptual 'intergranular' fracture strength σ_{IF} which refers to the strength of the embrittled prior grain boundaries. The variation of σ_{IF} with temperature has been shown to be similar to that of σ_y above the DBTT, since both are governed by the ease of void nucleation at second phase particles (Fig. 6.40). Fig. 7.1 shows how this 'intergranular' strength compares to the yield strength and cleavage strengths at a given temperature. At low temperatures, cleavage is the most favourable mechanism, since σ_{cl} is low. Increasing the temperature results in a transition to an intergranular mode of failure, whilst at high temperatures when σ_y is low, fibrous failures predominate. The reason for this second transition to fibrous failures is that the yield strength falls below the intergranular fracture strength (See Fig. 7.1). This is thought to arise due to the constraints involved in fracture along the grain boundary which tend to increase σ_{IF} with respect to the uniaxial yield stress.

In the region of each transition temperature it is to be expected that there will be mixed modes of failure, which is verified by the fractographs presented in Fig. 6.45. Thus with decreasing

temperature there will be a continuous range of fracture mechanisms from fibrous, through mixed fibrous/IF to IF and through mixed IF/ cleavage to cleavage.

Fig. 7.1 can be used to interpret several of the results of this work, and will be referred to again in latersections. Clearly the position of the 'intergranular' curve relative to the other curves will be determined by the severity of the AlN embrittlement. In heavily embrittled material, for example, this strength will be reduced and reference to Fig. 7.1 shows that there will be an increase in the temperature interval over which IF occurs. Reducing the amount of AlN present at the boundary may increase σ_{IF} to such an extent that IF is not observed at any temperature. In this case a simple transition from cleavage to fibrous fracture takes place.

The hardness and condition of heat treatment of a casting will also affect the relative positions of the strength vs temperature curves in Fig. 7.1, although here matters are more complex. This is because the yield strength, intergranular strength and cleavage strength may all be changed. The results of the Charpy tests carried out on material of different matrix hardness (Fig. 6.49) show how the temperature interval over which IF occurs tends to increase with increasing matrix hardness. This corresponds to a relative movement of the σ_y vs temperature curve upwards and to the right in Fig. 7.1, which broadens the IF region.

7.3 AlN Precipitation

The role of each form of AlN in the fracture process has been discussed in Section 7.2.

Although the presence of two morphologies of AlN has been recognised for a number of years, the temperature and mechanism of its precipitation has not been clear. The metallographic observations and directional solidification experiments of the present work have shown that the dendritic form of the nitride can precipitate from solute-enriched liquid at a late stage of solidification when it is effectively confined to the as-cast grain boundaries. Precipitation of the plate-like form takes place in the solid state at a later stage of primary cooling, and there is evidence to suggest that the dendritic form of AlN may in some cases act as a nucleation site (Fig. 6.31 and Appendix 2, Fig. 9). These observations will now be discussed with reference to the solubility data available for AlN, (Section 4.4).

7.3.1 Dendritic AlN

If we consider a steel containing 0.1%Al and 0.01%N, the data of Gladman and Pickering (1967) given in Table 4.1 predict a solution temperature of 1401°C for AlN in austenite. For higher Al and N contents this temperature would of course be increased and it will be recognised that the solubility limit may well lie outside the austenite region and in the solid/liquid phase field.

The temperature at which precipitation can begin during solidification may be calculated knowing the microsegregation characteristics of the Al and N. The concentration of each of these in the residual liquid is determined using the Scheil equation (Scheil, 1945) and the equilibrium lever rule respectively (see Section 2.4.2). The latter is appropriate for nitrogen in view of its rapid diffusion in iron. Details of the calculation are given in

Appendix 5, and the results are plotted in Fig. 7.2.

For initial bulk concentrations of Al and N, precipitation will become possible when the Al and N contents of the residual liquid exceed the AlN solubility limit. Although for a rigorous treatment it would be necessary to consider also the kinetics of the precipitation process, Fig. 7.2 does show that for a starting composition with $C_o^{Al} \times C_o^{N} = 0.001$, it should be possible for precipitation to begin when solidification is more than about 70% complete.

This model does not, of course, take into account any solute interactions with carbon which also segregates into the residual liquid during solidification. Since the interaction coefficients of carbon with Al and N are both positive, (Table 4.2), any local increase in carbon content will tend to decrease the AlN solubility and promote precipitation at a still higher temperature. These effects have been examined theoretically and experimentally by Valencia (1981) in the context of nitrogen blowhole formation. Dendritic AlN was observed on the surface of blowholes, confirming that AlN precipitation can occur during the later stages of solidification.

The limitations in using the Scheil equation to model Al micro-segregation are recognised, but it is considered that up to approximately 90% solid, the model is sufficiently accurate. Beyond this point, however, the predicted Al content in the residual liquid increases asymptotically and the model would always predict some AlN precipitation in the very final stages of solidification.

It has been shown that precipitation of AlN can occur in the liquid with relatively modest Al and N contents. When the effects of macrosegregation of Al and N are also considered (see Section 2.4.2) it is not difficult to see why a large casting may exhibit I.F. even when the bulk Al and N contents are not excessive. Foundries producing castings of up to 200 tonnes have been known to have problems with I.F. with bulk Al contents of only 0.03% and nitrogen levels of 0.013%. (Wilson, 1981).

The precise mechanism of formation of the dendritic AlN precipitates still remains uncertain, although it is likely that the driving force for such a morphology will be the concentration gradient of Al and N in the residual liquid as a function of the distance behind the solid/liquid interface. This will also be coupled with a temperature gradient parallel to the direction of growth of the solidification dendrites, which will further favour a dendritic AlN morphology. An analogous situation is the precipitation of dendritic silicate inclusions in iron-nickel-silicon alloys which were the subject of directional solidification studies by Aritomo and Gunji (1979) and Sakaganu et al (1969). These workers concluded that precipitation took place in the residual liquid during solidification, the driving force in this case being the microsegregation of oxygen.

Once the AlN has begun to precipitate in the interdendritic solute-enriched liquid, it may then be pushed ahead of the growing solidification dendrite. As solidification proceeds it will eventually become entrapped between two independent solidification dendrites which form the grain boundary. Uhlmann et al (1964)

have studied the "pushing" of particles by liquid-solid interfaces in several different organic materials and Myers and Flemings (1972) examined the particular case of silica inclusions in steel. For each particular type of particle examined by Uhlmann, a critical growth velocity of the solidification dendrites was observed, below which the particles were pushed by the interface and above which they became entrapped in the growing solid. This may provide a further explanation of the effect of cooling rate on the tendency for I.F. If the cooling rate is sufficiently high, not only will the precipitation of AlN in the liquid become less favourable, but if such precipitation does occur, there will be less likelihood of the precipitates being pushed ahead of the growing solid/liquid interface and eventually becoming trapped at the grain boundary.

7.3.2 Plate-like AlN

The crystallographic nature of the plate-like form of AlN seen in Fig. 6.4 has been confirmed by the SEM studies which were described in Section 6.2.1. The plates nucleate in the austenite grain boundaries during primary cooling of the casting and grow into the adjacent austenite grains with an orientation relation of the form $(0001)_{AlN}$// $\{111\}_{\gamma}$. These are the most closely packed planes in each structure and examination of the atomic arrangements within the planes shows that the best matching is obtained with $\langle 10\bar{1}0\rangle_{AlN}$// $\langle 1\bar{1}0\rangle_{\gamma}$ (Fig. 7.3). This gives a misfit of 6.5% along these directions, and whilst the generally accepted threshold for a coherent interface is ~5% misfit, (Chadwick, 1972), the misfit within these planes is significantly smaller than the misfit in the perpendicular $[0001]_{AlN}$// $\langle 111\rangle_{\gamma}$ directions. This explains why

the precipitates are so thin, since growth occurs by movement of the incoherent interface into the austenite grains and coarsening in the $[0001]_{AlN}$ (thickness) direction is not favoured. With an estimated thickness of ~500Å, this means that the plates are about one hundred unit cells thick (Section 6.2).

It is not suggested that this is the only possible orientation relationship which can be established for AlN since the precipitate is often found in other morphologies. For example, Yamanaka and Ohmori (1978) observed intragranular acicular precipitates of AlN in a 0.20C-1.40Mn steel containing 0.04%Al and 0.015%N. These were formed under conditions of isothermal transformation and had an orientation relationship with the parent austenite of the form $\{11\bar{2}0\}_{AlN}$// $\{\bar{1}10\}_{\gamma}$. The preferential growth direction of the rods was $[0001]_{AlN}$// $\langle\bar{1}10\rangle_{\gamma}$. This relationship was determined by electron diffraction studies of the AlN/martensite orientation relationship in thin foils. Using the Kurdjumov-Sachs relationship ($\{111\}_{\gamma}$ // $\{101\}_{\alpha'}$ and $\langle\bar{1}10\rangle_{\gamma}$ // $\langle11\bar{1}\rangle_{\alpha'}$) this was transformed to give the AlN/γ orientation relationship, which is therefore rather indirect.

The most familiar orientation relationship between an h.c.p. structure and austenite is that derived by Raynor et al (1966) for Mo_2C which gives $\{0001\}_{Mo_2C}$ // $\{111\}_{\gamma}$ and $\langle11\bar{2}0\rangle_{Mo_2C}$ // $\langle1\bar{1}0\rangle_{\gamma}$. The atomic arrangements on the $(0001)_{Mo_2C}$ // $(111)_{\gamma}$ planes are shown in Fig. 7.4(a) and it can be seen that there is good matching of Mo and Fe atoms when the close packed directions are also parallel. However, if the AlN were to assume an orientation relation of this kind, Fig. 7.4(b) shows that there would be a considerable strain (~18%) at the AlN/γ interface and large distortions of the austenite

lattice would be necessary to accommodate the AlN. With the orientation relationship proposed in the present work, the excess volume of the AlN unit cell is incorporated by allowing Fe atoms in the austenite to be positioned at inter-atomic sites in the corresponding $(0001)_{AlN}$ plane, as in Fig. 7.3.

7.4 The Effect of Processing Variables on the Susceptibility to I.F.

7.4.1 Aluminium and Nitrogen Contents

It is now well established that increasing the aluminium and nitrogen contents of a casting will increase the susceptibility to I.F. at a given cooling rate. For the case of the 75mm square castings used in this study which were cooled at a rate of $0.1^{o}C\ sec^{-1}$ the 'critical' levels of Al and N required to cause I.F. were such that $[\%Al] \times [\%N] \sim 1.5 \times 10^{-3}$. If this is compared with Fig. 7.2, it can be seen that at this level of Al and N, AlN precipitation is predicted when solidification is more than 50% completed. However, the kinetics of the precipitation process at this cooling rate will probably explain why I.F. is avoided for Al and N contents below this level.

It is important to remember that the model described in Section 7.3.1 only determines the temperature at which the solubility limit is exceeded. It should not be inferred that precipitation will necessarily occur at this temperature. Moreover, the fact that AlN precipitation has occurred does not necessarily mean that a casting will be susceptible to I.F. Other factors such as the grain size, microstructure and hardness have also been shown to play an important role. In commercial foundry practice, it should be

possible to minimise the incidence of I.F. by careful control of Al and N contents. Sources of nitrogen have already been discussed in Sections 2.1.1 and 2.2.2, but for a given nitrogen content there has to be sufficient Al in solution (i.e. not combined as Al_2O_3) to exceed the AlN solubility limit before AlN precipitation can occur. This condition can be satisfied in two ways:

(i) In small castings, by the addition of excessive amounts of Al beyond that which is required for full deoxidation and the avoidance of Type II MnS. Here, the steelmaking practice and final carbon content of the melt are important since these determine the oxygen content prior to deoxidation and hence the amount of Al required. (See also Section 2.2.1).

During the examination of commercial failures from several foundries, Al contents in excess of 0.15% have been encountered which are considered to be totally superfluous. The failures reported in Appendices 2 and 3 had Al contents of 0.053% and 0.12% respectively, but in the first case this was coupled with a nitrogen content of 0.018% which gave rise to the I.F. Appendix 3 also highlights the dangers of taking ladle samples to analyse for Al or 'N as AlN', since both these analyses were unable to account for the observed incidence of I.F.

(ii) In larger castings even when only a modest amount of Al has been added, the effects of micro- and (more importantly) macro-segregation may be such that areas of the casting are rendered susceptible to I.F. This is particularly the case at the centre of large castings where the cooling rate is also extremely slow. It is suggested that under these circumstances, an addition of

titanium and/or zirconium would be justified after deoxidation with a bare minimum of Al. In this way most of the Al is used for deoxidation, whilst the Ti/Zr additions prevent pinholing without the danger of encountering I.F. The reluctant attitudes towards the adoption of such a practice have already been discussed in Section 4.3.2.

7.4.2 Carbon Content

By increasing the carbon content of the base composition, it has been shown (Fig. 6.33) that I.F. still occurs even at the eutectoid composition when there is no ferrite network formed at the prior austenite grain boundaries during primary cooling. Hence it is possible to discount the theory that the presence of a ferrite network may in some way be necessary for intergranular fracture behaviour (Wolf, 1980). Fig. 6.33 does show, however, that increasing the carbon content results in a finer grain structure on the intergranular fracture surface. This coincides with a change from peritectic solidification below ~0.5%C (0.51%C for a pure Fe-C alloy) to solidification directly to austenite above this composition. Few experimental data exist regarding the effect of the peritectic transformation on the grain size of steels. However, West (1950) and Bibby (1972) have shown that less dendritic fragmentation occurs during peritectic solidification than in higher carbon alloys, and this would tend to promote a larger grain size for low C contents. Moreover, Bibby and Beech (1973) have shown that the size of the columnar region also decreases as the carbon content of the melt is increased.

It has been shown in Section 4.3.2 that increasing the carbon content will tend to increase the susceptibility to I.F. by increasing the matrix strength (Wright and Quarrell, 1962). However, another way in which carbon can influence I.F. is by reducing the solubility of AlN in steel, thereby increasing the precipitation temperature and the amount of AlN that is formed. The effect of carbon on the solubility product of AlN at 1300°C is shown in Fig. 7.5, using the solubility data of Gladman and Pickering (1969) and interaction coefficients taken from Table 4.3.

7.4.3 Pouring Temperature and Cooling Rate

Neither of these two variables has been studied extensively in the present work. However, the results suggest that pouring temperature has little effect on the susceptibility to I.F. in cases where the primary grain size remains constant. Any increase in grain size as a result of excessive superheat would tend to increase the density of AlN precipitates per unit of grain boundary area, but these effects were not noted, even with a superheat of 200°C (Section 6.3.3).

The cooling rate has in the past been shown to have quite a marked effect on the susceptibility to I.F. (Lorig and Elsea, 1947; Woodfine and Quarrell, 1960). The results of the present work have confirmed that a slow cooling rate tends to promote I.F., since the larger (100mm square) castings exhibited I.F. at significantly lower Al and N contents than the smaller 75mm square and 25mm keel block castings, (Table 6.4). One possible explanation has already been discussed in Section 7.3.1.

In normal foundry practice, the cooling rate of a casting is usually fixed by the physical size of the casting and considerations such as the need to avoid excessive thermal stresses. It has already been noted that in large, slowly cooled castings it is imperative to avoid high Al and N contents. There is, however, another implication of the cooling rate effect, and that concerns the relevance of small cast-on test bars which are often used to determine the mechanical properties of a casting. It must be remembered that not only are these likely to be cooled significantly faster than the bulk of the casting, but they are also unlikely to contain macro-segregates. Both these factors tend to reduce the susceptibility of the test bar to I.F., and any results must be treated with caution when applied to the parent casting. The present work has, however, shown ways in which any susceptibility to I.F. may be emphasised by other means in order to take such factors into account. For example, it may be prudent to test for I.F. in a quenched and lightly tempered test bar even though the casting is intended to be used in the as-cast or normalised state (see Sections 6.3.4, 7.2 and 7.4.4). Moreover, if the test bar gives a fully fibrous fracture at room temperature, a further test should be carried out at a lower temperature, since this can also emphasise any tendency for I.F., as shown in Fig. 6.45.

7.4.4 Heat Treatment

The effect of relative matrix to grain boundary strengths has already been noted in Section 7.2. It is important to realise that I.F. may not only be enhanced by the effects of heat treatment - it may also be disguised. For example, in the as-cast or as-quenched

condition, the most favourable fracture mechanism is often one of cleavage in pearlite or martensite respectively (Fig. 6.34), and I.F. will rarely be observed. Similarly, if the steel is annealed or extensively tempered to reduce the yield strength fracture may occur by a fibrous mechanism. In both cases, however, the resulting mechanical properties are likely to be inadequate, despite the fact that no I.F. is observed.

The use of a high temperature solution treatment to redissolve the AlN precipitates is not considered to be of commercial significance. The results of this work have shown that treatment of a 0.17%Al-0.017%N steel at temperatures of up to 1300°C followed by water quenching merely results in a coarsening of the precipitates, and that fracture remains intergranular. This is only to be expected from the solubility data available for AlN in austenite (Fig. 4.4) which predicts an [Al] x [N] solubility product of only 5×10^{-4} at 1300°C. In steels containing lower amounts of Al and N, Lorig and Elsea (1947) and Woodfine and Quarrell (1962) claimed a reduction in the amount of I.F. by heat treating at 1250°C, but it may be that in this case the intergranular fracture mode was simply masked by changes in the matrix strength. Whatever the reason, it is considered that the practical implications of using temperatures in excess of 1200°C and the high cooling rates necessary to avoid reprecipitation virtually preclude the use of this method in industry. Also at these temperatures there are the added dangers of overheating and burning (Section 3.4.2.2).

7.5 The Effect of I.F. on Mechanical Properties

The results of the mechanical testing programme have highlighted several ways in which the presence of an intergranular network of AlN can affect mechanical properties. The temperature and conditions of the specific test employed have been shown to be particularly important in determining the extent to which embrittlement may be detected.

7.5.1 Tensile Properties

In the simple case of a room temperature uniaxial tensile test, the presence of I.F. results in a deterioration of ductility as measured by both the % elongation and reduction in area (Table 6.6). The extent to which I.F. affects these properties will largely depend on the relative orientation of the embrittled grain boundaries to the tensile axis, and hence a wide variation in these properties would be expected. For example, Harris and Chandley (1962) obtained reductions in area ranging from 5.5% to 32.2% for fully intergranular fractures. This compared to typical values of 40% R/A for ductile material. The effect becomes more pronounced the larger the grain size of the material in relation to the size of the test piece. Therefore, even if a tensile result indicates I.F. with an adequate ductility to meet the specification, the properties of the casting may be significantly worse than this.

The variation in tensile properties with temperature indicate a dependence of the intergranular fracture strength on the yield strength of the matrix (Fig. 6.40). Bearing in mind once again that 'intergranular' fracture is actually transgranular with respect to the microstructure present at the time of testing this is

not unexpected, since the strength in the ductile regime depends on the ease of void nucleation at second phase particles (in this case the AlN). As the testing temperature is increased, the ease of void nucleation at MnS inclusions also becomes more favourable, (Thompson and Weihrauch, 1976), and because of geometrical considerations and the constraints involved in fracture along the AlN embrittled grain boundaries, a temperature is reached when it becomes preferable for fracture to proceed in a truly 'transgranular' manner around the MnS. This has already been discussed in Section 7.2.

7.5.2 Impact Properties

The effects of temperature on the fracture behaviour of impact specimens has already been discussed in Section 7.2. The main observation is that instead of a simple transition from cleavage to mixed I.F./fibrous failures as reported by Wright and Quarrell (1960) (Fig. 3.1) the presence of I.F. results in two transitions. The lower temperature transition is from cleavage to I.F., and the higher temperature one from I.F. to fibrous failures, as shown in Fig. 6.43. This behaviour has been interpreted in terms of the relative strengths of the matrix and grain boundary (Section 7.2). In less severely embrittled steels, however, the double transition may not be well defined and the impact energy absorbed increases gradually with increasing temperature as in Fig. 6.45. In this case there is not a large difference between the inter- and intragranular strengths and hence the I.F. is only manifest over a relatively small temperature range.

The effect of I.F. on the impact energy in the mixed I.F./fibrous region of Fig. 6.43 is shown in Fig. 6.44, and it can be seen that increasing the amount of I.F. results in a decrease in impact energy which satisfies the empirical relation

$$E \text{ (in J)} = 83 - 0.685 \times (\%\text{I.F.}).$$

Hence, even in samples which were 100% I.F. the impact energy was still ~15J. The reason for this is the mechanism of I.F. discussed in Section 7.2, which incorporates some micro-ductility.

Fig. 6.43 shows that within the mixed I.F./fibrous region, there is a large scatter of results which correspond to the differing proportions of I.F. and fibrous features on the fracture surface. These do not appear to be a function of temperature within the mixed mode regime, and are likely to depend on the orientation of the test piece relative to the grain boundaries. This effect was minimised by notching the specimens so that fracture occurred parallel to the length of the columnar grains, but inevitably the exact position of the notch root relative to the grain boundaries will have given rise to significant variations in %I.F. and impact energy.

The effects of matrix hardness on impact properties have been shown in Figs. 6.49 and 6.50. Increasing the tempering time at 600°C decreased the temperature interval over which I.F. occurred and improved the upper shelf energy. The fractographs in Fig. 6.50 show that for hardnesses above HV30 = 200 (tempering times of less than two hours) the steel exhibits some I.F. over the whole range of testing temperatures investigated. This corresponds to the low upper shelf energies observed for casts 6B, 6D and 7A.

Cast 7B, which was tempered to a hardness of HV30 = 182, exhibited I.F. over a narrower range of temperatures and this had almost disappeared at temperatures above 50°C. Finally cast 7D (HV30 = 170) did not exhibit any I.F. and had an upper shelf energy of ~60J.

Comparing this behaviour with the strength model in Fig. 7.1, it can be seen that in the lightly tempered material the yield strength of the matrix is high compared to the strength of the grain boundaries, (Fig. 7.6(a)) and I.F. is observed over a range of temperatures. Increasing the tempering time reduces the strength of the matrix (Fig. 7.6(b)) so that the I.F. regime is contracted, and finally after tempering for 8 hours, it disappears (Fig. 7.6(c)).

7.5.3 Fracture Toughness

7.5.3.1 COD for Crack Initiation (δ_i)

The main feature of the COD test results was the insensitivity of the conventionally measured COD for crack initiation (δ_i) to the presence of I.F. at all temperatures. (Fig. 6.51). The reason for this is thought to arise from the highly localised position of the fatigue crack tip with respect to the embrittled grain boundaries. Since the microstructures of the embrittled and unembrittled samples are identical except for the distribution of AlN precipitates, unless the root of the fatigue crack coincides exactly with a line of AlN precipitates, the COD value measured will be representative of the properties of the matrix. It is not until some slow fibrous crack growth has occurred that the crack encounters an embrittled grain boundary along which it can propagate. This may involved a significant step in the plane of the crack front (Fig. 6.57).

This highlights a problem which often arises in fracture toughness testing and the need to consider the micro-mechanisms of crack extension should be emphasised, since in many cases these may invalidate the numerical data generated by a test. Another example has been reported for a temper embrittled steel by Berry and Brook (1975) who found that δ_i was not sensitive to the presence of T.E. because of the initiation of slow ductile crack growth prior to intergranular failure. Similarly, Gittos and Dolby (1979) found difficulties in measuring the heat affected zone (HAZ) toughness of welds because of the problems in locating the fatigue crack tip within the HAZ. The crack tip was correctly positioned in only 20% of the specimens examined, and the remainder gave erroneously high values of the COD. The effects of crack tip specificity have also been cited by Ritchie et al (1976) to explain anomalies observed during toughness testing of AISI 4340 steel.

7.5.3.2 COD at Maximum Load (δ_{max})

Fig. 6.52 has shown that the presence of I.F. lowers the value of COD at maximum load (δ_{max}) quite significantly. This is because δ_{max} is largely governed by necking in the uncracked ligament of the sample after the initiation of slow crack growth (Knott, 1973c) and is therefore sensitive to the presence of I.F. in much the same way as is the tensile ductility. Fatigue crack location effects have little influence on δ_{max}, because the parameter being measured is dependent on properties some distance from the crack tip, and which are averaged over the cross-sectional area of the sample. In a sample tested under displacement control, intergranular cracking may take place by rapid bursts ahead of the

main crack front after initiation. This will tend to reduce the load-bearing cross-sectional area of the sample and hence reduce δ_{max}. In contrast, under the conditions of load control which usually apply in service, it would be expected that once I.F. has been initiated it will propagate rapidly and give rise to catastrophic failure.

7.5.3.3 Commentary on δ_c, δ_i, δ_u and δ_{max}

Some of the considerations involved in choosing a 'critical' value of the COD for design purposes have been outlined in Appendix 1b. The only value of COD for which there is no ambiguity is δ_c, which is unanimously accepted as being a critical event in the fracture process (Harrison, 1980).

It is only in the last 10 years that emphasis has been placed on the need to detect initiation and to record δ_i values. These are considerably more pessimistic with regard to crack-tip ductility than are δ_{max} values and there is still discussion as to which figure is more relevant to service application (Knott, 1973c). Towers and Garwood (1979) have put forward an argument justifying the application of maximum load COD values. This was based on geometrical considerations which suggest that the results from a bend-test will underestimate the toughness which may be expected from other configurations. Certainly designs have in the past been based quite successfully on δ_u and δ_{max} data (Knott, 1973c), and Harrison (1980) advocates their continued use.

Hence, with regard to the specific problem of I.F., it appears that if a design is based on the COD for crack initiation, δ_i, this will be sufficiently conservative to incorporate any lowering of toughness as a result of I.F. In normal circumstances, however, the use of δ_{max} or other design criteria mean that an intergranular mode of failure cannot be tolerated.

Chapter 8

Conclusions

8.1 The precipitation of aluminium nitride on the as-cast grain boundaries is a major cause of intergranular fracture in steel castings. It is not, however, the only cause.

8.2 AlN-induced IF usually results from excessive additions of aluminium coupled with a high bulk nitrogen content. It is also exacerbated by a slow cooling rate. In large castings, the macrosegregation of Al and N may give rise to IF even though the bulk Al and N concentrations are not high.

8.3 AlN often precipitates in two morphologies. At high temperatures during the later stages of solidification a dendritic form can occur in the residual solute-enriched liquid. There is evidence to suggest that in some cases this may act as a nucleus for subsequent solid-state precipitation of a plate-like form of AlN. The latter grows into the austenite grains on either side of the grain boundary with $(0001)_{AlN}$// $\{111\}_{\gamma}$. Examination of the atomic arrangements within these planes reveals close matching with $\langle 10\bar{1}0\rangle_{AlN}$// $\langle 1\bar{1}0\rangle_{\gamma}$.

8.4 For a cooling rate of $0.1^{o}C\ sec^{-1}$, the thickness of the AlN precipitates is approximately 50nm. This means that the AlN can rarely be resolved when viewed optically in a metallographic section. Hence the inability to detect a grain boundary network in the optical microscope cannot be taken to imply freedom from I.F.

8.5 The mechanism of fracture changes with the temperature of testing and embrittled steels exhibit a full transition from

cleavage to intergranular to fibrous failures with increasing temperature. Because the 'intergranular' fracture path is usually transgranular with respect to the microstructure present at the time of testing, the micro-mechanisms of failure are to some extent dependent on matrix properties. At low temperatures the precipitates of AlN on the as-cast grain boundaries are linked by areas of cleavage. Above the DBTT of the matrix, however, the intergranular fracture possesses some microductility. Here, the dendritic form of the nitride acts as a void-initiating inclusion and the plate-like AlN is responsible for the highly reflecting crystallographically oriented facets often seen on the fracture surface. These occur as a result of decohesion at the AlN/matrix interface.

8.6 The 0.30C-1.50Mn steels examined were most susceptible to I.F. in the quenched and tempered condition, when the matrix strength is high compared to the strength of the AlN embrittled boundaries.

8.7 The Charpy impact energy is sensitive to the presence of intergranular fracture. For the 0.30C-1.50Mn steel studied in the quenched and tempered condition, an empirical relationship was established between the impact energy observed and the amount of intergranular fracture in the mixed IF/fibrous region of the curve: E (in Joules) = 83 - 0.685x(%I.F.).

8.8 Initiation values of the crack opening displacement (δ_i) showed little difference between embrittled and unembrittled steels despite the overall change in fracture morphology. This was because in all cases above the transition temperature, fast

intergranular fracture was preceded by slow fibrous crack growth at the root of the fatigue crack. However, values of the COD at maximum load (δ_{max}) were significantly lower for the embrittled steels than for the unembrittled.

8.9 Heat treatment to remove I.F. from embrittled castings is considered to be impractical because of the high temperatures and fast cooling rates required to dissolve the AlN and avoid reprecipitation.

8.10 The precipitation of AlN can be avoided by the use of Ti and Zr for final deoxidation after the addition of a small amount (<0.02%) of aluminium.

8.11 Results obtained from test bars taken from large castings should be treated with caution. Differences in cooling rate and levels of segregation may mask any tendencies for I.F.

Acknowledgements

I am most grateful to my supervisors, Dr. A. R. Entwisle, Professor G. J. Davies and Dr. W. J. Jackson for their guidance and encouragement during the course of this work, and to the Science Research Council and Steel Castings Research and Trade Association for the provision of funds.

Most research projects depend to a large extent on the interest and co-operation of numerous people, and this one has been no exception. I would therefore like to thank all my colleagues and friends at the University, at SCRATA, and at home for their own personal contributions. In particular, I would like to acknowledge the help given to me over the last three years by 'Bill' Beech, Martin Bridge, Kate Croft, John DeVine, Naila Dinis, Bob Hough, Steve Joel, Ted Needham, Ernest Ridal, Kevin Selby, Alan Sheldon, and last but by no means least, my parents.

Finally, a special word of thanks to Mrs. Anne Bower for typing this thesis much faster than I could write it.

REFERENCES

Allen, A. H. (1879), JISI, 11, 480.

Altmann, P., et al (1965), App. Mat. Res., 4, 20.

Aritomi, N and Gunji K. (1979), Trans. ISIJ, 19, 152.

Armstrong, R. W. (1977), 'Advances in Research on the Strength and Fracture of Materials'. Vol. 4, p. 61. Ed: D. M. R. Taplin, Waterloo, Canada.

Ashby, M. F. (1966), Phil. Mag., 14, 1157.

Bainbridge, B. G. (1972), D. Phil. Thesis, Univ. of Sussex.

Baker, A. A., et al (1979), Anal. Chim. Acta, 107, 339.

Baker, T. J. and Charles, J. A. (1972), JISI, 210, 702.

Baker, T. J. and Charles, J. A. (1973), JISI, 211, 187.

Baker, T. J. and Harrison, W. D. (1975), Met. Tech. 2, 201.

Baker, T. N. (1962), Nature, 196, 566.

Baliktay, S. (1976), Dr-ing Dissertation, University of Berlin.

Banerji, S. K. and Briant, C. L. (1980), Canad. Met. Qrtrly, 18, 169.

Banerji. S. K., et al (1978), Met. Trans. 9A, 237.

Barron, M. E. (1974), B.S.C. Report No. FP/7228/-/74/E.

Barnard, L. and Brook, R. (1967), JISI, 205, 756.

Beeghly, H. F. (1949), Anal. Chem. 21, 1513.

Berry, G. and Brook, R. (1975), Int. J. of Fracture, 11, 933.

Bibby, P. A. (1972), PhD Thesis, University of Sheffield.

Bibby, P. A. and Beech, J. (1973), JISI, 211, 290.

Bishop. H. F., et al (1958), Trans. Amer. Found. Soc. 65, 247.

Blake, P. D. and Jordan, M. F. (1971), JISI, 209, 197.

Bower, T. F. and Flemings, M. C. (1967), Trans. Met. Soc. AIME, 239, 216.

Brammar, I. S., et al (1959), I.S.I. Special Report No. 64.

Briant, C. L. and Banerji, S. K. (1978), Int. Met. Rev. 23, 164.

Briant, C. L. and Banerji, S. K. (1979a) Met. Trans. 10A, 123.

Briant, C. L. and Banerji, S. K. (1979b) ibid, 10A, 1729.

Briant, C. L. and Banerji, S. K. (1979c) ibid, 10A, 1151.

Bridge, M. R. (1981), PhD Thesis, University of Sheffield.

Bridge, M. R. and Beech, J. (1980), 'Solidification Technology in the Foundry and Casthouse", Paper 73, Metals Society, London. (To be published).

Broek, D. (1973), Eng. Fract. Mech. 5, 55.

Carney, D. J. (1953), 'Gases in Metals', ASM Cleveland, Ohio, 118, 69.

Chadwick, G. A. (1972), 'Metallography of Phase Transformations', Butterworths, London, p. 190.

Chalmers, B. (1963), J. Australian Inst. Metals, 8, 255.

Chojecki, A. and Kowalowka, M. (1978), Przeglad Odlewnictwa, 28, 139.

Clyne, T. W. (1976), PhD Thesis, University of Cambridge.

Clyne, T. W. and Davies, G. J. (1975), British Foundryman, 68, 238.

Cottrell, A. H. (1958), Trans. Am. Inst. Min. Metall. Petrol. Engineers, 212, 192.

Cottrell, A. (1975a), 'An Introduction to Metallurgy', p. 246, Edward Arnold.

Cottrell, A. (1975b), ibid, p. 414.

Cox, T. B. (1973), PhD Thesis, Carnegie-Mellon University of Pittsburgh.

Croft, N. H., Telejko, I. and Chojecki, A. (1979), Unpublished work, AGH Krakow.

Crussard, C., et al (1956), JISI, 183, 146.

Darken, L. S. and Gurry, R. W. (1953), 'Physical Chemistry of Metals', p. 372, McGraw Hill, London.

Darken, L. S., et al (1951), Trans. AIME, 191, 1174, (1951).

Davies, G. J. and Garland, J. G. (1975), Int. Met. Reviews, 20, 83.

Dawes, M. G. (1976), PhD Thesis, The Welding Institute, England.

Desai, S. C. (1959), JISI, 191, 250.

Edvardsson, T., et al (1976), Metal Science, 3, 298.

El-Soudani, S. M. (1980), PhD Thesis, University of Cambridge.

Erasmus, L. A. (1964), JISI, 202, 32.

Erasmus, L. A. and Mech, G. I. (1964), JISI, 204, 32.

Eruslu, M. N. (1976), PhD Thesis, University of Sheffield.

Evans, D. R. and Pehlke, R. D. (1964), Trans. Met. Soc. AIME, 230, 1651.

Fast, J. D. (1965), 'Interaction of Metals and Gases' Vol. 1, Macmillan, London.

Flemings, M. C. (1974), 'Solidification Processing', McGraw Hill, New York, Ch.7.

Flemings, M. C. and Nereo, G. E. (1968), Trans. AIME, 242, 50.

Flemings, M. C., et al (1968), Trans. AIME, 242, 41.

Fremunt, P. (1962), Slevarenstvi, 10, 205.

Funnell, G. D. (1979), 'Hot Working and Forming Processes', The Metals Society, London, p. 104.

Funnell, G. D. and Davies, R. J. (1978), Met. Tech. 5, 150.

Gibson, S. (1979), B.S.C. Technical Note PROD/PM/12/79.

Gilman, J. J. (1956), Trans. AIME, 212, 310.

Gittos, M. and Dolby, R. E. (1979), Welding Res. Int. 9, (6), 22.

Gladman, T. and McIvor, I.D. (1972), Scand. Jnl. of Met. 1, 247.

Gladman, T. and Pickering, F. B. (1967), JISI, 205, 653.

Gladman, T., et al (1971), 'Effect of Second Phase Particles on Mechanical Properties of Steel', 68, I.S.I. London.

Gomersall, D. W., et al (1968), Trans. Met. Soc. AIME, 242, 1309.

Hagger, P. M. (1975), M. Met. Dissertation, University of Sheffield.

Hahn, G. T., et al (1959), 'Conference on Fracture', Wiley, M.I.T. p. 91.

Halley, J. W. (1946), Trans. AIME, 167, 224.

Hannerz, N. E. (1968), Metal Science Journal, 2, 148.

Hannerz, N. E., et al (1968), JISI, 206, 68.

Harris, R. G. and Chandley, C. D. (1962), Modern Castings, 41, 97.

Harrison, J. D. (1980), Metal Construction, 12, 415.

Haynes, F. G. (1974), '20th Annual Conference Proceedings', SCRATA, Sheffield, Paper 11.

Heckler, A. J. and Peterson, J. A. (1969), Trans. Met. Soc. AIME, 245, 2537.

Hellawell, A. and Herbert, P. M. (1962), Proc. Roy. Soc. A269, 560.

Herzberg, R. W. (1976), 'Deformation and Fracture Mechanics of Engineering Materials', Wiley, Ch. 7.

Holt, J., et al (1971), '17th Annual Conference Proceedings', SCRATA, Sheffield, Paper 1.

Holt, J., et al (1973), Monograph No. 2, 'Electric Arc Furnace Practice', SCRATA, Sheffield.

Holt, J. and Hubbard, M. W. (1971), '17th Annual Conference', SCRATA, Sheffield, Paper No. 5.

Hondros, E. D. and McLean, M. (1970), Colloques Internationeaux de CRNS, 187, 219.

Hondros, E. D. and McLean, D. (1976), 'Grain Boundary Fragility', Academic Press, London, Ch. 10.

Hondros, E. D. and Stuart, L. E. H. (1968), Phil. Mag. 17, 711.

Honer, K. E. and Baliktay, S. (1978a), Giesserei Forschung, 30, 53.

Honer, K. E. and Baliktay, S. (1978b), ibid, 30, 83.

Honer, K. E. and Baliktay, S. (1978c), ibid, 30, 153.

Hubbard, M. W. (1972), Monograph No. 1, SCRATA, Sheffield.

Ichise, E., et al (1971), Trans. ISIJ, 11, 535.

Irvine, K. J. and Pickering, F. B. (1957), Iron and Steel, 30, 219.

Irvine, K. J., et al (1967), JISI, 205, 161.

Iwase, K. and Fukusima, M. (1953), Sci. Repts. Tohoku, 27, 162.

Jackson, K. A., et al (1966), Trans. Met. Soc. AIME, 236, 149.

Jackson, R. P. (1978), Private Communication from B.S.C. Rotherham Works.

Jackson, W. J. (1979), SCRATA Journal Report No. 1977, Project 4030.

Jackson, W. J. (1975), Monograph No. 4, 'Gases in Steel', SCRATA, Sheffield.

Jackson, W. J. (1977), Monograph No. 8, 'Control of Steelmaking in Relation to Casting Quality', SCRATA, Sheffield.

Jackson, W. J. (1980), Private Communication from SCRATA.

Jackson, W. J. and Bradshaw, J. (1970), SCRATA Jnl. of Research, 11, 11.

Jackson, W. J. and Wright, J. C. (1977), Met. Tech. 4, 425.

Jolivet, H. (1942), Rev. Met. 39, 233.

Kameda, J. and McMahon, C. J. (1980), Met. Trans. 11A, 91.

Knott, J. F. (1973a), 'Fundamentals of Fracture Mechanics', Butterworths, London, Ch. 8.

Knott, J. F. (1973b), ibid, Ch. 7.

Knott, J. F. (1973c), ibid, Ch. 6.

Knott, J. F. (1981), Private Communication from the University of Cambridge.

Kondic, V. (1968), 'Metallurgical Principles of Founding', Arnold, London, p.49.

König, P. Scholz, W. and Ulmer, H. (1961), Arch. Eisenhüttenwes, 32, 541.

Kuhn, V. and Detrez, P. (1962), Modern Casting, 27, p. 469.

Kunio, T., et al (1977), 'Advances in Research on the Strength and Fracture of Materials', Vol. 2, Ed: D. M. R. Taplin, Waterloo, Canada.

Leewis, K. G. and MacLean, A. (1979), Canadian Met. Quarterly, 18, 333.

Leger, M. T. and Guillaume, B. (1979), Fonderie, 385, 19.

Lement, B. S., et al (1954), Trans. ASM, 46, 851.

Leslie, W. C., et al (1954), Trans. ASM, 46, 1470.

Lorig, C. H. (1952), Trans. ASM, 44, 30.

Lorig, C. H. and Elsea, A. R. (1947), Trans. AFS, 55, 160.

Low, J. R. (1954), 'Symposium on Relation of Properties to Microstructure', ASM, p. 163.

Low, J. R. (1959), 'Atomic Mechanisms of Fracture', Wiley, Swampscott, Mass., p. 68.

McMahon, C. J. (1975), 'Grain Boundaries in Engineering Materials', Baton Rouge, Bolton Landing, p. 525.

McMahon, C. J. and Cohen, M. (1965), Acta. Met. 13, 591.

Maekawa, S. and Nakagawa, Y. (1975), Tetsu to Hagane, 45, 255.

Mahmoud, (1974), S.F.S.A. Project 90, Rocky River, Ohio.

Marshall, S. and Chipman, J. (1942), Trans. ASM, 30, 695.

Matasova, M. and Tuma, H. (1973), Neue Hütte, 18, 430.

Mayrhofer, M. (173), Berg und Hüttenmänische Monatshefte, 120, 312.

Mehrebian, et al (1970), Met. Trans. 1, 1209.

Metz, S. A. and Flemings, M. C. (1970), Trans. A.F.S. 78, 453.

Middleton, J. M. (1966), Proc. 1966 BSCRA Conf., Paper 7.

Mills, B., et al (1973), Phil. Mag. 27, 361.

Mori, T. and Ichise, E. (1968), Nippon Kunzoku Gakkan, 32, 949.

Mulford, R. A., et al (1976), Met. Trans. 7A, 1269.

Myers, M. and Flemings, M. C. (1972), Met. Trans. 3, 2225.

Nakajima, H. (1977), Trans. National Research Inst. for Metals, 19, 26.

Naumann, F. K. and Spiess, F. (1973), Prak. Met. 10, 230.

Navara, E. and Easterling, K. E. (1971), Jernkontoret Ann., 155, 437.

Orowan, E. (1945), Trans. Inst. Engs. Shipbuilders Scot. 89, 165.

Paranjpe, V. G., et al (1950), Trans. AIME, 188, 261.

Pearson, J. and Ende, U. J. C. (1953), JISI, 175, 52.

Pehlke, R. D. and Elliott, J. F. (1960), Trans. AIME, 218, 1088.

Pereira, O. J. (1979), PhD Thesis, University of Sheffield.

Petch, N. J. (1958), Phil. Mag. 3, 1089.

Pfann, W. G. (1952), Trans. AIME, 194, 747.

Plateau, J., et al (1960), 3eme Coll. de Met. Corrosion, p. 185.

Puttick, K. E. (1950), Phil. Mag. 4, 964.

Raynor, D., et al (1966), JISI, 204, 349.

Reed-Hill, R. E. (1972), 'Physical Metallurgy Principles', Van Nostrand-Reinhold, New York, p. 553.

Reynolds, J. A. (1979), Engineers Digest, 40, 39.

Reynolds, J. H. and Gladman, T. (1979), 'Hot Working and Forming Processes', The Metals Society, London, p. 171.

Rickett, R. L. and Leslie, W. C. (1957), Met. Treatment, 24, 59.

Ritchie, R. O., et al (1976), Met. Trans. 7A, 831.

Rogers, H. C. (1960), Trans. AIME, 218, 498.

Sakagami, R., et al (1969), Tetsu to Hagane, 55, 550.

Scheil, E. (1942), Z. Metallkunde, 34, 70.

Schenck, H., et al (1958), Arch. Eisenhüttenwes, 29, 673.

Schenck, H., et al (1959), ibid, 30, 533.

Schenck, H., et al (1963), Stahl und Eisen, 83, 93.

Schurmann, E. and Kunze, H. C. (1967), Arch. Eisenhüttenwes, 41, 585.

Seah, M. P. and Hondros, E. D. (1973), Proc. Roy. Soc., A335, 191.

Seah, M. P., et al (1979), Met. Sci. 13, 307.

Selby, K. (1977), SCRATA J. of Research, 38, 12.

Selby, K. (1979), SCRATA Report No. 1983.

Selby, K. and Danson, P. J. (1977), SCRATA Report No. 1872.

Shin, Y. K. (1981), PhD Thesis, University of Sheffield.

Sidey, M. P. (1967a), Iron and Steel, 40, 168.

Sidey, M. P. (1967b), ibid, 40, 269.

Sieverts, A. (1929), Z. Metallkunde, 21, 37.

Sieverts, A. (1931), Z. für Phys. Chem. 155A, 299.

Sieverts, A., et al (1938), ibid, 168A, 19.

Smith, E. (1966), 'Physical Basis of Yield and Fracture', Inst. Phys. Phys. Soc. Oxford, p. 36.

Smith, E. and Barnby, J. T. (1967), Metal. Sci. J. 1, 56.

Southin, R. T. (1967), Trans. Met. Soc. AIME, 239, 220.

Speith, K. G. and VomEnde, H. (1959), Journal of Metals, 11, 333.

Stachura, S. and Szkoda, F. (1969), Przeglad Odlewnictwa, 19, 403.

Stachura, S. (1971), Przeglad Odlewnictwa, 21, 233.

Stachura, S. (1977), Archiwum Hutnictwa, 22, 490.

Stachura, S. (1980), Private Communication from Polytechnic of Czestochowa, Poland.

Steck, A. B. (1969), Jnl. of Steel Castings Research, 49, 1.

Stephenson, S. D. (1974), Unpublished Work, SCRATA, Sheffield.

Stickler, R. and Vinckier, A. (1961), Acta. Met. 9, 898.

Stroh, A. N. (1957), Adv. Phys. 6, 418.

Svensson, I. and Fredriksson, H. (1980), 'Solidification Technology in the Foundry and Casthouse', Metals Society, London, Paper 59. (To be published).

Swinburn, D. G. and Melia, P. J. (1970), Metallurgia, 81, 37.

Takei, T., et al (1964), Tetsu to Hagane, 50, 2006.

Thompson, A. W. and Weihrauch, P. F. (1976), Scripta Met. 10, 205.

Tipper, C. F. (1949), Metallurgia, 39, 133.

Towers, O. L and Garwood, S. J. (1979), Welding Institute Res. Bulletin, 20, 292

Uda, M. and Pehlke, R. D. (1974), Cast Metals Res. J. 10, 30.

Uhlmann, D. R., et al (1964), J. Appl. Phys. 35, 2986.

Valencia, J. J. (1981), PhD Thesis, University of Sheffield.

Veerman, C. C. and Muller, T. (1972), Eng. Fract. Mech. 4, 25.

Wada, H. and Pehlke, R. D. (1978), Met. Trans. B. 9B, 441.

Walker, J. L. (1958), 'Liquid Metals and Solidification', ASM, Cleveland, p.319.

Wertebach, P. and Hoff, H. (1958), Stahl und Eisen, 78, 736.

West, D. R. F. (1950), JISI, 164, 182.

Wiester, H. J., et al (1957), Stahl und Eisen, 77, 773.

Wilder, T. C. and Elliott, J. F. (1960), J. Electrochem. Soc. 107, 628.

Wilson, F. G. (1971), JISI, 209, 126.

Wilson, F. G. (1981), Private Communication, from B.S.C. Sheffield Laboratories.

Wirth, A. and Clarke, B. (1981), Met. Tech. 8, 161.

Wolf, M. (1980), Private Communication from Concast AG, Zurich.

Woodfine, B. C. and Quarrell, A. G. (1960), JISI, 195, 409.

Wright, J. A. and Quarrell, A. G. (1962), ibid, 200, 299.

Wright, J. A. (1962), PhD Thesis, University of Sheffield.

Yamanaka, K. and Ohmori, Y. (1978), Trans. ISIJ, 4, 25.

APPENDICES

APPENDIX 1

Fracture Toughness Testing

1a. Sample size requirements for valid K_{IC} measurements

BS 5447 (1977) specifies that for a valid K_{IC} measurement, both the crack length (a) and the thickness (B) shall be not less than

$$2.5\left(\frac{K_{IC}}{\sigma_y}\right)^2 \qquad (1a.1)$$

where σ_y is the 0.2% proof stress of the material under the conditions of test.

Initially, the test piece dimensions should be based on either

i) An estimate of the K_{IC} of the material
(preferably an over-estimate)

or ii) The ratio of 0.2% P.S. to Young's Modulus which can be related to the size requirements via a table.

To take into account uncertainties such as underestimation of the K_{IC} value and the possibility of the test not meeting other validity criteria, BS 5447 further recommends that the criterion for selection of sample size should be

$$B > 4\left(\frac{K_{IC}}{\sigma_y}\right)^2 \qquad (1a.2)$$

Using the data of Selby (1977) for a 0.23C-1.25Mn steel, the K_{IC} value for the 0.30C-1.50Mn steel used in this work was estimated to be ~120MNm$^{-3/2}$.

The minimum value of the proof stress given in the specification for this material is $\sigma_y = 370MNm^{-2}$, (BS 3100 A5, 1976)
Therefore, in equation (1a.2), $B \geq 4\left(\frac{120}{370}\right)^2 = 0.42m$

i.e. the minimum thickness B = 420mm.

With a typical thickness to width ratio of 0.5, this would mean that in order to obtain a valid K_{IC} result the samples would have to be of the approximate dimensions 4m x 1m x 0.5m.

1b. Procedure for the Calculation of COD Values

i) Nomenclature

Symbol	Term
W	Test piece width
B	Test piece thickness
N	Notch width
a	Effective crack length
Z	Distance of clip gauge location from test piece surface
P_f	Fatigue pre-cracking force
Y	Stress intensity coefficient (compliance function)
K	Stress intensity factor
P	Applied force
V	Clip gauge displacement
δ	Value of crack opening displacement
σ_y	0.2% proof stress
E	Young's Modulus
ν	Poisson's ratio

Additionally, the following suffices are used to denote significant events in the fracture process, and can be applied to P, V and δ (see Fig. A1.1).

Suffix	Event
C	Onset of unstable fracture or an arrested brittle crack. This term only applies where there is no evidence to suggest prior slow crack growth.
i	Initiation of slow crack growth.
max	Point of first attainment of maximum load.
u	Onset of unstable fracture or an arrested brittle crack which has been preceded by slow crack growth.

ii) Definition of a 'Critical' Event in the Fracture Process

For situations where unstable fracture takes place without prior slow crack growth, the critical event in the fracture process is clearly represented by δ_c. This is the normal state of affairs at low temperatures, as shown schematically in Fig. A1.1(a).

However, at temperatures where slow crack growth precedes either rapid fracture or the attainment of a maximum force plateau the critical event in the fracture process may be represented by either δ_i, δ_u or δ_{max}, (Figs. A1.1(b) and (c)).

The choice of an appropriate value depends to a large extent on the design criteria which are being used, and whether or not slow crack growth in a structure or component can be tolerated. If not, then δ_i would be chosen as a critical value of the crack opening displacement. If the design criterion is based on plastic collapse, then it would be appropriate to consider δ_{max} as a critical value.

iii) Calculation of COD Values

The case of an unembrittled steel tested at room temperature will be considered, and the autographically plotted traces of load vs. clip gauge displacement (V_1) and clip gauge 1 (V_1) vs. clip gauge 2 (V_2) are shown in Figs. A1.2 and A1.3. An enlarged photograph of the fracture surface was used for measurements of the crack length (a).

The specimen dimensions (B, W and N) were measured using a micrometer prior to testing.

Fig. A1.2 shows that fracture has occurred by the initiation of a slow crack and that general yielding of the sample has occurred. The point of initiation of the crack was determined by noting the first change in slope of the double clip gauge plot towards the V_1 axis in Fig. A1.3. This clip gauge displacement was then translated onto the load/displacement graph to determine the load for the initiation of slow crack growth (P_i). By constructing a tangent to the initial elastic region of this curve, it was possible to measure the plastic component of the clip gauge displacement at initiation $(V_p)_i$, as shown in Fig. A1.2.

The equations used for calculating COD values were originally due to Dawes (1976) and are as recommended by BS 5762 (1979).

$$\delta = \frac{K^2 (1 - \nu^2)}{2\sigma_y E} + \frac{0.4 (W - a) V_p}{0.4W + 0.6a + Z} \qquad (1b.1)$$

where $K = YP/BW^{\frac{1}{2}}$ (1b.2)

and Y is determined from tables of the compliance as a function of a/W.

Hence for sample 46/1D, the calculation is as follows:

a = 20.08mm (measured on fracture surface)

B = 20.12mm
W = 40.00mm
N = 2.52mm
} measured prior to testing

$\therefore$ a/W = 0.502 which gives Y = 10.68 from Table 1 of BS 5762 (1979).

σ_y = 348MNm^{-2} (from independent tensile tests).

P_i = 23800 N
$(V_p)_i$ = 0.185mm
} measured from Fig. A1.2.

from equation (1b.2)

$$K = \frac{YP}{BW^{\frac{1}{2}}} = \frac{10.68 \times 23800}{20.12 \times (40.00)^{\frac{1}{2}}} = 1997.5 \text{ Nmm}^{-3/2}$$

$\therefore$ in equation (1b.1) and taking E = 207570, ν = 0.3 and Z = 3.6mm

$$\delta_i = \frac{1997.5^2 (1 - 0.3^2)}{2 \times 348 \times 207571} + \frac{0.4 (40.00 - 20.08) \times 0.185}{(0.4 \times 40) + (0.6 \times 20.08) + 3.6}$$

$\underline{\delta_i = 0.072\text{mm}}$

Similar calculations can be used to determine the COD at other significant points on the curve.

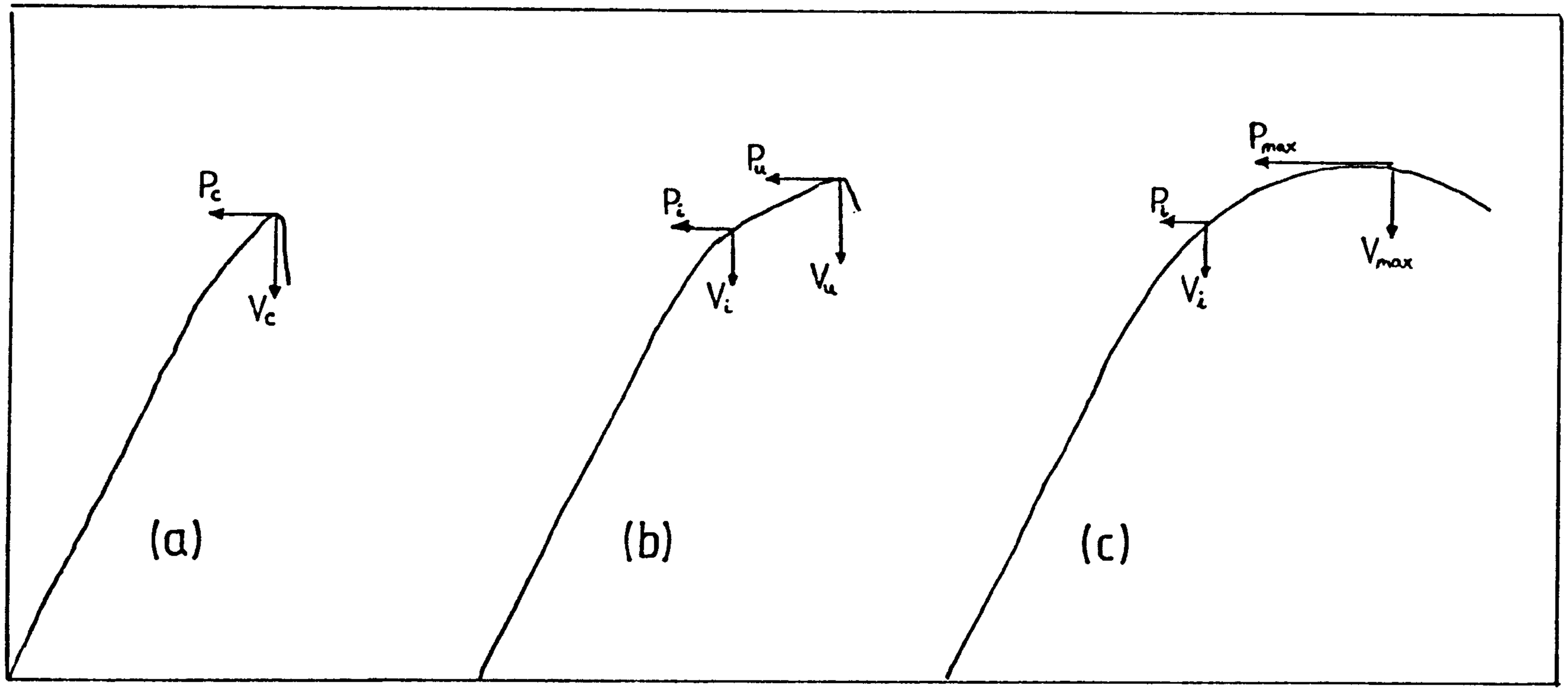

Fig. A1.1 Schematic load/displacement curves showing the position of 'significant' events in the fracture process.
(a) low temperature : δ_c (unambiguous)
(b) intermediate temperatures : δ_i and δ_u
(c) higher temperatures : δ_i and δ_{max}.

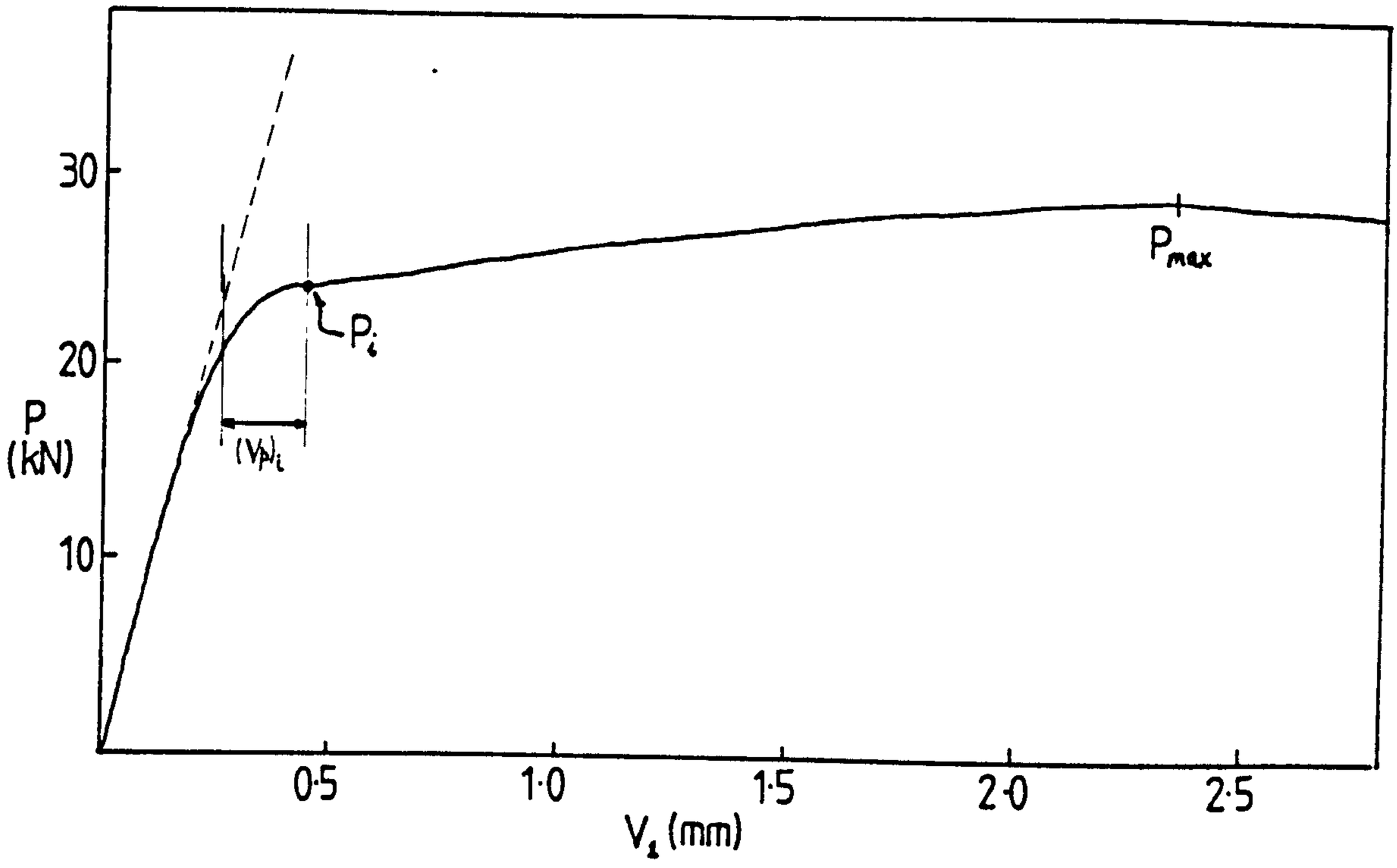

Fig. A1.2 Load/clip gauge displacement curve for COD sample 46/1D at room temperature.

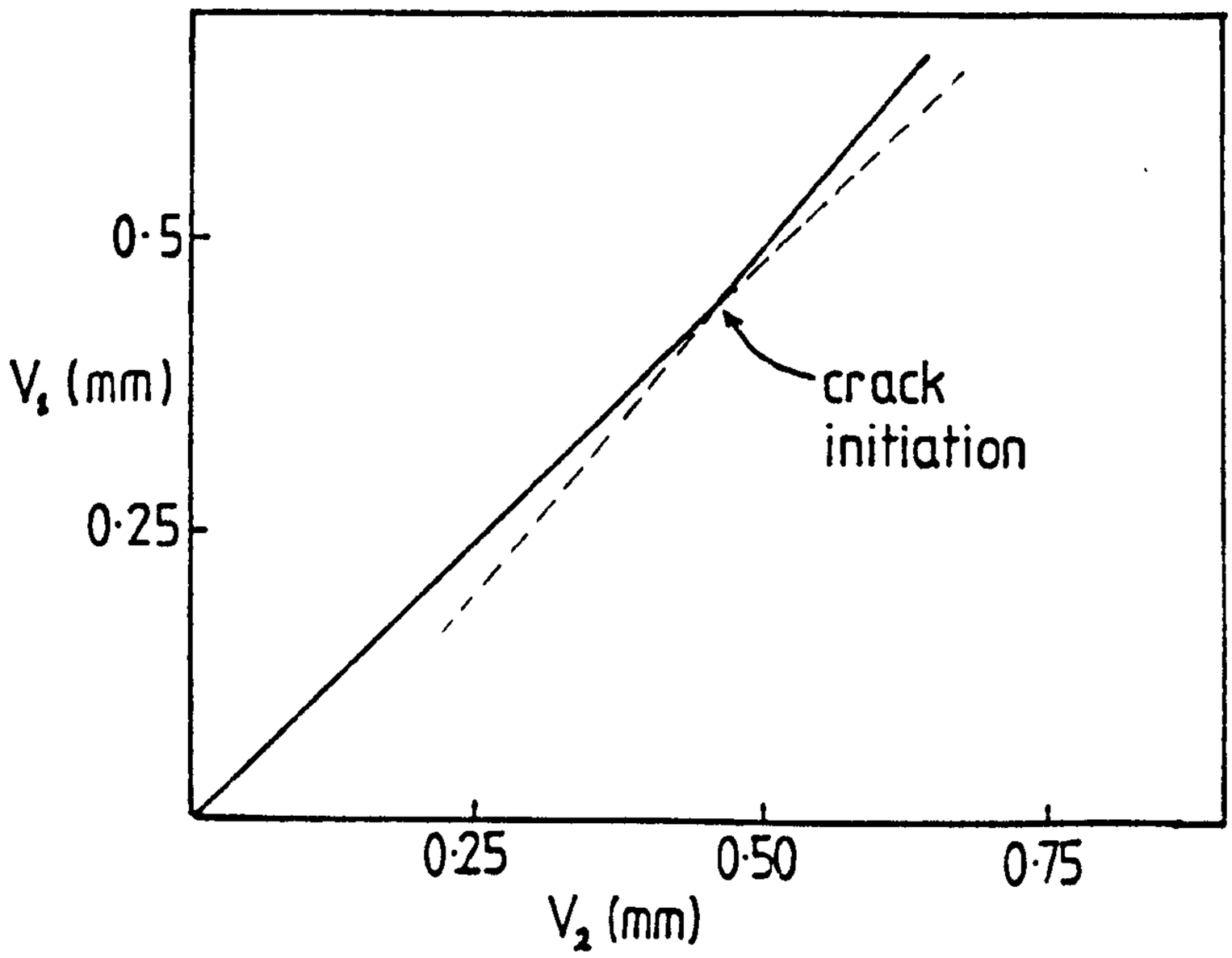

Fig. A1.3 Clip gauge (V_1) vs clip gauge (V_2) curve for COD sample 46/1D at room temperature. Initiation of slow crack growth is defined at the first significant change of slope towards the V_1 axis.

Director: J. A. Reynolds, B.Sc., Ph.D., F.I.B.F., F.I.M.

Steel Castings Research and Trade Association

Your reference:
Our reference:

Registered Office: 5 EAST BANK ROAD, SHEFFIELD S2
Telephone: 0742 28647 Telex: 54281 S.C.R.T.A. Sheffield

29th February, 1980
Report No. MQ/E 19753

Report to

Foundry 'A'

Investigation into the Fracture of a Mill Housing

by

N. H. Croft

Introduction

The aim of this investigation was to determine the cause of failure of a large mill housing which had fractured in a coarse intergranular manner. Intergranular fracture of cast steels has frequently been associated with the precipitation of aluminium nitride on the primary (as-cast) grain boundaries (Refs. 1-5), but this is by no means the only possible cause. Other factors which may result in failure of this kind are the presence of a ferrite network, extreme Type II manganese sulphide inclusions, or small internal hot tears, all of which favour preferential crack propagation along the grain boundaries.

Chemical Analysis

C%	Si%	Mn%	P%	S%	Cr%	Mo%	Ni%	Cu%
0.35	0.36	1.11	0.022	0.033	0.06	<0.02	0.08	0.05

Al% (total)	N% (total)
0.053	0.018

Hardness

HV30 = 174 ± 3 in the as-received condition.

Microscopical Examination

Samples cold sawn from the mill housing were fractured by slow three-point bending, and confirmed the coarse intergranular mode of failure (Fig. 1).

Microsections taken from a region near to the fracture surface showed no apparent reason for the intergranular fracture when viewed under the optical microscope (Fig. 2). In the unetched condition, the inclusions observed comprised Type III manganese sulphides, and oxide inclusions resulting from primary deoxidation. It was not possible to resolve any precipitates of aluminium nitride, but these are invariably very fine and can only be seen using electron optical techniques.

After etching in 2% Nital, the structure of the as-received casting was shown to be a mixture of fine equiaxed ferrite and pearlite, suggesting that the component had been normalised. There was no evidence of a ferrite network.

Samples were cold sawn from the fracture surface and mounted on aluminium stubs for examination in a Philips PSEM 500X Scanning Electron Microscope. In addition, a polished microsample taken from a position perpendicular to the fracture surface, and incorporating the root of an intergranular crack, was also mounted for examination.

The fracture surface, when viewed at a relatively low magnification, revealed features typical of a "Rock Candy" fracture caused by the presence of aluminium nitride (Fig. 3). The coarse intergranular facets exhibited large areas of cleavage fracture (Fig. 4), interspersed with terrace-like platelet features crystallographically oriented on the fracture surface. Also in evidence, though much less common, were fine dendritic features, which can also be seen in Fig. 4. Energy dispersive X-ray analysis of the fracture, using a LINK system showed an increase in the amount of aluminium on the surface of the platelets, but unfortunately it is not possible to detect nitrogen using this technique because of atomic number limitations.

Examination of the polished microsection in the SEM showed needle-like precipitates extending into the matrix ahead of the crack tip (see Fig. 5), and again these regions appeared slightly enriched in aluminium.

Positive evidence as to the cause of failure resulted from the use of the transmission electron microscope (TEM). Carbon extraction replicas were taken from a freshly fractured surface, using an electrolytic etching technique to remove the carbon film from the fracture. Examination of these replicas in a Philips EM301 microscope revealed networks of a grey plate-like precipitate, which was heavily fractured, presumably either during the fracturing of the steel, or as a result of the replication technique (see Figs. 6 and 7). These were identified as AlN using selected area electron diffraction, the observed "d" spacings being within 1% of the published values for aluminium nitride (hexagonal structure with $a = b = 3.11\text{Å}$, $C = 4.99\text{Å}$).

Also present in occasional areas were grey dendritic precipitates, again identified by electron diffraction as AlN (Figs. 8 and 9), and in some cases these were continuous with the plate-like precipitate. (Fig. 9).

Discussion

From the results of the microscopic examination, it is clear that the coarse intergranular fracture of the mill housing results from the precipitation of aluminium nitride (mainly in the form of plates) on the as-cast grain boundaries during primary cooling of the casting.

Although the aluminium content of the steel is not unduly high at 0.053%, the total nitrogen content (0.018%) is well above what would normally be expected for a steel of this composition, and it is likely that the aluminium nitride precipitation has been favoured by this high nitrogen content, together with a slow cooling rate through the precipitation temperature range (between 1100°C and 700°C).

Woodfine (Ref. 3) has described a method of removing intergranular fracture by heat treating at high temperature to dissolve the aluminium nitride, followed by rapid cooling to avoid reprecipitation in the massive form. However, this does not provide a practical solution in this instance, since the temperature required to dissolve 0.053%Al and 0.018%N would be well in excess of 1300°C. (Calculated from thermodynamic data given by Gladman and Pickering in Ref. 6).

More preferable would be to prevent precipitation of the grain boundary nitride in future castings of this type, and here there are three possibilities:

i) Endeavour to keep the nitrogen content at a lower level (~0.01%).

ii) Increase the cooling rate through the precipitation temperature range.

iii) Use titanium, as reported by Woodfine (Ref. 3), in addition to aluminium to form the more stable TiN which does not precipitate in massive forms at the grain boundaries.

Conclusions

The coarse intergranular fracture of the mill housing has resulted from the presence of a grain boundary network of aluminium nitride precipitated during primary cooling of the casting, and probably in the temperature range 1100°C-700°C.

References

1. C. H. Lorig and A. R. Elsea. Trans. A.F.S., 55, 160 (1947).

2. B. C. Woodfine and A. G. Quarrell. J.I.S.I. 195, 409 (1960).

3. J. A. Wright and A. G. Quarrell. J.I.S.I. 200, 299 (1962).

4. W. J. Jackson and J. Bradshaw. SCRATA J. of Research No. 11, Dec. 1970.

5. M. P. Sidey. Iron and Steel 40, 269 (1967).

6. T. Gladman and F. B. Pickering. J.I.S.I. 205, 653 (1967).

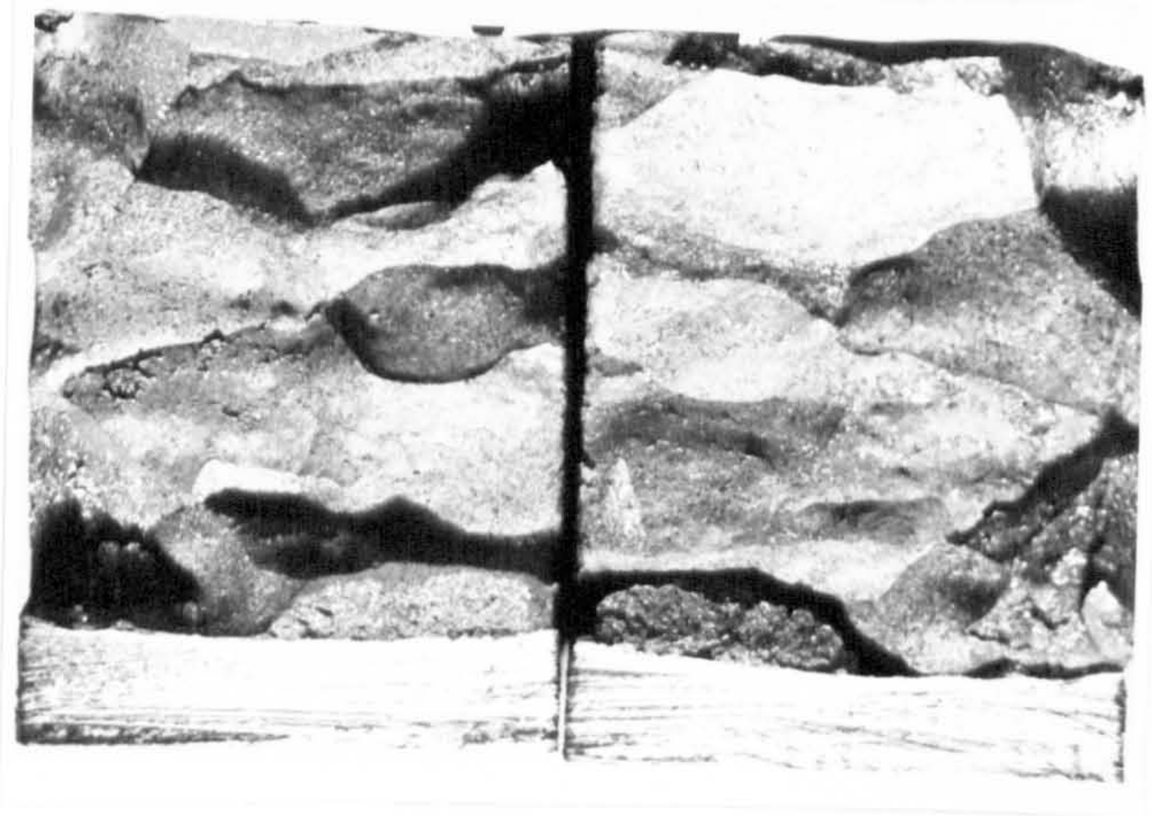

Fig. 1 Macroscopic view of the freshly fractured surface, broken by slow three-point bending.

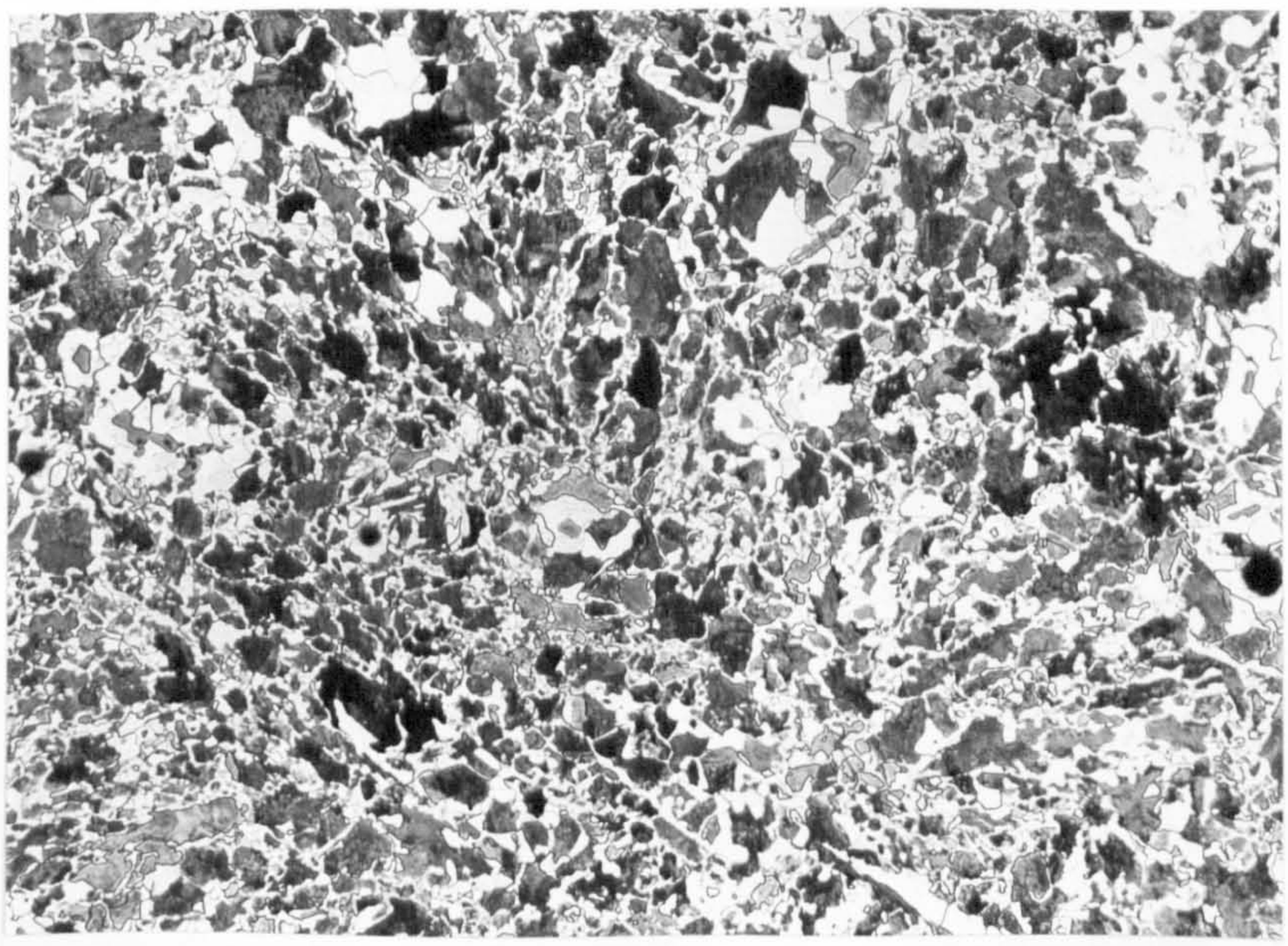

Fig. 2 Microstructure from a section taken near the fracture surface, revealing fine equiaxed ferrite and pearlite.
Etch: 2% Nital Mag X75

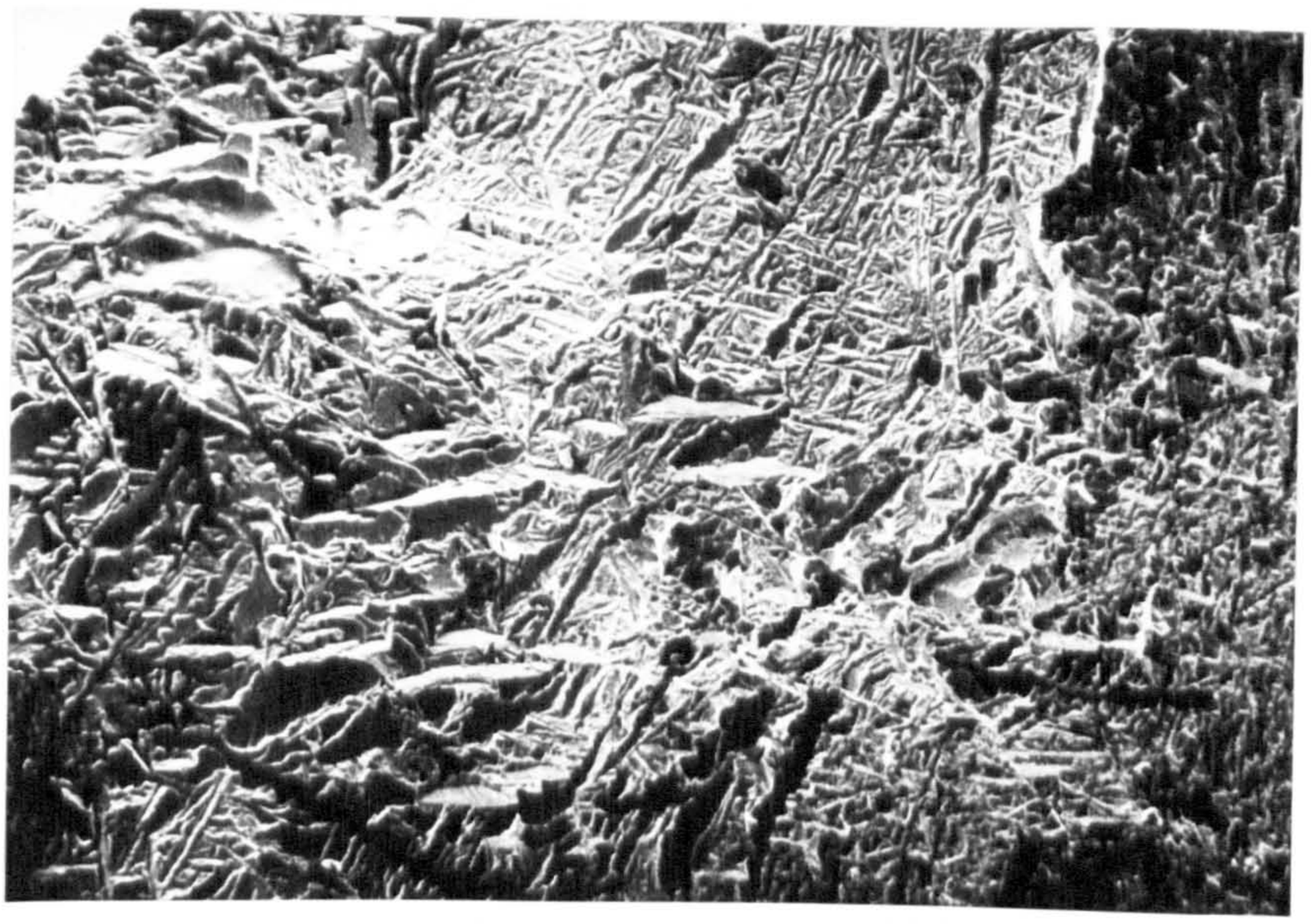

Fig. 3 Low-power scanning electron micrograph of a freshly fractured surface revealing typical "Rock Candy" features.
Mag X80

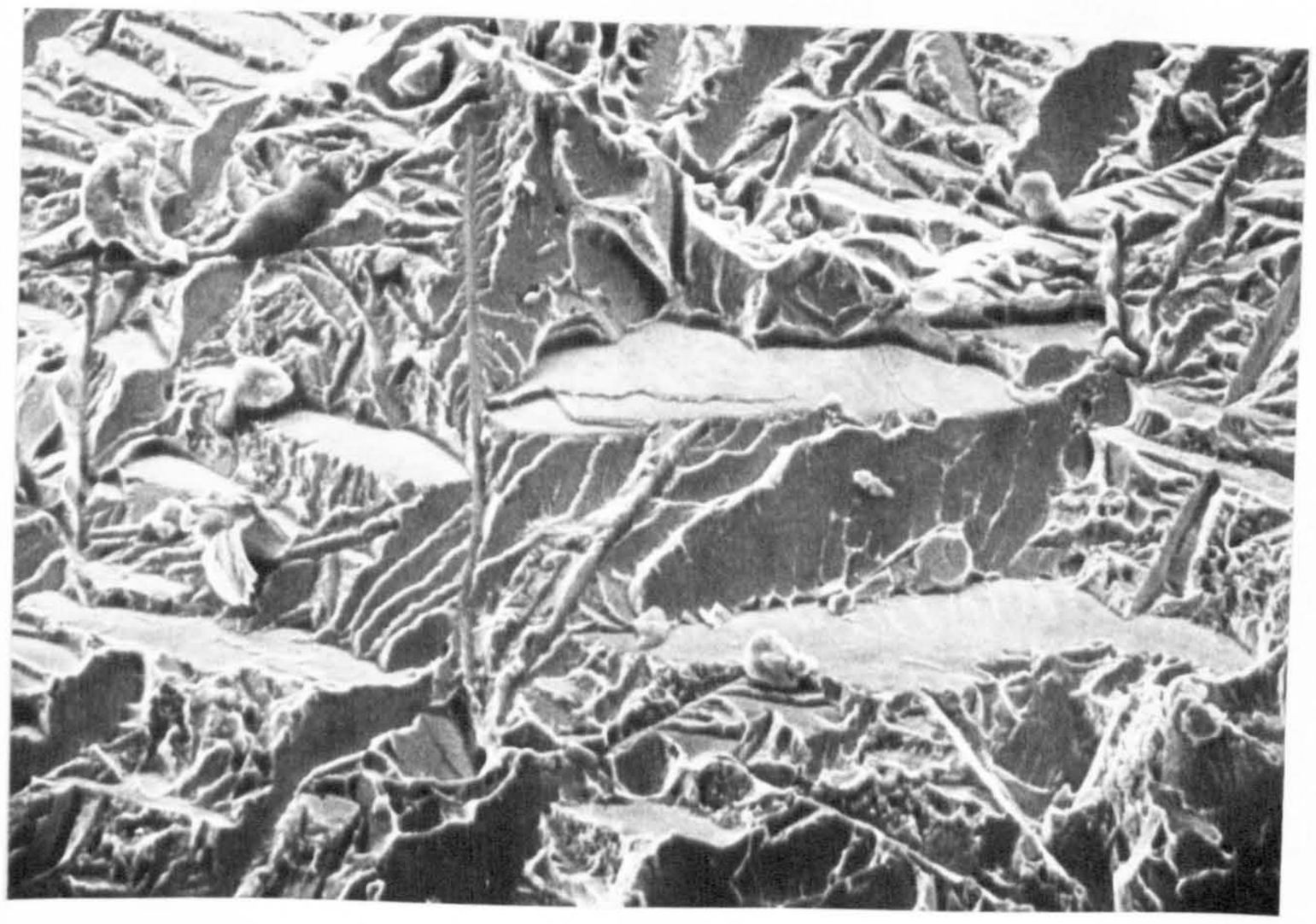

Fig. 4 Scanning electron micrograph showing the system of platelets at higher magnification.
Mag X320

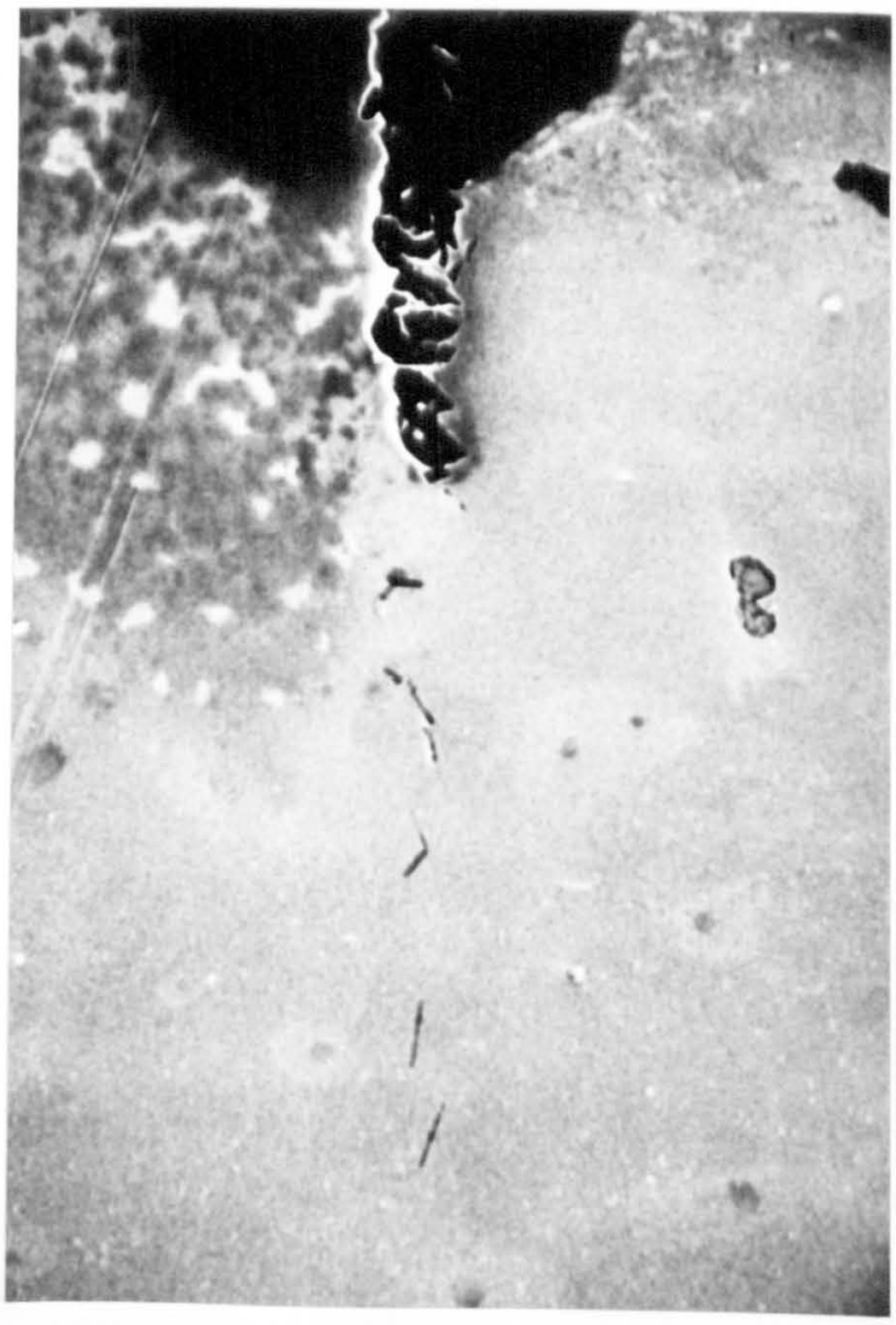

Fig. 5 Scanning electron micrograph showing needle-like precipitates extending beyond the root of the crack.
Mag X320

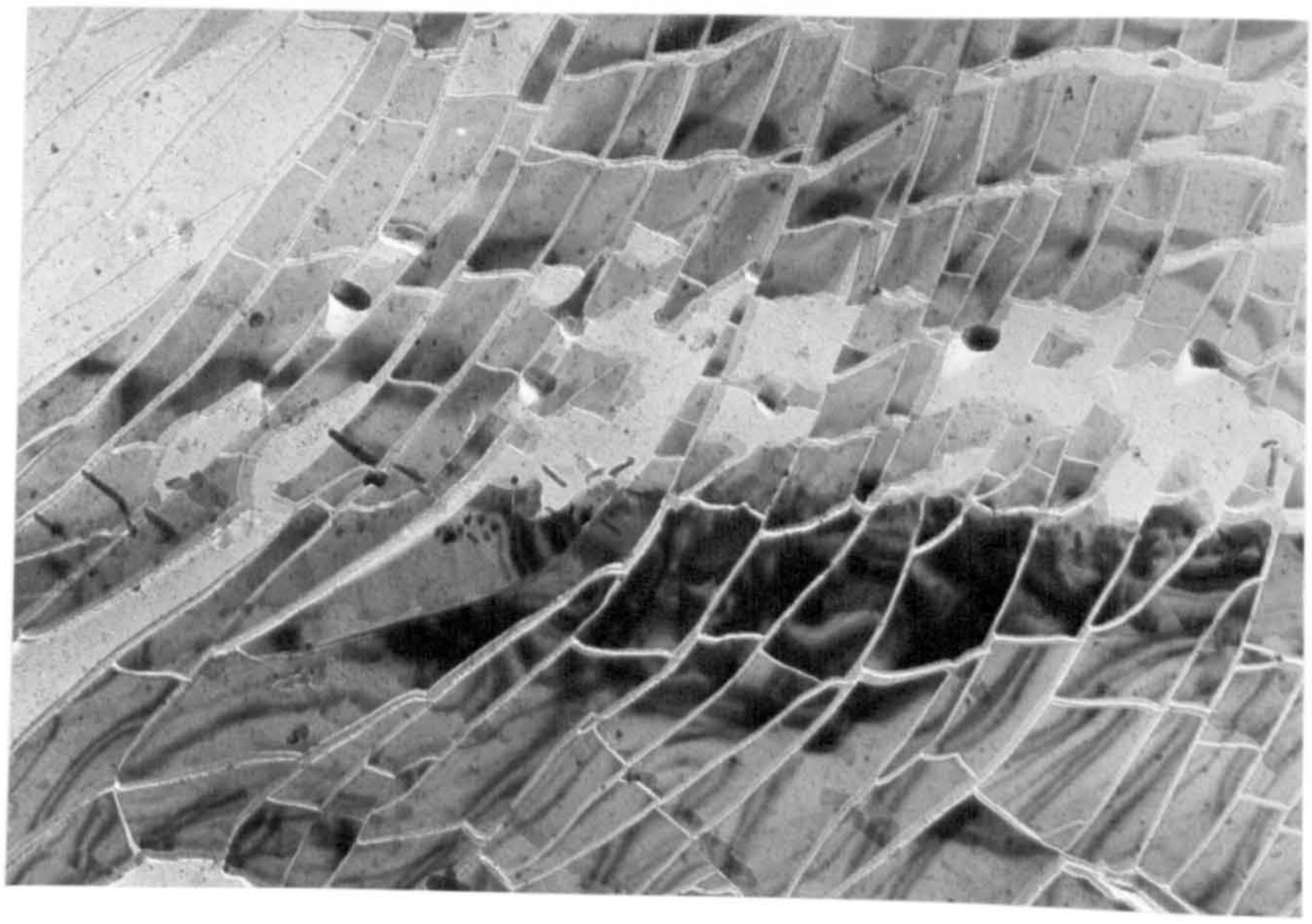

Fig. 6 Transmission electron micrograph of a direct carbon extraction replica of the fracture surface, showing the heavily fragmented plate of aluminium nitride.
Mag X22000

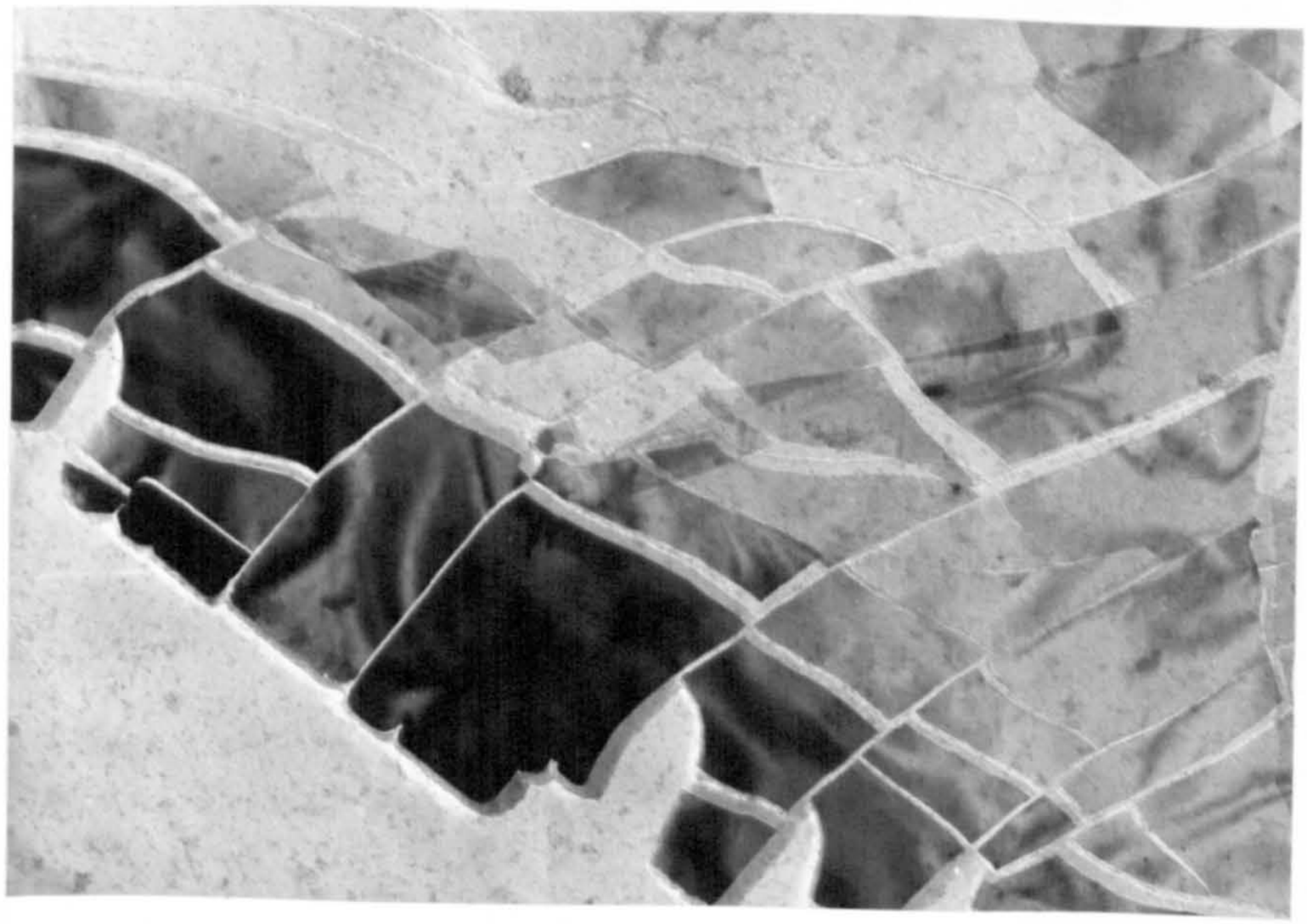

Fig. 7 Transmission electron micrograph showing the aluminium nitride plate in more detail.
Mag X36000

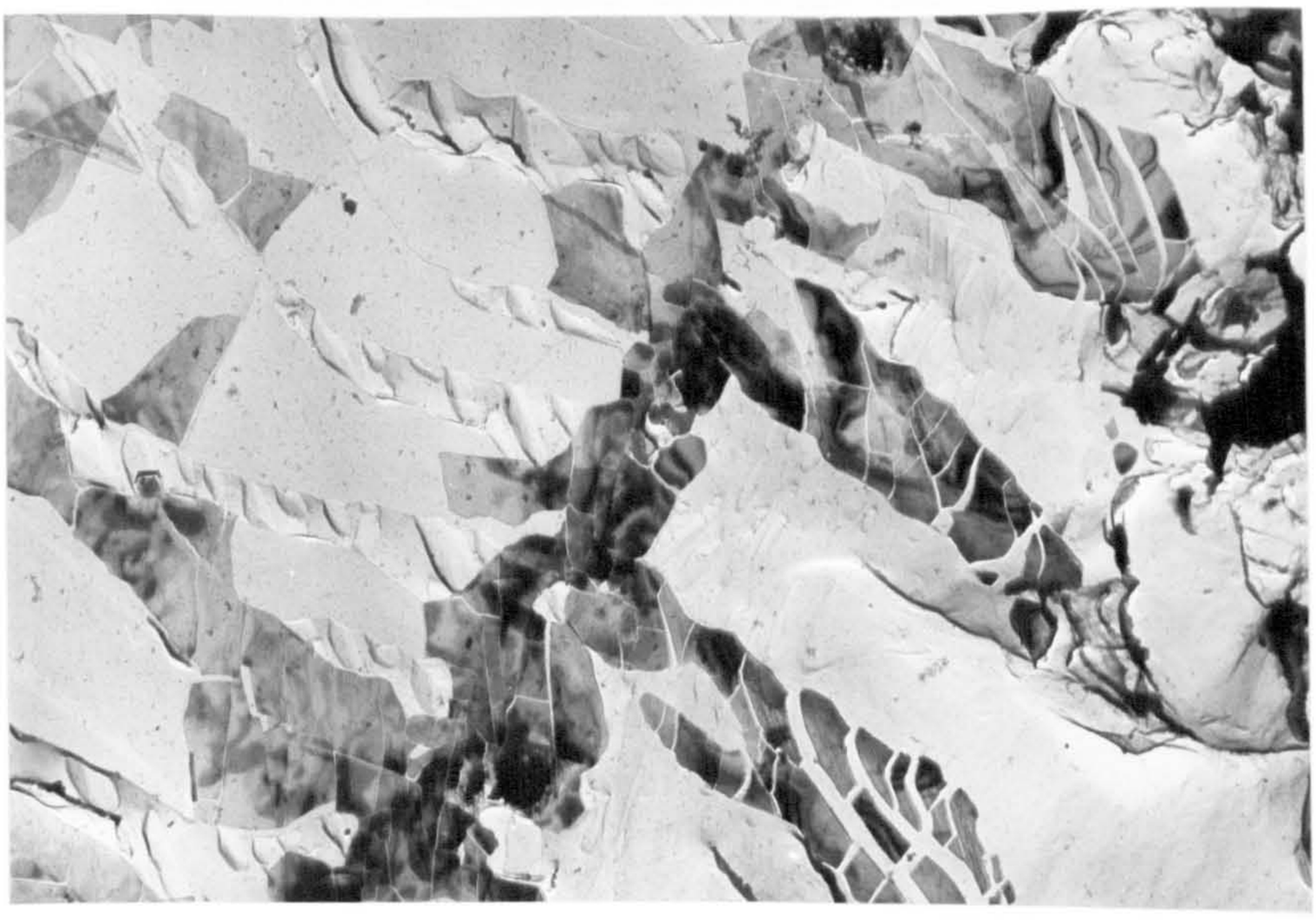

Fig. 8 Transmission electron micrograph of a direct carbon extraction replica of the fracture surface. The dendritic form of the precipitate can clearly be seen.
Mag X28000

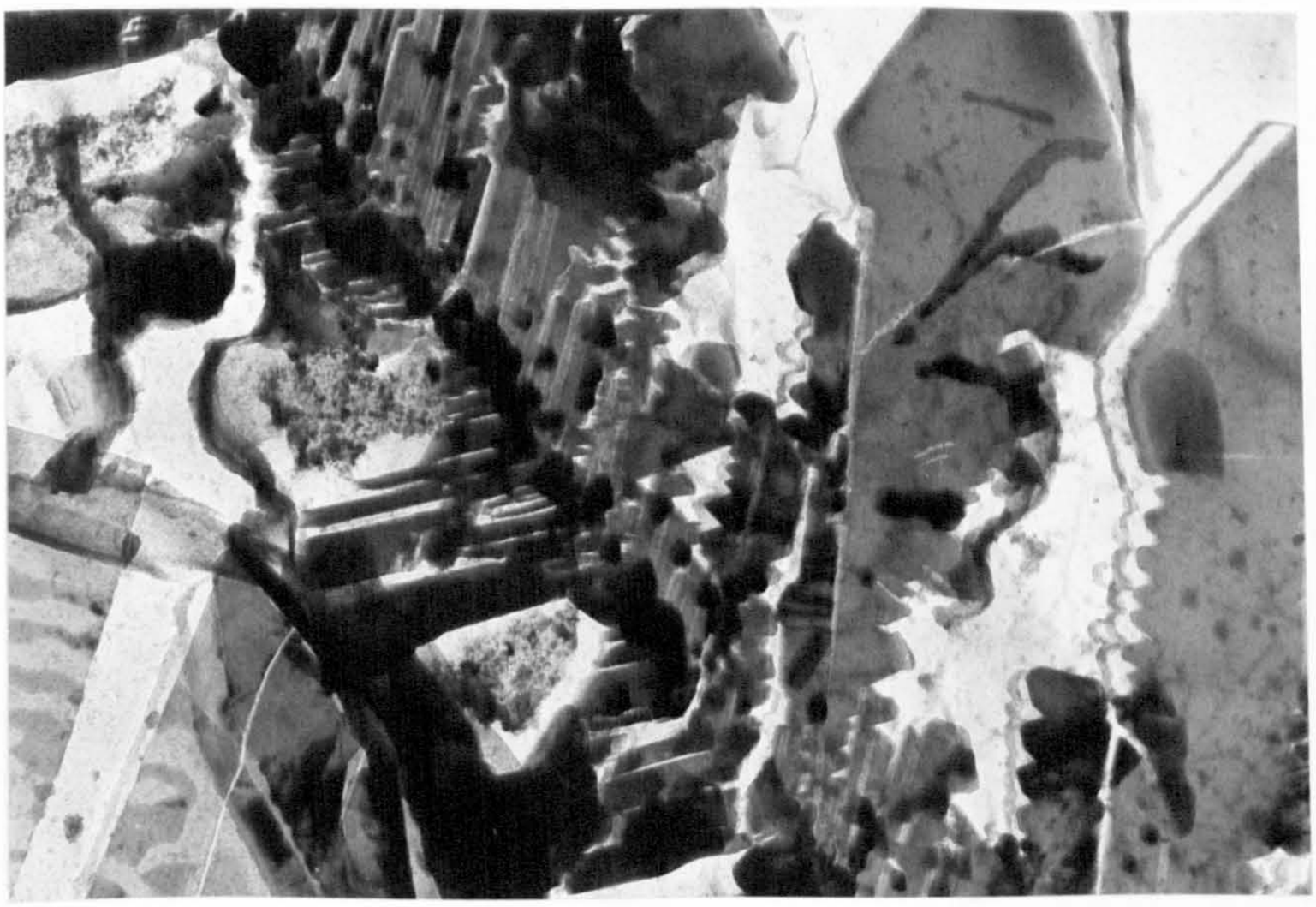

Fig. 9 Transmission electron micrograph showing the continuous nature of the dendritic and plate-like precipitates.
Mag X5900

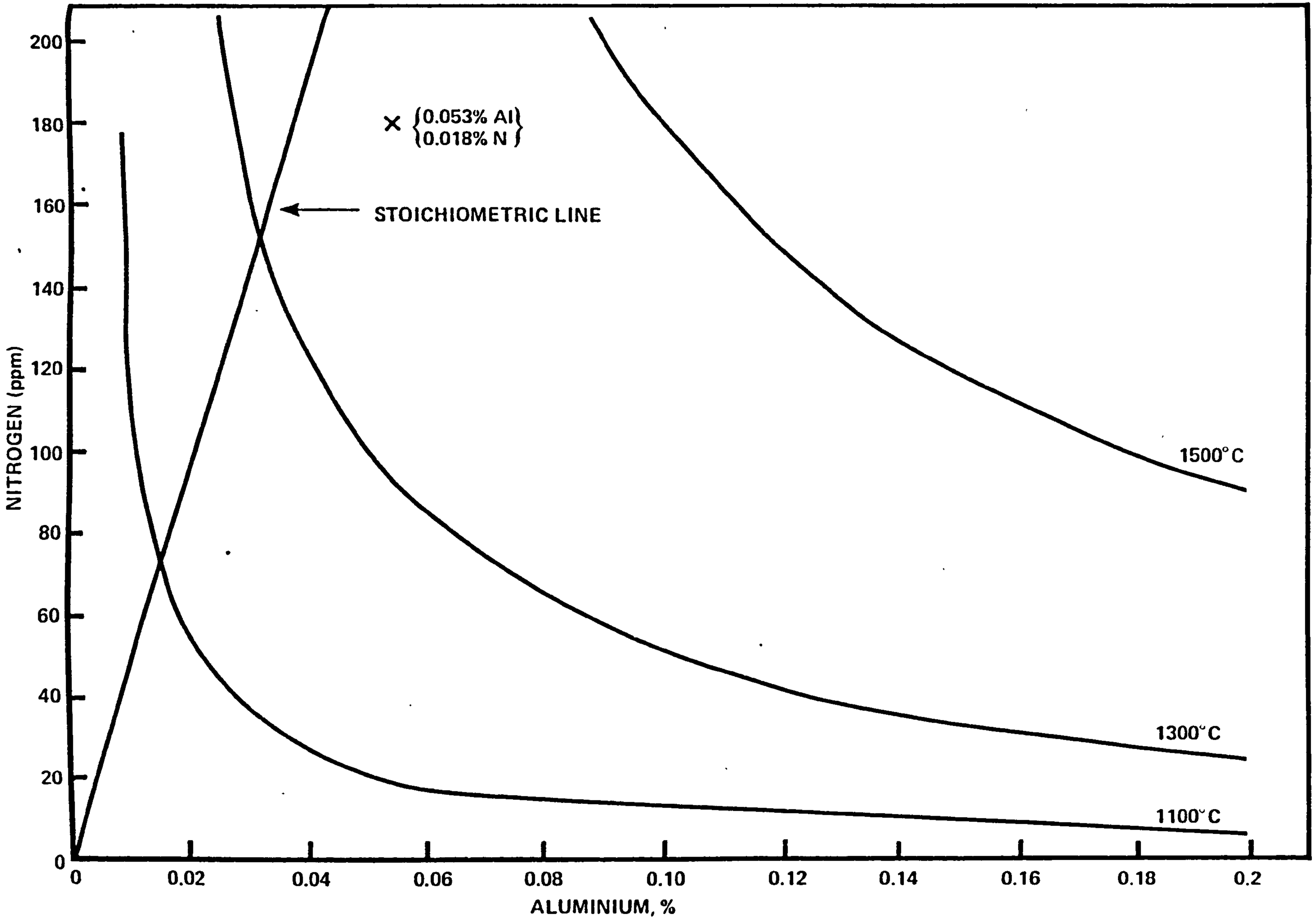

Fig.10.—Solubility of Al and N in austenite.

Director: J. A. Reynolds, B.Sc., Ph.D., F.I.B.F., F.I.M.

Steel Castings Research and Trade Association

Your reference:
Our reference:

Registered Office: 5 EAST BANK ROAD, SHEFFIELD S2 3PT
Telephone: 0742 28647 Telex: 54281 S.C.R.T.A. Sheffield

24th June, 1980
Report No. MQ/E 134

Report to

Foundry 'B'

on

Cracking of a 0.35%C 'Spider' Casting

by

N. H. Croft

Introduction

Severe cracking problems have been encountered in the region of the feeder head of a 0.35%C, 0.7%Mn spider casting. These cracks appeared to be intergranular in nature, and slow bend tests performed on samples taken from the casting revealed small areas of intergranular faceting. Moreover, chemical analyses carried out at the foundry implied a pick-up of aluminium near to the feeder head (0.11%Al compared to a ladle analysis of 0.06%), suggesting AlN precipitation as a possible cause of the cracking.

The casting had a finished weight of approximately 8 tonnes, having been made from a 16 tonne electric arc heat. This was the fifteenth casting in a batch of fifteen, and was the first one to exhibit cracking.

Chemical Analysis

The results of analyses carried out at the foundry were as follows:-

	C	Si	Mn	P	S	Cr	Mo	Ni	Al	N
Ladle analysis	0.35	0.34	0.69	0.011	0.016	0.24	0.05	0.16	0.064	0.009
Centre of head	0.34	0.34	0.69	0.011	0.016	0.25	0.05	0.17	0.111	0.009

In addition, the AlN contents had been determined by the Beeghly method and were found to be:

	%AlN	%N as AlN
Ladle	0.0017	0.0006
Head	0.016	0.005

Check analyses (spectrographic) were made at the Department of Metallurgy, Sheffield University, on samples taken from the region immediately below the feeder head and from the bulk of the casting away from the head:-

	C	Si	Mn	P	S	Cr	Mo	Ni	Al
Head	0.36	0.32	0.66	0.010	0.016	0.23	0.06	0.17	0.11
Bulk	0.38	0.32	0.67	0.011	0.015	0.23	0.06	0.17	0.12

Metallographic Examination

Sections taken from the cracked region of the casting confirmed the intergranular morphology, (see Fig. 1), and micro-sections revealed the cracks to be extensively decarburised (Fig. 2), with some oxidation of the surface having occurred.

One cracked sample, broken open by slow three-point bending, exhibited several large intergranular facets (Fig. 3).

Examination of a freshly fractured surface of the material in the Scanning Electron microscope revealed features typical of "Rock Candy" fractures caused by aluminium nitride precipitation (Figs. 4 and 5), although much of the fracture was by cleavage (Fig. 6), as would be expected in the as-cast condition.

Discussion

From the results of the chemical analysis carried out at the University, it appears that the aluminium content at the base of the feeder head is no higher than in the bulk of the casting. Thus, any possibility of pick-up having occurred as a result of the exothermic topping compound used can be excluded. The most likely explanation seems to be that additional aluminium had been added to the melt at some stage after the ladle analysis was taken, thus explaining the discrepancy between the ladle analysis and the analysis of the finished casting.

The fact that the aluminium nitride content of the ladle sample is so extremely low compared to the product analysis probably results from the rapid cooling of the ladle sample which has not allowed sufficient time for the AlN to precipitate. The product sample, however, will have been cooled at a much slower rate in the bulk of the casting, and therefore this latter figure will be the one representative of the true AlN content of the steel. It is noteworthy that the total nitrogen content of the steels is the same for both the ladle and product analyses, and that in the first instance the nitrogen will have been in super-saturated solid solution, whilst in the product it will have been in the form of the nitride.

Macroscopic and microscopic examinations have shown the cracking to be intergranular, resulting from excessive aluminium nitride precipitation at the as-cast grain boundaries. Fig. 7 shows solubility data for aluminium and nitrogen in austenite[1], and it can be seen that with 0.11%Al and 0.011%N present, supersaturation will occur at temperatures below about 1400°C. This, in conjunction with the slow cooling rate in the region of the feeder head, has resulted in the formation of cracks under the thermal stresses induced during the cooling of the casting. These will have been increased by the change in section of the component near to the head.

From the extent of the decarburisation of the crack and the oxidation observed, it is estimated that cracking has occurred in the region of 900°C and was possibly accentuated by the austenite to ferrite/pearlite phase transformation.

Conclusions

1. The cracking arose from a lack of ductility as a result of aluminium nitride precipitation at the prior austenite grain boundaries.

2. The nitrogen content of the steel was not high, but at 0.11% the aluminium content was high.

3. There is a discrepancy between the ladle aluminium analysis and the product analysis. No pick-up in the region of the feeder head was apparent.

4. The apparent discrepancy between the AlN content in the ladle and in the product arises from the rapid cooling of the ladle sample, which does not give the AlN precipitate time to form. The valid analysis is the one taken from the finished casting, i.e. 0.016%AlN.

Reference

1. N. H. Croft.
Fracture Mechanisms in Cast Steels - Intergranular Fracture.
SCRATA Progress Report No. 2012, 12th March, 1980.

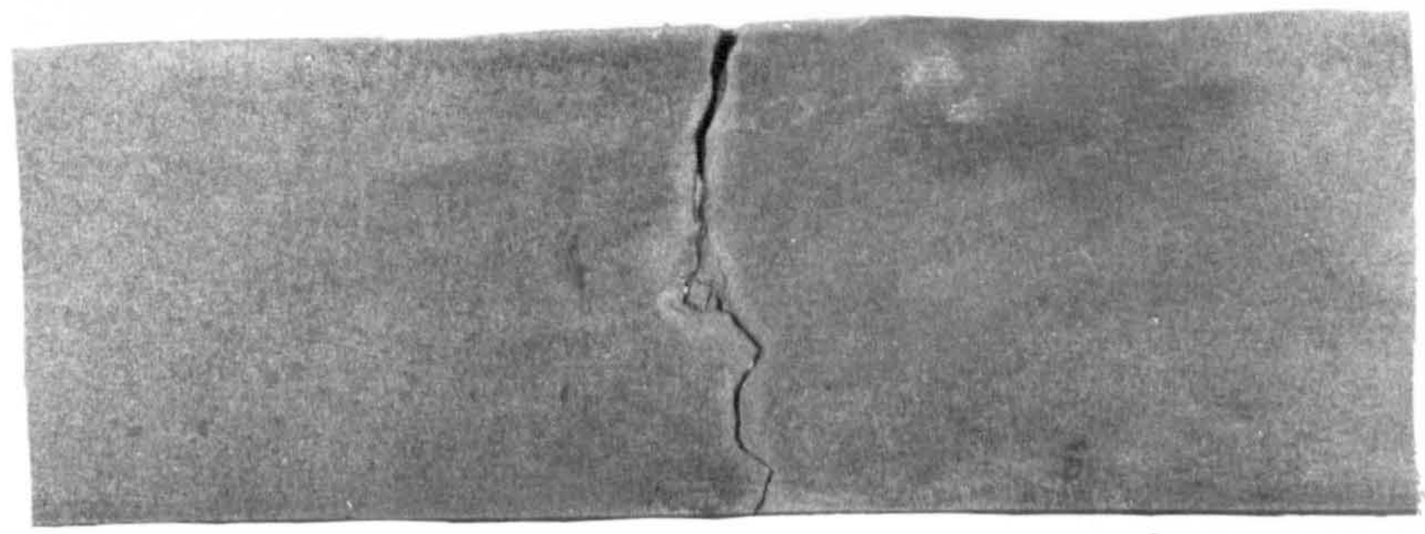

Fig. 1 Macro-etched section through a crack, showing the intergranular path. Mag XO.75

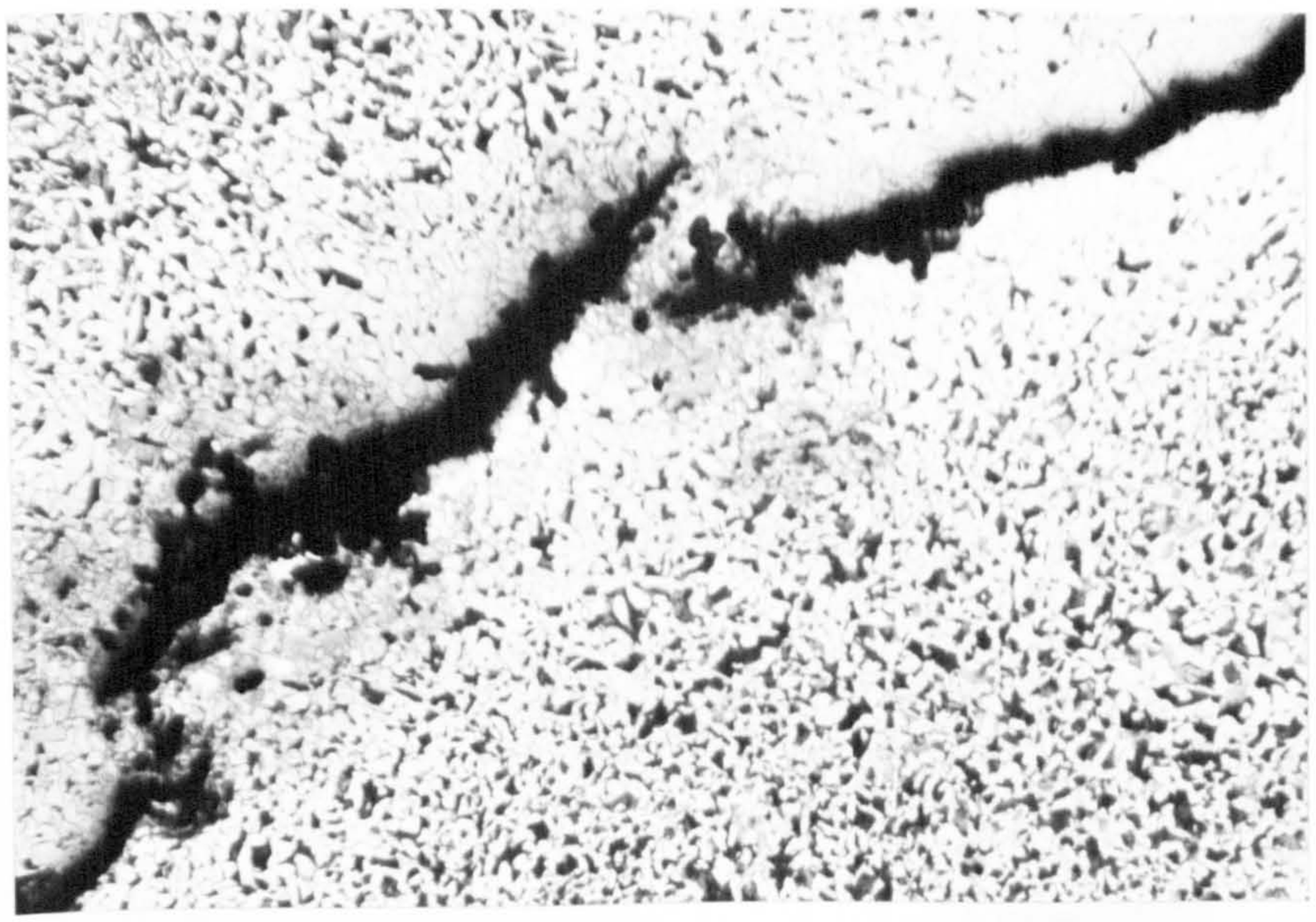

Fig. 2 Optical micrograph showing the decarburisation associated with the cracks. The matrix is fine ferrite and pearlite. Etch: 2% Nital Mag X40

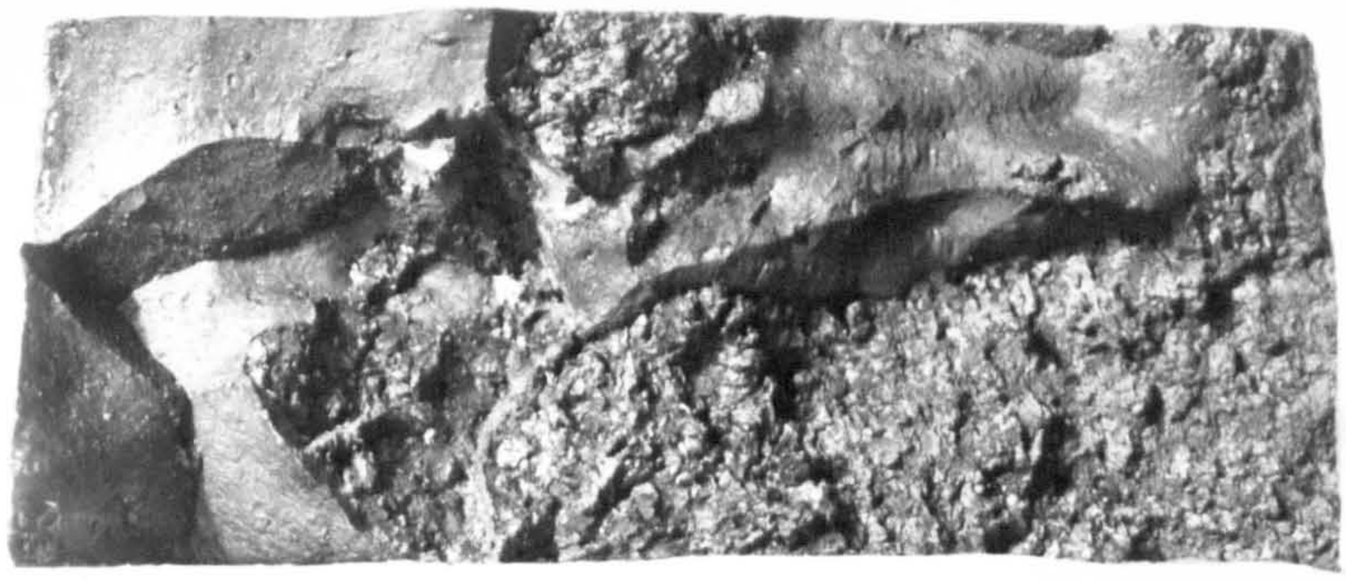

Fig. 3 Fracture surface obtained by breaking open one of the cracks. Note the large intergranular facets.
Mag X2

Fig. 4 Low-power scanning electron micrograph showing the intergranular morphology of a freshly fractured surface.
Mag X40

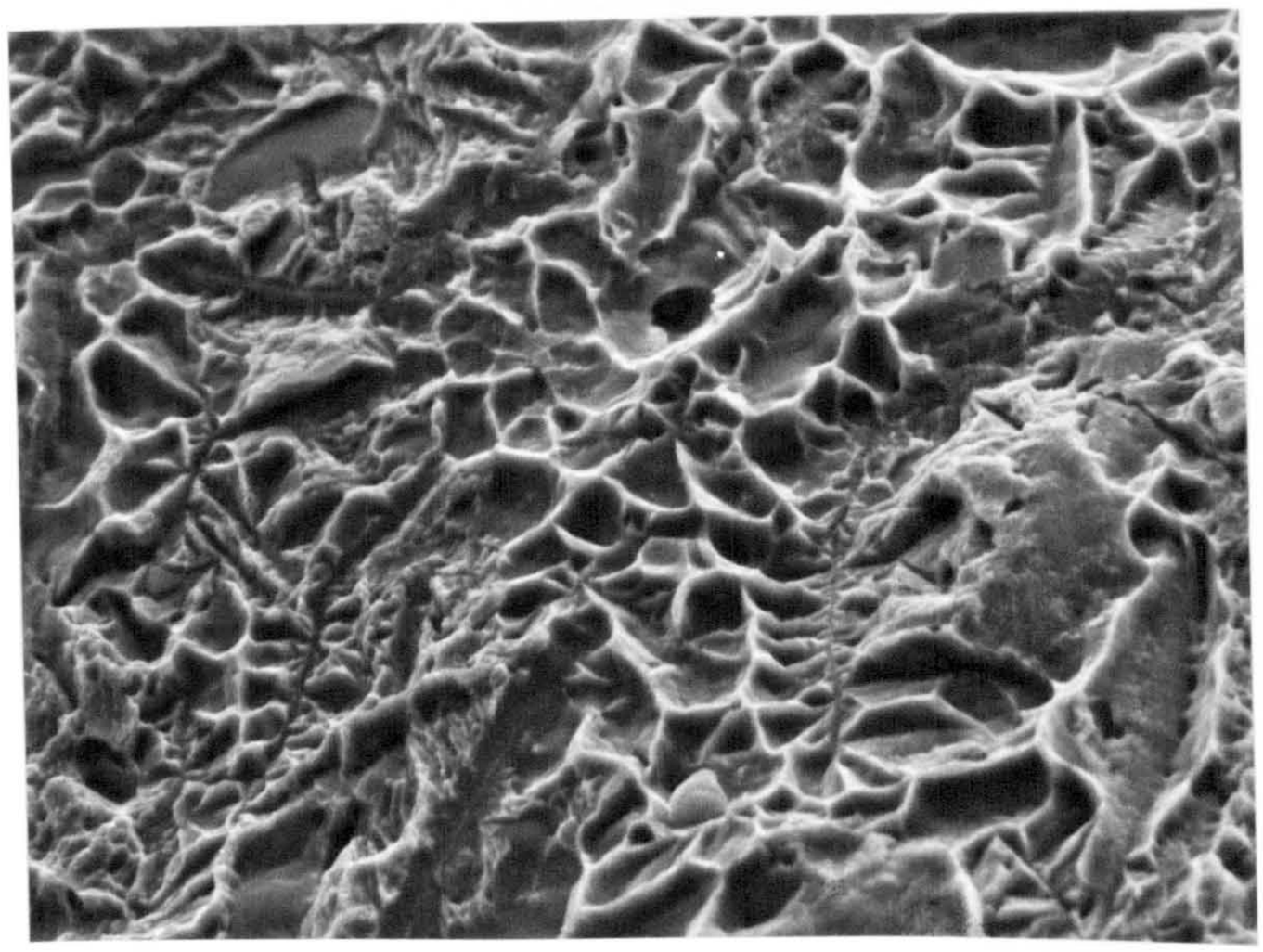

Fig. 5 Intergranular facet in more detail. Note the dendritic markings, normally associated with the dendritic form of aluminium nitride.
Mag X640

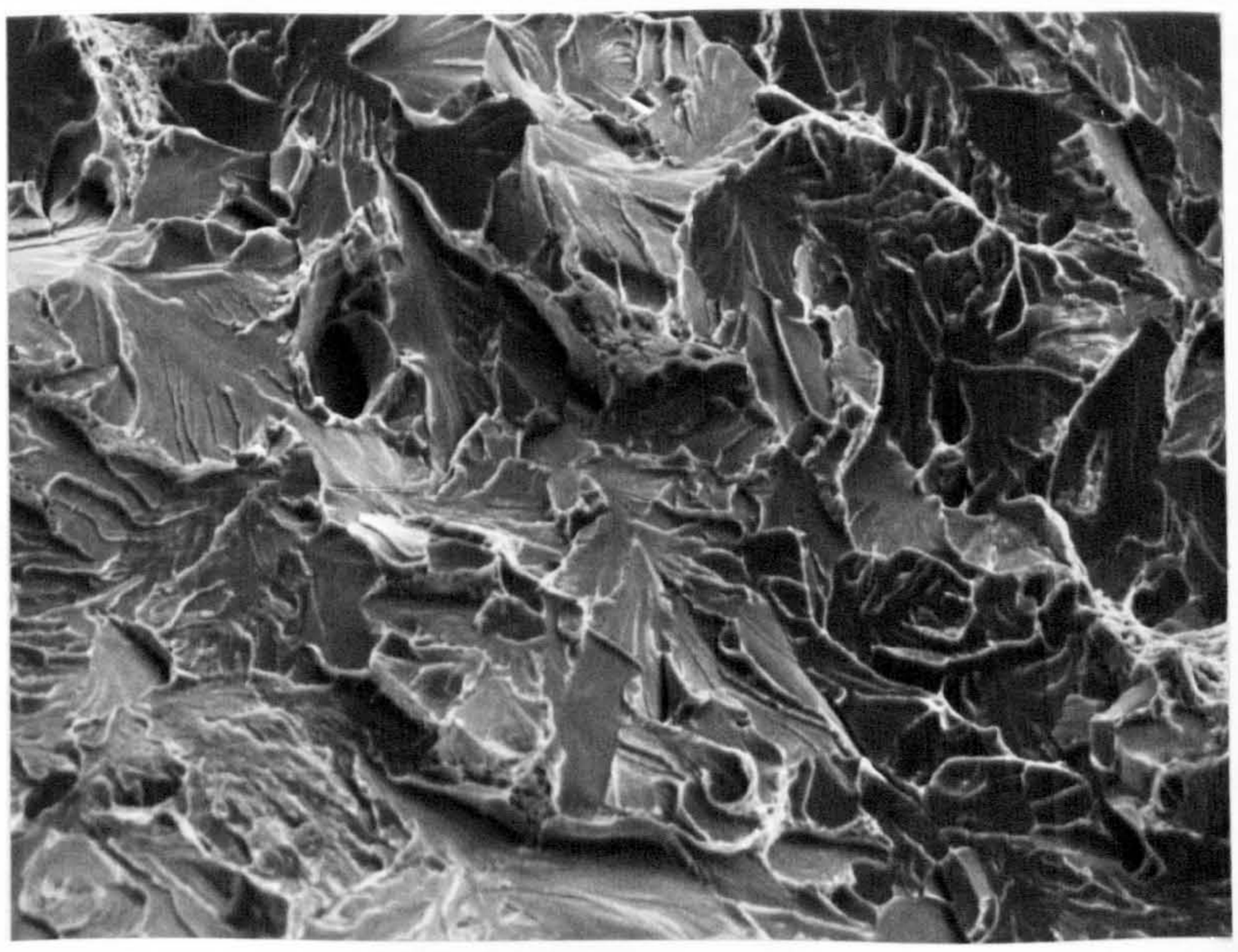

Fig. 6 Scanning electron micrograph showing the main mode of fracture during slow three point bending, one of cleavage.
Mag X160

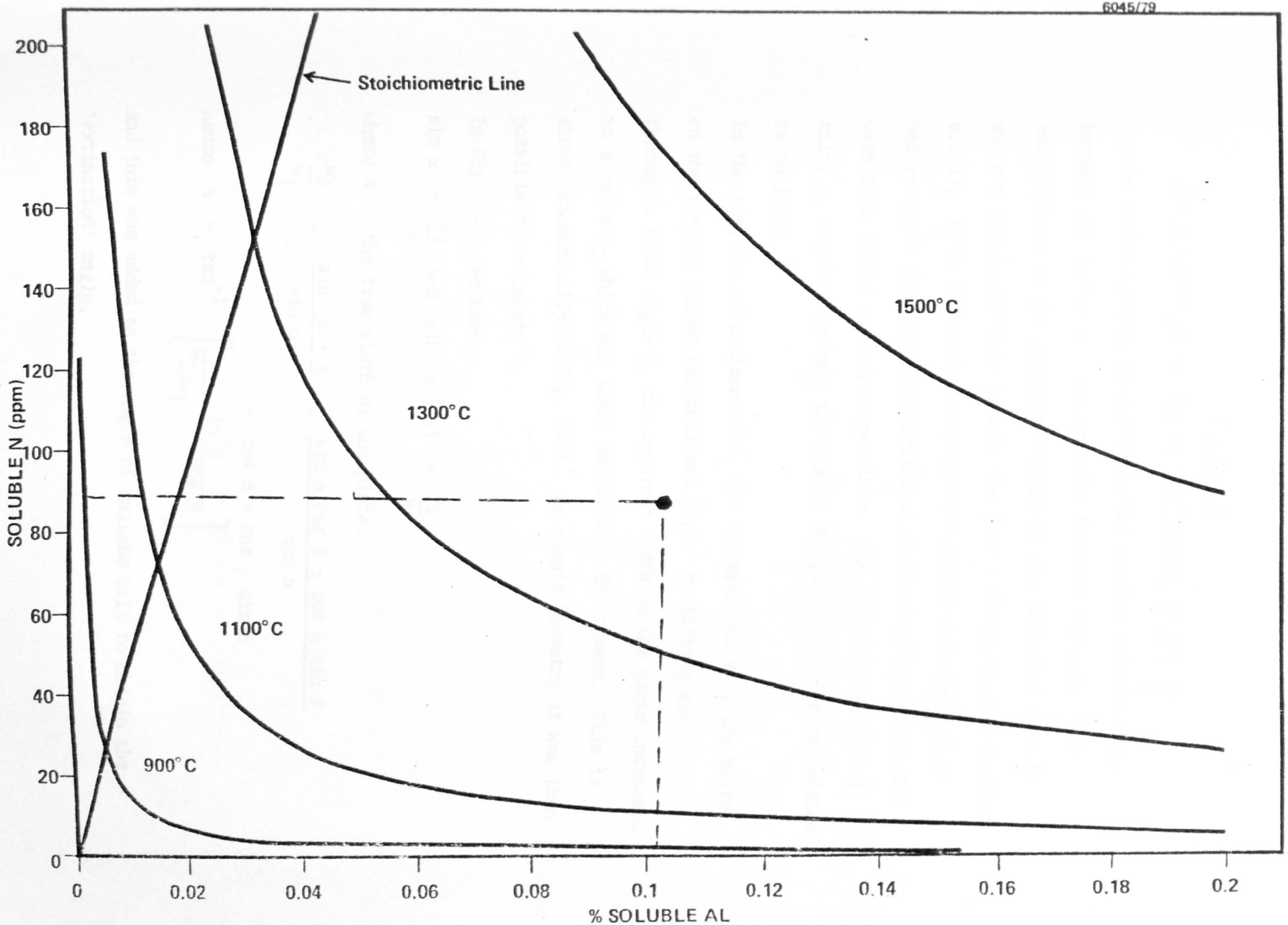
Stoichiometric Line
1500° C
1300° C
1100° C
900° C
SOLUBLE N (ppm)
200
180
160
140
120
100
80
60
40
20
0
0
0.02
0.04
0.06
0.08
0.1
0.12
0.14
0.16
0.18
0.2
% SOLUBLE AL

APPENDIX 4

The Measurement of 'Extinction' Angles in the SEM

In the technique used to determine the angular relationships between AlN plates on intergranular fracture surfaces, tilt restrictions on the goniometer stage of the SEM meant that it was not always possible to make the plates disappear (see Section 6.2.1). Under these circumstances the plates were rotated as before until they appeared horizontal on the viewing screen and were then tilted as much as possible. The additional angle of tilt, α, required to make the plates disappear was then calculated as follows:

In the position of maximum tilt, the apparent width of the plate on the viewing screen was measured (w_1). By tilting back through a known angle β, the apparent width of the plate increased to a value w_2 which was again measured on the screen. This is shown schematically in Fig. A4.1. By simple geometry it was then possible to calculate α.

In Fig. A4.2, we have

$$\sin \alpha = \frac{w_1}{W} \quad \text{and} \quad \sin (\alpha + \beta) = \frac{w_2}{W}$$

where W is the true width of the plate.

$$\therefore \frac{w_2}{w_1} = \frac{\sin (\alpha + \beta)}{\sin \alpha} = \frac{\sin \alpha \cos \beta + \cos \alpha \sin \beta}{\sin \alpha}$$

$$= \cos \beta + \cot \alpha \sin \beta$$

$$\text{hence} \quad \alpha = \tan^{-1} \left[\frac{\sin \beta}{w_2/w_1 - \cos \beta} \right]$$

and this was added to the angle of maximum tilt to obtain the 'extinction' angle.

Fig. A4.1 Measurement of w_1 and w_2 on the viewing screen of the SEM. (cf Figs. 6.17 and 6.18).

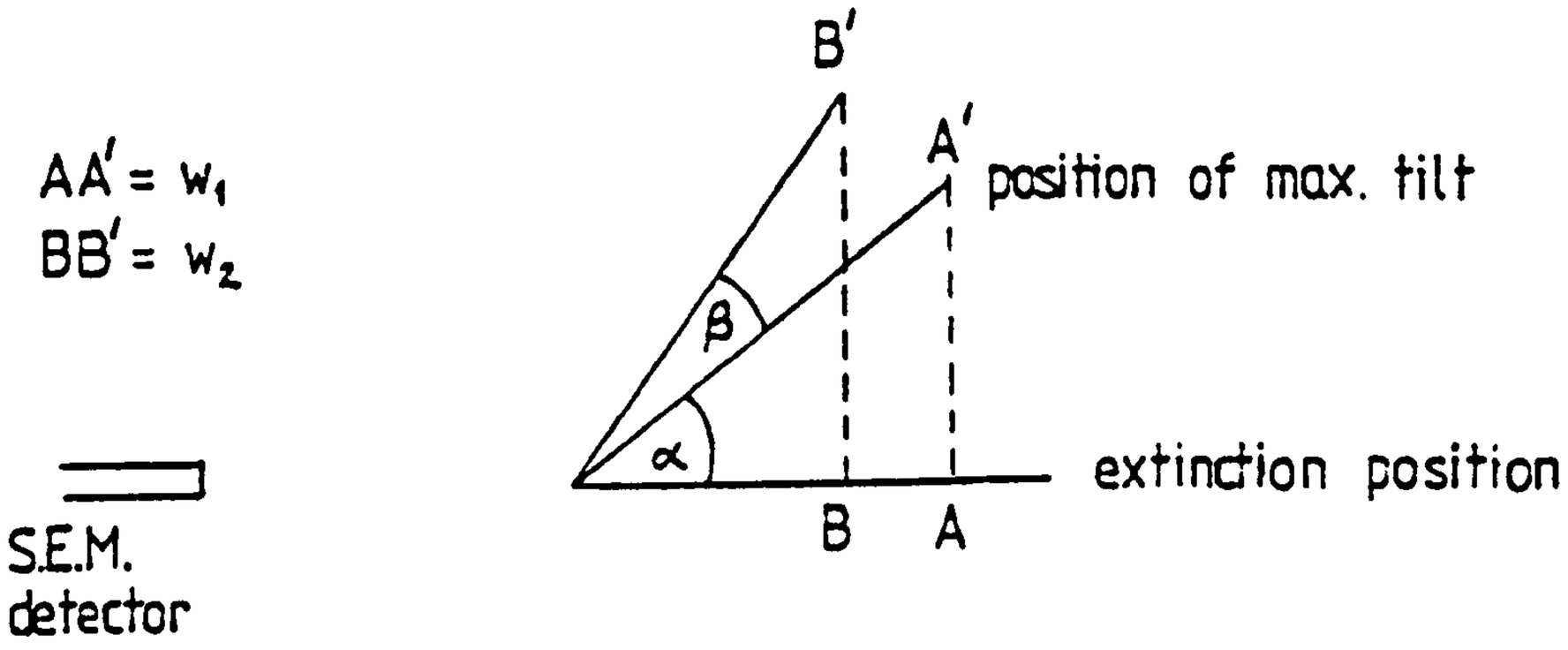

Fig. A4.2 Geometrical relationships at the two different angles of tilt.

Appendix 5

Calculation of the Microsegregation Characteristics of Al and N during Solidification

As noted in Section 2.4.2 solute redistribution usually occurs during solidification. This results in local increases of Al and N content in the residual liquid and precipitation of AlN can begin once the solubility limit for AlN in liquid steel is exceeded.

The solubility data used in these calculations are those due to Höner and Baliktay (1978a) for GS-60 grade steel which were presented in Section 4.4.2. The limit of solubility in Fig. 7.2 is therefore based on the empirical equation

$$\log [Al][N] = \frac{-8490}{T} + 2.37$$

For the purposes of this model, it is assumed that T_L = 1773K and T_S = 1723K. As will be seen from Fig. 7.2, however, the results are relatively insensitive to slight errors in estimation of these temperatures.

The local concentrations of Al and N in the residual liquid (C_L^{Al} and C_L^N) were calculated for increasing fractions solid (f_s) and three starting compositions (C_o^{Al} and C_o^N). For Al, this was carried out using the Scheil equation[1] in the form

$$C_L^{Al} = C_o^{Al} \cdot (1 - f_s)^{k_{Al} - 1}$$

as in equation 2.2 of Section 2.4.2.

The equilibrium partition coefficient of aluminium in δ-ferrite (k_{Al}) was taken as 0.6 as determined by Tiller[2] and Oeters et al[3], and was

assumed to remain constant during solidification.

For nitrogen, which is an interstitial alloying element, the Scheil equation does not apply, since rapid back diffusion can occur. In this case, C_L^N was calculated using the equilibrium lever rule.

$$C_L^N = C_o^N \left[1 - (1 - k_N) f_s\right]^{-1}$$

k_N was taken to be 0.3, as determined by Oeters et al[3], Chipman[4] and Sims[5] and was again assumed to remain constant during solidification.

These values were then used to plot $C_L^{Al} \times C_L^N$ vs f_s as shown in Fig. 7.2. The points at which these curves cross the maximum solubility line gives the value of f_s beyond which precipitation of AlN becomes possible.

References:

1. E. Scheil, Z. Metallkunde, 1942, 34, 70.

2. W. A. Tiller, J.I.S.I., 1959, 192, 338.

3. F. Oeters et al, Arch. Eisenhuttenwes, 1969, 40, 603.

4. J. Chipman, Physical Chemistry of Steelmaking, AIMME (1951), p. 632.

5. C. E. Sims, Electric Furnace Steelmaking Vol. 2 (1962) p. 99, Pub:Wiley.

TABLES AND FIGURES

TABLES

Table 2.1

See Text, Page 7

Table 2.2

Nitrogen contents of different steelmaking routes (Wright, 1962)

Method of Manufacture	Nitrogen Content (wt.%)
Basic Open Hearth	0.004-0.007*
Basic Electric Arc	0.004-0.010* 0.008-0.011+
L-D	<0.005*
Basic Bessemer - Air Blown	0.010-0.025* 0.009-0.012+
- O_2 Enriched	0.006-0.012* 0.003-0.006+
Induction Melted	0.008-0.012+
Vacuum Melted	0.002-0.006

* Speith and Vom Ende

\+ Kuhn and Detrez

Table 2.3

See Text, Page 24

Table 3.1

See Text, Page 37

Table 3.2

See Text, Page 41

Table 4.1

Temperature dependence of the solubility product [Al][N] in austenite from various sources, and the predicted solution temperature for a steel containing 0.1%Al and 0.01%N

$\log_{10}$ Al N	Source	Steel Composition	T(°C)
$-\frac{7400}{T}$ + 1.95	Darken et al (1951)	0.1%C, 0.4%Mn	1221
$-\frac{7750}{T}$ + 1.80	König et al (1961)	0.2%C, 1.50%Mn, 0.5%Si	1342
$-\frac{6180}{T}$ + 0.725	Erasmus and Mech (1964)	0.2%C, 1.50%Mn, 0.15%Si	1386
$-\frac{6015}{T}$ + 0.31	Idem	0.15%C, 0.4%Mn, 0.2%Si 3.5%Ni, 1.0%Cr	1544+
$-\frac{9200}{T}$ + 2.92	Höner and Baliktay (1978a)	0.40%C, 0.8%Mn, 0.6%Si	1281
$-\frac{7500}{T}$ + 1.48	*Gladman and Pickering (1967)	0.1%C, 0.8%Mn, 0.2%Si	1401

* "Mean" solubility product incorporating the results of prior work.

\+ i.e. above the liquidus.

Table 4.2

Interaction parameters $e_N^{\times}$ and $e_{Al}^{\times}$ for some common alloying elements in liquid steel

Element $\times$	$e_{Al}^{\times}$	$e_n^{\times}$	Temperature (°C)	Ref*
C	0.091	-	1600	1
		0.123	1600	2
Si	0.056	-	1600	1
		0.0547	1600	2
Mn	-	-0.02	1600	2
Cr	-	-0.047	1600	2
Ni	-	-0.01	1600	2
Mo	-	-0.0115	1600	2
Al	0.043		1600	1
		$\frac{828}{T}$ -0.472	1600-1750	3
N	$\frac{1602}{T}$ -0.912	-	1600-1750	3

*Refs.

1. Wilder and Elliott (1960)

2. Schurmann and Kunze (1967)

3. Evans and Pehlke (1964)

Table 4.3

Interaction parameters e_N^x and e_{Al}^x for some common alloying elements in austenite

Element x	e_{Al}^x	e_N^x	Temperature (°C)	Ref*
Al	-2.4	-	1100-1300	1
C	-	0.125	1050-1200	2
Si	-	0.0595	1000-1200	2
Mn	-	$\frac{-141}{T}$ +0.076	1000-1200	3
Ni	-	$\frac{32.4}{T}$ +0.0056	900-1200	4
Cr	-	$\frac{-360}{T}$ +0.136	1050-1350	5
Mo	-	-0.05	1000-1200	2

*Refs.

1. Mayrhofer (1973)
2. Schenck et al (1963)
3. Matasova and Tuma (1973)
4. Heckler and Peterson (1969)
5. Ichise et al (1971)

Table 5.1 Details of the Experimental Castings

Cast No.	Practice	Pouring Temp. (°C)	C	Si	Mn	P	S	Al	Total N	Comments
4169	A	1565	0.28	0.38	1.44	-	-	0.10	0.026	Extensive porosity.
4176	A	1560	0.27	0.49	1.54	0.004	0.006	0.18	0.015	Used to examine effects of heat treatment.
4210	A	1560	0.30	0.51	1.76	0.005	0.007	0.17	0.017	Charpies.
4211	A	1565	0.29	0.49	1.65	0.005	0.006	0.07	0.017	High T heat treatments.
4231	A	1560	0.29	0.46	1.55	0.005	0.007	0.08	0.008	Charpies.
4351	A	1565	0.28	0.38	1.56	0.005	0.007	0.12	0.014	Charpies and high T heat treatments.
4353	A	1550	0.42	0.48	1.55	0.009	0.009	0.20	0.018	Effect of C content.
4354	A	1540	0.56	0.51	1.68	0.010	0.011	0.22	0.020	Effect of C content.
4355	A	1550	0.65	0.56	1.63	0.010	0.011	0.21	0.023	Effect of C content.
4382	A	1570	0.30	0.42	1.58	0.005	0.009	0.08	0.014	Directional solidification work.
4383	A	1570	0.30	0.45	1.55	0.006	0.009	0.17	0.017	Directional solidification work.
46/1	B	1600	0.29	0.20	1.28	0.010	0.015	0.14	0.009	Fracture toughness testing.
46/2	B	1610	0.31	0.32	1.27	0.010	0.014	0.14	0.008	Fracture toughness testing.
46/3	B	1610	0.30	0.21	1.29	0.010	0.015	0.15	0.009	Fracture toughness testing.
46/4	B	1610	0.28	0.15	1.13	0.009	0.007	0.07	0.011	Fracture toughness testing.

Table Continued

Table 5.1 Details of the Experimental Castings (Continued)

Cast No.	Practice	Pouring Temp. (°C)	C	Si	Mn	P	S	Al	Total N	Comments
46/5	B	1610	0.29	0.17	1.23	0.008	0.011	0.22	0.015	Charpies.
46/6	B	1620	0.31	0.20	1.09	0.010	0.014	0.23	0.016	Charpies.
46/7	B	1610	0.29	0.26	1.46	0.010	0.015	0.21	0.017	Charpies.
46/8	B	1610	0.29	0.18	1.11	0.009	0.005	0.08	0.010	Fracture toughness testing.
46/89	C	1620	0.31	0.59	1.37	0.013	0.017	0.18	0.010	Fracture toughness testing.

N.B. The higher pouring temperatures for Practice B and C were to allow for a 30°C temperature drop between the furnace and ladle.

Table 5.2

See Text, Page 82

Table 6.1 Electron Diffraction Data for AlN Plate

Camera constant = 25.4mm Å

Zone axis : <0001>

Diffracting Planes	d Å (calculated)	d Å (observed)	% Error in d.
$\bar{3}210$	1.018	1.008	0.99
$\bar{2}200$	1.347	1.344	0.20
$\bar{1}2\bar{1}0$	1.555	1.558	0.21
$02\bar{2}0$	1.347	1.351	0.33
$12\bar{3}0$	1.018	1.016	0.20
$\bar{2}110$	1.555	1.549	0.39
$\bar{1}100$	2.693	2.688	0.20
$01\bar{1}0$	2.693	2.688	0.20
$11\bar{2}0$	1.555	1.568	0.83
$\bar{2}020$	1.347	1.351	0.33
$\bar{1}010$	2.693	2.687	0.20
$10\bar{1}0$	2.693	2.687	0.20
$20\bar{2}0$	1.347	1.351	0.33
$\bar{1}\bar{1}20$	1.555	1.568	0.83
$0\bar{1}10$	2.693	2.687	0.20
$1\bar{1}00$	2.693	2.687	0.20
$2\bar{1}\bar{1}0$	1.555	1.549	0.40
$3\bar{1}\bar{2}0$	1.018	1.016	0.19
$\bar{3}300$	0.898	0.894	0.20
$\bar{2}3\bar{1}0$	1.018	1.016	0.20
$\bar{1}3\bar{2}0$	1.018	1.016	0.20
$03\bar{3}0$	0.898	0.897	0.02
$13\bar{4}0$	0.747	0.726	2.85

Table 6.2 Electron Diffraction Data for AlN Dendrite

Camera Constant = 25.4mm Å

Zone axis : $\langle\bar{1}\bar{1}23\rangle$

Diffracting Planes	d Å (calculated)	d Å (observed)	% Error in d.
$\bar{2}02\bar{2}$	1.185	1.181	0.31
$\bar{3}12\bar{2}$	0.943	0.937	0.56
$\bar{4}22\bar{2}$	0.742	0.726	2.23
$\bar{1}01\bar{1}$	2.370	2.363	0.31
$\bar{2}11\bar{1}$	1.485	1.451	2.23
$\bar{3}21\bar{1}$	0.997	0.996	0.14
$\bar{4}31\bar{1}$	0.739	0.726	1.77
$1\bar{1}00$	2.693	2.688	0.20
$\bar{1}100$	2.693	2.688	0.20
$\bar{2}200$	1.347	1.344	0.20
$\bar{3}300$	0.898	0.894	0.38
$2\bar{1}\bar{1}1$	1.485	1.451	2.23
$10\bar{1}1$	2.370	2.363	0.31
$01\bar{1}1$	2.370	2.374	0.16
$\bar{1}2\bar{1}1$	1.485	1.530	3.07
$\bar{2}3\bar{1}1$	0.997	1.016	1.86
$3\bar{1}\bar{2}2$	0.943	0.937	0.56
$20\bar{2}2$	1.185	1.181	0.31
$11\bar{2}2$	1.320	1.344	1.84
$02\bar{2}2$	1.185	1.187	0.16
$\bar{1}3\bar{2}2$	0.943	0.985	1.69
$4\bar{1}\bar{3}3$	0.681	0.667	2.17
$30\bar{3}3$	0.790	0.782	1.08
$21\bar{3}3$	0.868	0.864	0.50
$12\bar{3}3$	0.868	0.864	0.50
$03\bar{3}3$	0.790	0.791	0.16
$14\bar{3}3$	0.681	0.671	1.35

Table 6.3 The Angles between AlN plates (in degrees) Calculated from Measurements in the Goniometer Stage of the S.E.M.

Plate designation	1	2	3	4	5
1	-	53	108	68	39
2	53	-	109	31	74
3	108	109	-	76	70
4	68	31	76	-	71
5	39	74	70	71	-

Table 1a

Angle between plates 1:3 = 108°
1:4 = 68°
3:4 = 76°

Angle between plates 2:3 = 109°
2:5 = 74°
3:5 = 70°

Table 6.4

The effect of aluminium and nitrogen contents on the room temperature fracture mechanism of 0.30C - 1.50Mn steel castings

Cast No.	Practice	Al (%)	Total N (%)	[Al] [N] x10^{-3}	Fracture Morphology
4169	A	0.10	0.026	2.6	Extensive porosity, but remainder 100% I.F.
4176	A	0.18	0.015	2.7	100% I.F., 0% Fibrous
4210	A	0.17	0.017	2.9	90% I.F., 10% Fibrous
4211	A	0.07	0.017	1.2	0% I.F., 100% Fibrous
4231	A	0.08	0.008	0.6	0% I.F., 100% Fibrous
4351	A	0.12	0.014	1.7	50% I.F., 50% Fibrous
46/1	B	0.14	0.009	1.3	0% I.F., 100% Fibrous
46/2	B	0.14	0.008	1.1	0% I.F., 100% Fibrous
46/3	B	0.15	0.009	1.4	0% I.F., 100% Fibrous
46/4	B	0.07	0.011	0.8	0% I.F., 100% Fibrous
46/5	B	0.22	0.015	3.3	40% I.F., 60% Fibrous
46/6	B	0.23	0.016	3.7	50% I.F., 50% Fibrous
46/7	B	0.21	0.017	3.6	50% I.F., 50% Fibrous
46/8	B	0.08	0.010	0.8	0% I.F., 100% Fibrous
46/89	C	0.18	0.010	1.8	90% I.F., 10% Fibrous

The samples had been quenched from 950°C and tempered for 1hr at 600°C. They were broken by slow three-point bending.

Table 6.5 The Effects of Heat Treatment on the Room Temperature Fracture Mechanism of Cast 4176 (0.27C, 1.54Mn, 0.18Al, 0.015N)

Sample No.	Heat Treatment	Hardness (Hv30)	Fracture Mechanism
4176/1	As cast	202	95% cleavage, 5% I.F.
4176/2	900°C 1hr WQ, 650°C 1hr WQ	247	10% Fibrous, 90% I.F.
4176/3	900°C 1hr WQ, 650°C ½hr WQ	254	0% Fibrous, 100% I.F.
4176/4	900°C 1hr OQ, 650°C 1hr WQ	227	20% Fibrous, 80% I.F.
4176/5	900°C 1hr OQ, 650°C ½hr WQ	244	5% Fibrous, 95% I.F.
4176/6	900°C 1hr WQ	504	10% Fibrous, 90% I.F.
4176/7	900°C 1hr air cool	210	0% Fibrous, 100% I.F.
4176/8	900°C 1hr furnace cool	161	60% Fibrous, 40% I.F.

Table 6.6

Room Temperature Tensile Test Results

Sample Number	Heat Treatment	0.2% P.S. (MNm^{-2})	U.T.S. (MNm^{-2})	Elongation on 5.65 $\sqrt{So}$ (%)	Reduction of Area (%)	Fracture Morphology
46/4C	950°C for 1½hrs, WQ 600°C for 1hr, WQ	406 425	627 641	17 16	54 57	Fibrous.
46/89/1/2	950°C for 1½hrs, WQ 600°C for 1hr, WQ	646	767	3	12	80% I.F., 20% Fibrous.
46/1A	950°C for 1½hrs, air cool	353 343	577 570	21 26	24 52	Fibrous.
46/89/2/8	950°C for 1½hrs, air cool	448 448	732 740	18 19	20 30	Fibrous.

Table 6.7

Variation in the Tensile Properties of Cast 46/89 with Temperature of Testing

Sample Number	Test Temperature (^{o}C)	0.2% P.S. (MNm^{-2})	U.T.S. (MNm^{-2})	Elongation on 5.65 $\sqrt{So}$ (%)	Reduction of Area (%)	Comments
1/4B	-50	768	895	13	9.0	Predominantly I.F.
2/4B	20	732	850	10	14.4	Predominantly I.F.
2/4D	50	710	830	10	19.8	Predominantly I.F.
3/5A	75	675	802	14	21.6	≈20% fibrous, remainder I.F.
3/5B	100	645	778	14	33.0	Predominantly I.F.
3/5C	125	648	778	12	31.4	Predominantly I.F.
3/5D	150	612	768	13	27.6	Predominantly I.F.
4/4A	175	585	750	13	27.0	Predominantly I.F.
4/4B	200	595	760	14	37.2	Predominantly I.F.
4/4C	225	585	755	17	42.2	Predominantly I.F.
4/4D	250	600	785	16	24.0	Fibrous Fracture.
4/5A	250	610	788	10	21.0	Mixed I.F./fibrous.
4/5B	300	555	825	15	16.4	Mixed I.F./fibrous.
4/5C	350	545	770	14	20.0	Mixed I.F./fibrous.
4/5D	400	498	682	19	35.4	Mixed I.F./fibrous.

The prior heat treatment of each sample was 950^{o}C for 1½hrs. WQ; 600^{o}C for 1hr. WQ.
Testing was performed at a strain rate of $0.002s^{-1}$.

Table 6.8

COD Test Results for Embrittled Castings (Quenched and Tempered)
Material Code : HHQT

Specimen Number	Test Temperature (^{o}C)	δ_c (mm)	δ_i (mm)	δ_u (mm)	δ_{max} (mm)	Fracture Morphology
89/1/6	-100	0.063	-	-	-	Brittle cleavage.
89/1/3	-50	-	0.069	0.166	-	Mixed I.F./cleavage preceded by fibrous thumbnail.
89/2/7	0	-	0.082	-	0.175	Fibrous thumbnail, then predominantly I.F.
89/3/6	+20	-	0.083	-	0.187	Fibrous thumbnail, then mixed I.F./fibrous.
89/3/7	+20	-	0.081	-	0.165	Fibrous thumbnail, then mixed I.F./fibrous.
89/2/3	+50	-	0.079	-	0.179	Fibrous thumbnail, then mixed I.F./fibrous.
89/2/6	+100	-	0.080	-	0.167	Fibrous thumbnail, then mixed I.F./fibrous.
89/2/2	+150	-	0.082	-	0.156	Predominantly fibrous.

Table 6.9

COD Test Results for Unembrittled Castings (Quenched and Tempered)

Material Code : LLQT

Specimen Number	Test Temperature (^{o}C)	δ_c (mm)	δ_i (mm)	δ_u (mm)	δ_{max} (mm)	Fracture Morphology
46/8D	-150	0.017	-	-	-	100% cleavage.
46/8C	-100	-	0.032	0.078	-	100% cleavage.
46/2H	-75	-	0.044	0.440	-	Fibrous thumbnail, then 100% cleavage.
46/3B	-50	-	0.064	-	0.441	100% fibrous.
46/8B	-25	-	0.068	-	0.533	100% fibrous.
46/3D	0	-	0.068	-	0.319	100% fibrous.
46/2G	+20	-	0.073	-	0.623	100% fibrous.
46/3C	+20	-	0.067	-	0.362	100% fibrous.
46/4D	+50	-	0.067	-	0.459	100% fibrous.
46/3A	+100	-	0.073	-	0.237	100% fibrous.
46/8A	+150	-	0.077	-	0.260	100% fibrous.

Table 6.10

COD Test Results for Embrittled Castings (Normalised)

Material Code : HHN

Specimen Number	Test Temperature (^{o}C)	δ_c (mm)	δ_i (mm)	δ_u (mm)	δ_{max} (mm)	Fracture Morphology
89/4/6	-100	0.011	-	-	-	100% cleavage.
89/4/3	-50	0.028	-	-	-	100% cleavage.
89/4/2	0	-	0.035	0.063	-	Fibrous thumbnail, then 100% cleavage.
89/4/7	+20	-	0.070	-	0.37	Mixed fibrous/I.F.

Table 6.11

COD Test Results for Unembrittled Castings (Normalised)

Material Code : LLN

Specimen Number	Test Temperature (^{o}C)	δ_c (mm)	δ_i (mm)	δ_u (mm)	δ_{max} (mm)	Fracture Morphology
46/2E	-100	0.051	-	-	-	100% cleavage.
46/4B	-50	-	0.042	-	0.50	100% fibrous.
46/2F	0	-	0.057	-	0.69	100% fibrous.
46/1D	+20	-	0.072	-	0.56	100% fibrous.
46/4A	+20	-	0.067	-	0.67	100% fibrous.

FIGURES

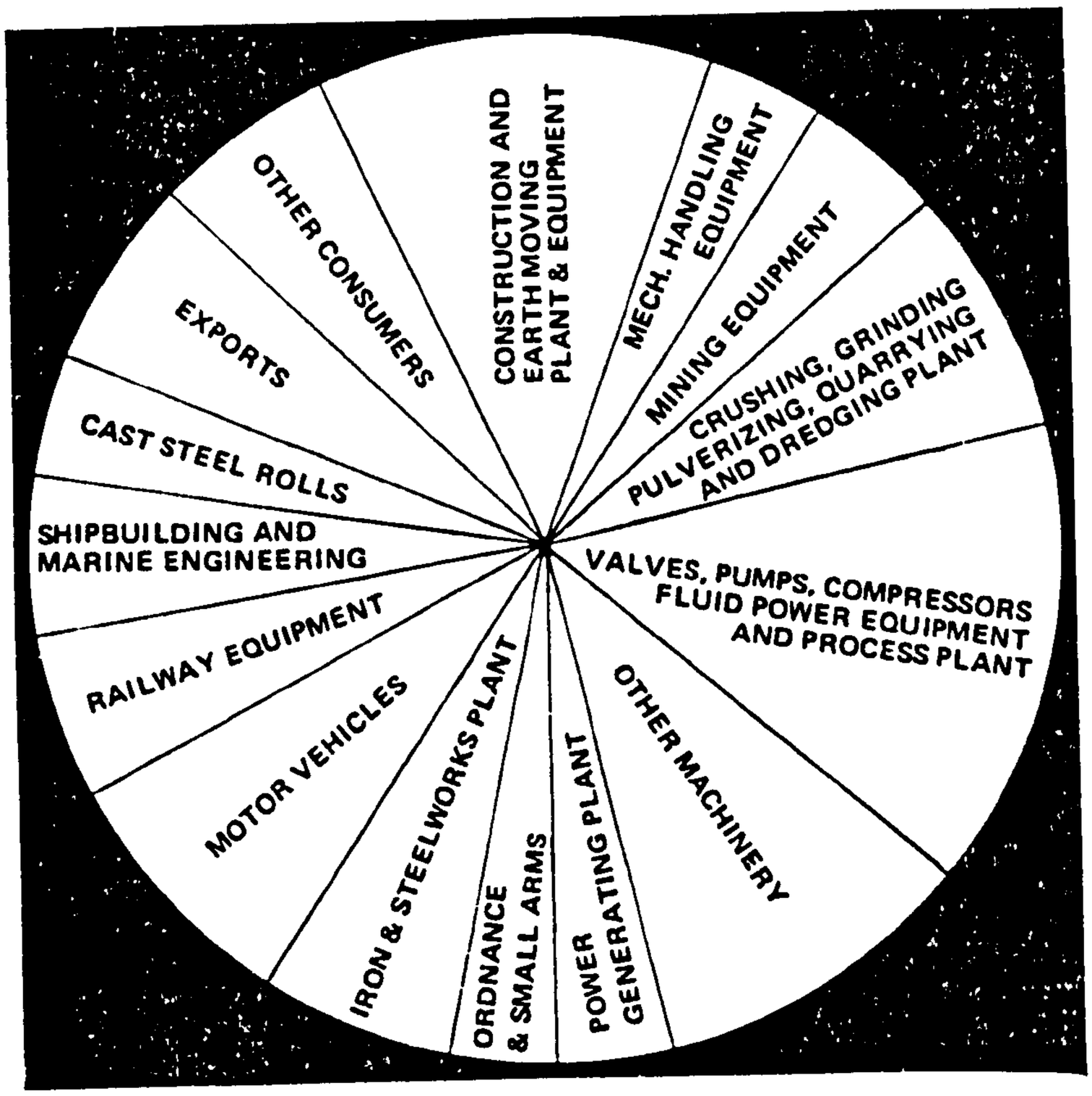

Fig. 2.1 A breakdown of the areas of application of steel castings (Haynes, 1974).

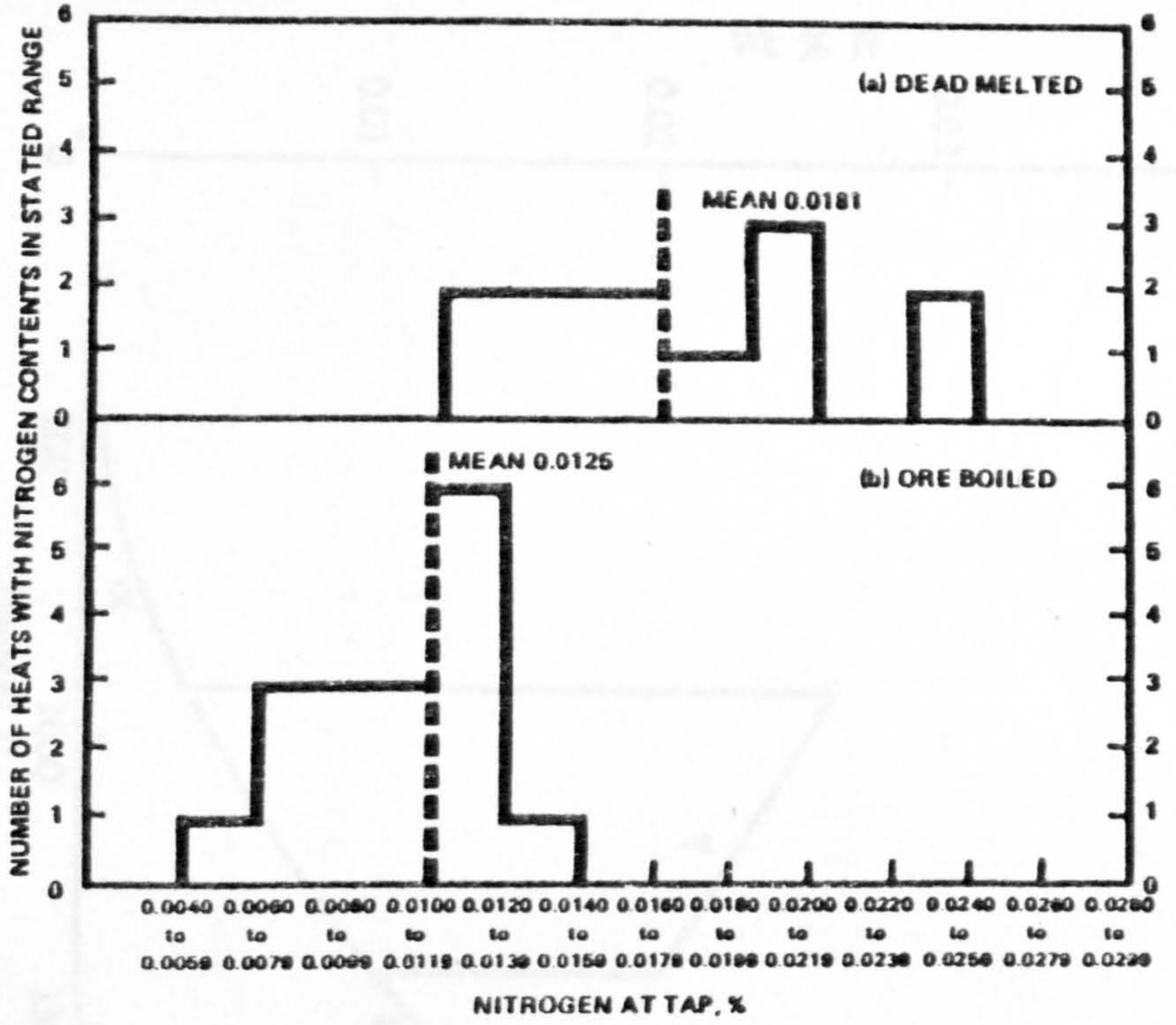

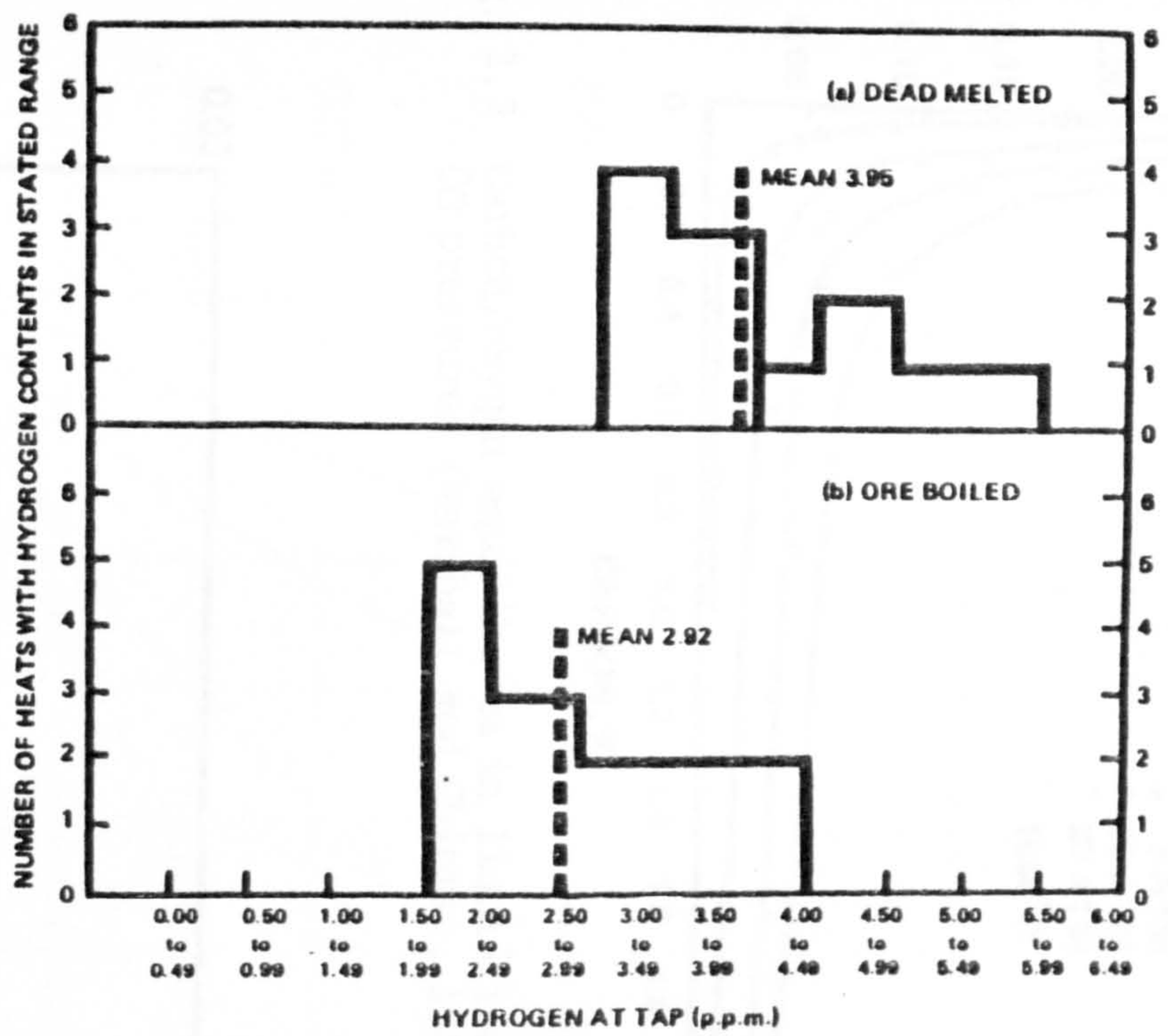

Fig. 2.2 Comparison of the typical gas contents for induction melted heats with
(a) dead melting practice
(b) an ore-induced carbon boil
(Holt and Hubbard, 1971).

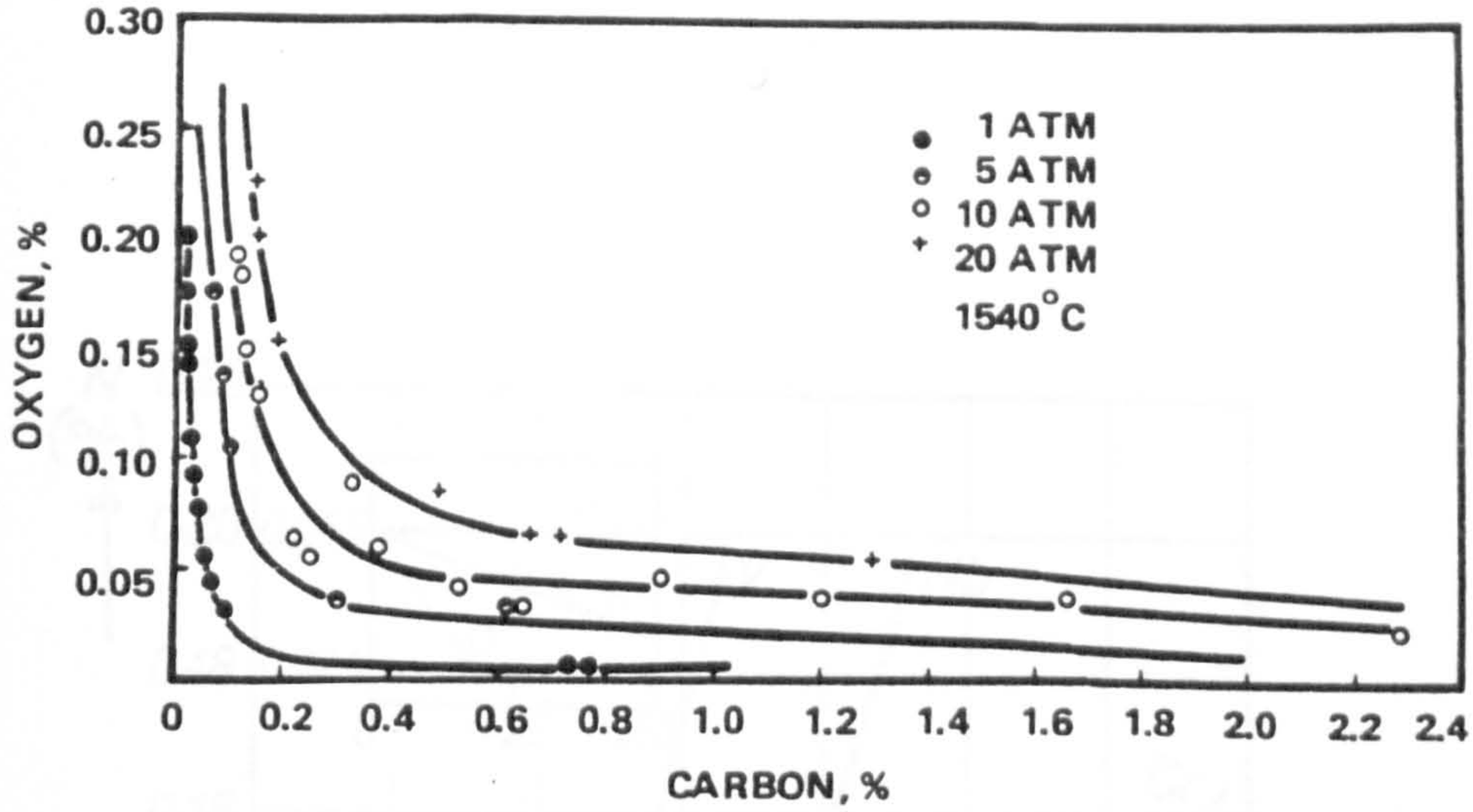

Fig. 2.3 Carbon/oxygen equilibrium in liquid iron at various CO pressures (Marshall and Chipman, 1942).

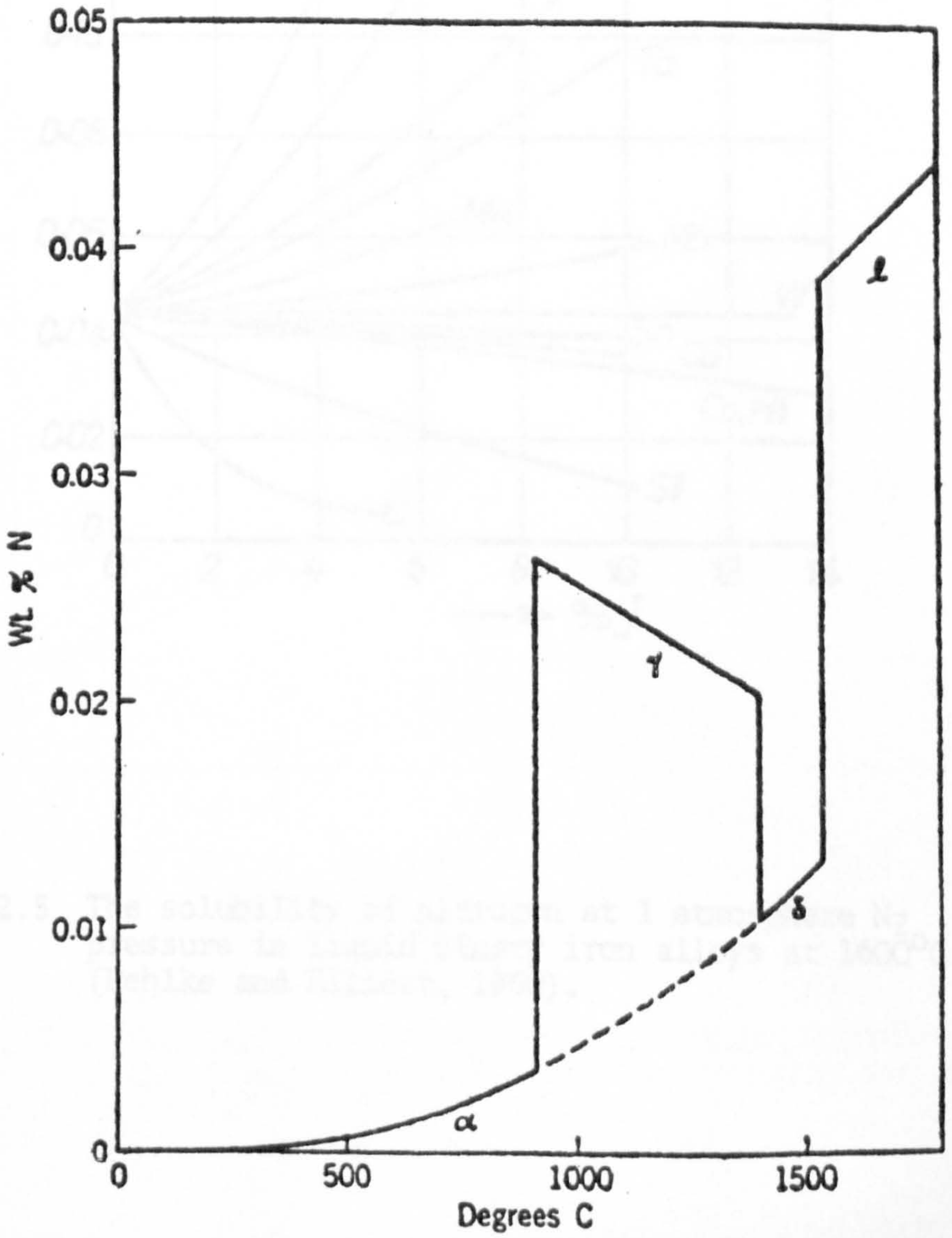

Fig. 2.4 The solubility of nitrogen gas at 1 atmosphere in pure iron under equilibrium conditions (Darken and Gurry, 1953).

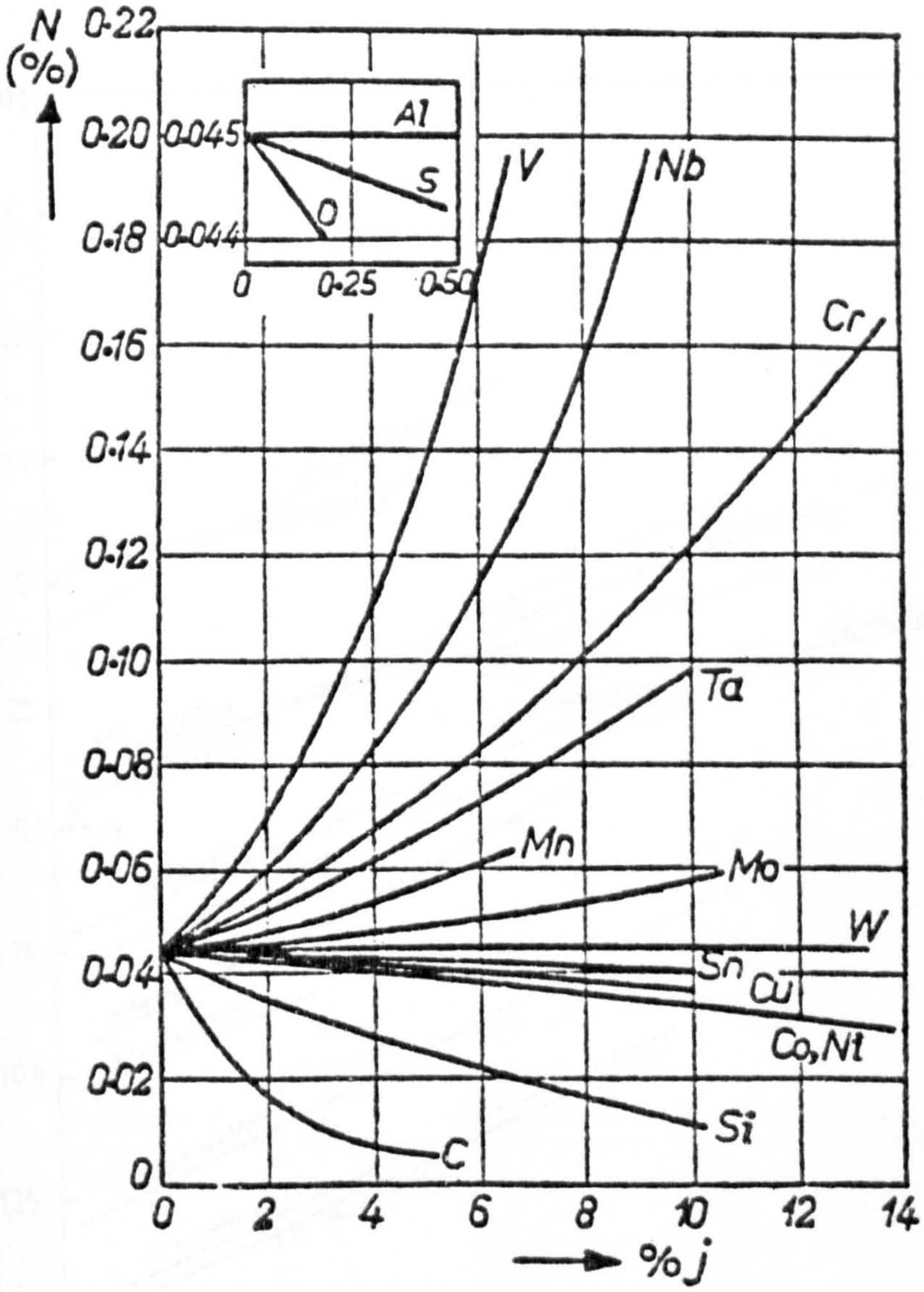

Fig. 2.5 The solubility of nitrogen at 1 atmosphere N_2 pressure in liquid binary iron alloys at 1600°C (Pehlke and Elliott, 1960).

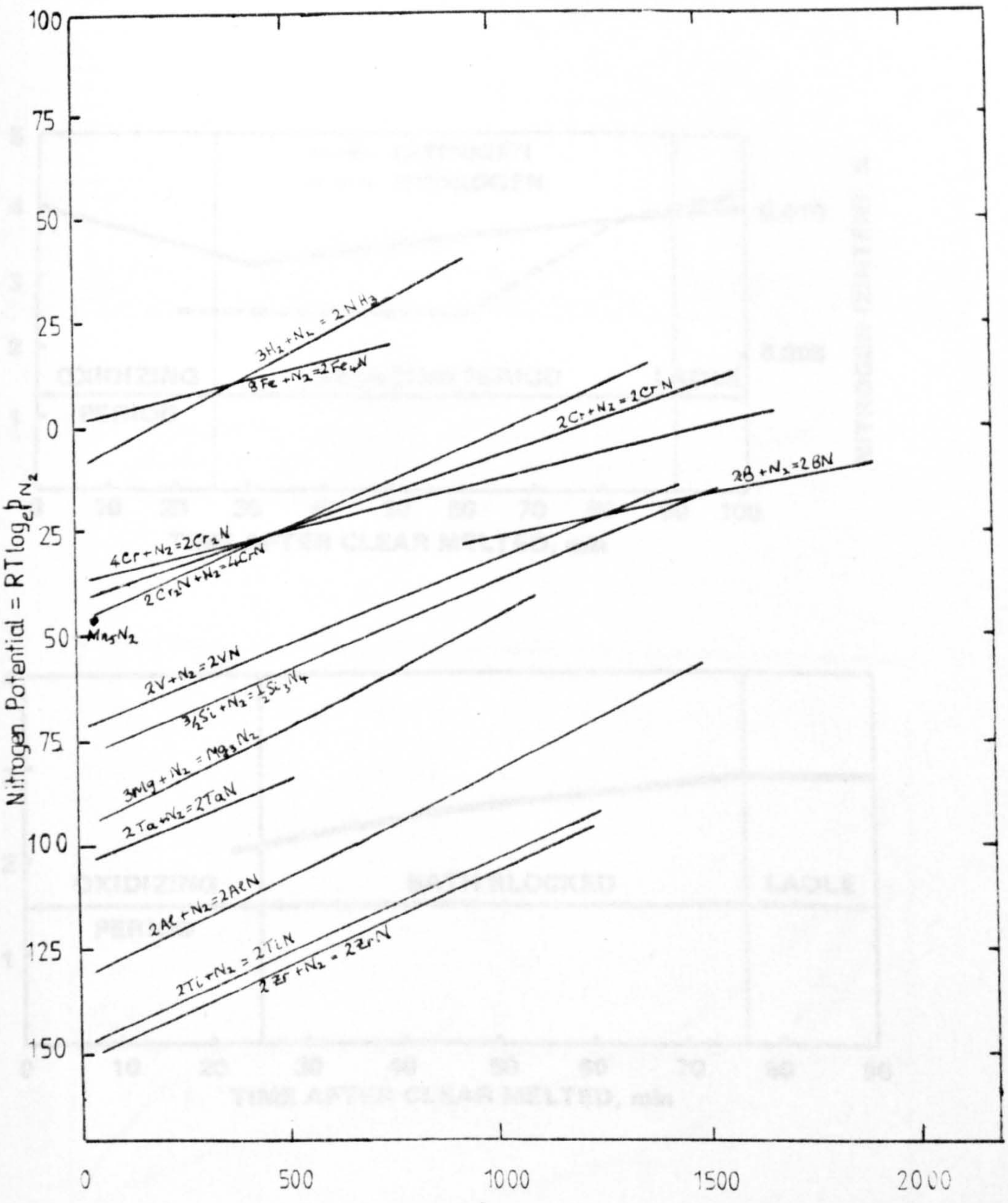

Fig. 2.6 Standard free-energy vs. temperature diagram for the formation of metal nitrides (Pearson and Ende, 1953).

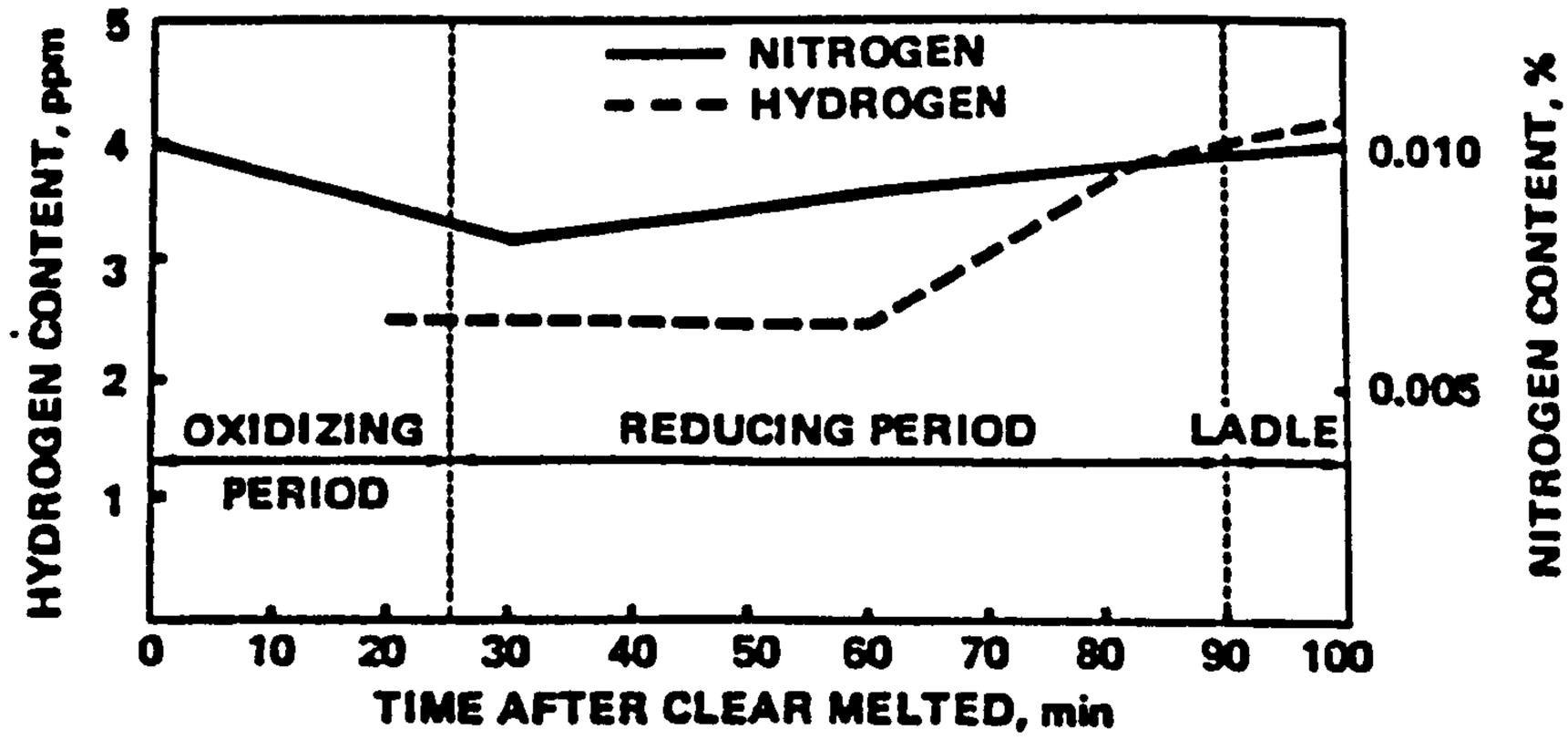

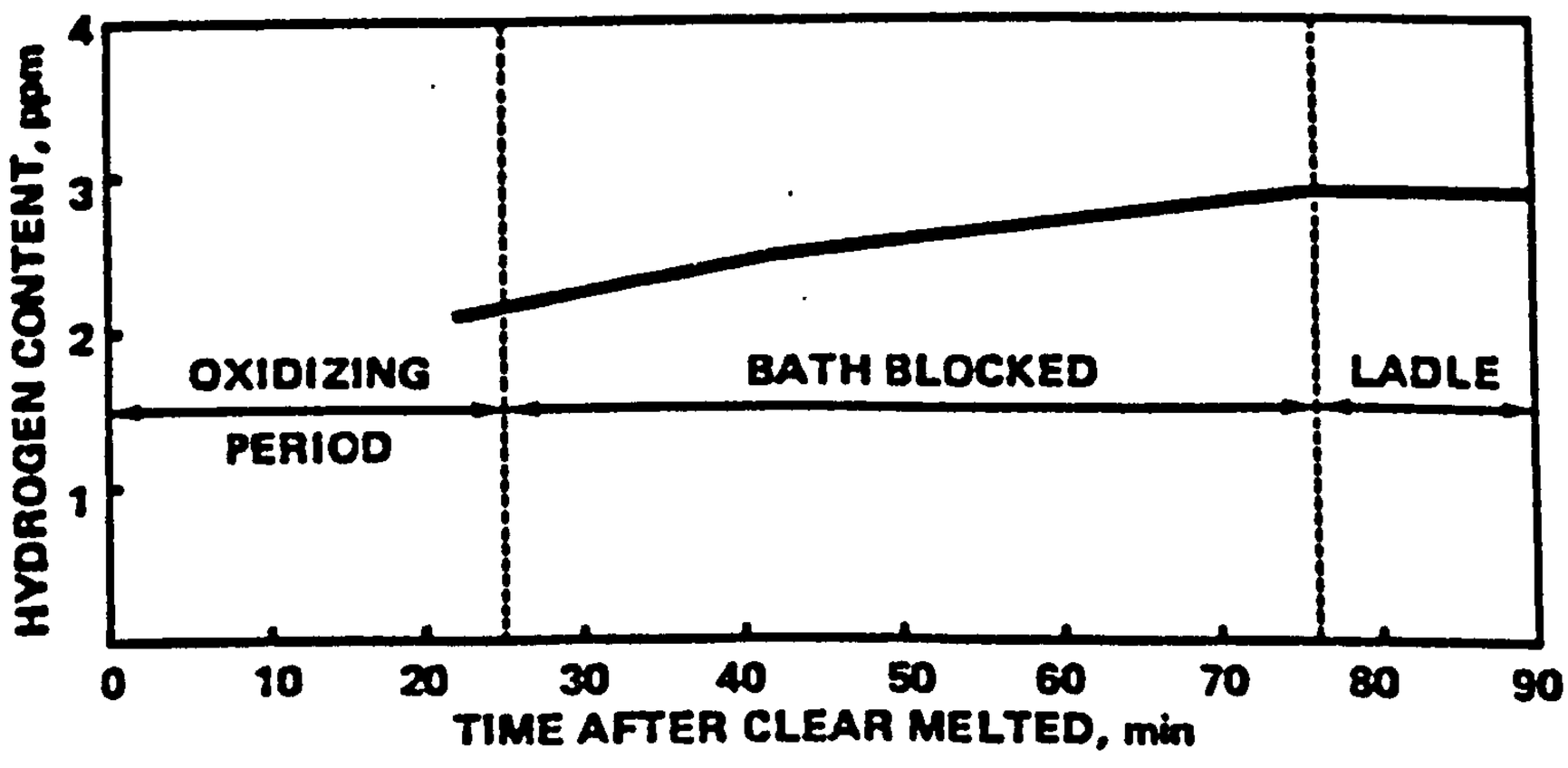

Fig. 2.7 Typical variations in hydrogen content during steelmaking for a 3½ tonne arc furnace heat
(a) using double slag practice
(b) using single slag practice
(Stephenson, 1974).

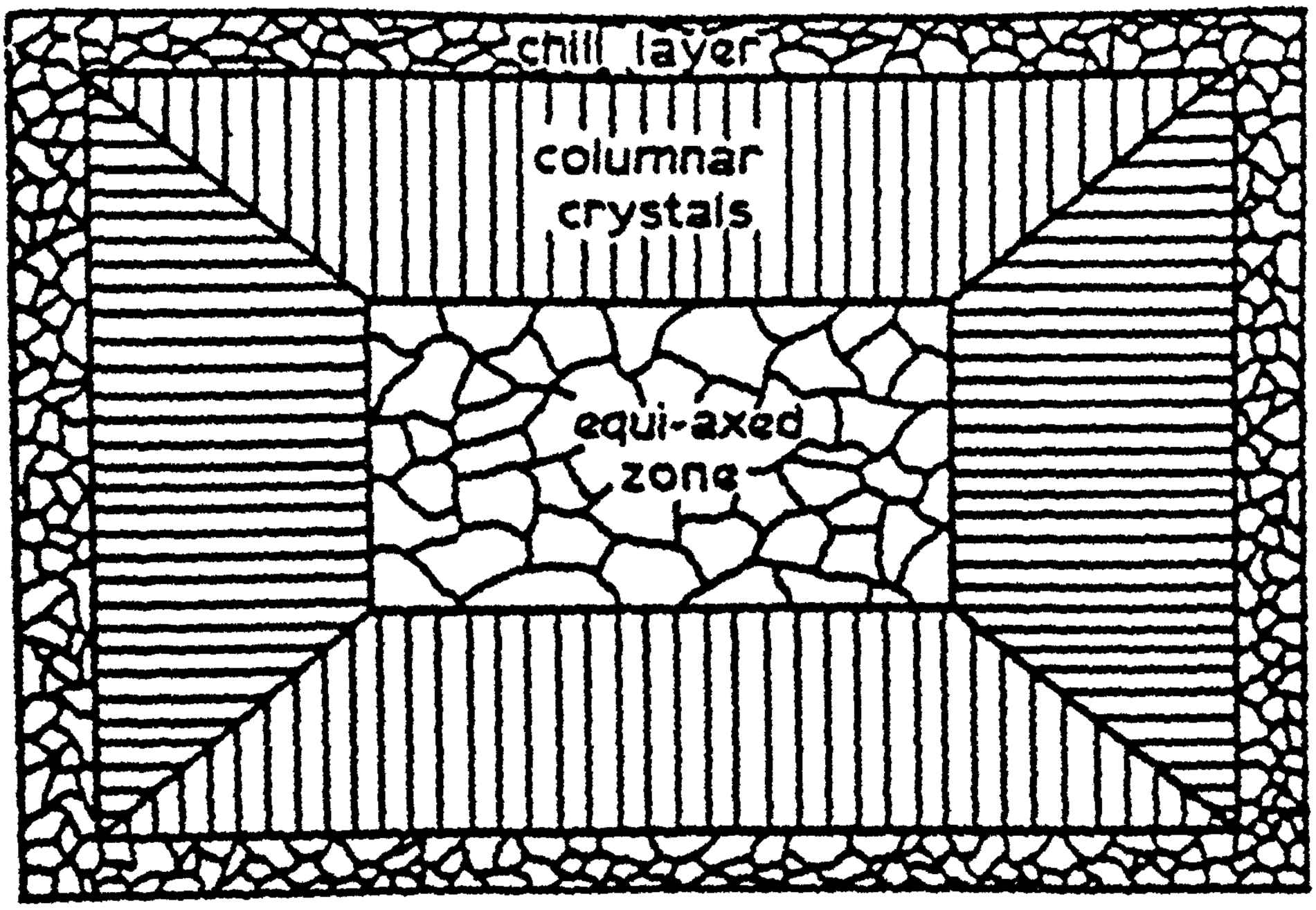

Fig. 2.8 Transverse section of an as-cast structure showing the chill zone, columnar zone and equiaxed zone (Walker, 1958).

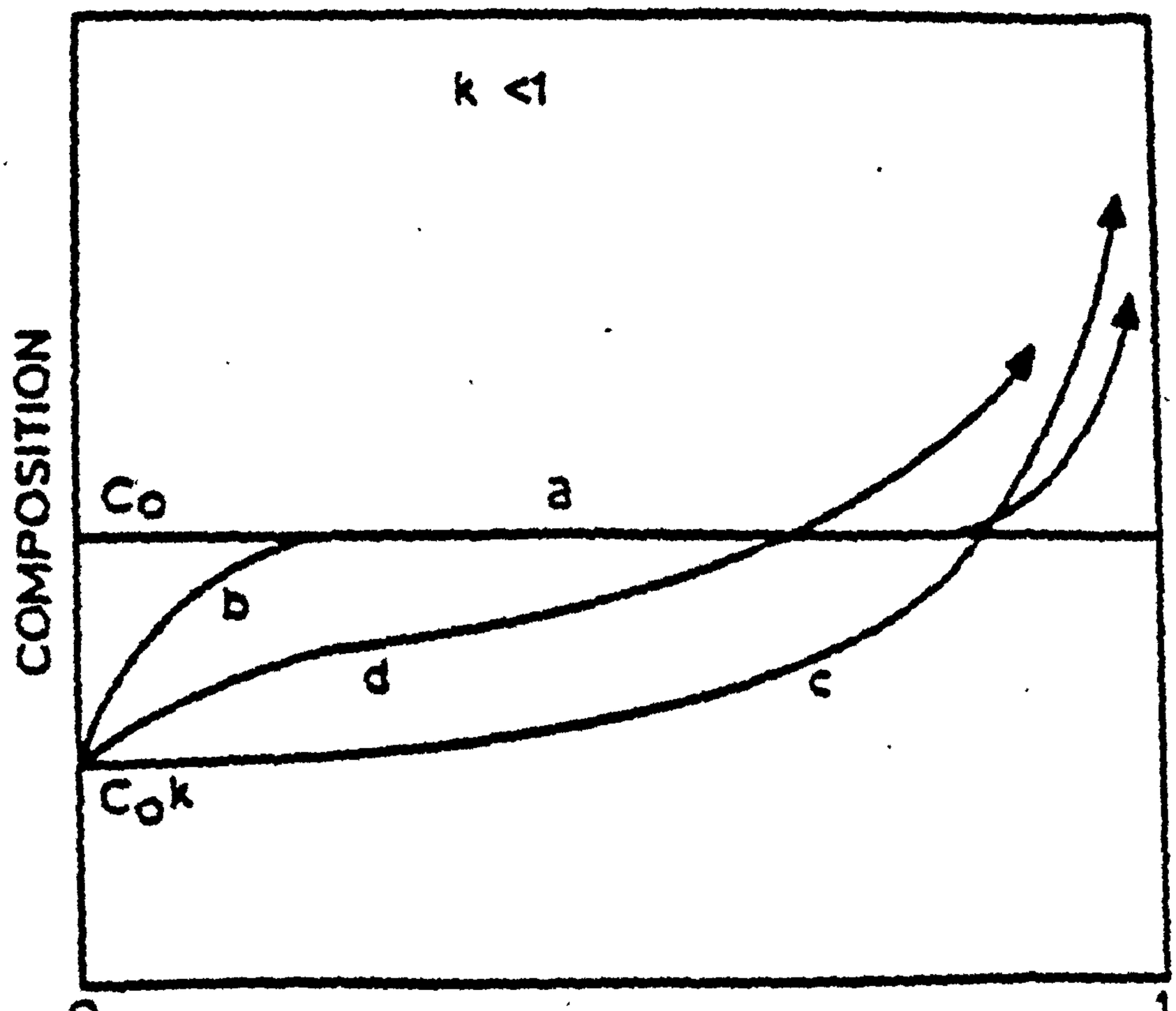

Fig. 2.9 Schematic solute distributions in a solid bar frozen from liquid of concentration Co:
(a) equilibrium freezing
(b) solute mixing in the liquid by diffusion only
(c) complete solute mixing in the liquid
(d) partial solute mixing in the liquid
(Davies and Garland, 1975).

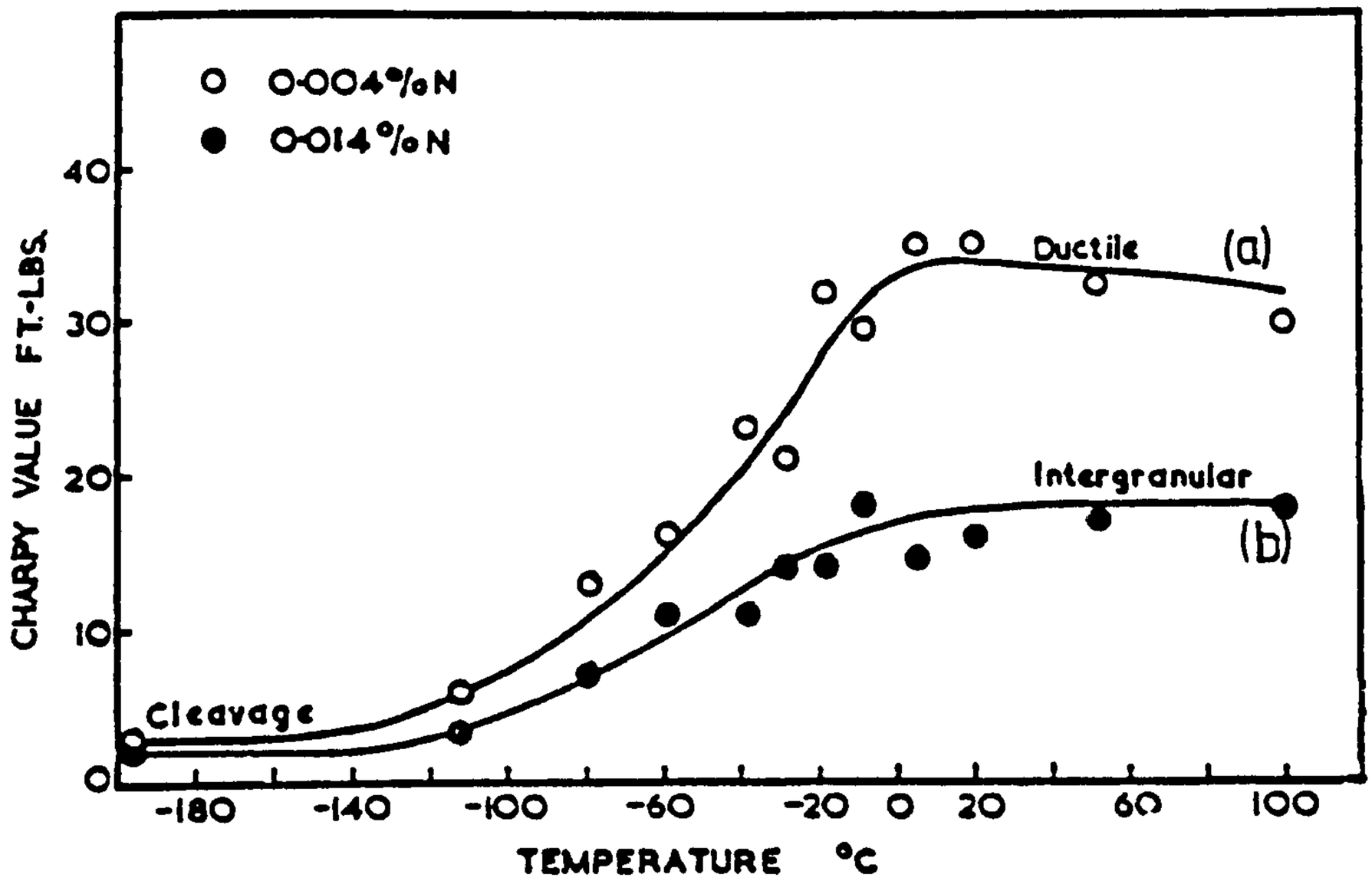

Fig. 3.1 Impact transition curves for a 0.26C-1.50Mn steel showing the effect of intergranular fracture (a) is the curve for a steel containing 0.004%N (b) is the curve for a steel containing 0.014%N (Wright, 1962).

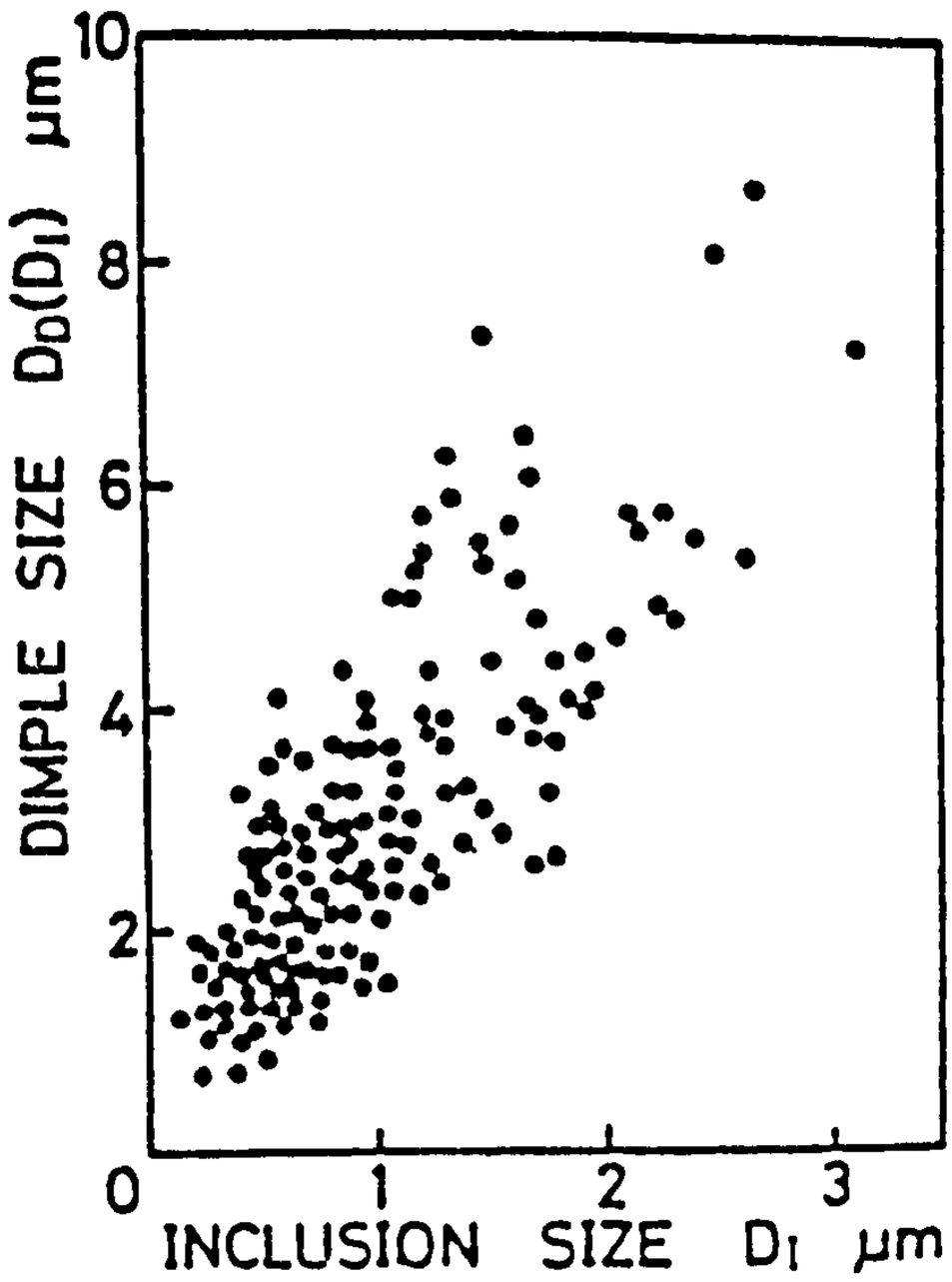

Fig. 3.2 Graph showing the effect of inclusion size on the size of dimples observed in the ductile fracture of electrolytically pure iron containing only FeO inclusions (Kunio et al, 1977).

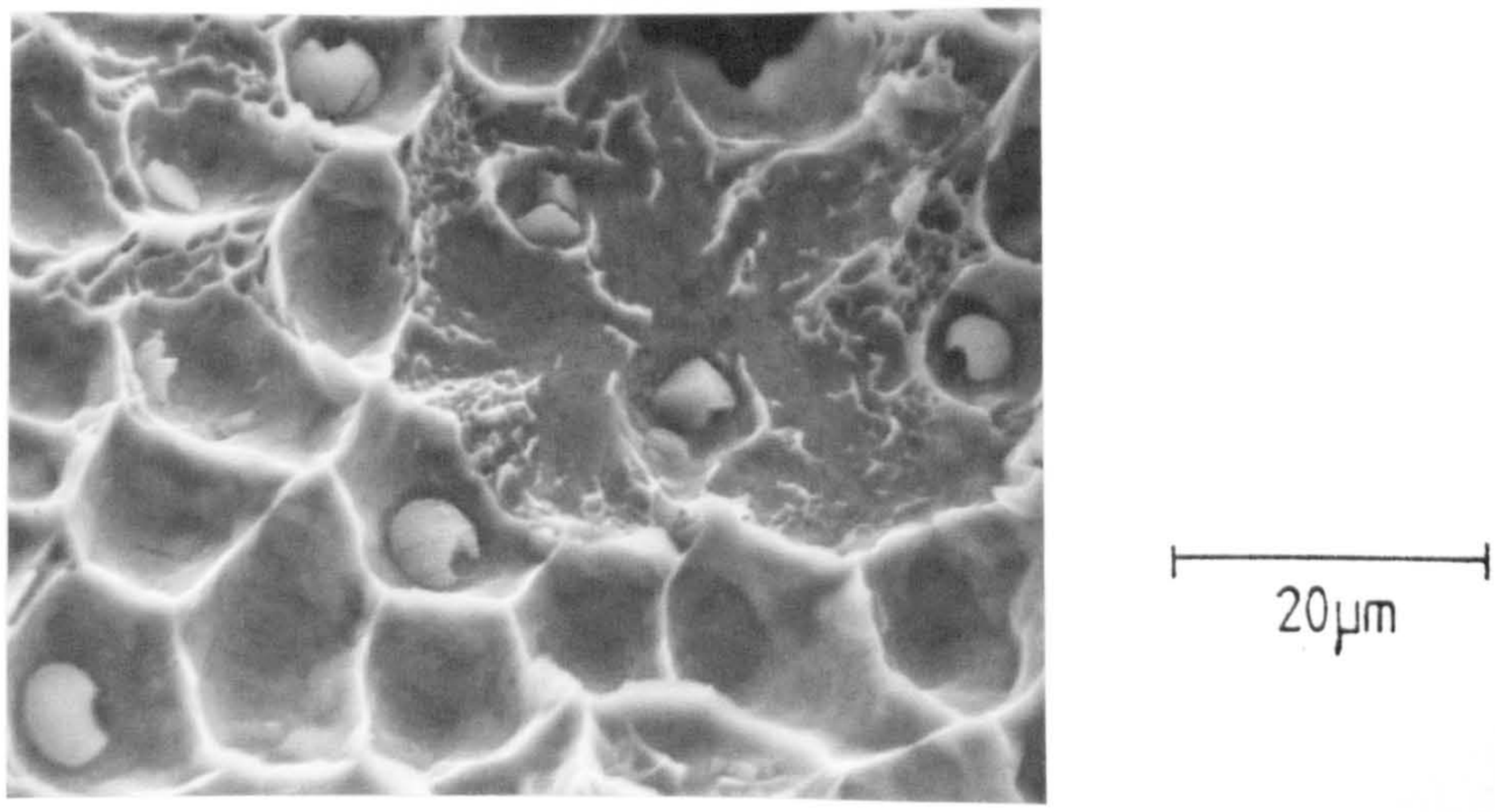

Fig. 3.3 Type I (spherical) MnS inclusions on the fibrous fracture surface of a 0.30C-1.50Mn steel.

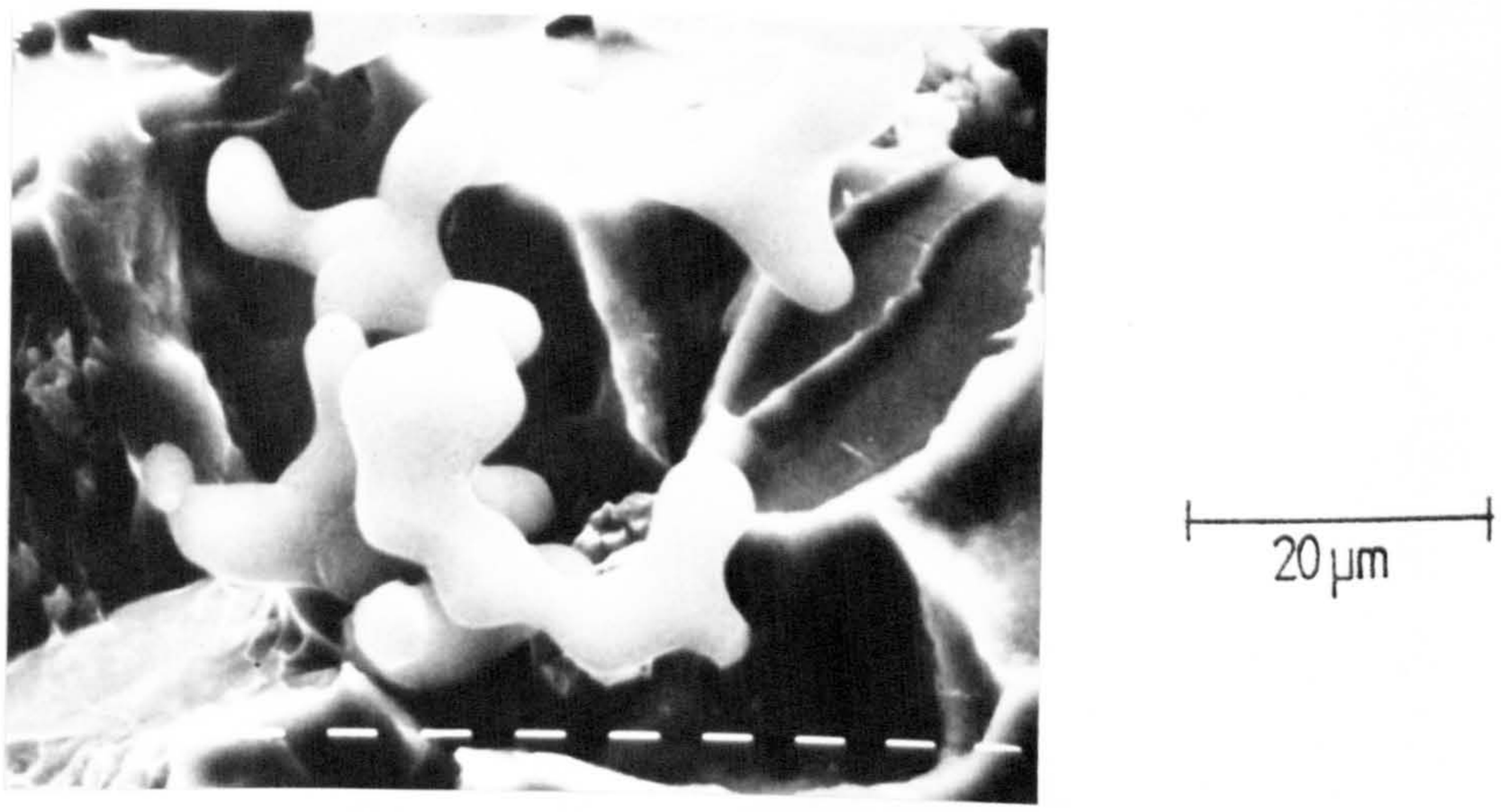

Fig. 3.4 Al_2O_3 inclusions on the fibrous fracture surface of a 0.30C-1.50Mn steel.

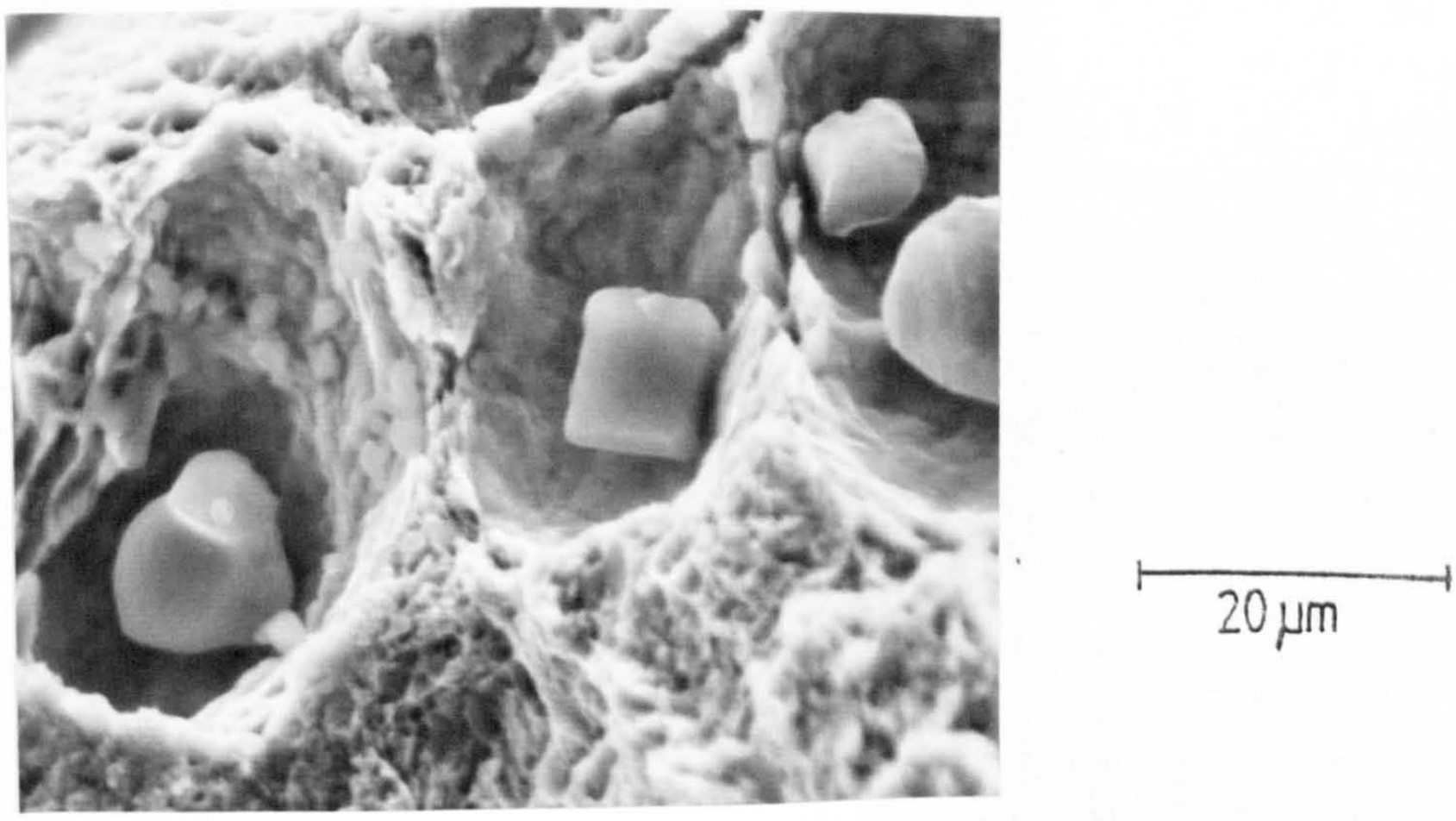

Fig. 3.5 Type III (angular) MnS inclusions on the fibrous fracture surface of a 0.30C-1.50Mn steel.

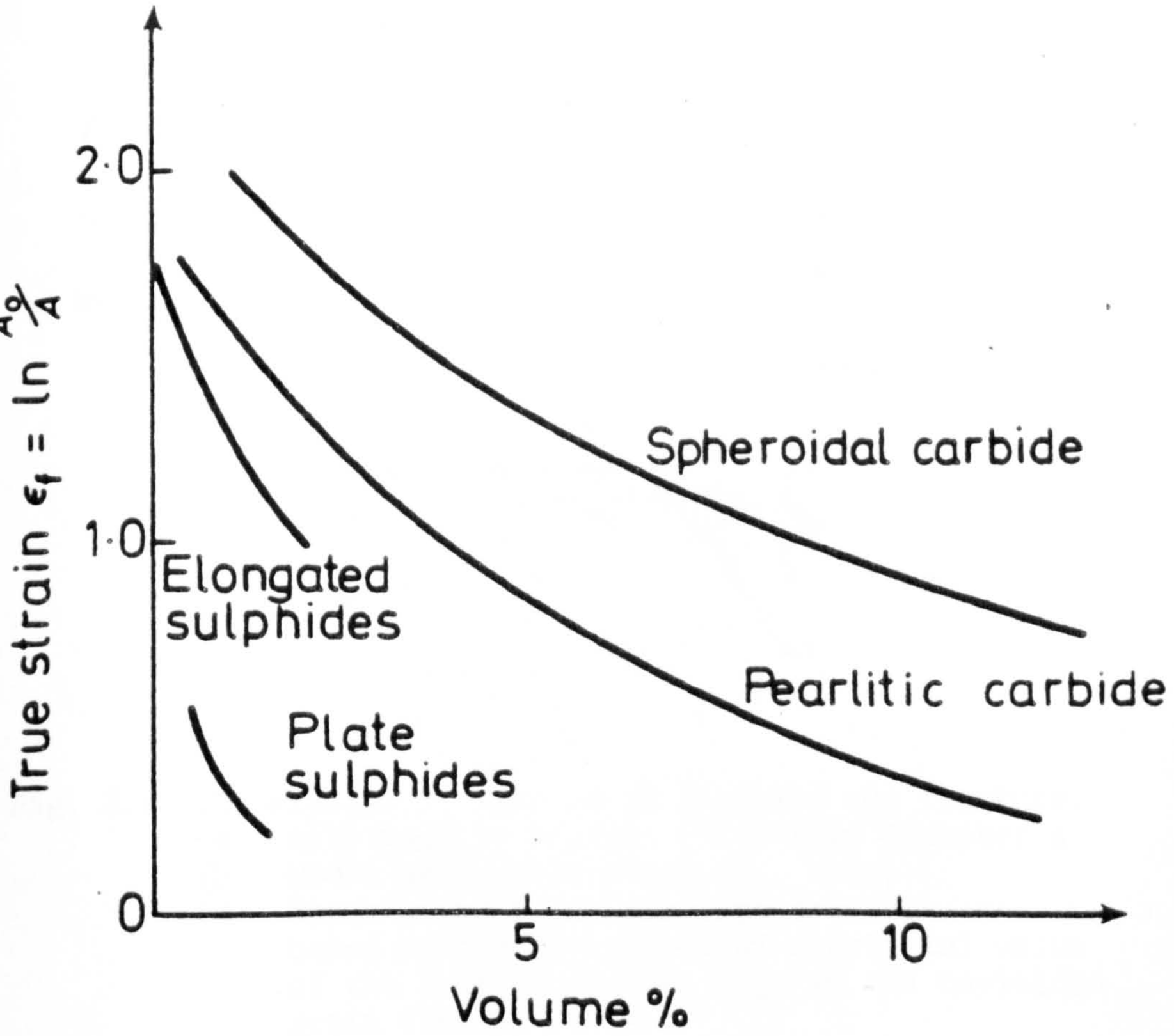

Fig. 3.6 Effects of the type and shape of second-phase particles on the tensile ductility of steel (Gladman et al, 1971).

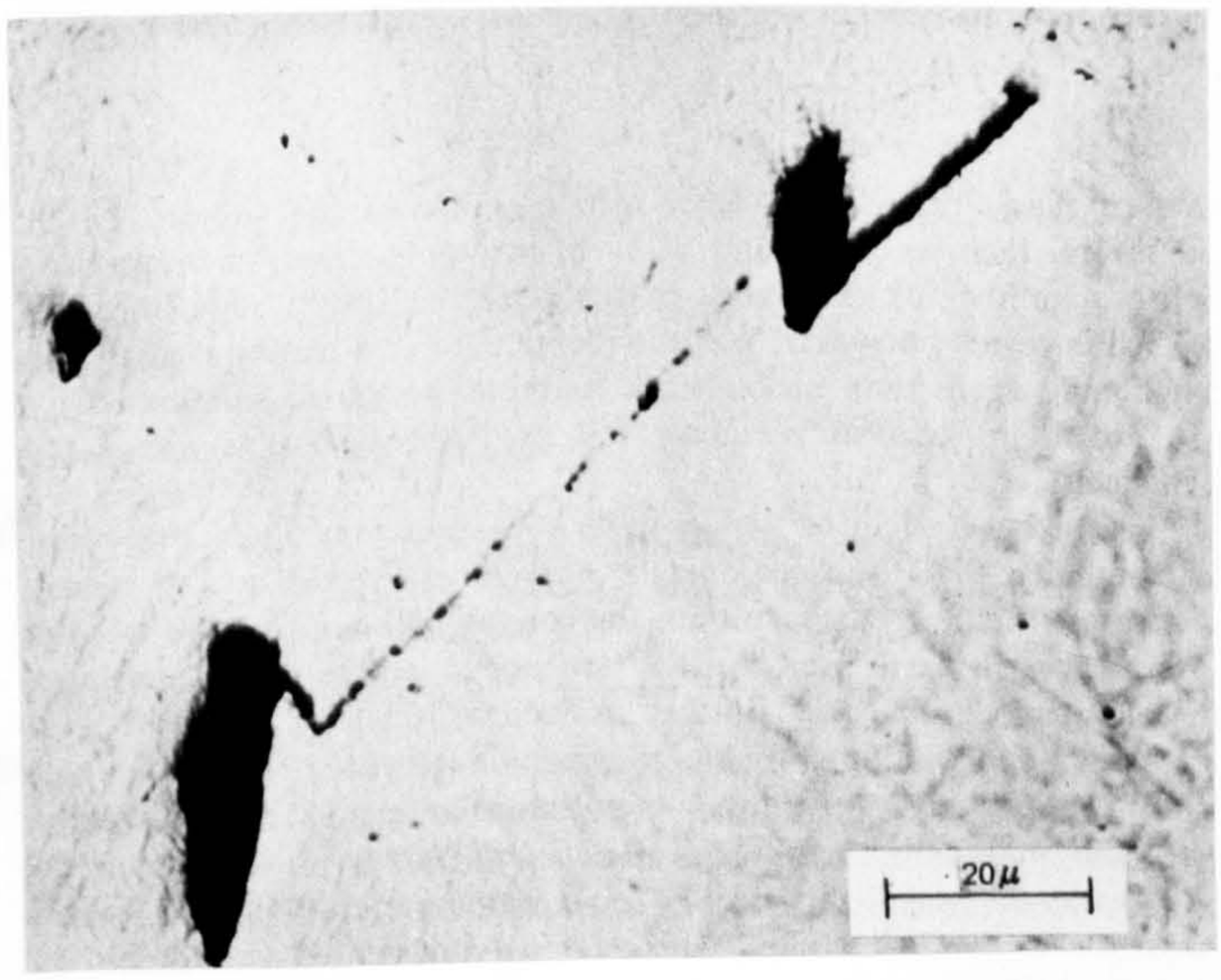

Fig. 3.7 The formation of a shear band between voids at two macro-inclusions in AISI 4340 steel. The band appears to contain a sheet of micro-voids (Cox, 1973).

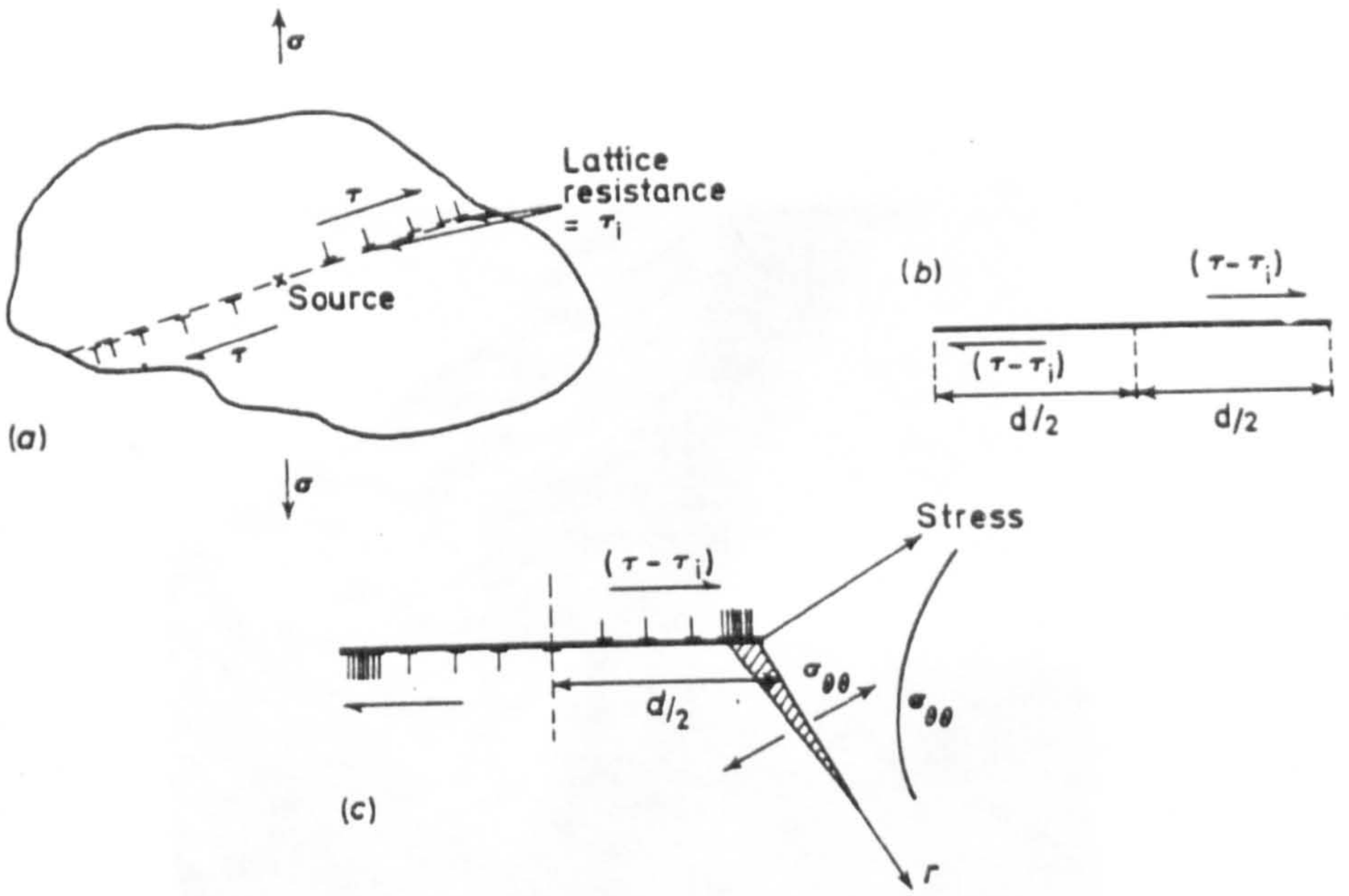

Fig. 3.8 The effects of slip bands in yield and fracture.
(a) slip band in a grain of average diameter d
(b) Model as a shear crack (K_{II} mode)
(c) Stroh's model for cleavage fracture based on the attainment of a critical value of the tensile stress, $\sigma_{\theta\theta}$, in the unyielded grain (Knott, 1973b).

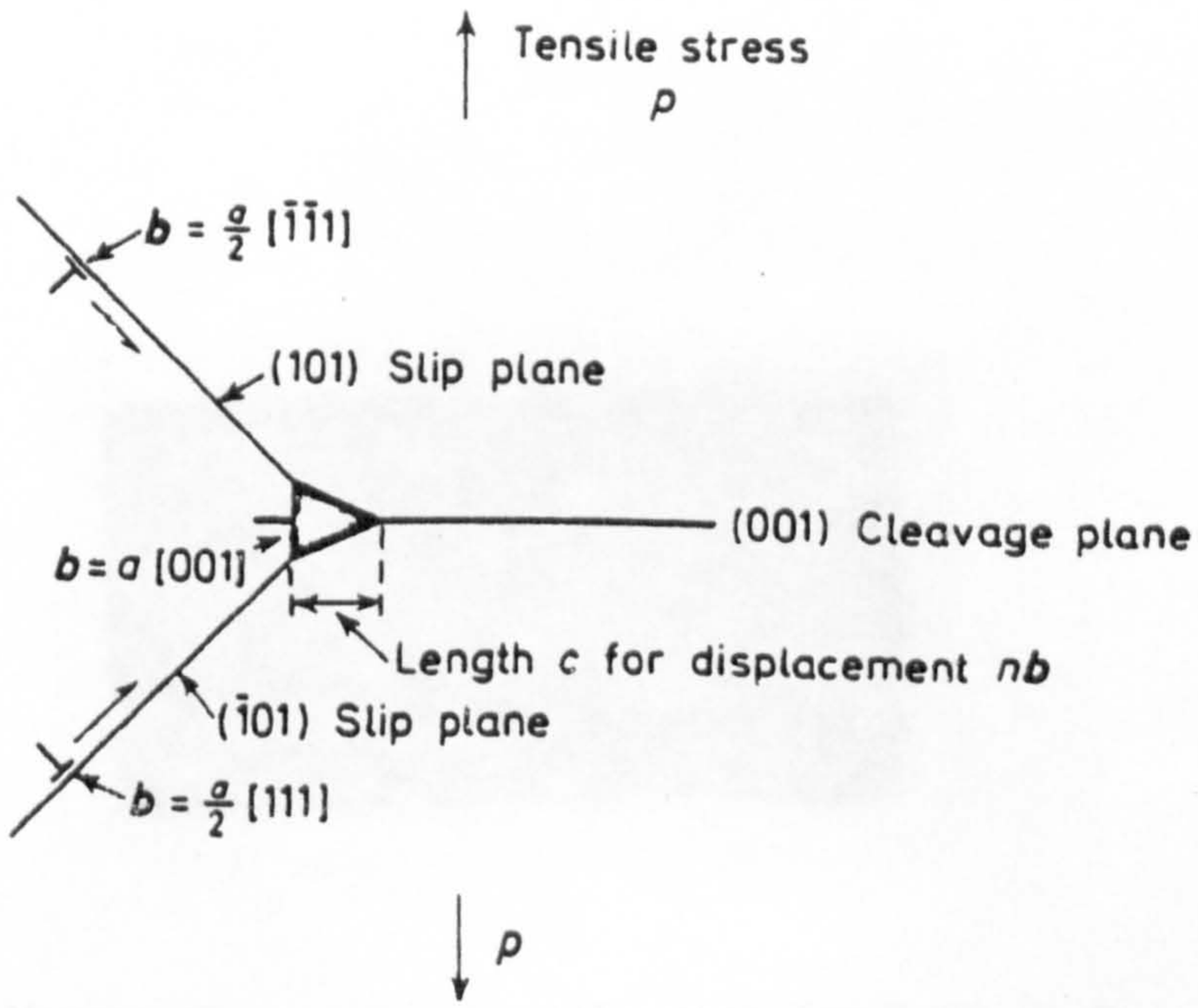

Fig. 3.9 Cottrell's model for cleavage fracture (Knott, 1973b).

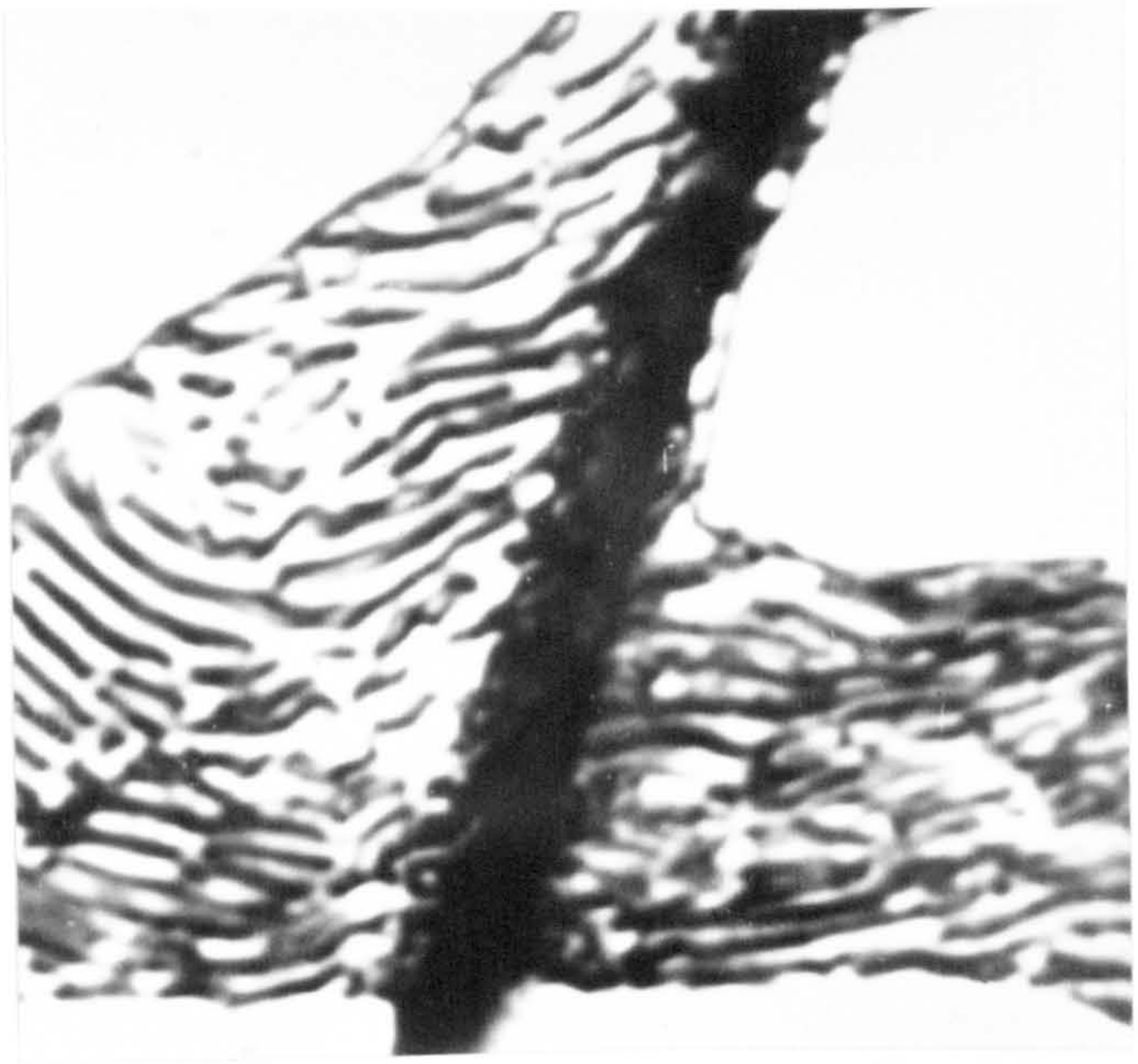

Fig. 3.10 Photomicrograph showing the nucleation of a cleavage crack in pearlitic cementite X1000 (Knott, 1981).

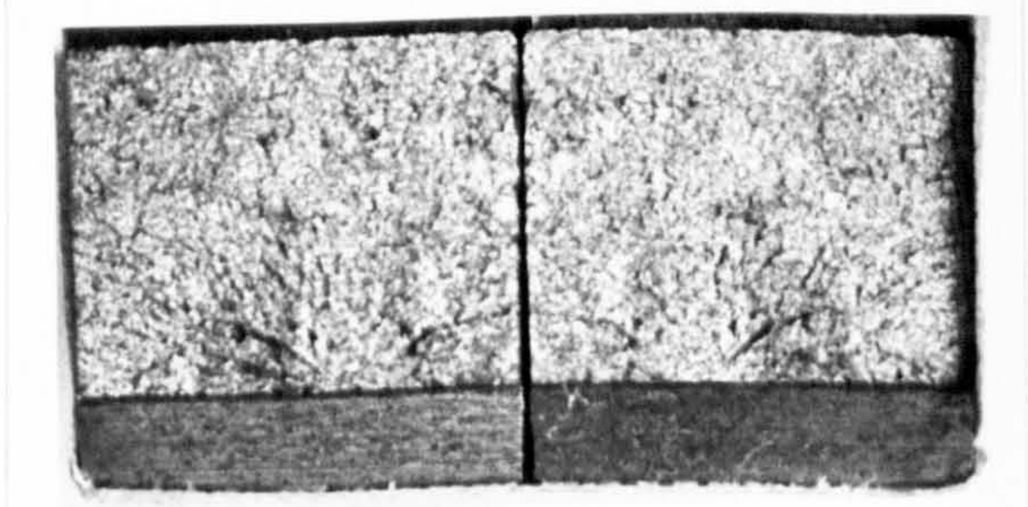

Fig. 3.11 Macroscopic view of a cleavage fracture in a 0.30C-1.50Mn steel broken at -196^{o}C.

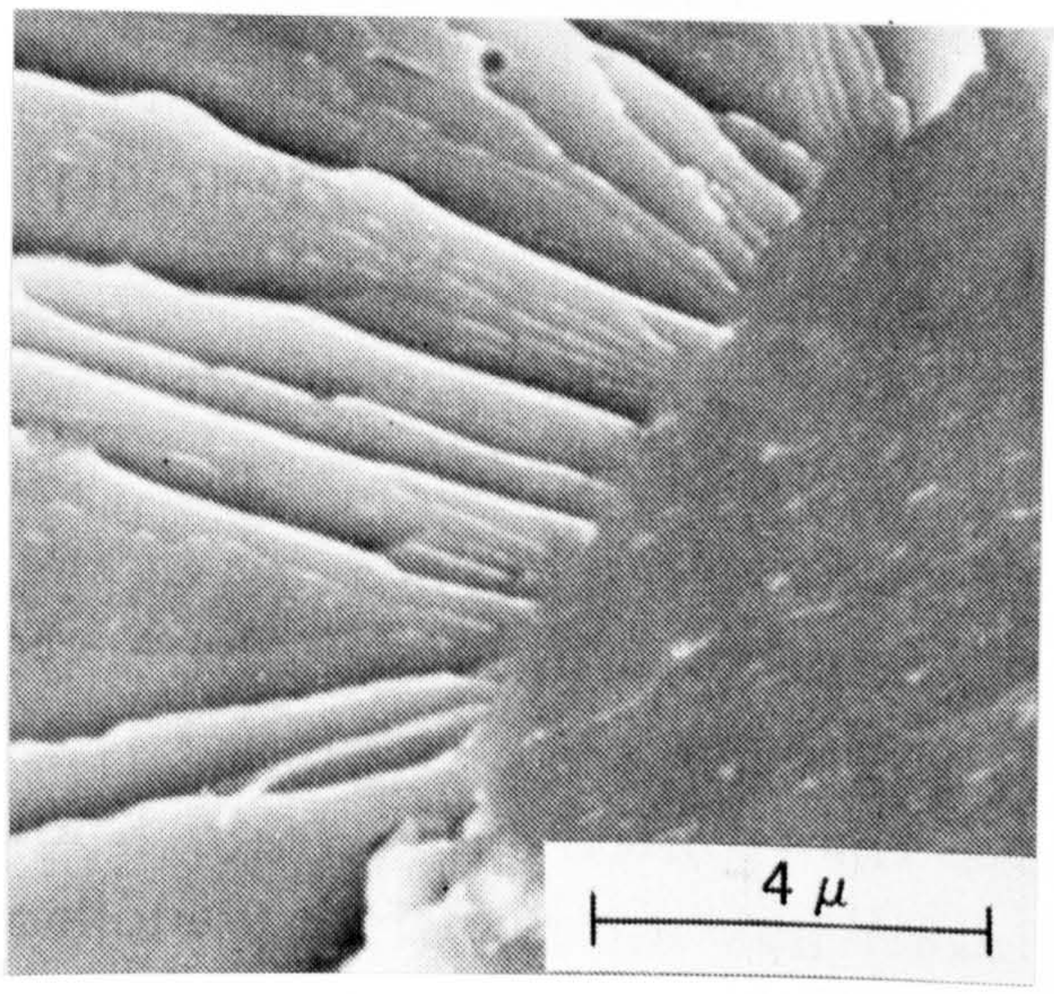

Fig. 3.12 Scanning electron micrograph showing cleavage fracture in a low carbon steel. Crack propagation has been from right to left (Hertzberg, 1976).

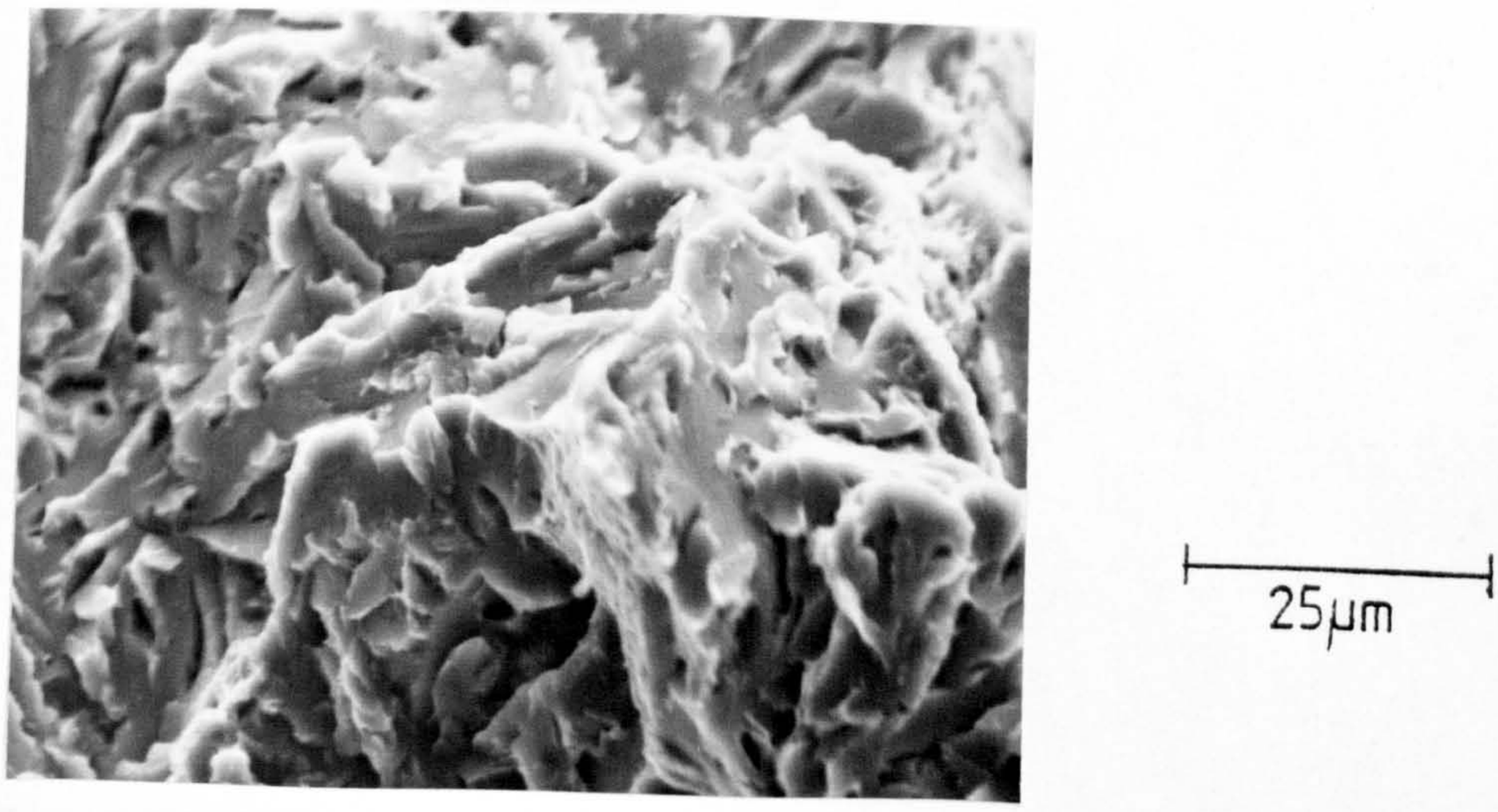

Fig. 3.13 Quasi-cleavage, typical of the low temperature fracture of quenched and tempered steels.

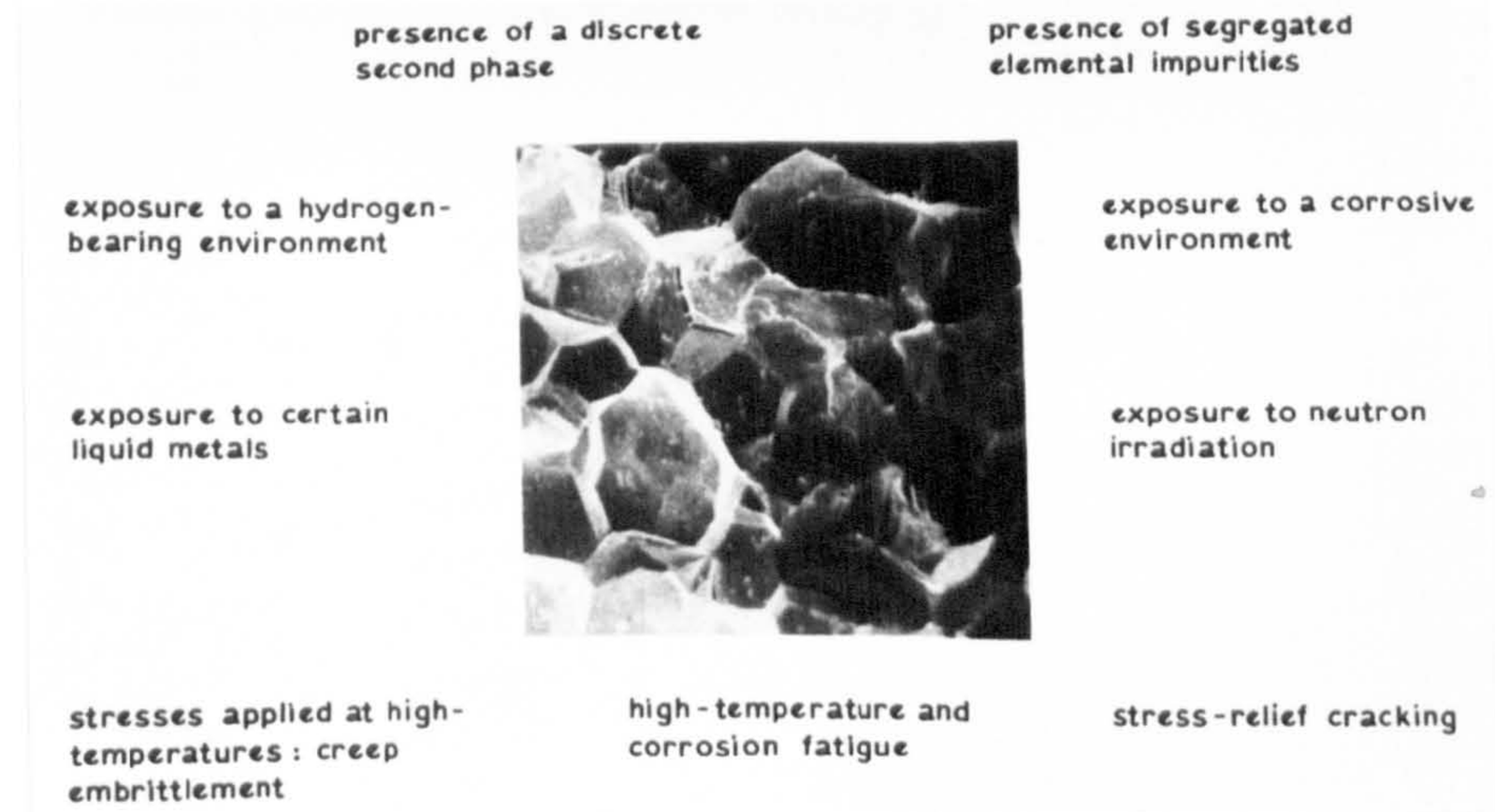

Fig. 3.14 The various circumstances under which steels are known to exhibit intergranular embrittlement. The micrograph in an SEM image of a temper-embrittled steel (Banerji and Briant, 1980).

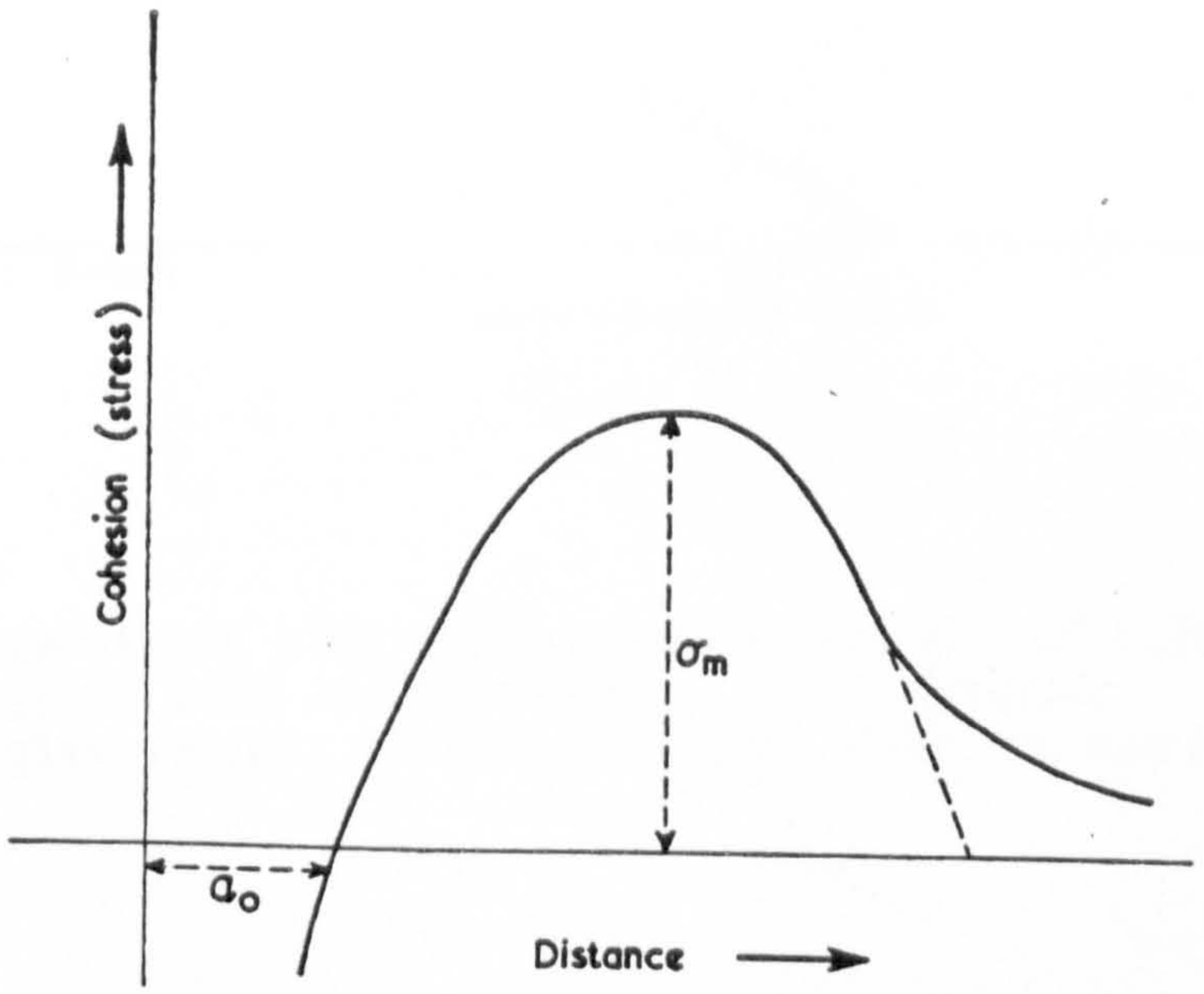

Fig. 3.15 Schematic representation of the cohesion between two atoms as a function of separation: a_o is the equilibrium separation, corresponding to a minimum in the force-distance relation, and σ_m is the maximum cohesion beyond which fracture should occur (Hondros and McLean, 1976).

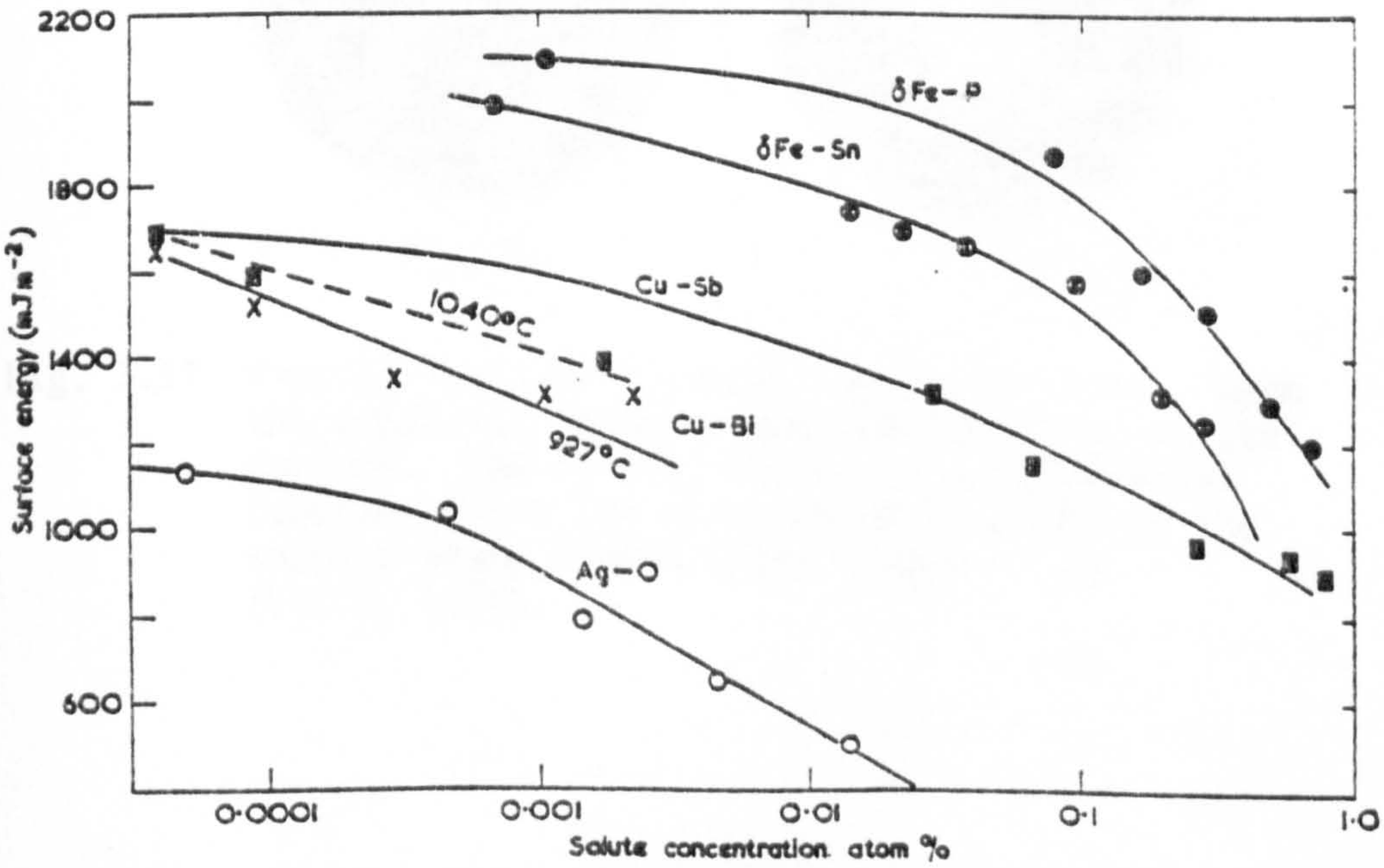

Fig. 3.16 A logarithmic plot showing the dependence of surface energy on bulk solute content. Grain boundary energies exhibit similar behaviour (Hondros and McLean, 1970).

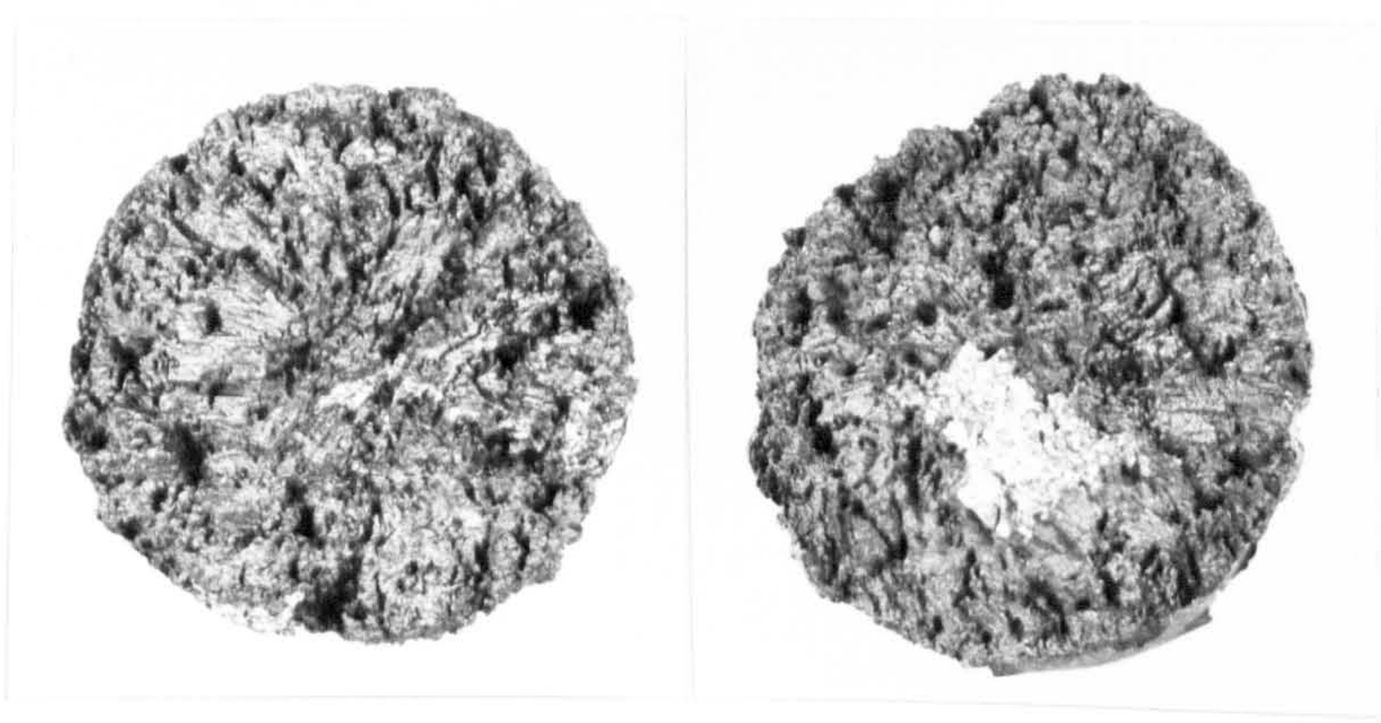

Fig. 3.17 Typical fracture surfaces from a hot tear. Note the dendritic features and the oxidation of the surface. The central bright area is cleavage fracture which has occurred as a result of the samples being broken after cooling X1 (Croft, 1979).

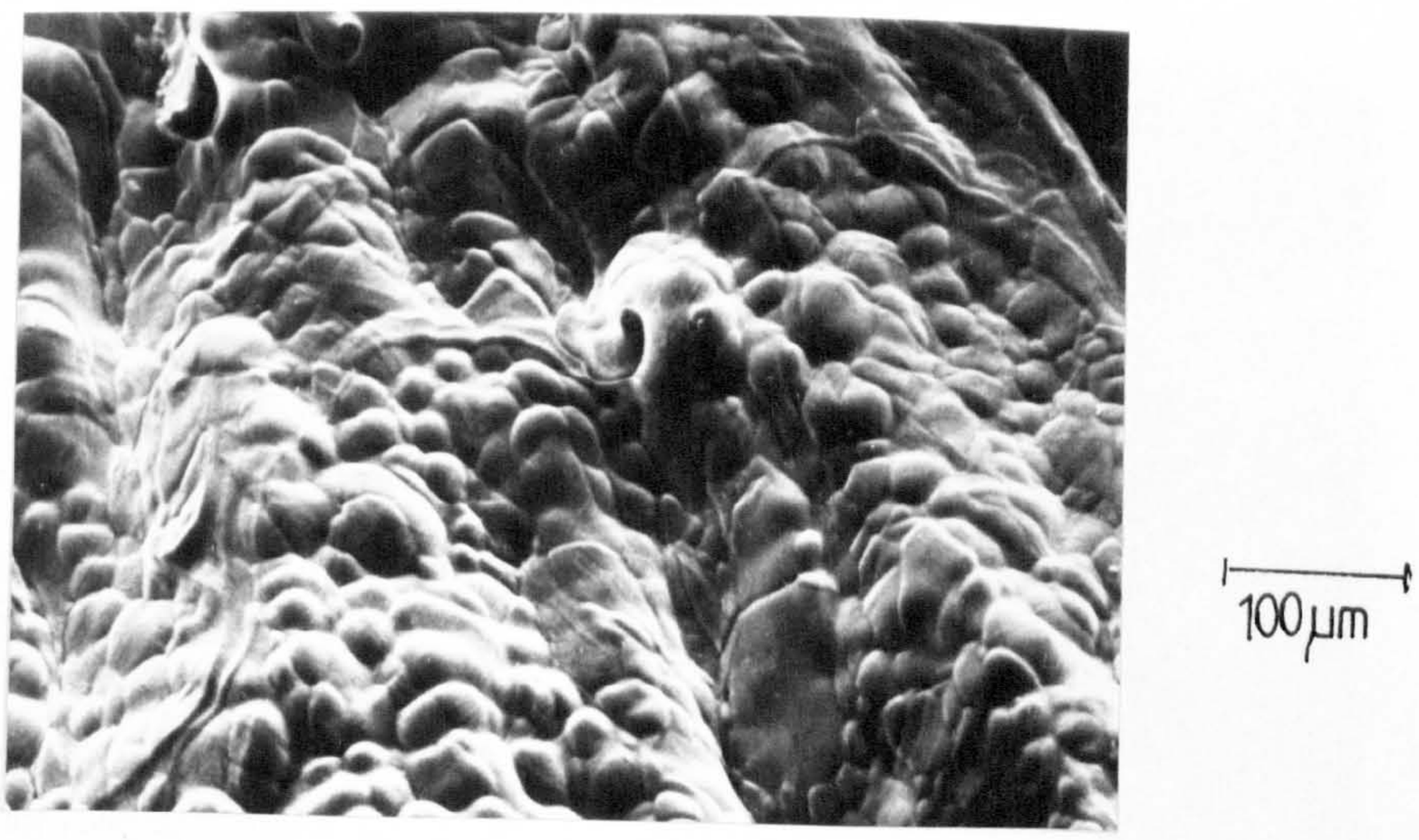

Fig. 3.18 The fracture surface of an Fe-0.08C alloy, showing the interdendritic morphology associated with hot tearing (Shin, 1981).

(a)

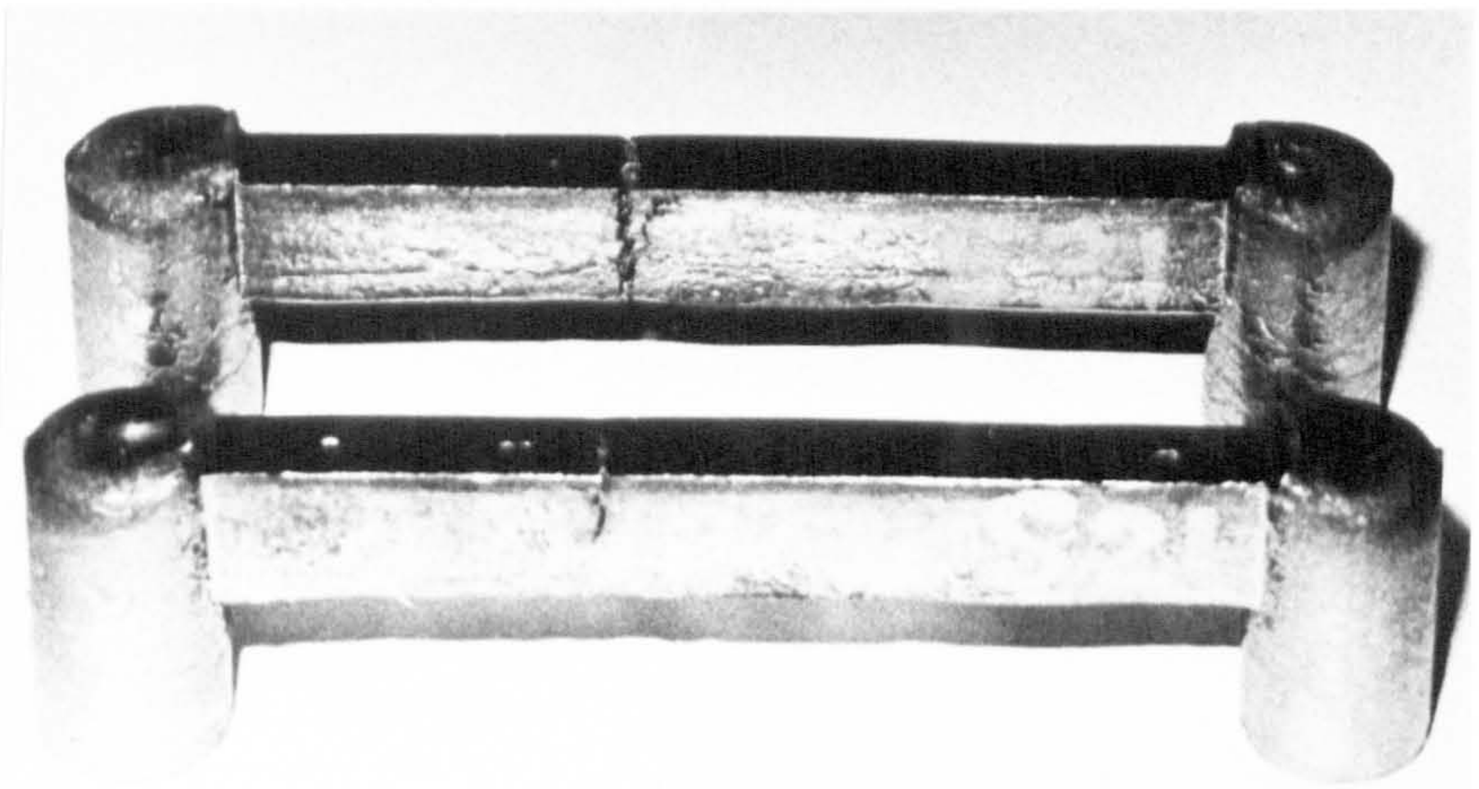

(b)

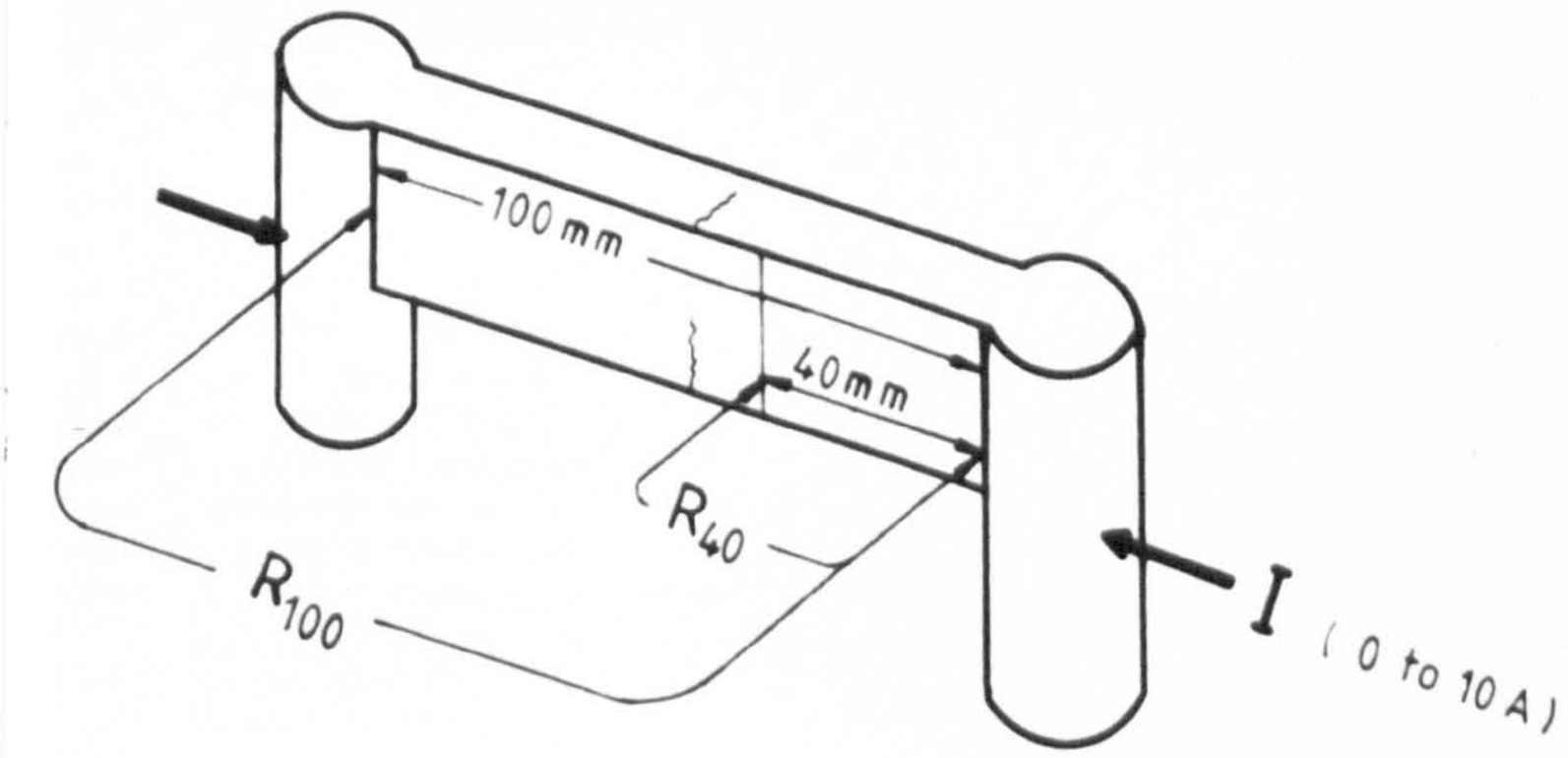

(c)

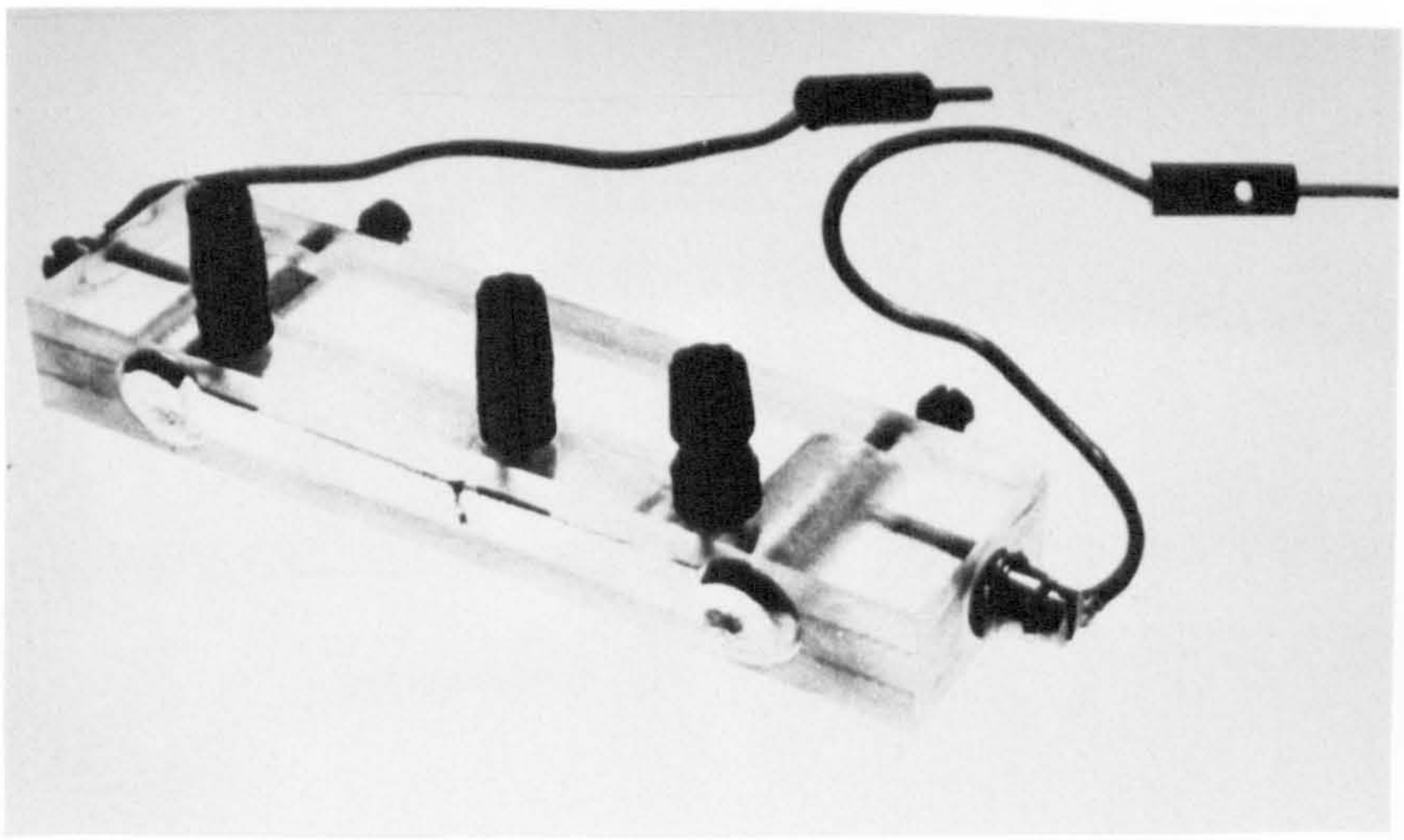

Fig. 3.19 (a) A typical solidification cracking test specimen
(b) The schematic layout for resistance measurements
(c) The milled casting in a perspex holder used for resistance measurements (Shin, 1981).

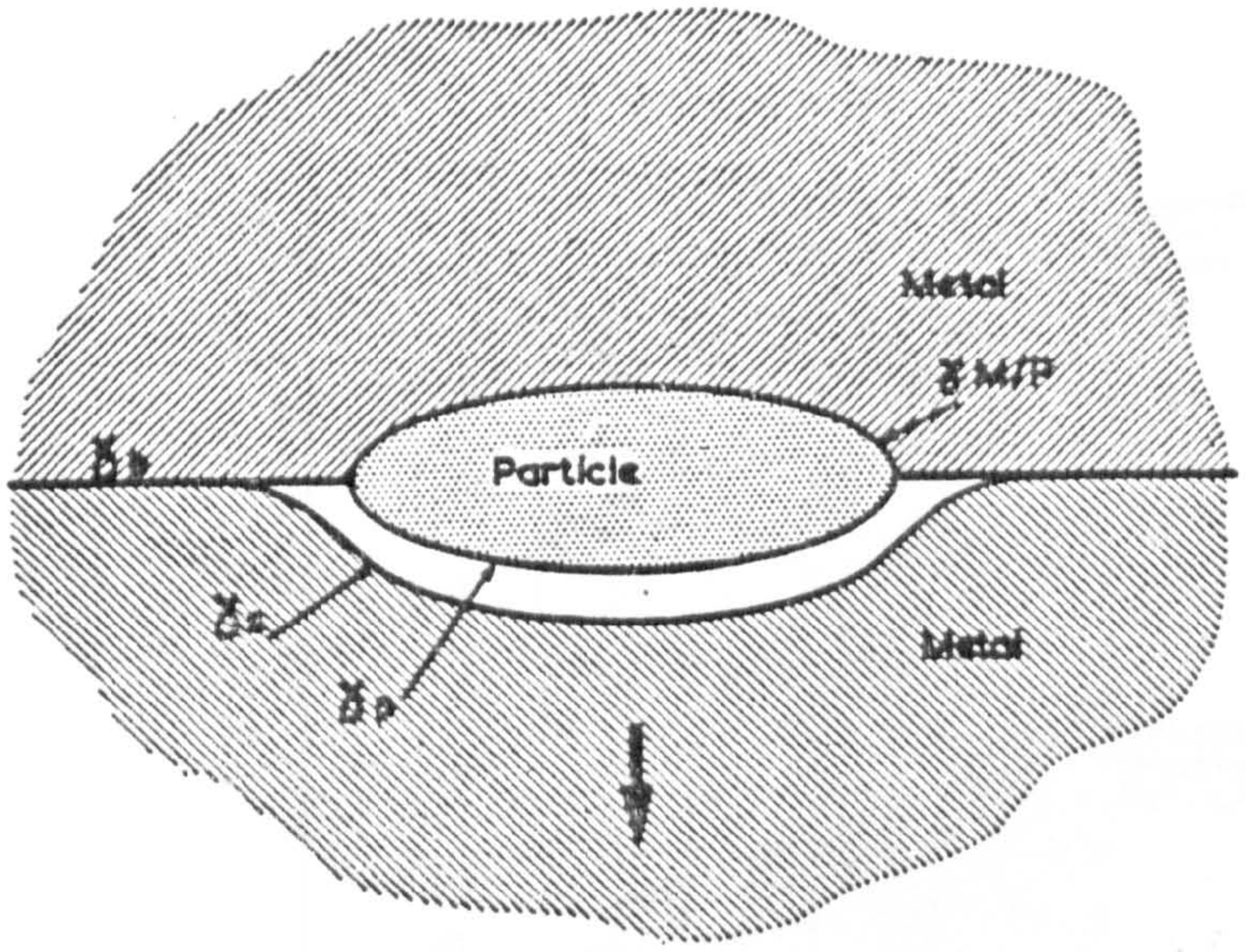

Fig. 3.20 Schematic diagram of a partially decohered particle at a grain boundary (Hondros and McLean, 1976).

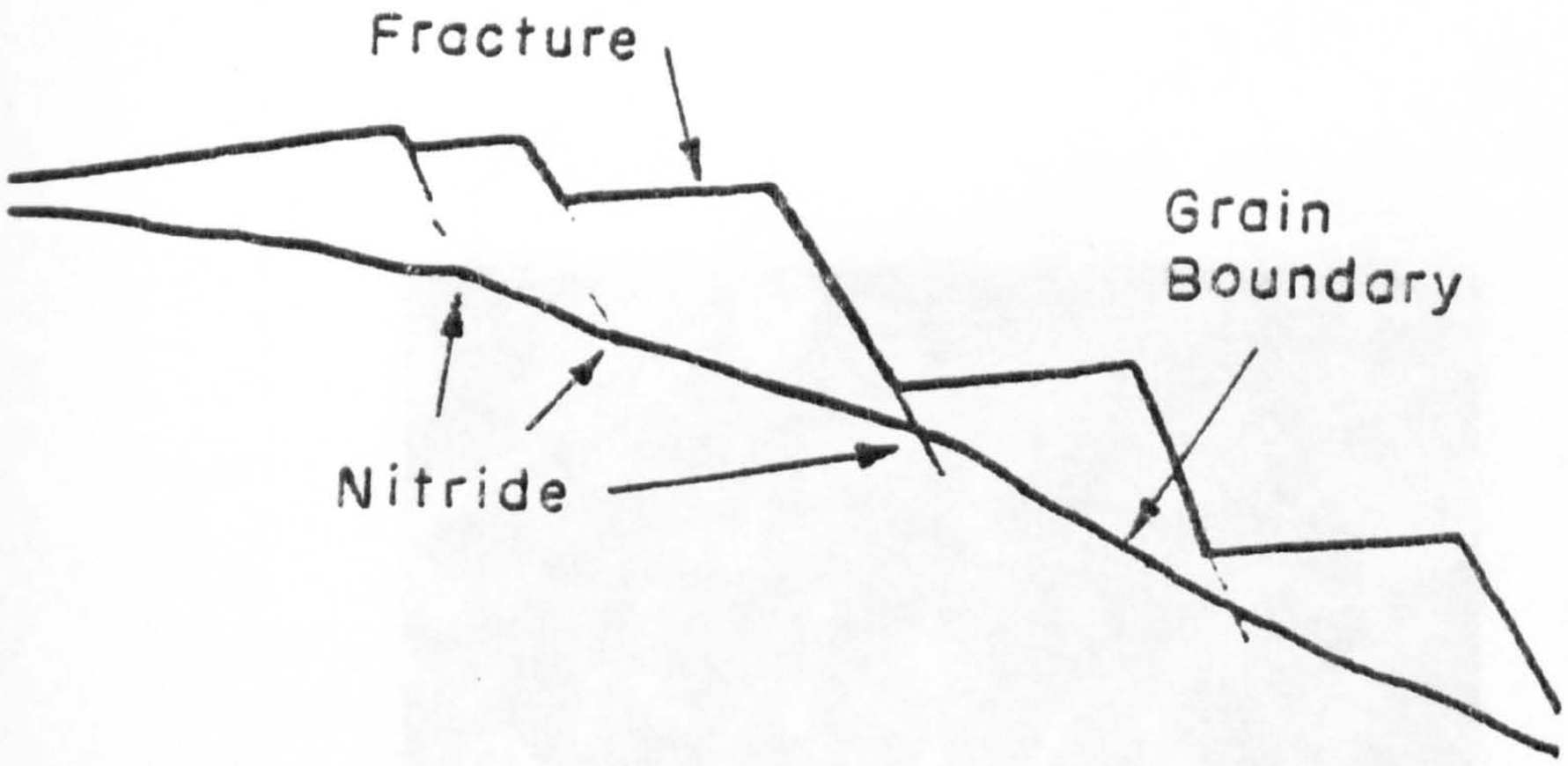

Fig. 3.21 The mechanism proposed by Lorig (1952) for the relation between the intergranular fracture path and the AlN embrittled grain boundary.

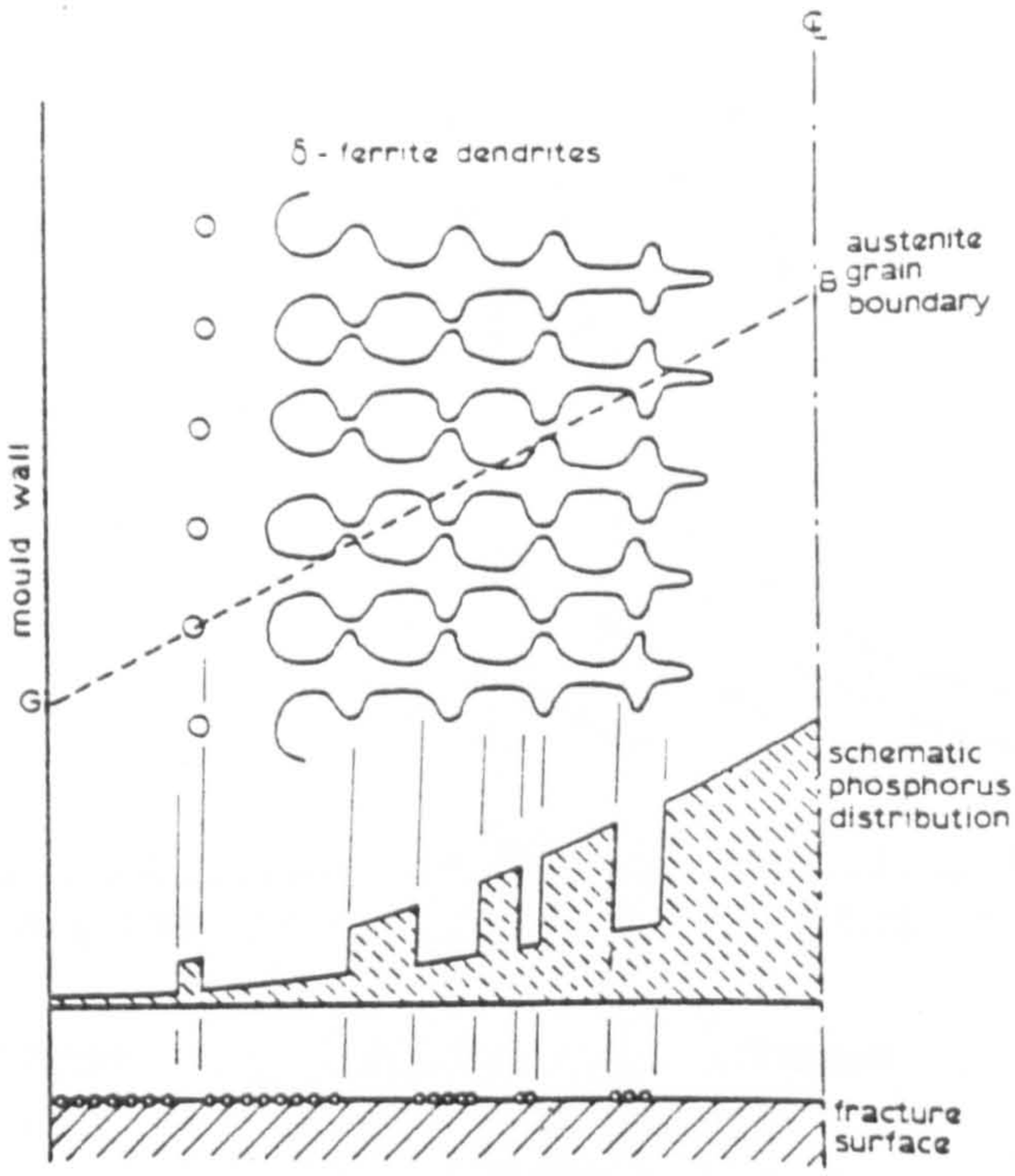

Fig. 3.22 Schematic diagram illustrating the distribution of the phosphide film and MnS precipitates in an overheated casting. At the surface of the casting, intergranular fracture was induced by grain boundary MnS, whilst at the centre failure resulted from an almost continuous film of FeP (not Fe_3P) (Baker and Harrison, 1975).

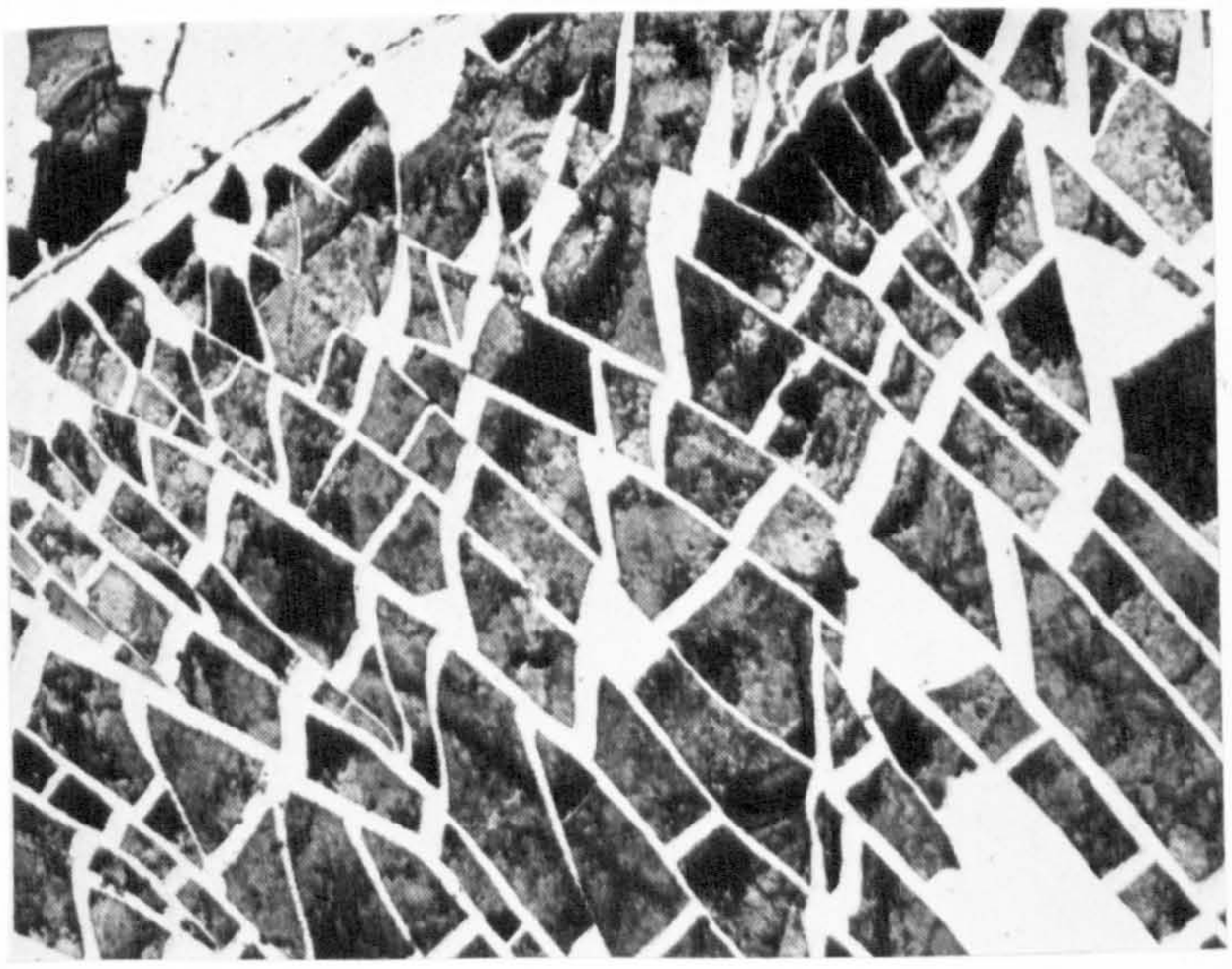

Fig. 3.23 Transmission electron micrograph of NbC plates extracted from the intergranular fracture surface of a 0.22C-0.75Mn steel casting containing 0.07%Nb (Hannerz et al, 1968).

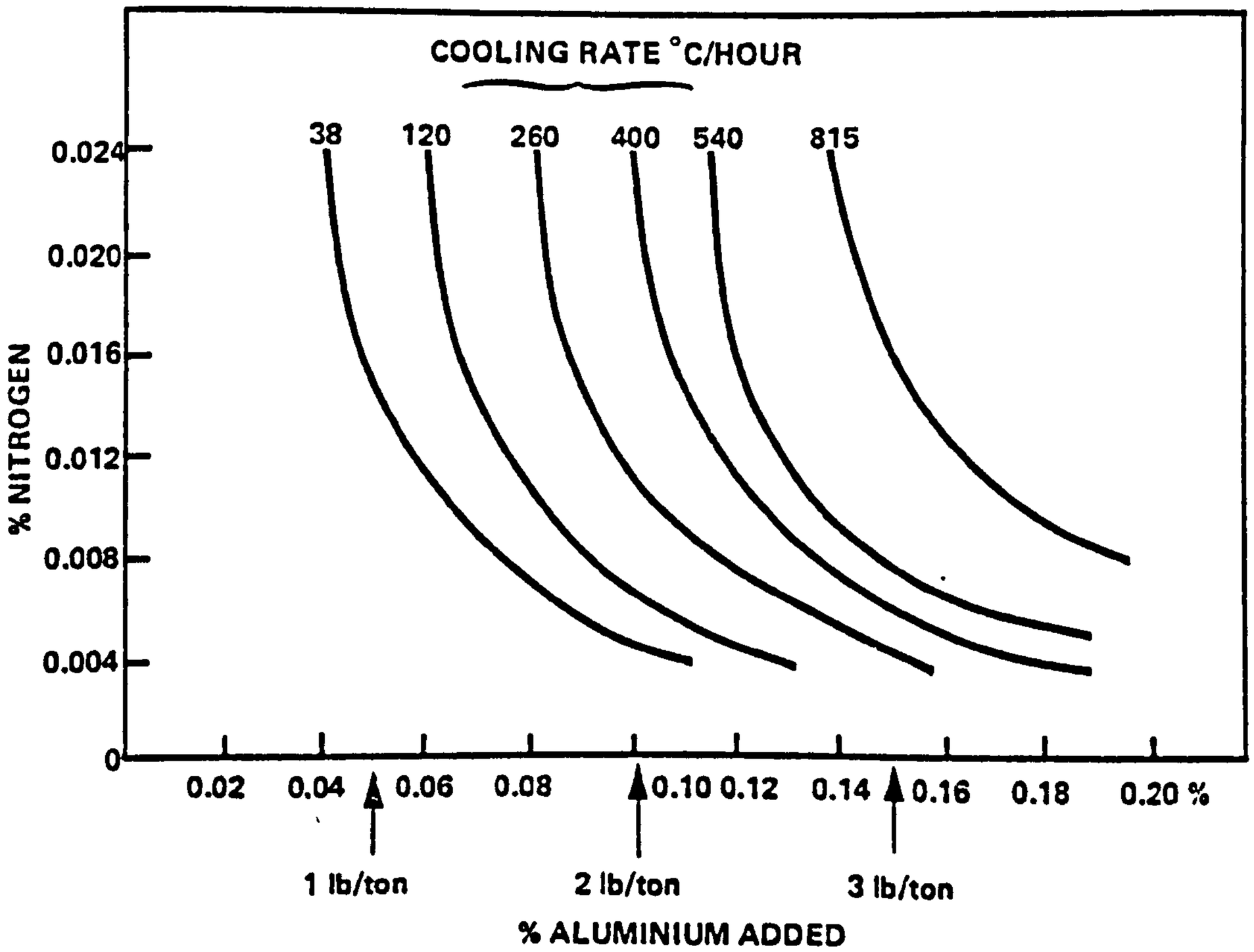

Fig. 4.1 Graph showing the effect of aluminium content, nitrogen content and cooling rate on the susceptibility for I.F. Compositions above and to the right of each curve are likely to be susceptible (Lorig and Elsea, 1947).

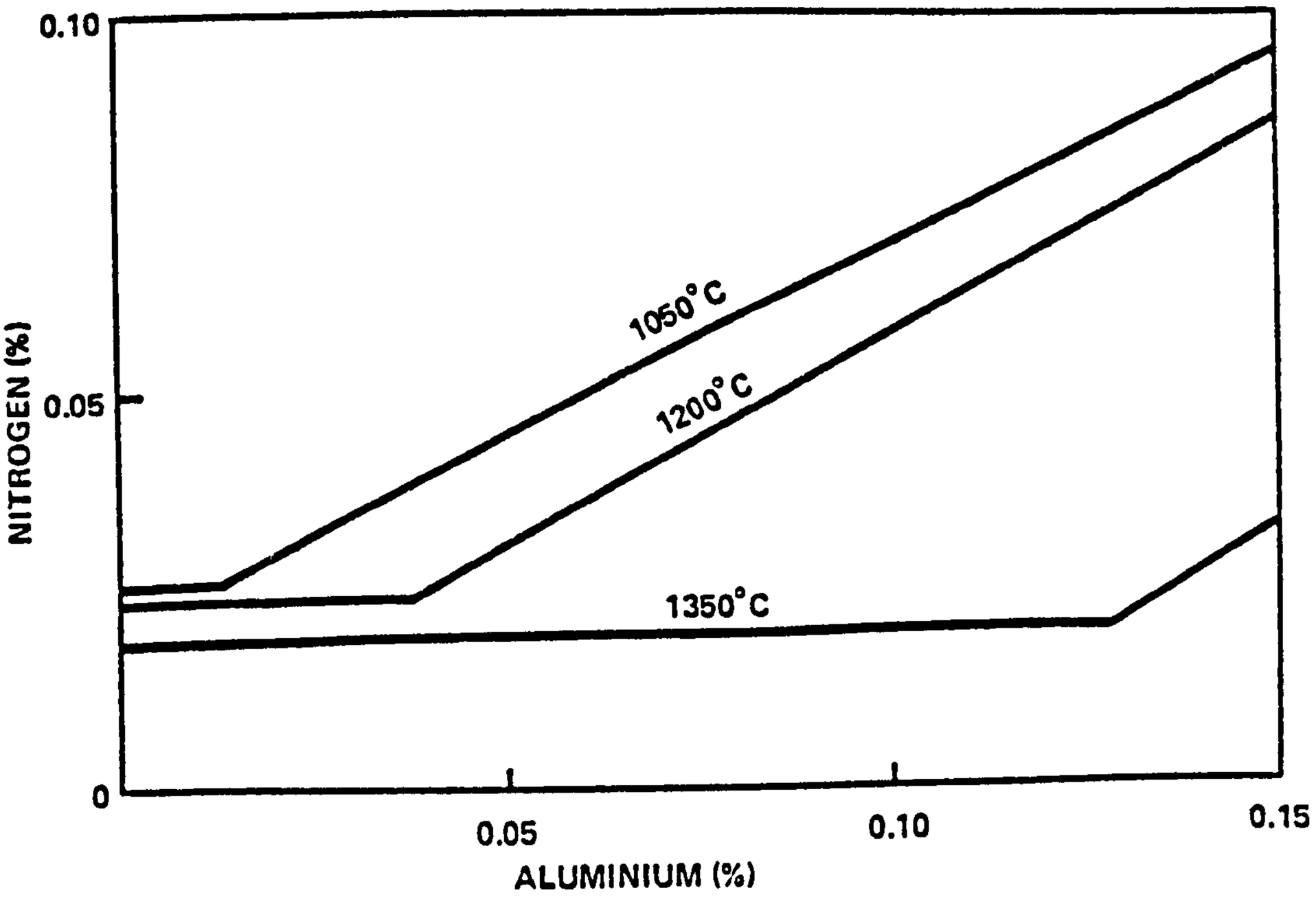

Fig. 4.2 The nitrogen content of aluminium-killed steels equilibrated with nitrogen gas at 1050°C, 1200°C and 1350°C. The position of the change in slope denotes the formation of AlN (Darken et al, 1951).

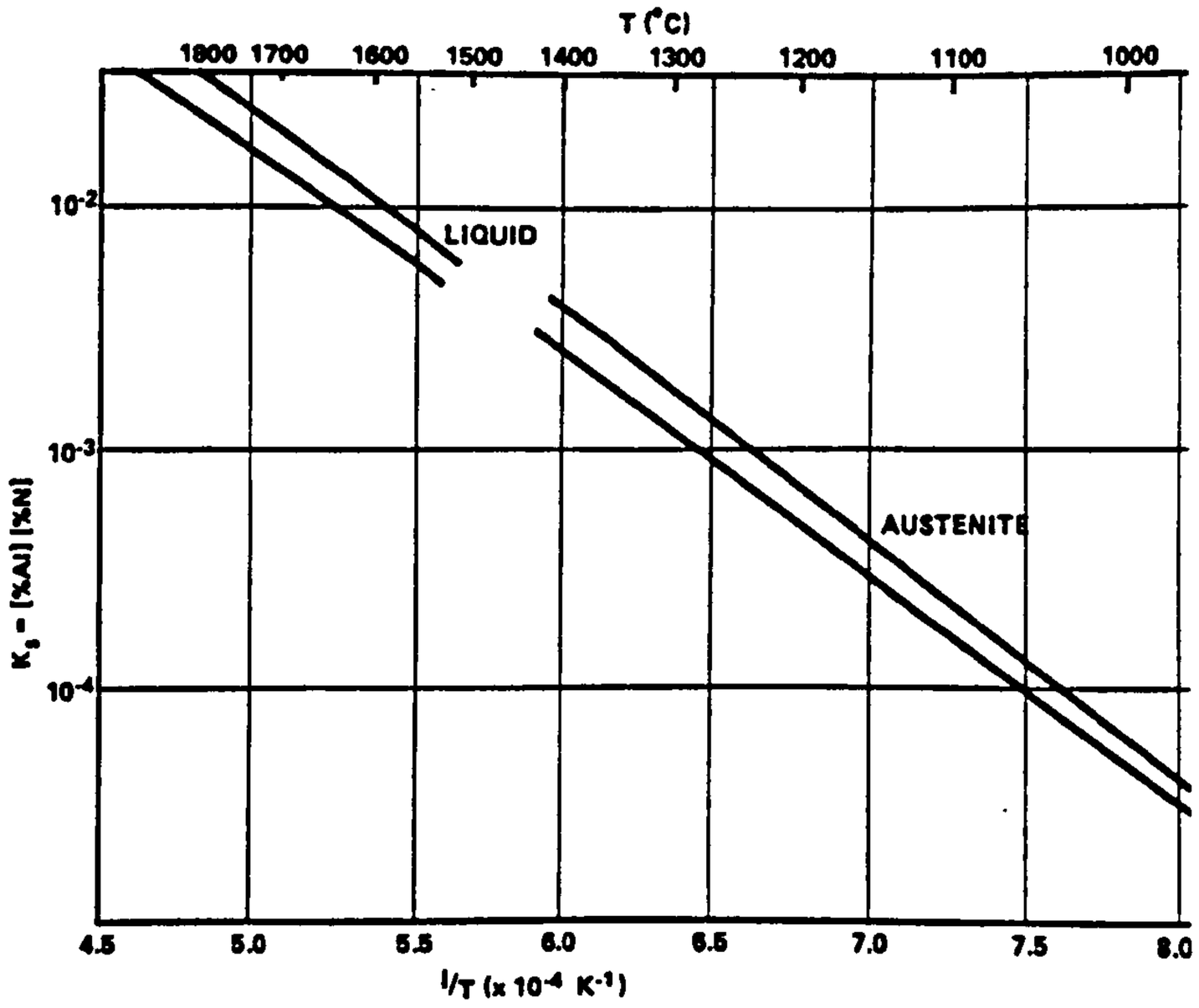

Fig. 4.3 The variation of AlN solubility product with temperature for liquid steel and austenite. The upper lines are for pure iron, and the lower lines for GS-40 steel. GS-60 grade steel (0.40C, 0.80Mn) lies between the two (Honer and Baliktay, 1978a).

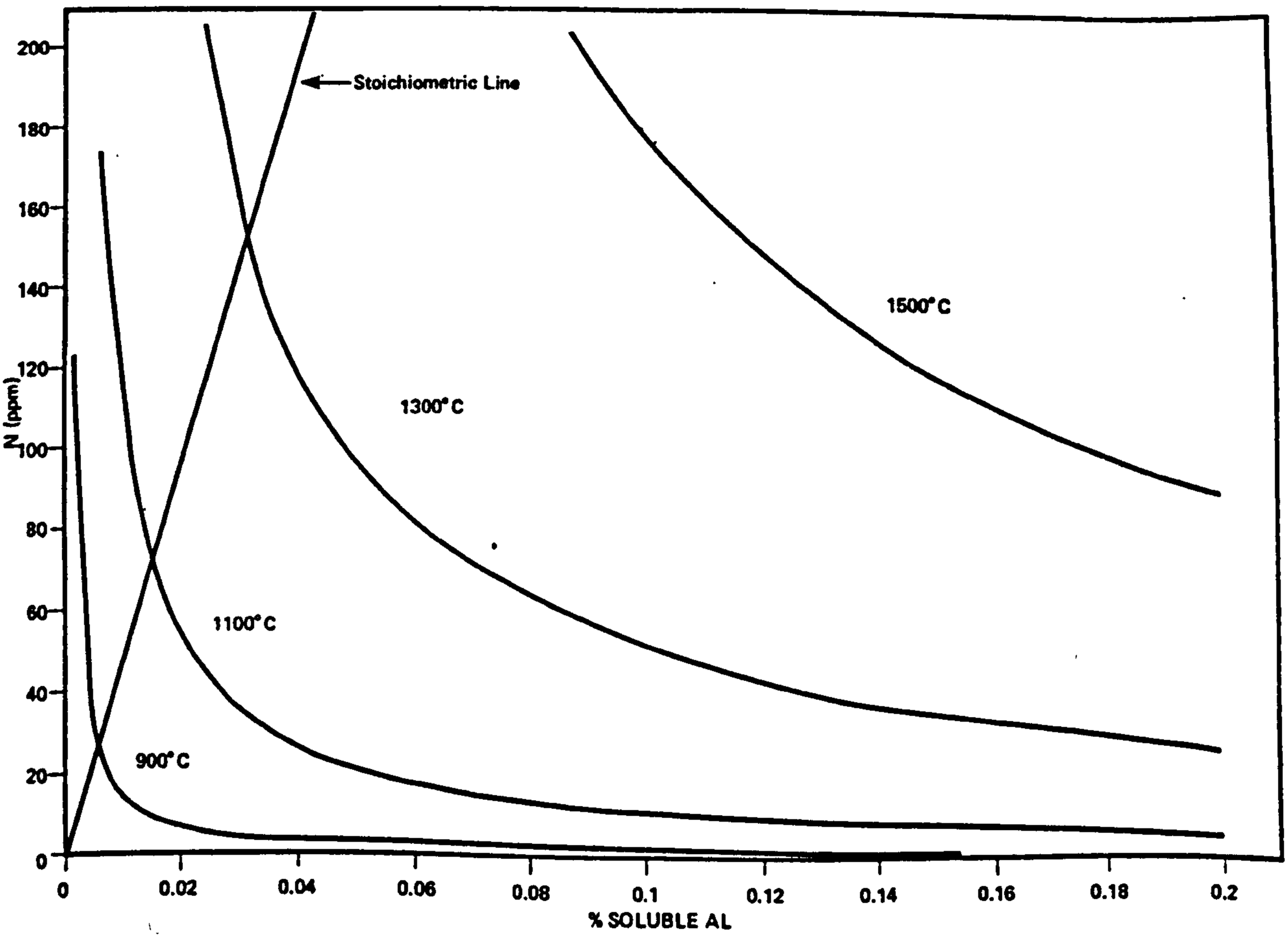

Fig. 4.4 The solubility of Al and N in austenite at different temperatures. Plotted using the data of Gladman and Pickering (1967).

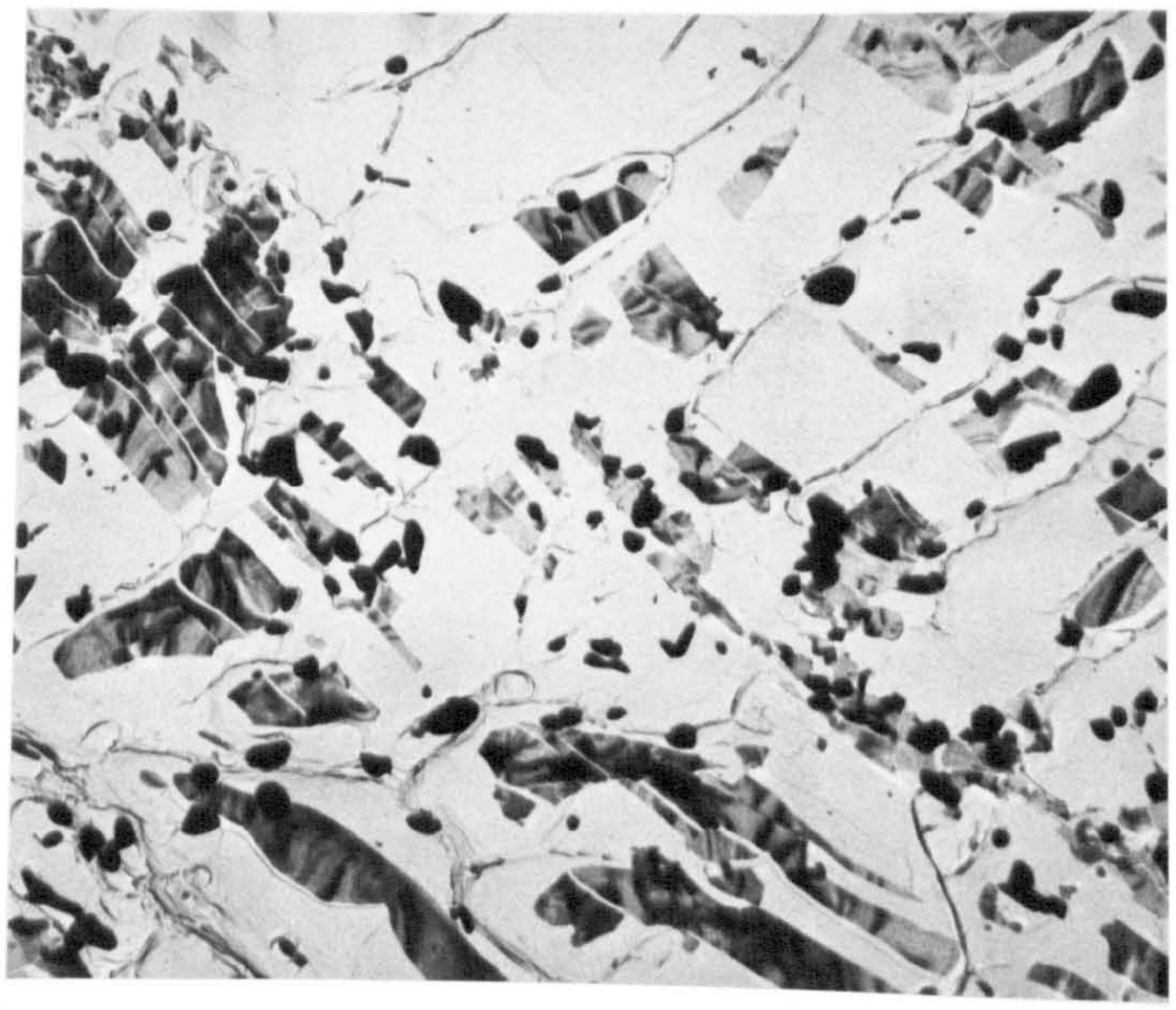

Fig. 4.5 Transmission electron micrograph showing plate-like precipitates of AlN extracted from the intergranular fracture surface of a 0.26C-1.50Mn steel X3500 (Wright, 1962).

Fig. 4.6 Transmission, electron micrograph showing the dendritic form of AlN X7000 (Wright, 1962).

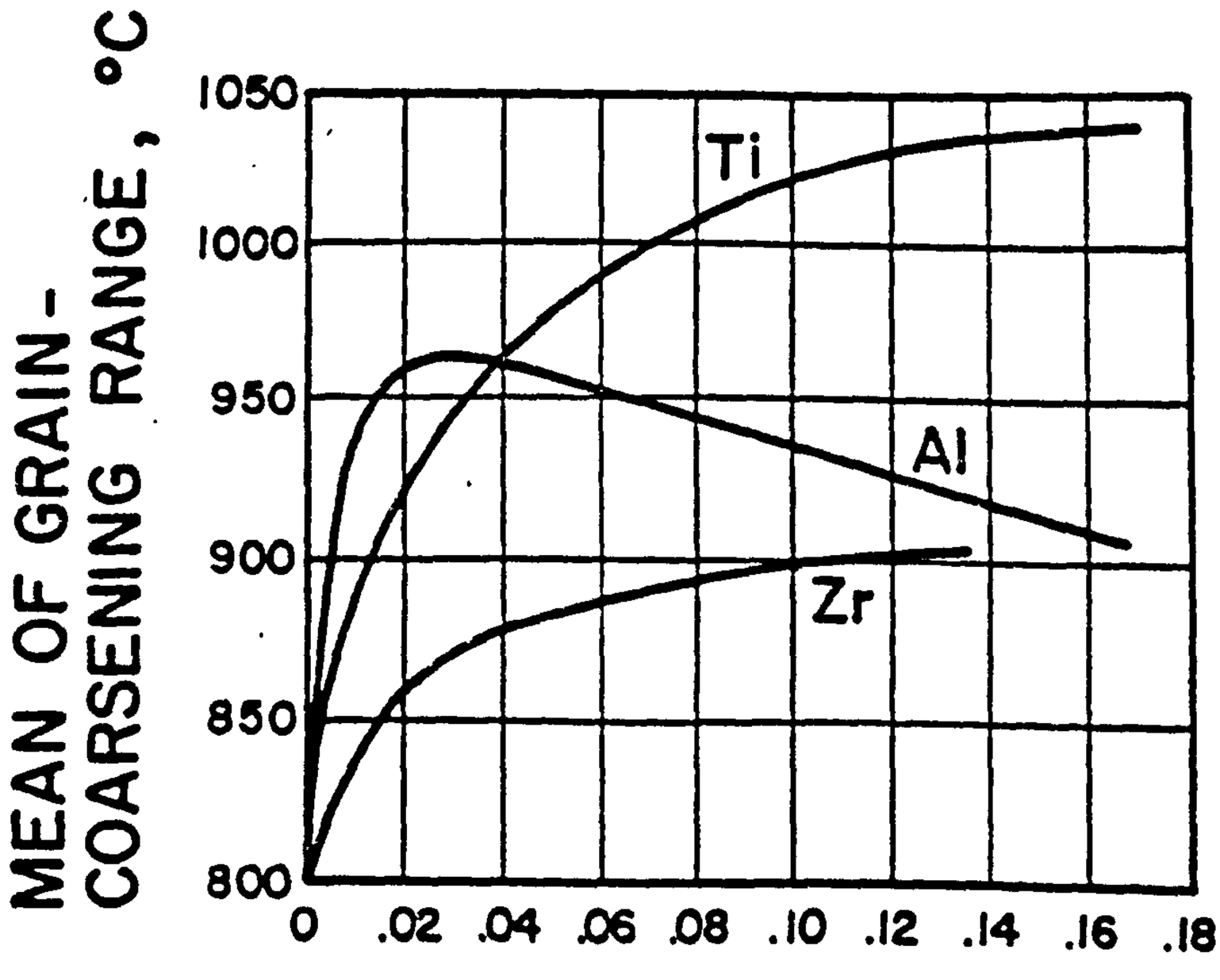

Fig. 4.7 The effect of titanium, aluminium and zirconium on the grain coarsening temperature of En5 steel (0.25-0.35%C) (Halley, 1946).

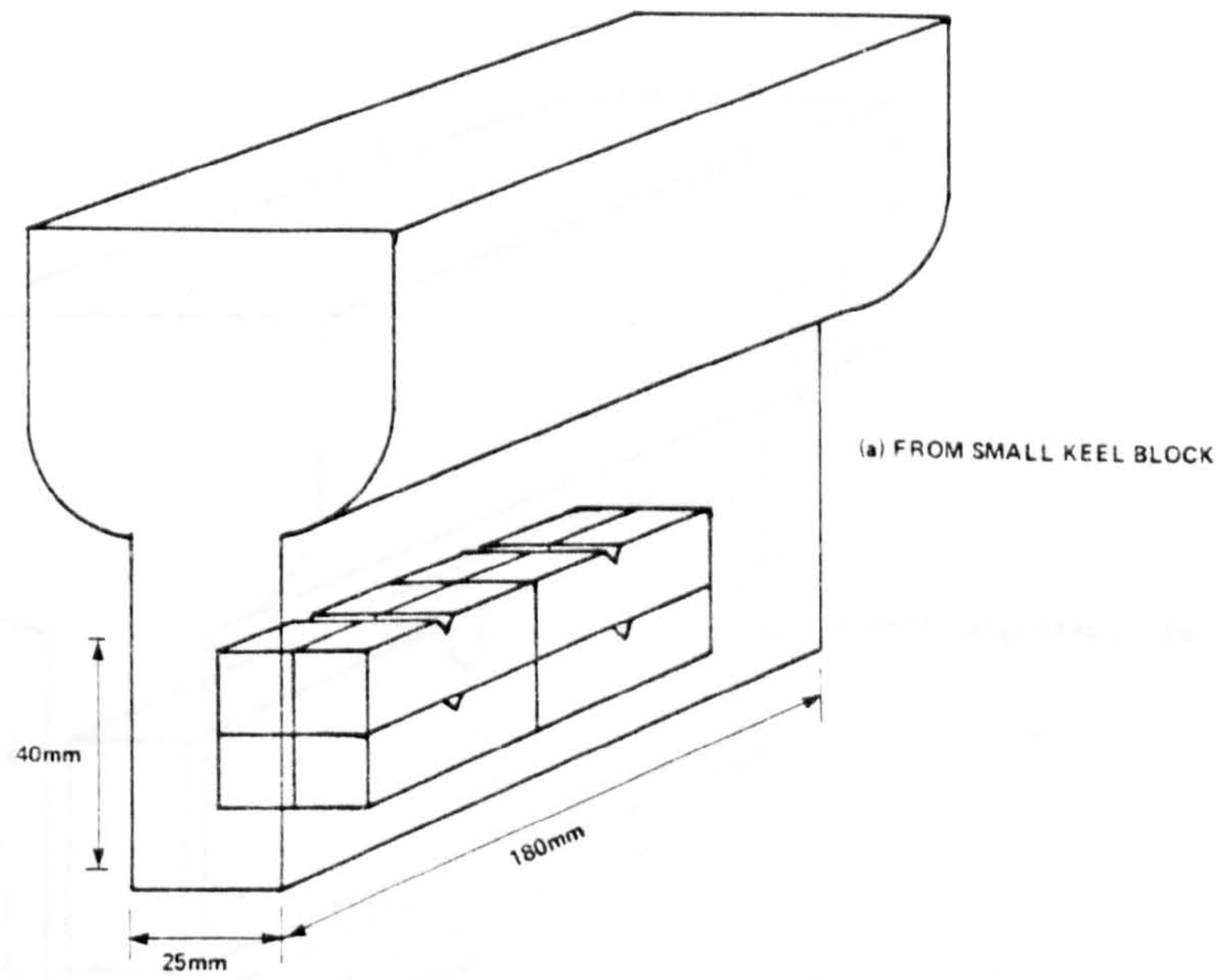

(a) FROM SMALL KEEL BLOCK

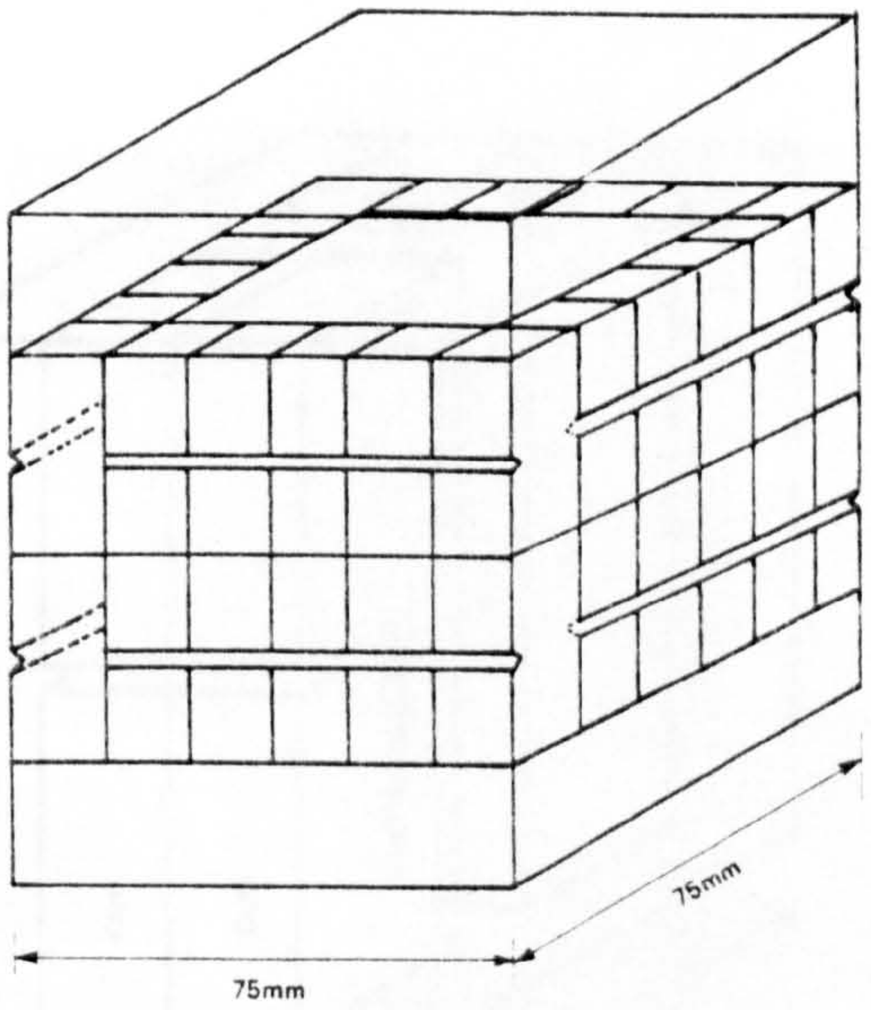

(b) FROM 75mm SQUARE CASTINGS

Fig. 5.1 The position of samples taken for impact testing from (a) the small keel block castings and (b) the 75mm square castings.

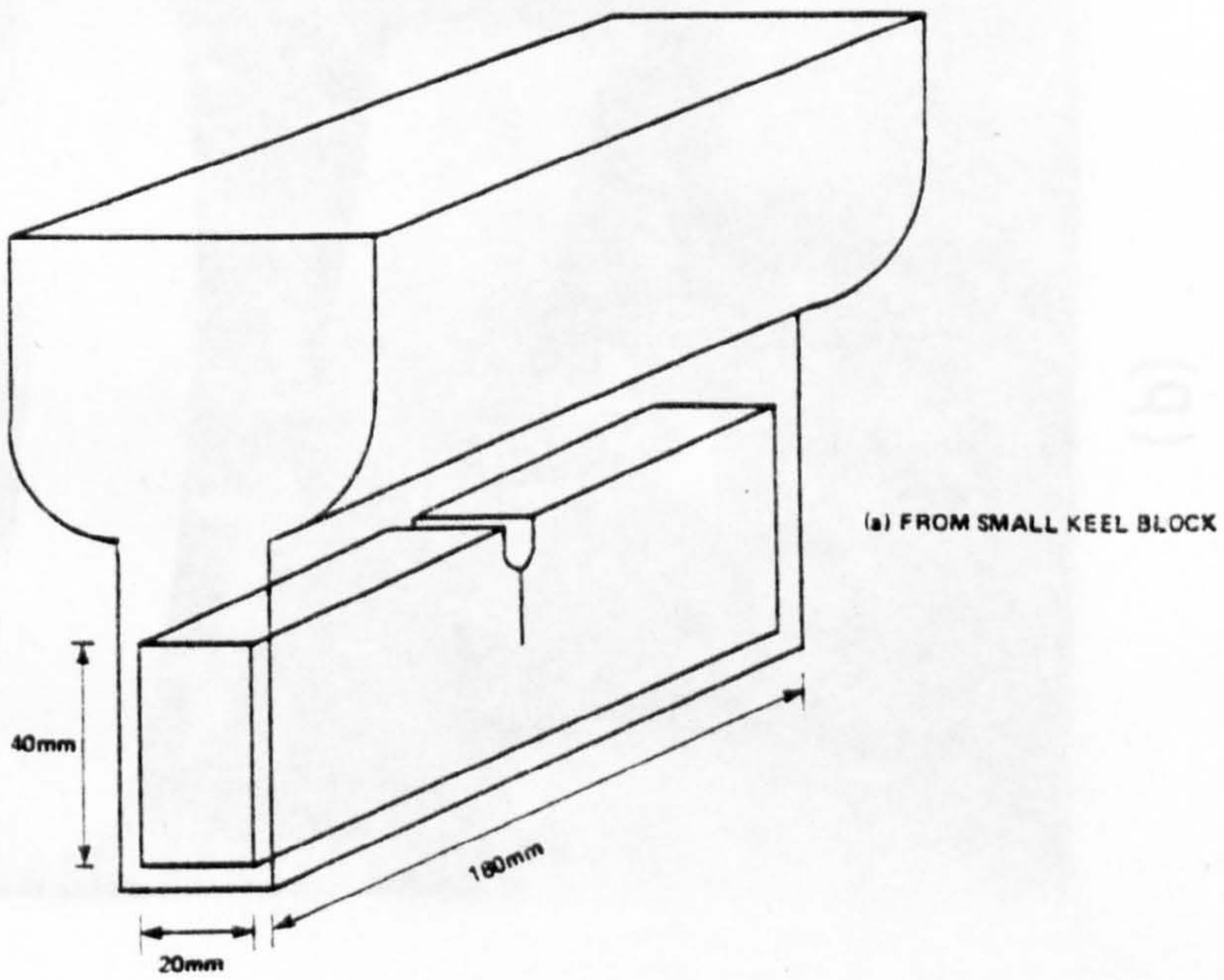

(a) FROM SMALL KEEL BLOCK

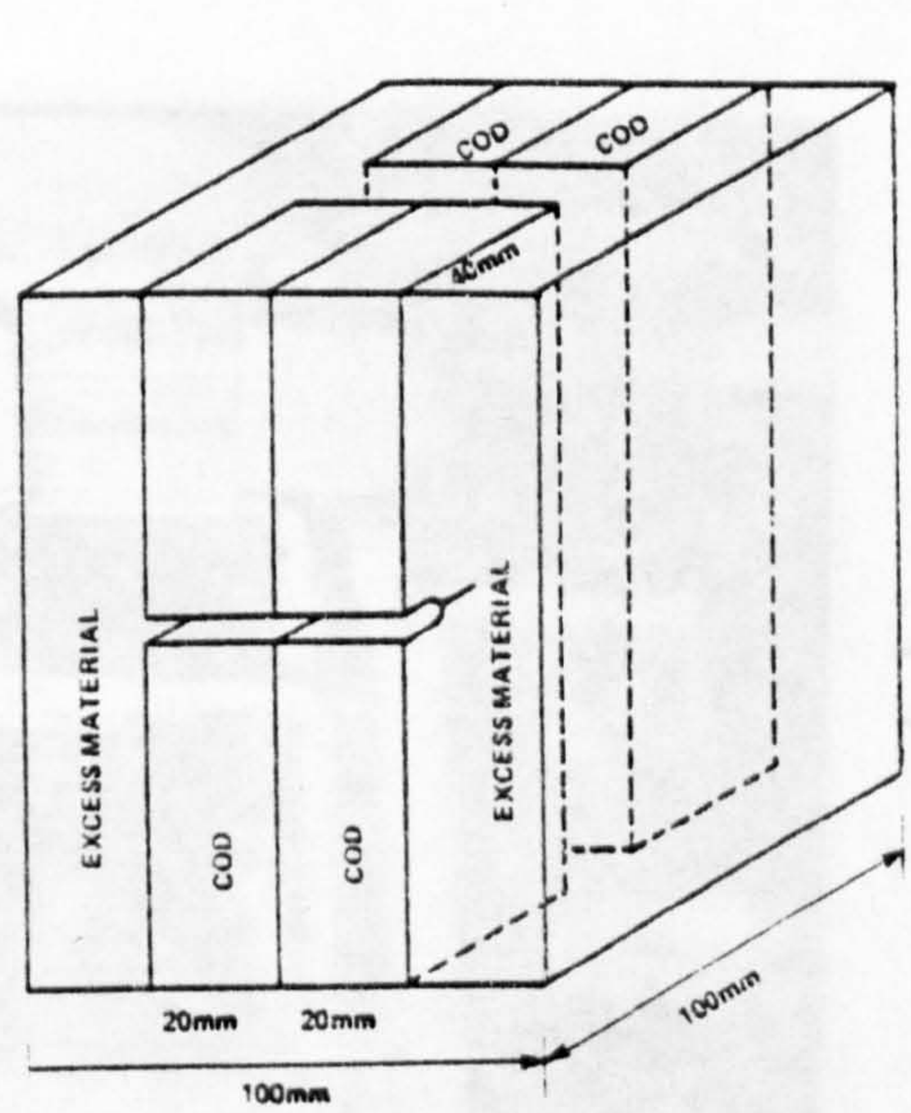

(b) FROM 100mm SQUARE CASTINGS

Fig. 5.2 The position of samples taken for fracture toughness testing from (a) the small keel block castings and (b) the 100mm square castings.

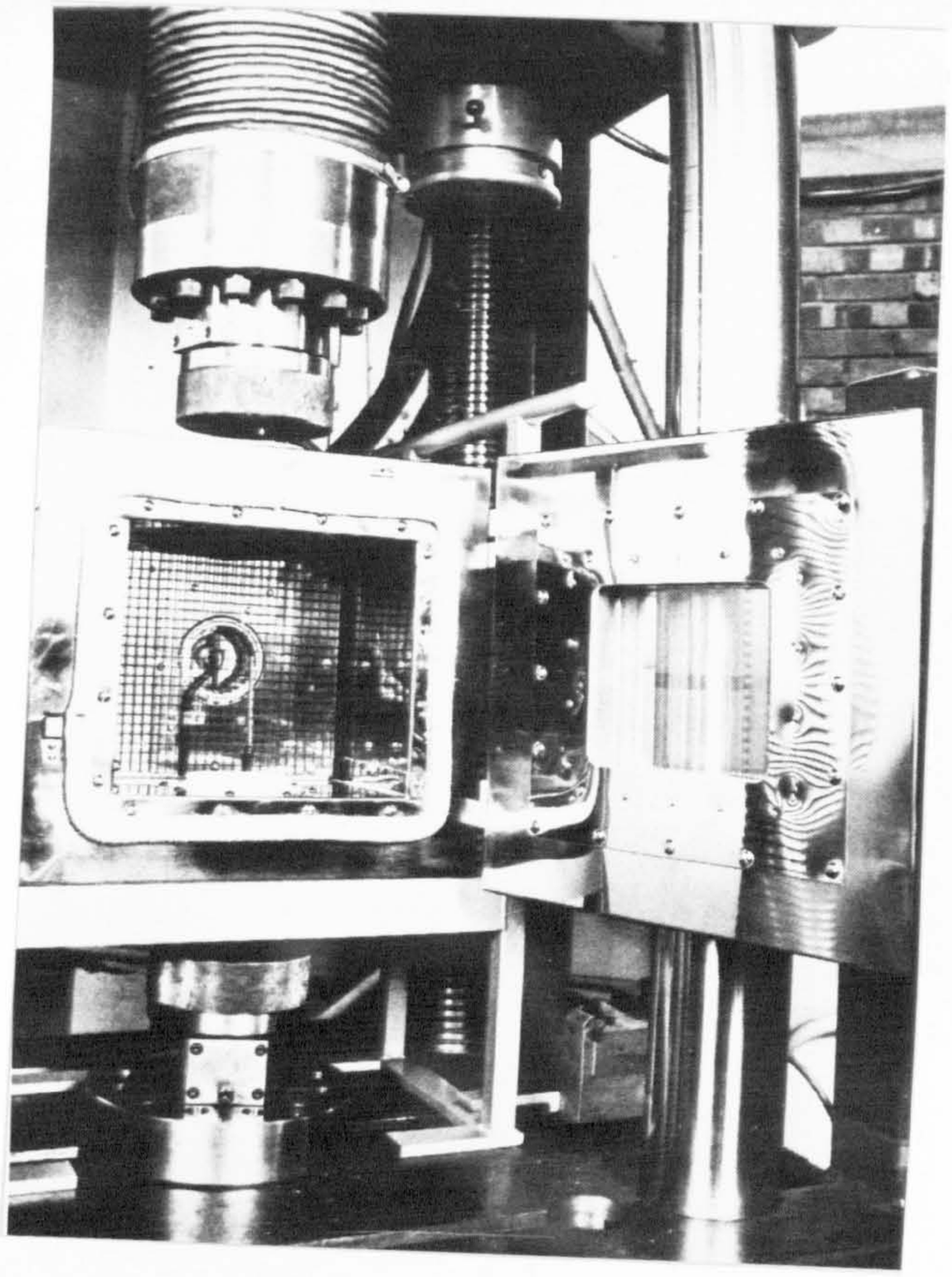

(a)

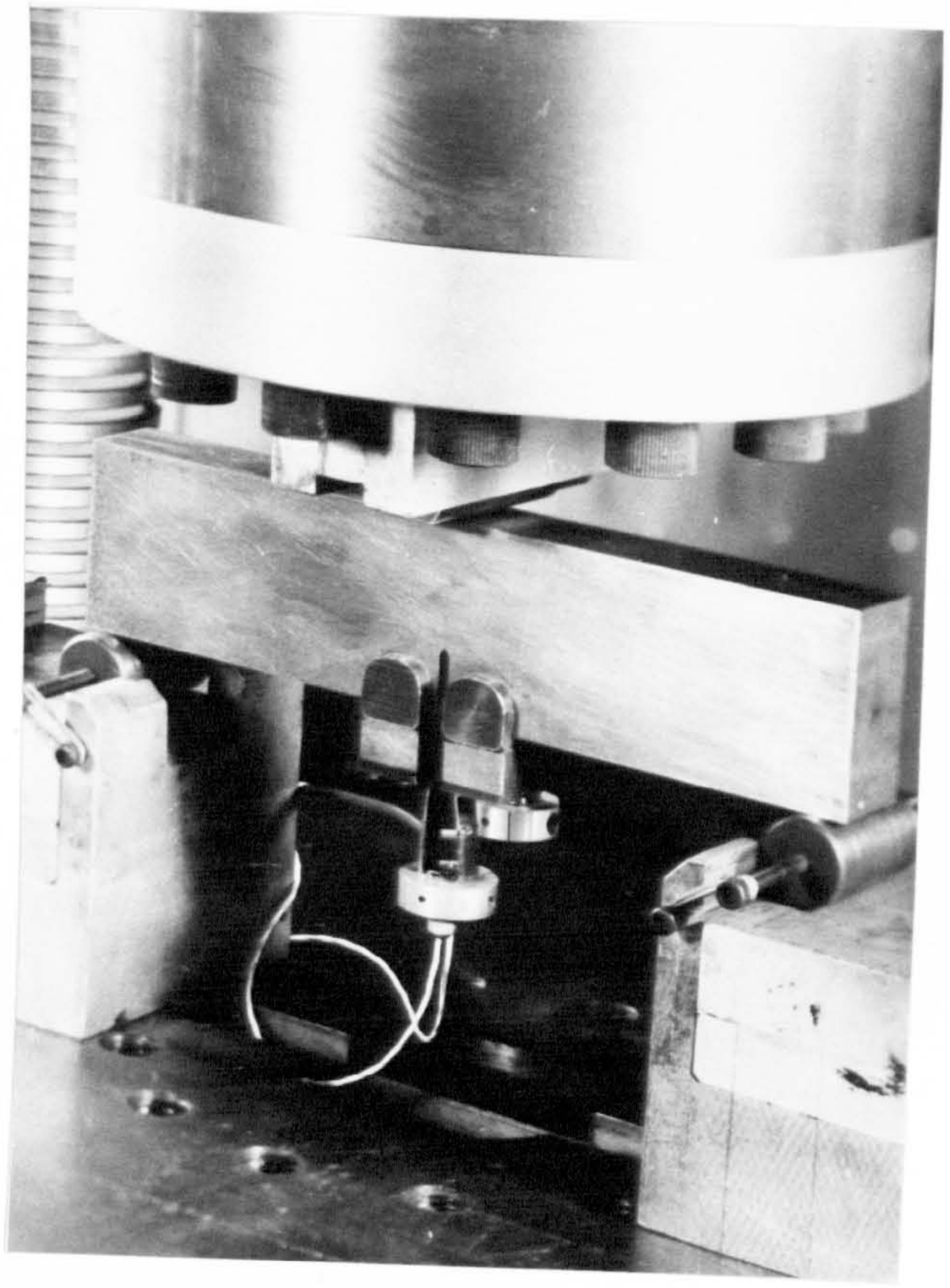

(b)

Fig. 5.3(a) The Dartec servo-hydraulic testing machine fitted with the environmental chamber.

(b) Details of the double clip gauge arrangement on a COD sample.

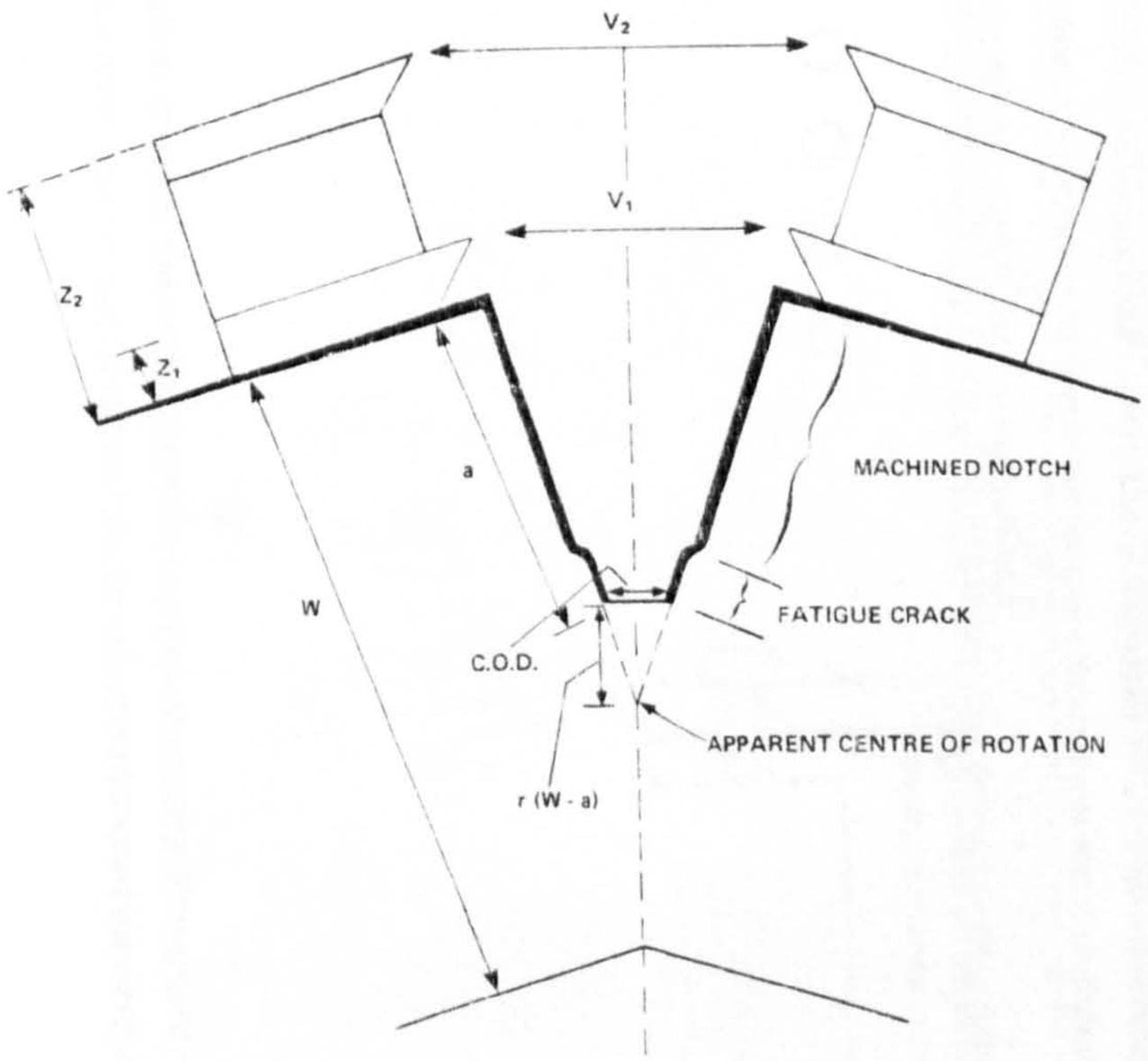

Fig. 5.4 Idealised notch profile during the bend testing of COD samples.

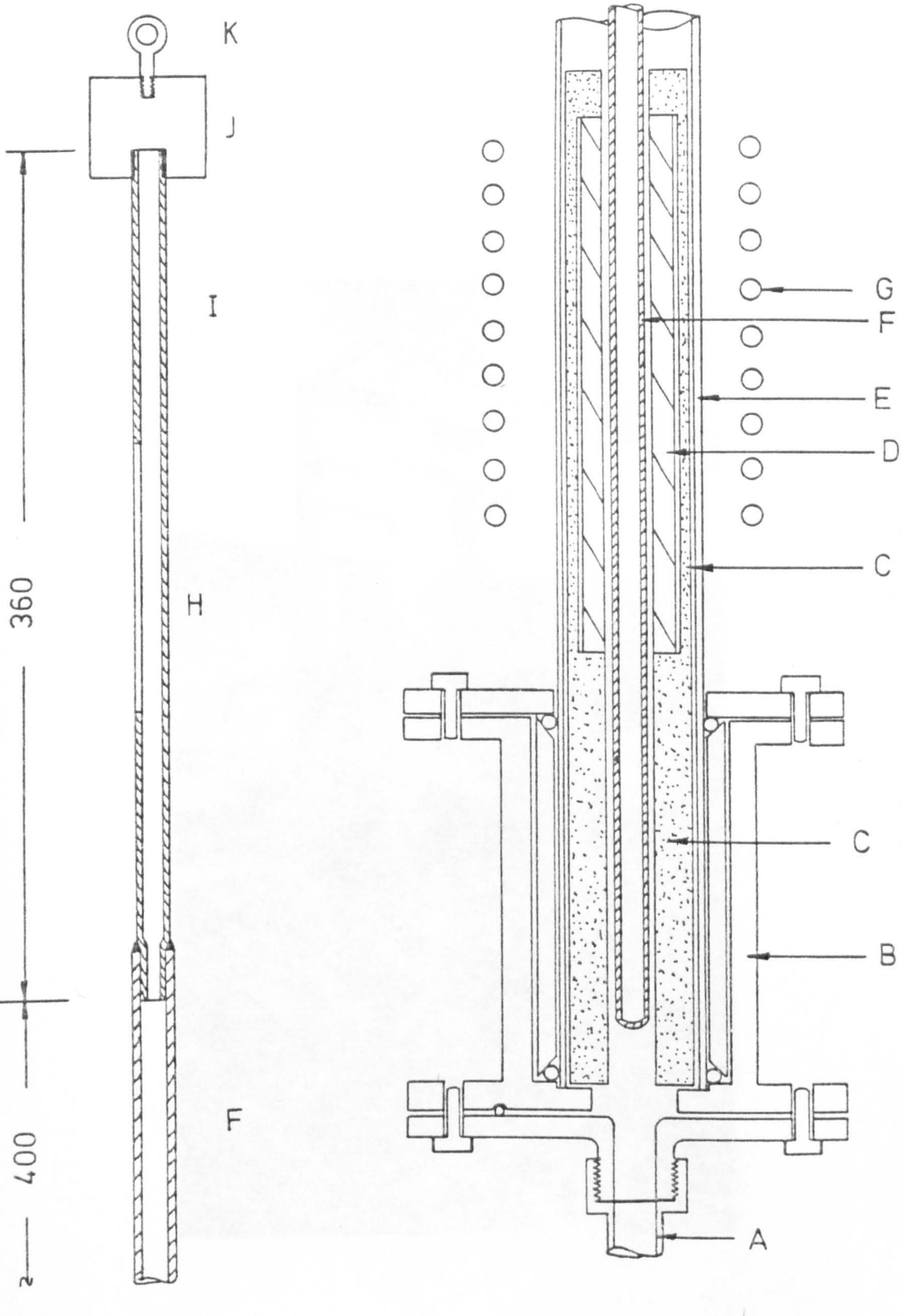

Fig. 5.5 Schematic view of the specimen assembly and the directional solidification apparatus.

Key:
- A Gas and sample exit port
- B Lower service head
- C Alumina tube
- D Graphite susceptor
- E Silica tube
- F Sample tube (alumina)
- G Heating coils
- H Gas and thermocouple access port
- I Stainless steel tube
- J Brass stopper block
- K Hook attachment for drive unit.

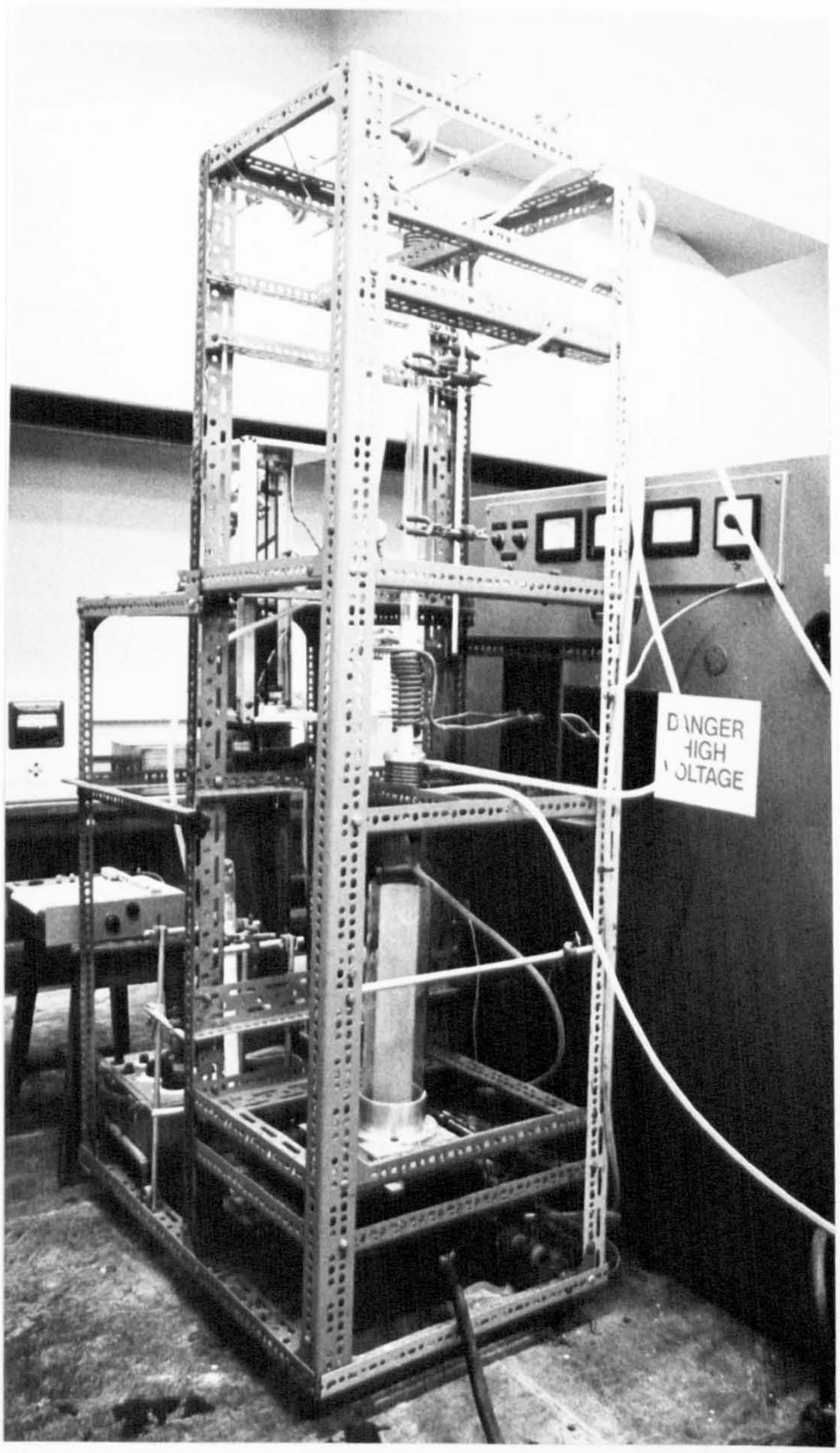

Fig. 5.6 Overall view of the directional solidification apparatus.

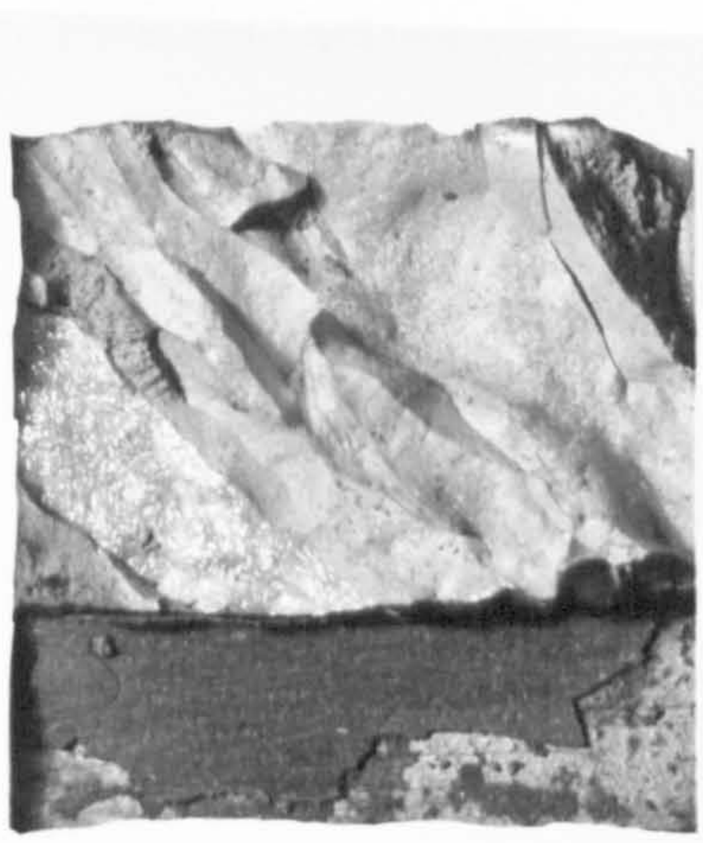

Fig. 6.1 A typical room temperature intergranular fracture surface. The sample was taken from cast 4176 and broken by slow three-point bending in the quenched and tempered condition. Note how the fracture delineates the columnar grain boundaries of the casting. (X2)

Fig. 6.2 Optical fractograph of an intergranular facet showing the crystallographically orientated surface markings. The bright areas all reflect simultaneously, and the dark linear features can also be seen to occur in parallel 'families'. Surrounding areas have been masked with lacquer. (X50)

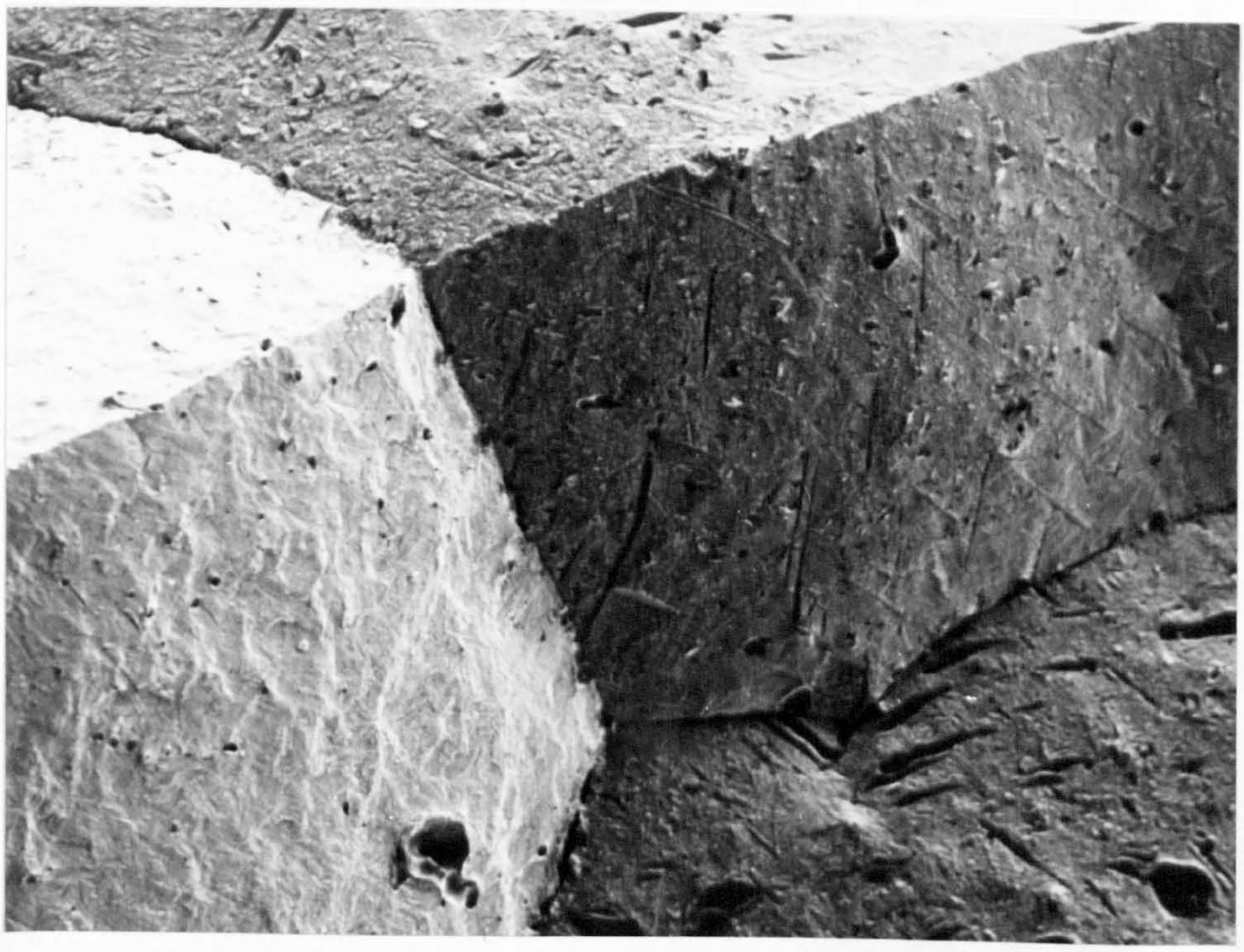

Fig. 6.3 Scanning electron micrograph showing the intersection of several grains on the fracture surface. Macroscopically, the fracture is brittle and follows the columnar grain boundaries. The surface markings are similar to those in Fig. 6.2. (X80)

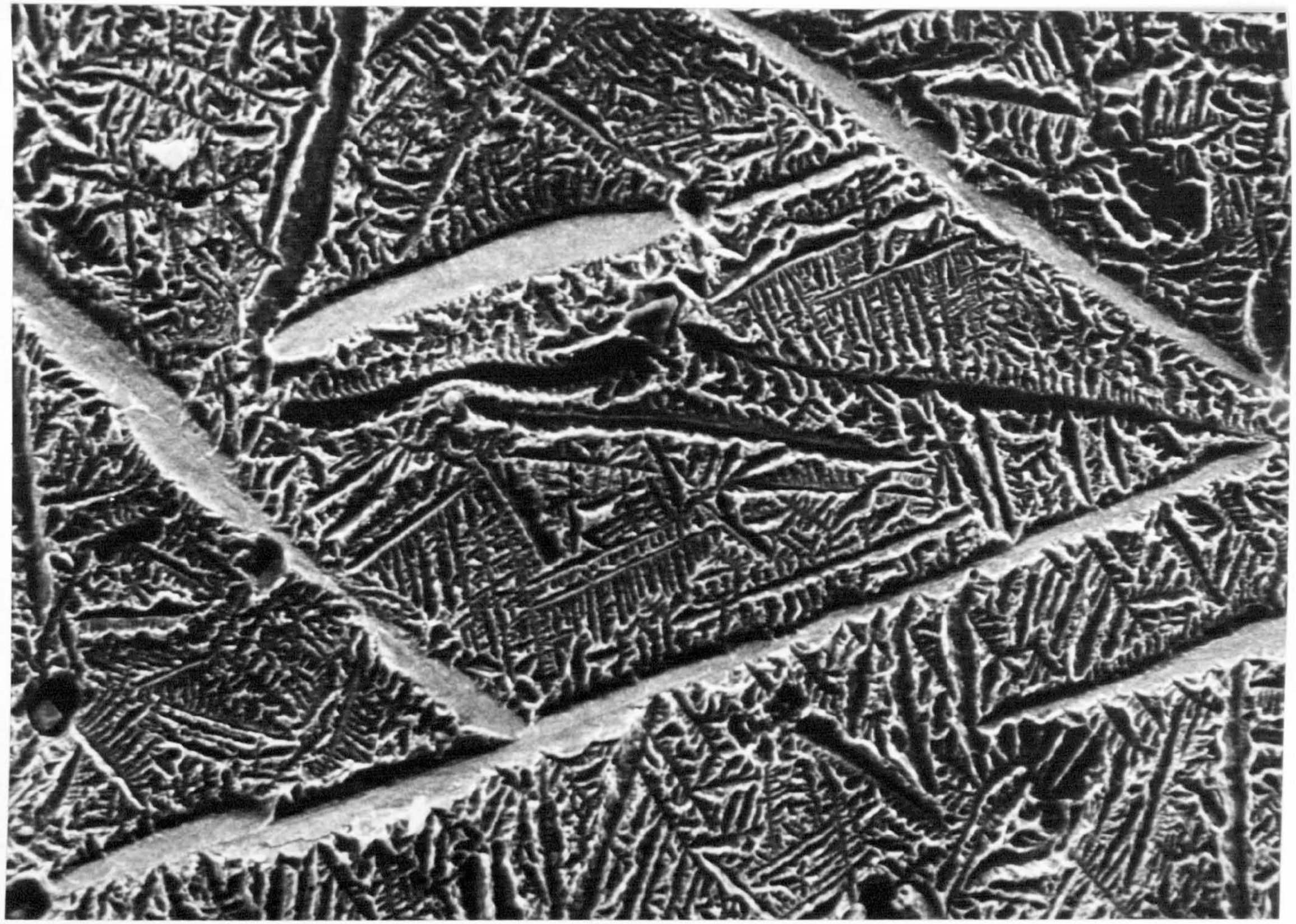

Fig. 6.4 Scanning electron micrograph showing the intergranular fracture surface in more detail. The overall mechanism of fracture is microductile with a fine dendritic appearance. Superimposed on this are the larger plate-like features which lie at specific angles to each other in the grain boundary surface. (X450)

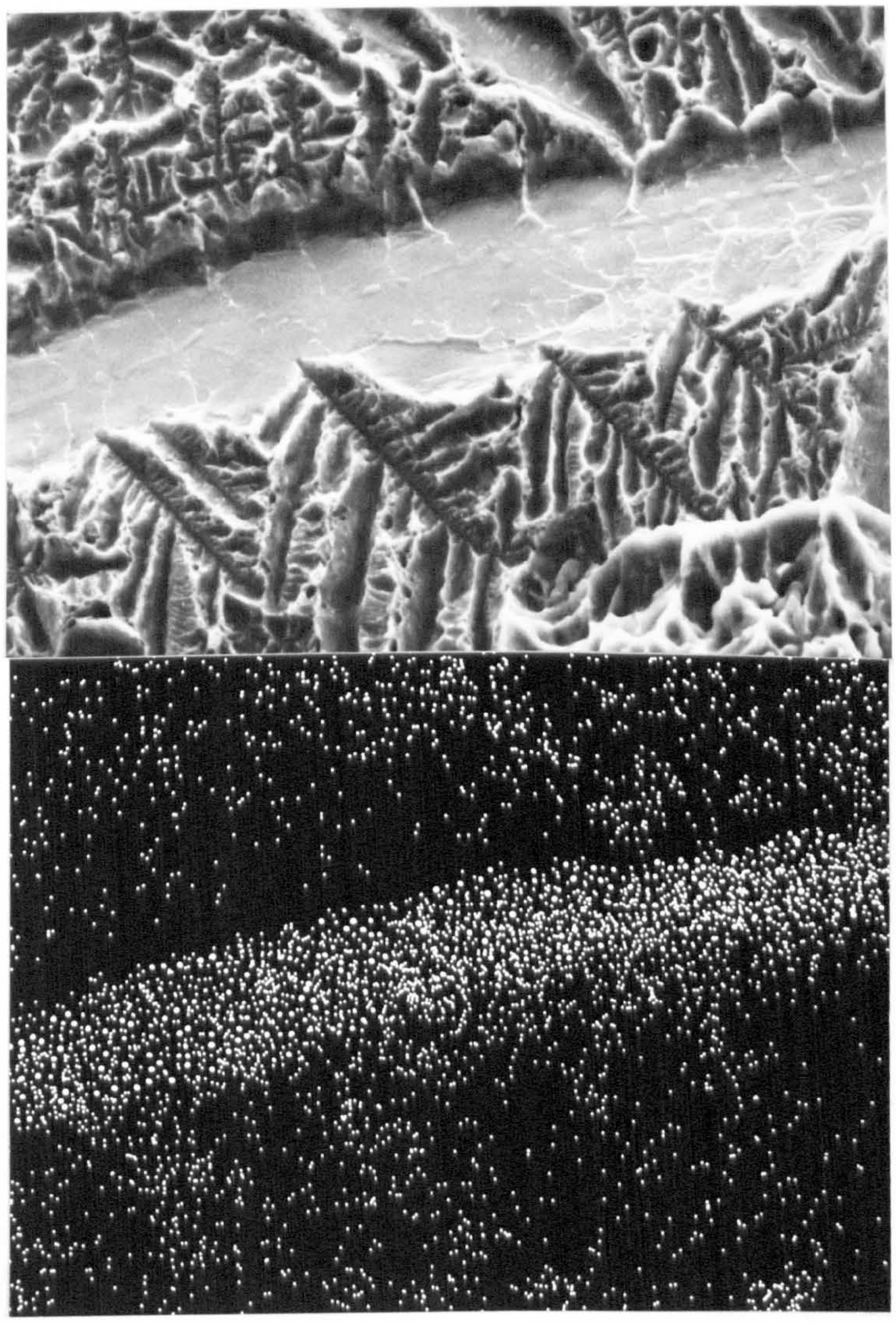

Fig. 6.5 Plate-like feature in more detail, with a corresponding X-ray map for AlKα radiation. (X1900)

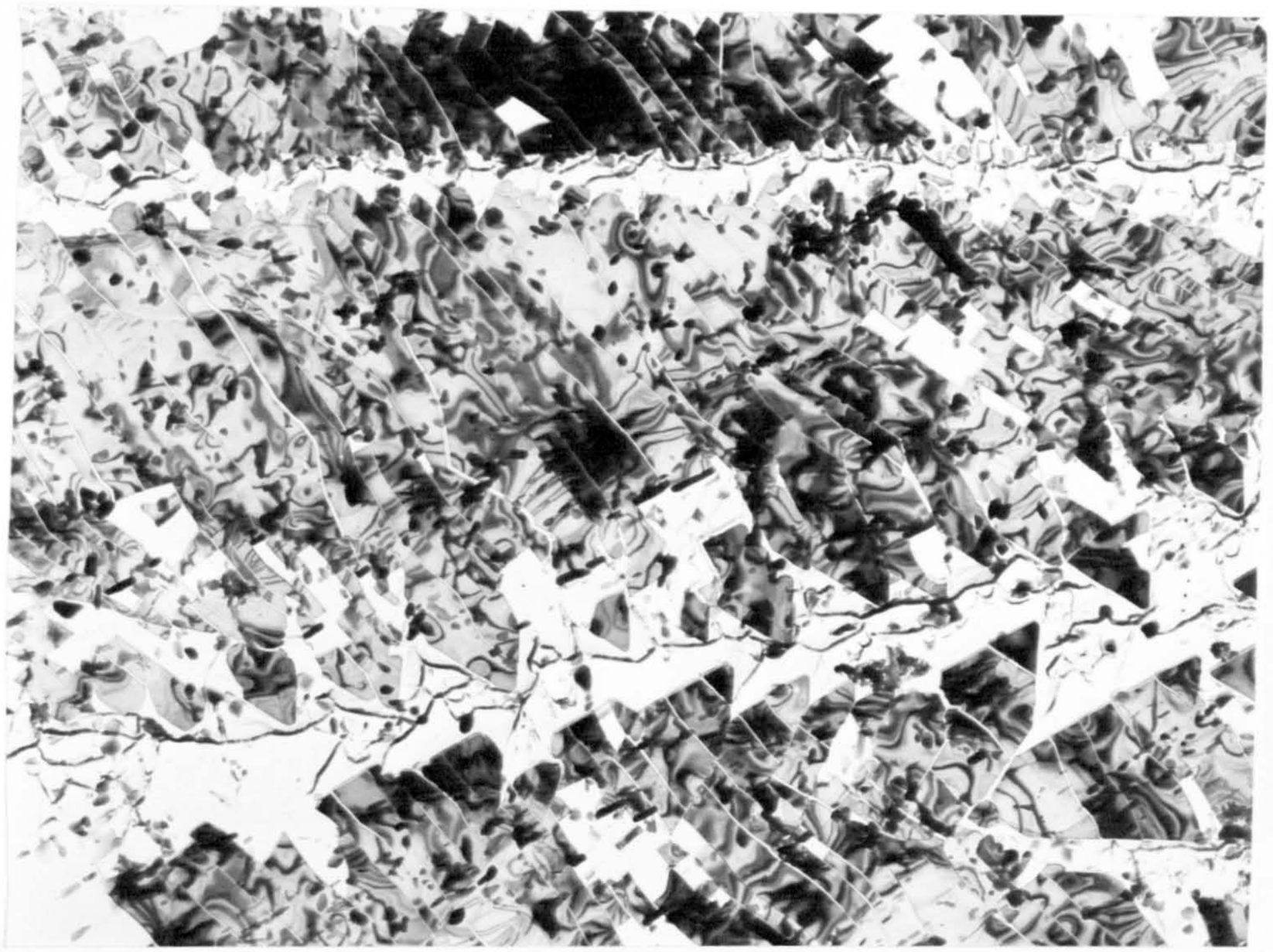

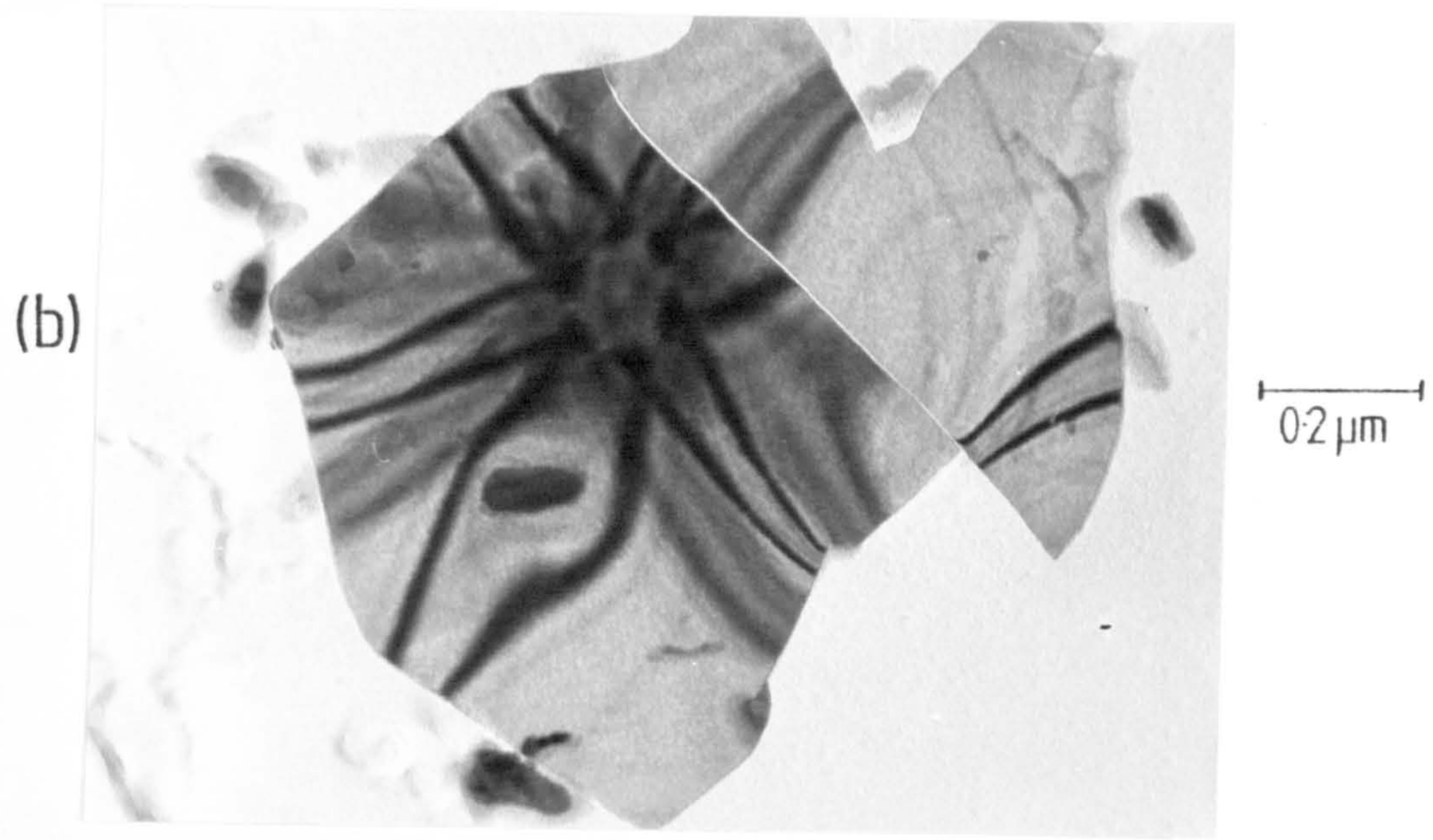

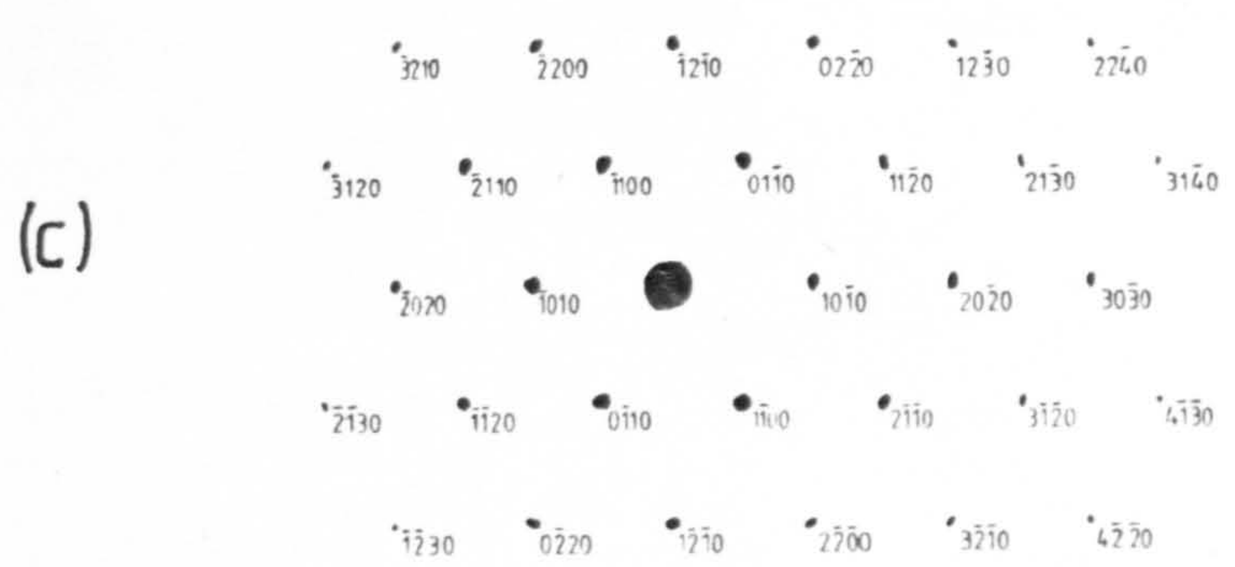

Fig. 6.6 Transmission electron micrographs of carbon extraction replicas taken from the intergranular fracture surface of sample 4176/2. The AlN was found in large sheets, (Fig. 6.6a), or as smaller plate-like fragments (Fig. 6.6b). Selected area electron diffraction patterns such as Fig. 6.6c show the plates to correspond to {0001} basal planes of AlN.

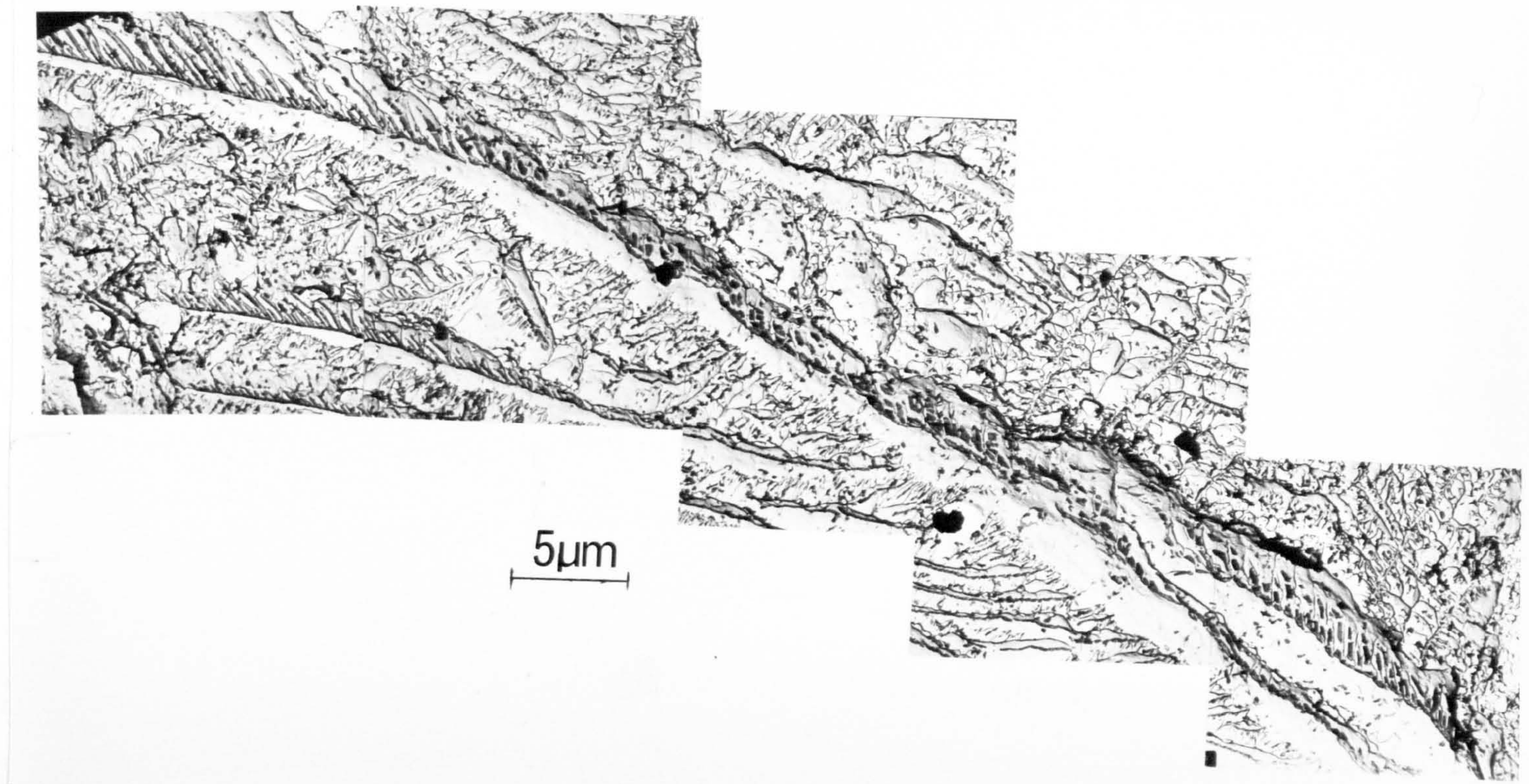

Fig. 6.7 A composite transmission electron micrograph showing the extensive array of AlN dendrites on the fracture surface of sample 4176/4. The dendrite arm spacing is approximately 1μm.

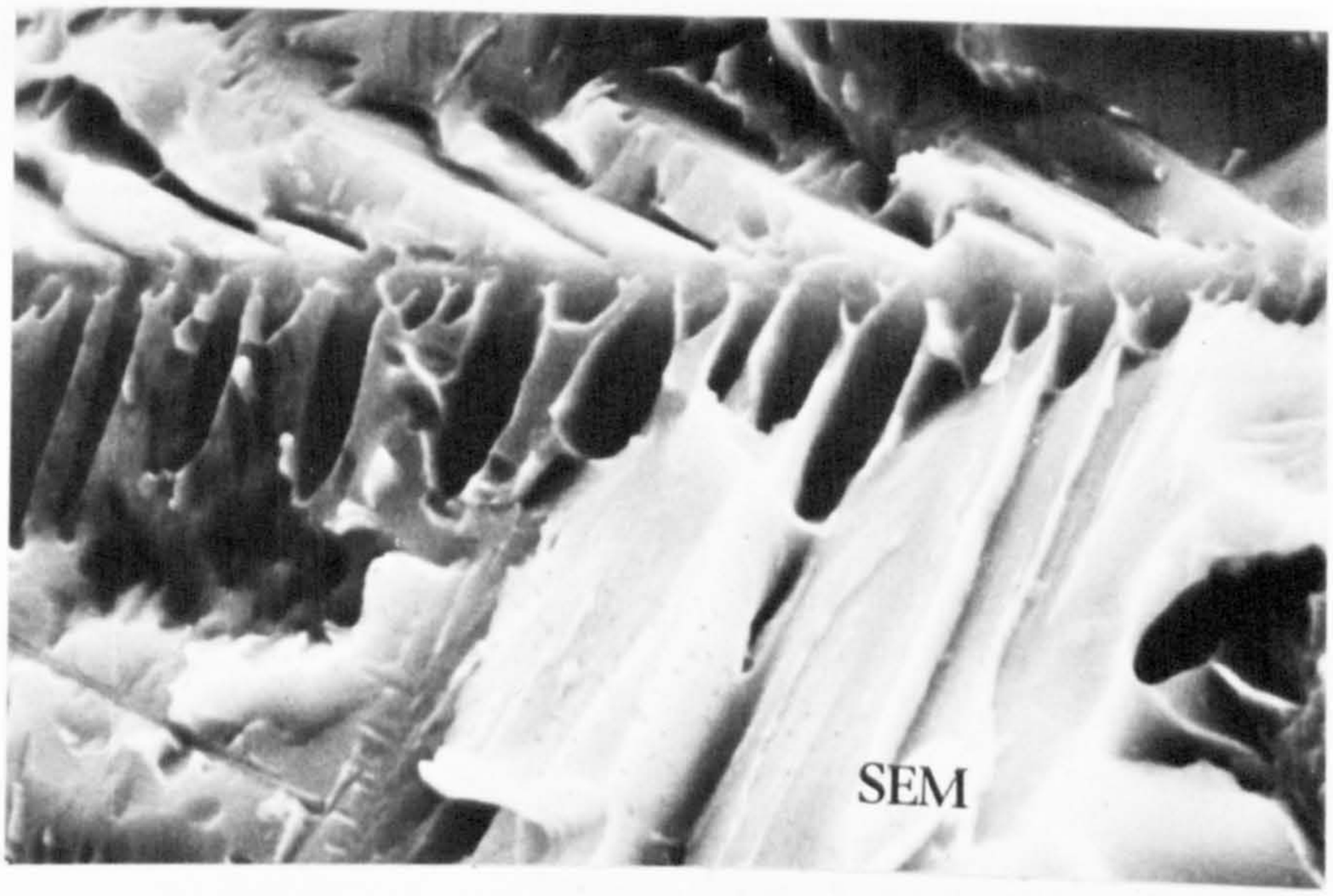

(a)

5μm

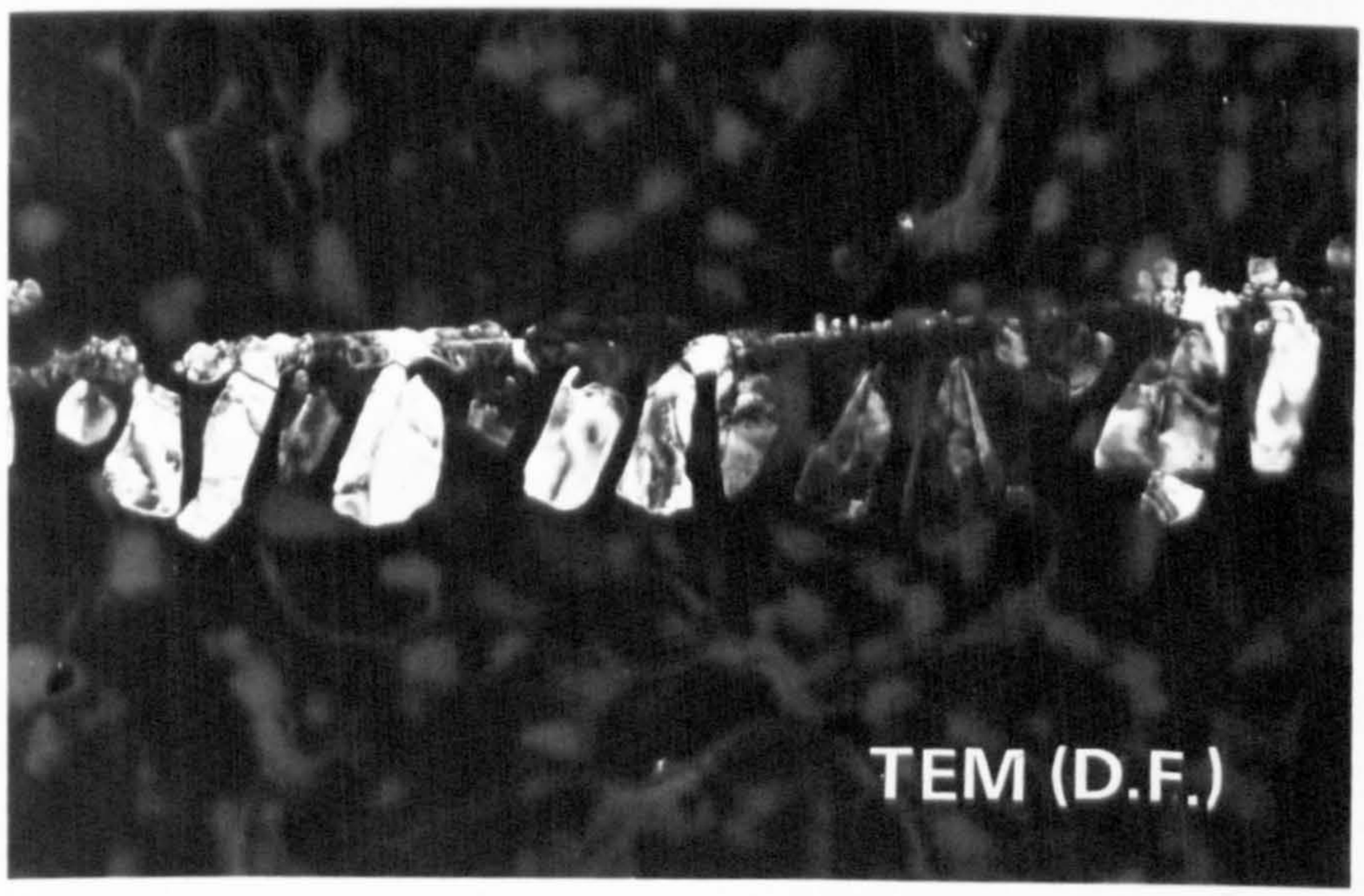

(b)

Fig. 6.8(a) is a scanning electron micrograph showing the imprint of the dendritic form of AlN on the fracture surface of sample 4176/1.

Fig. 6.8(b) shows a similar dendrite of AlN which has been extracted onto a carbon extraction replica of the fracture surface (dark field transmission electron micrograph).

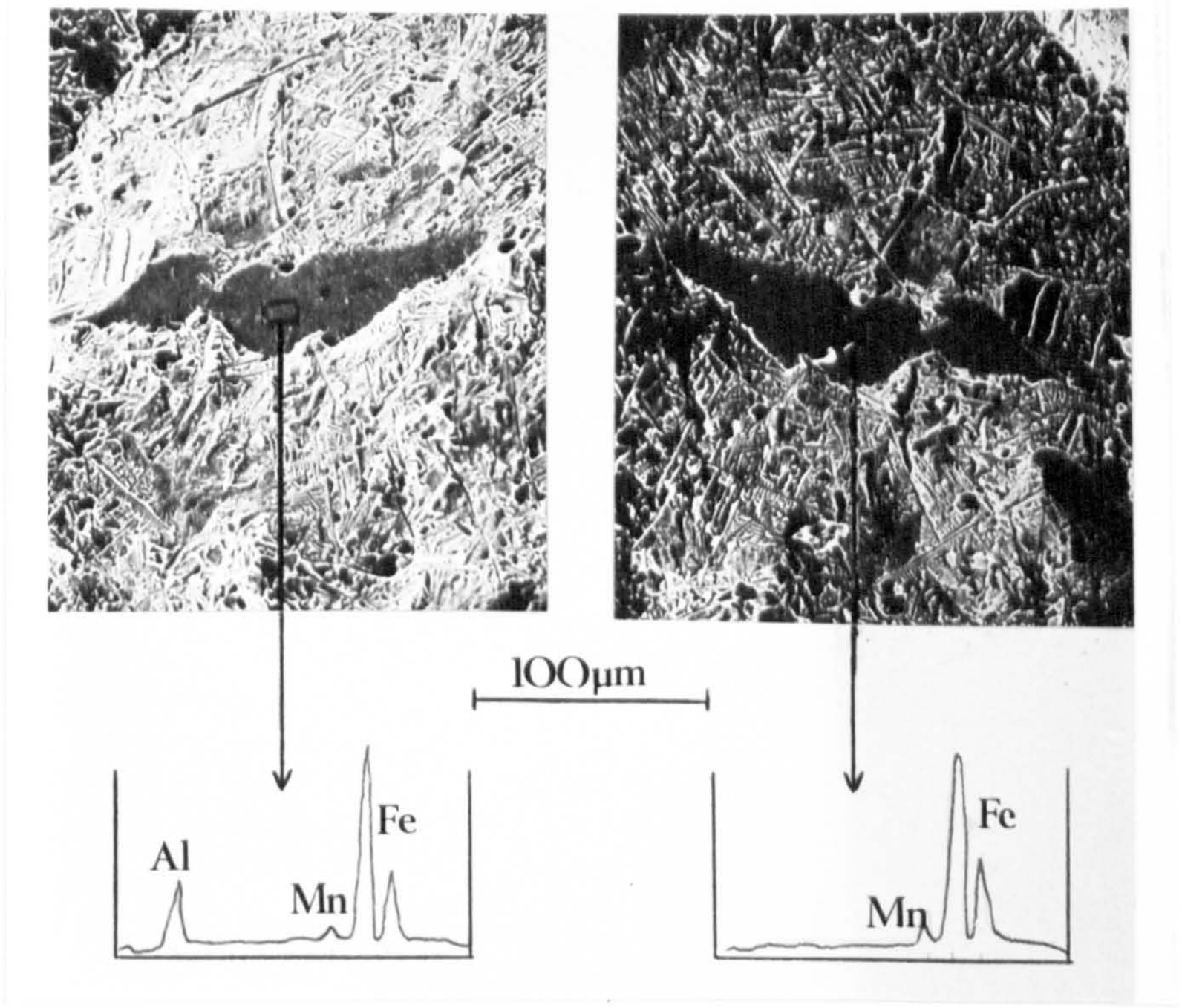

Fig. 6.9 Scanning electron micrograph showing the same plate-like feature on mating halves of a room temperature intergranular fracture surface. Energy dispersive analysis reveals one half to be Al-rich, whilst the other half shows no Al peak. It can be concluded that fracture has occurred by decohesion at the AlN/matrix interface which results in AlN being retained on only one half of the fracture surface.

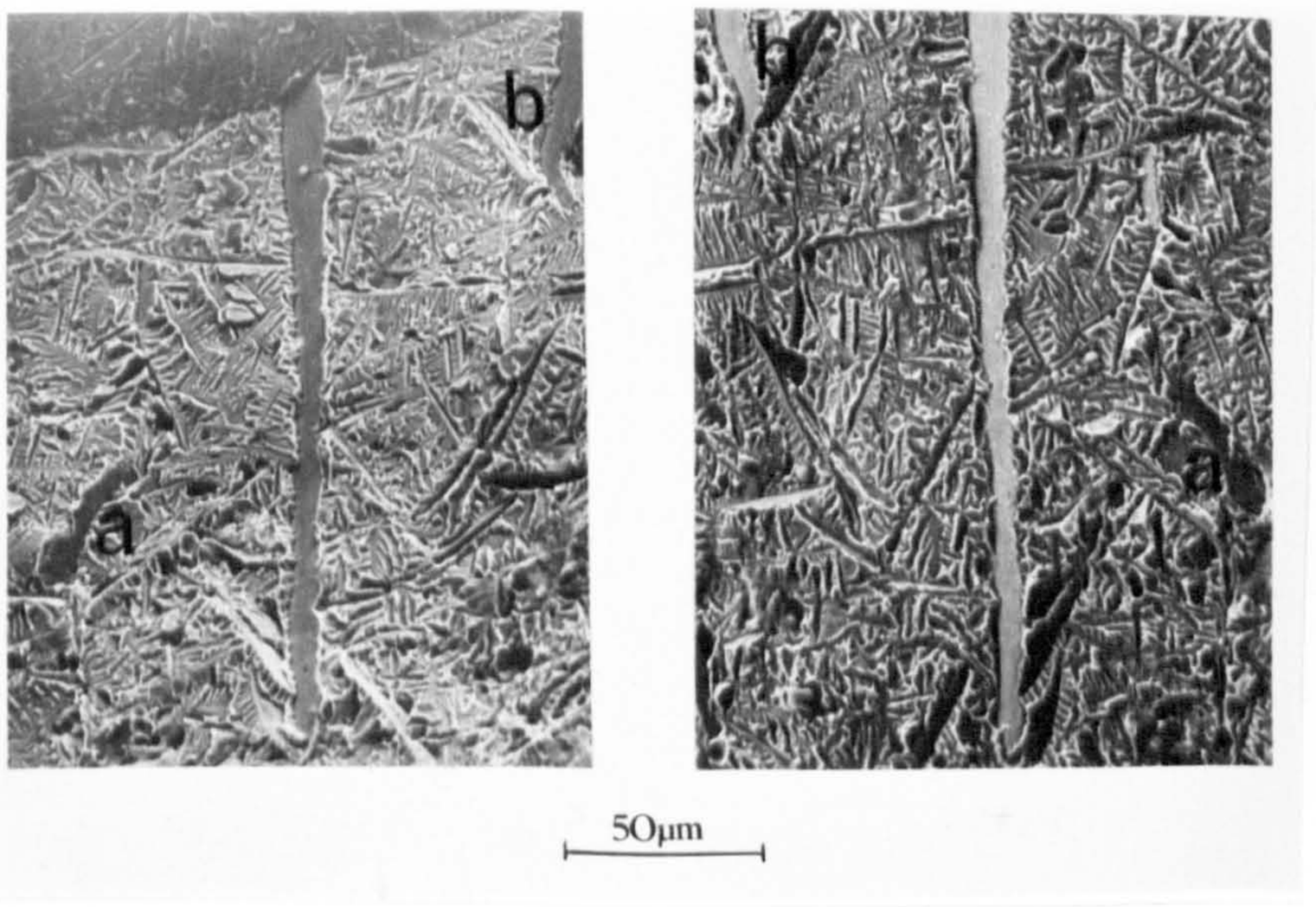

Fig. 6.10 Similar plate-like feature to that shown in Fig. 6.9, again with Al being detected on only one half of the fracture surface.

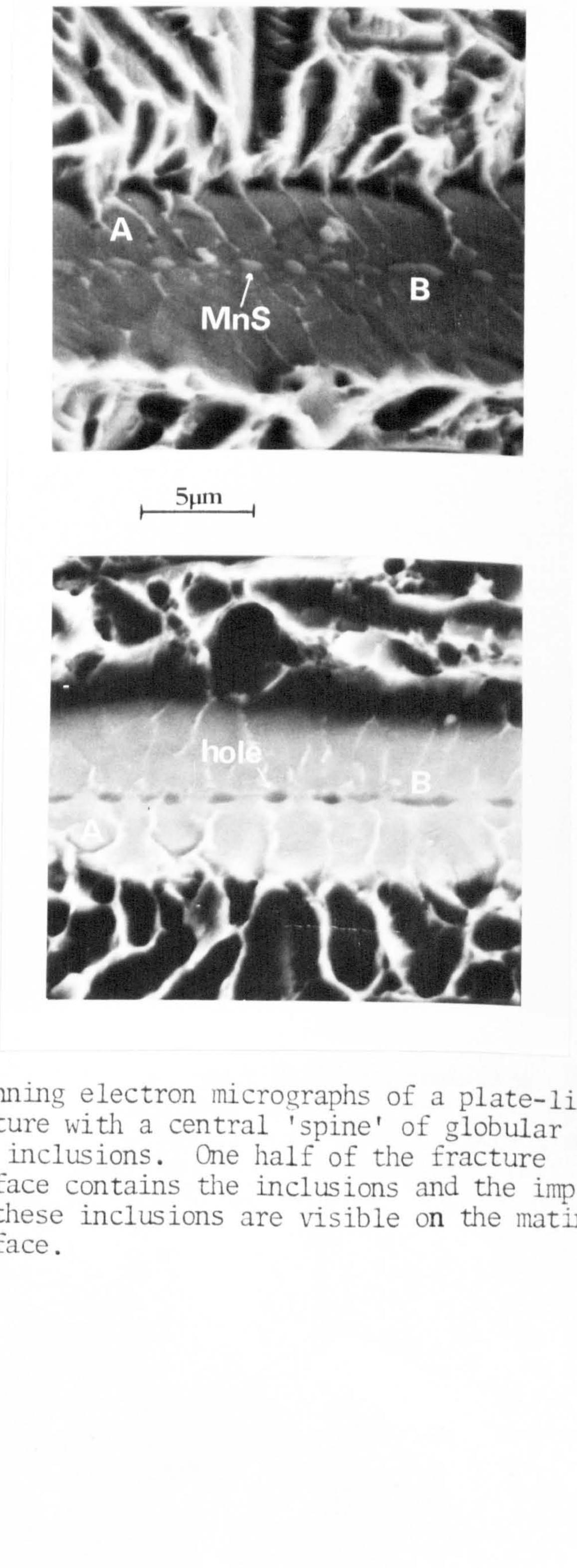

Fig. 6.11 Scanning electron micrographs of a plate-like feature with a central 'spine' of globular MnS inclusions. One half of the fracture surface contains the inclusions and the imprints of these inclusions are visible on the mating surface.

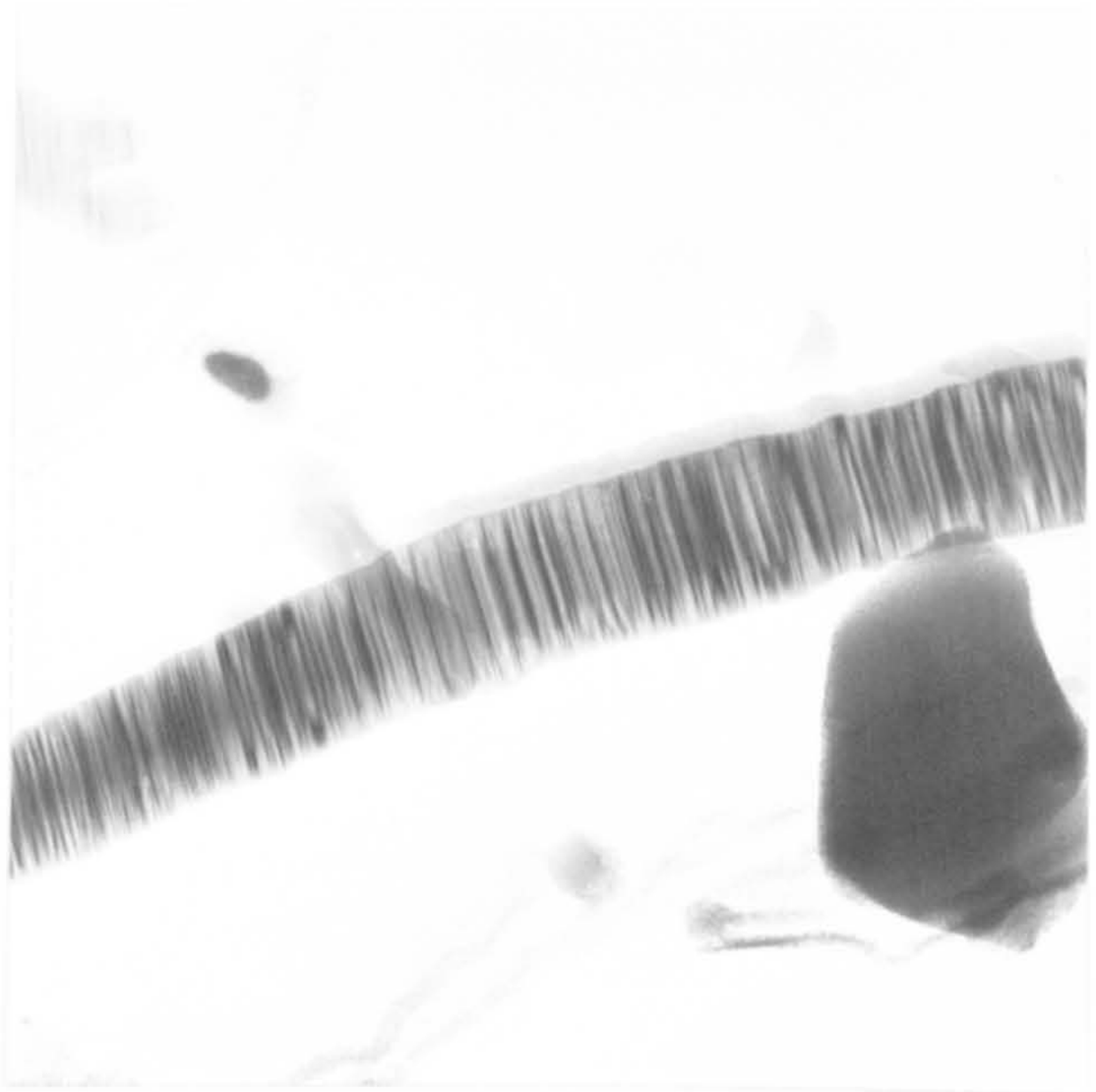

(B.F.)

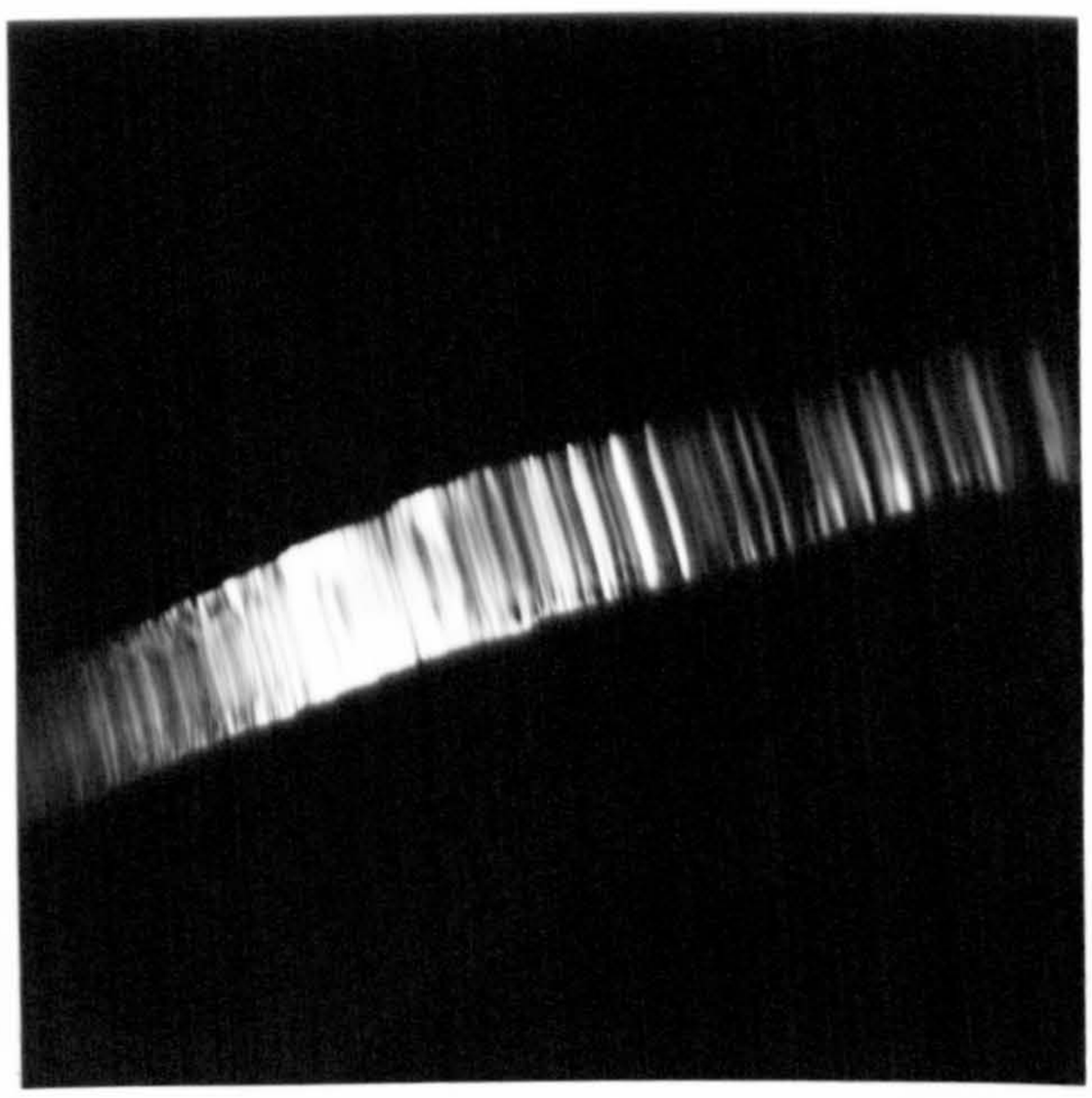

(D.F.)

Fig. 6.12 Bright field and dark field transmission electron micrographs showing a heavily faulted inclusion of MnS. Carbon extraction replica taken from the intergranular fracture surface of cast 4176/3. (X102 000)

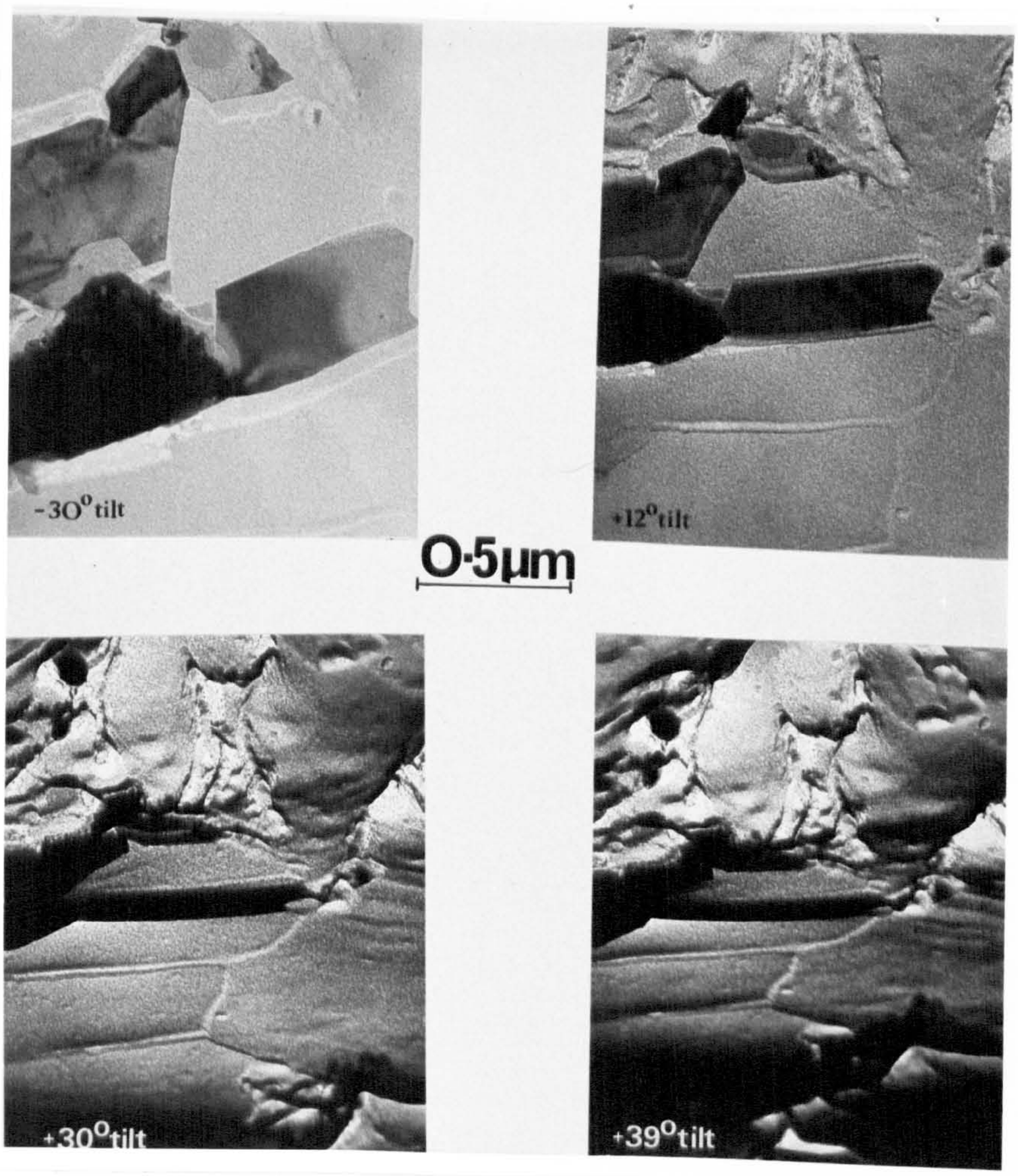

Fig. 6.13 A series of transmission electron micrographs showing the effects of tilting on the apparent thickness of an AlN plate. The thickness was a minimum with 39° tilt.

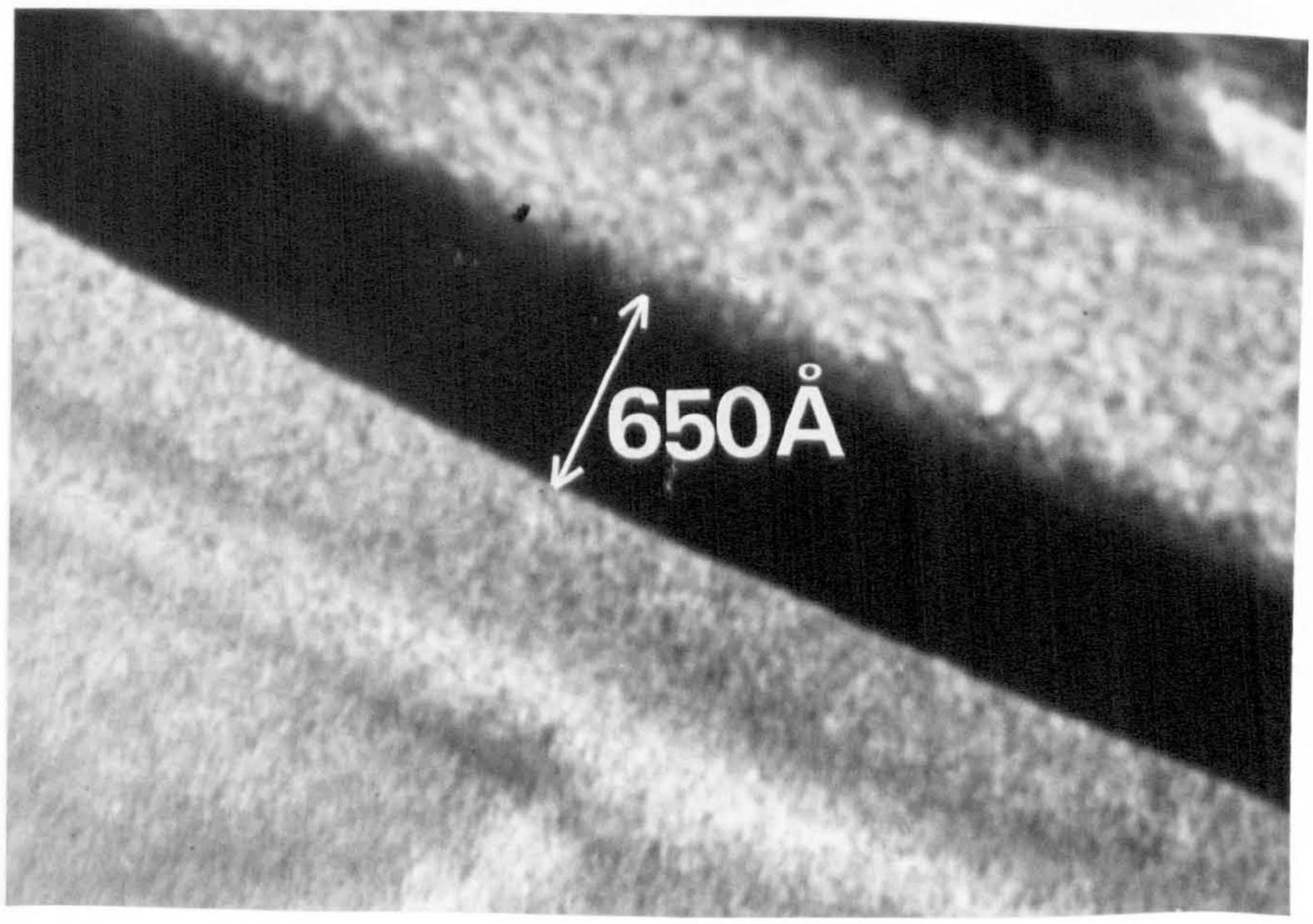

Fig. 6.14 High magnification transmission micrograph of the same AlN plate with 39° tilt. The thickness is measured to be 65nm (650Å).

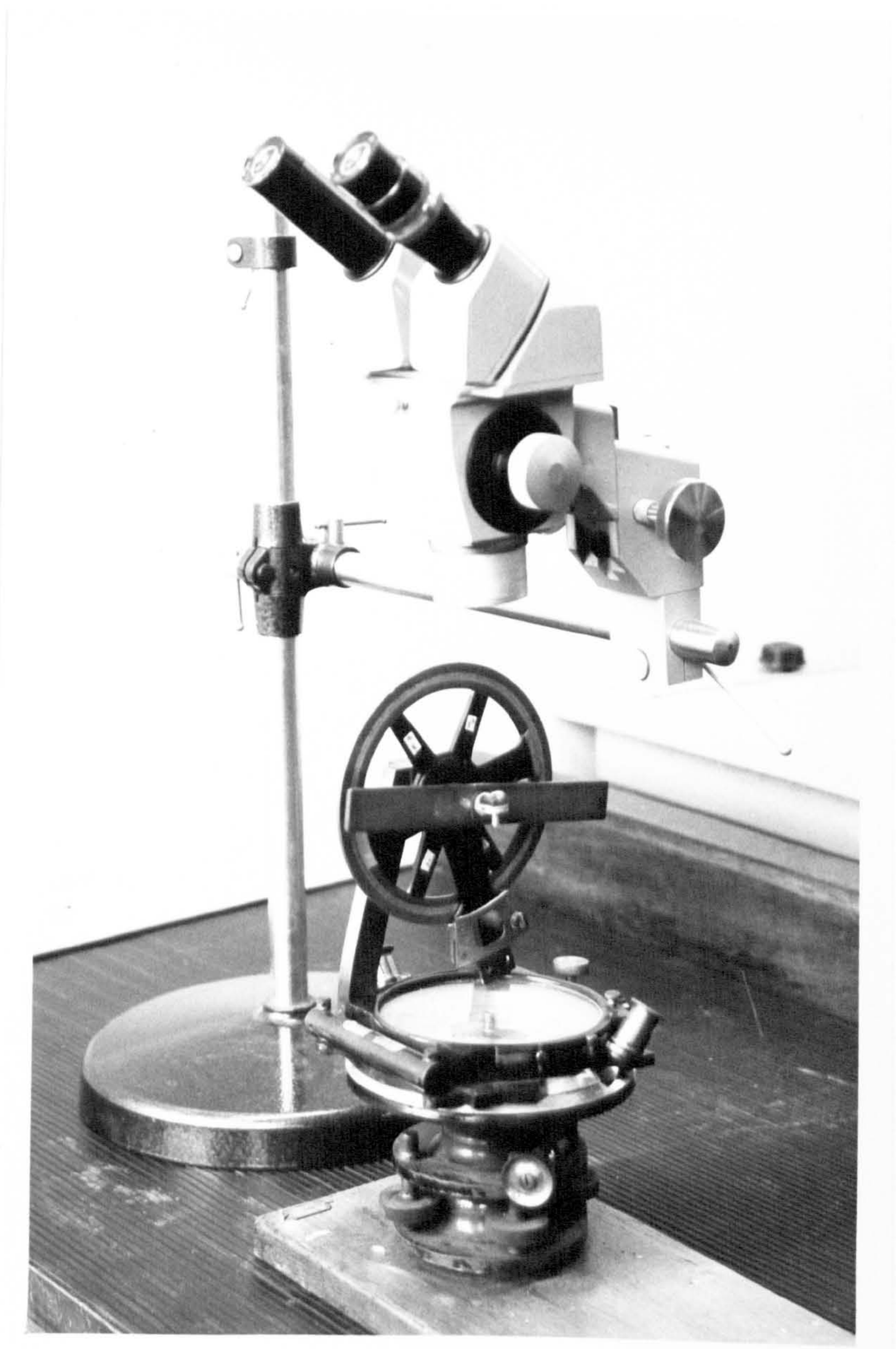

Fig. 6.15 The optical goniometer used for preliminary measurements of the angles between plate-like features observed on the fracture surfaces.

Fig. 6.16 A Charpy sample in position in the auxiliary tilt holder used for angular measurements in the S.E.M.

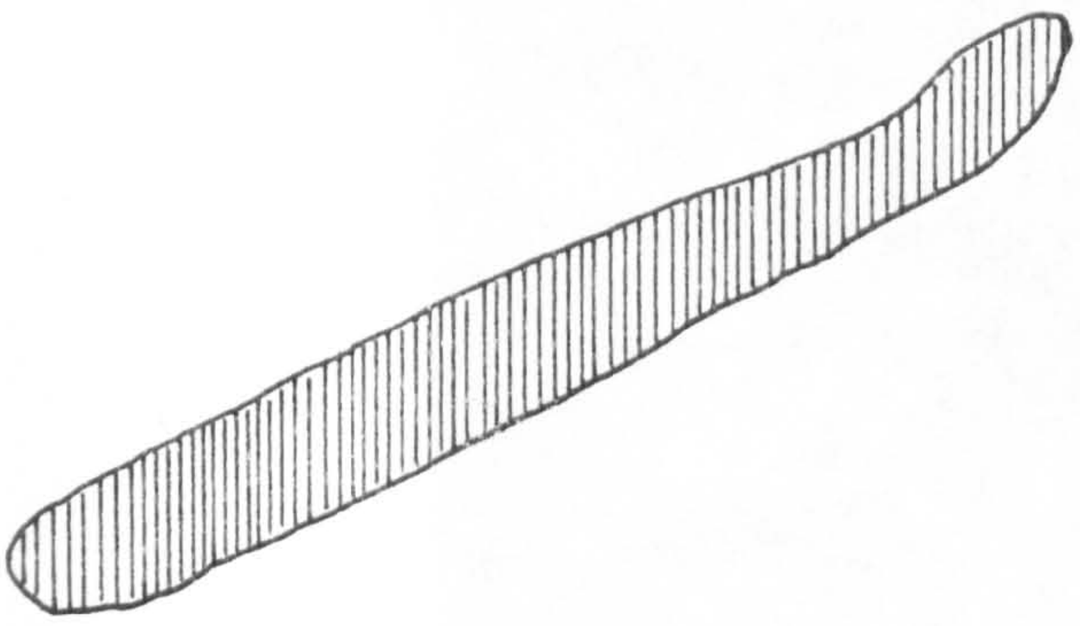

(i) Rotate until plate is horizontal

(ii) Tilt until plate disappears

(iii) Plate disappearing — values of R and T uniquely define the plate normal N.

Fig. 6.17 Schematic diagram illustrating the technique employed to determine the direction of a plate normal in the S.E.M.

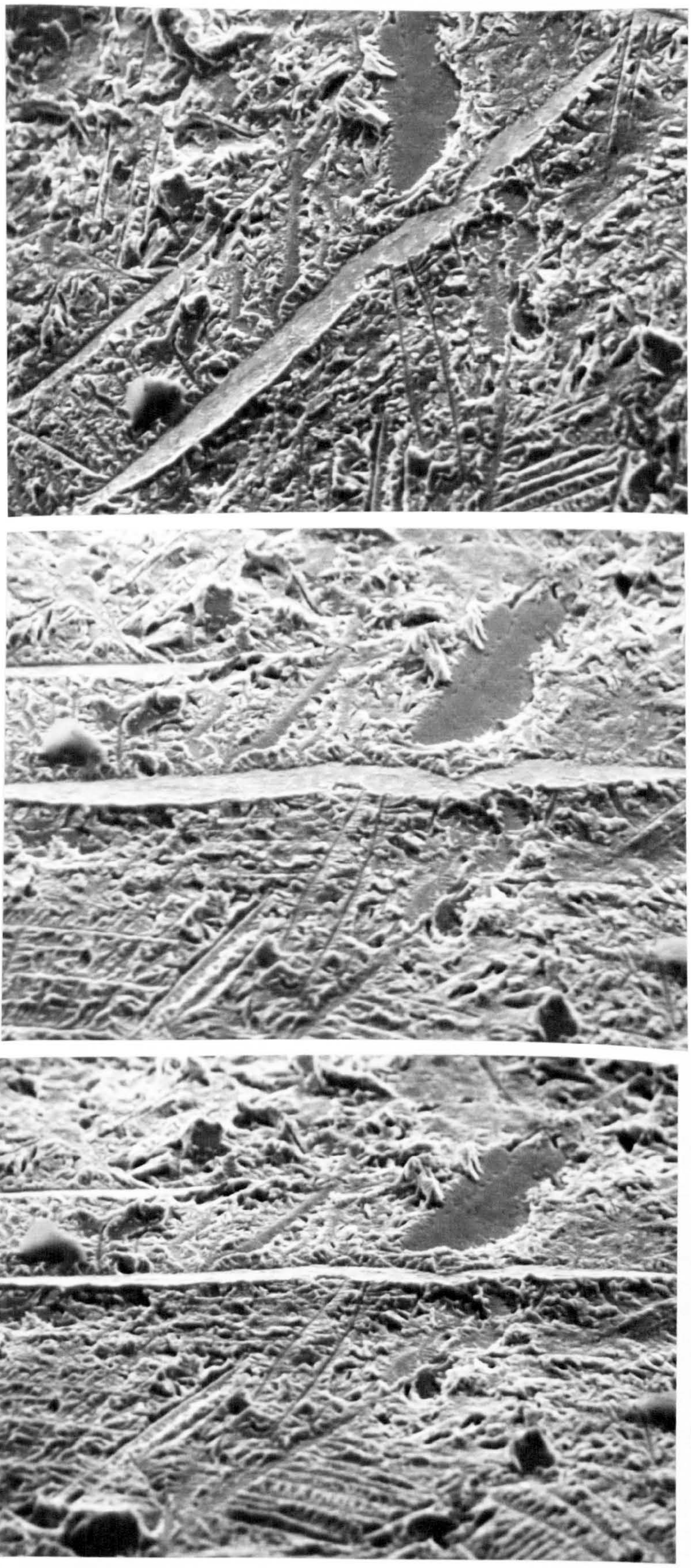

Fig. 6.18 A series of scanning electron micrographs showing plate-like features on an intergranular fracture surface which correspond to the stages described in Fig. 6.17.

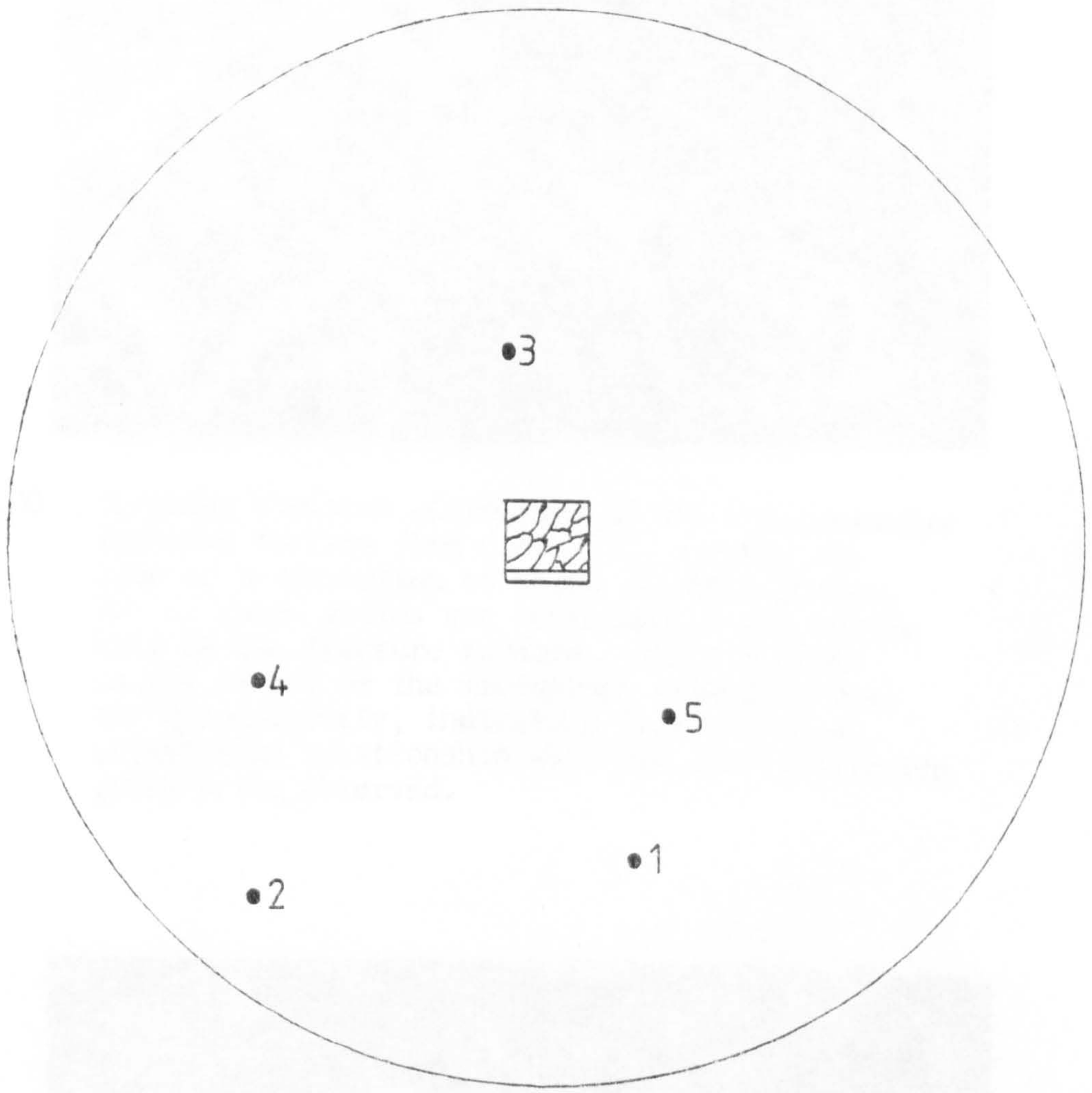

Fig. 6.19 Stereographic projection which relates the direction of the plate normals to the position of the fracture surface at the centre. The numbering of the plate normals corresponds to that in Table 6.3.

Fig. 6.20 Scanning electron micrograph of the intergranular fracture surface from cast 4210, showing the line of intersection of three columnar grains. Two of these grains are contained in the mating half of the fracture surface. The AlN plate in the centre of the micrograph extends across the discontinuity, indicating that it has an orientation relationship with the prior austenite grain being observed.

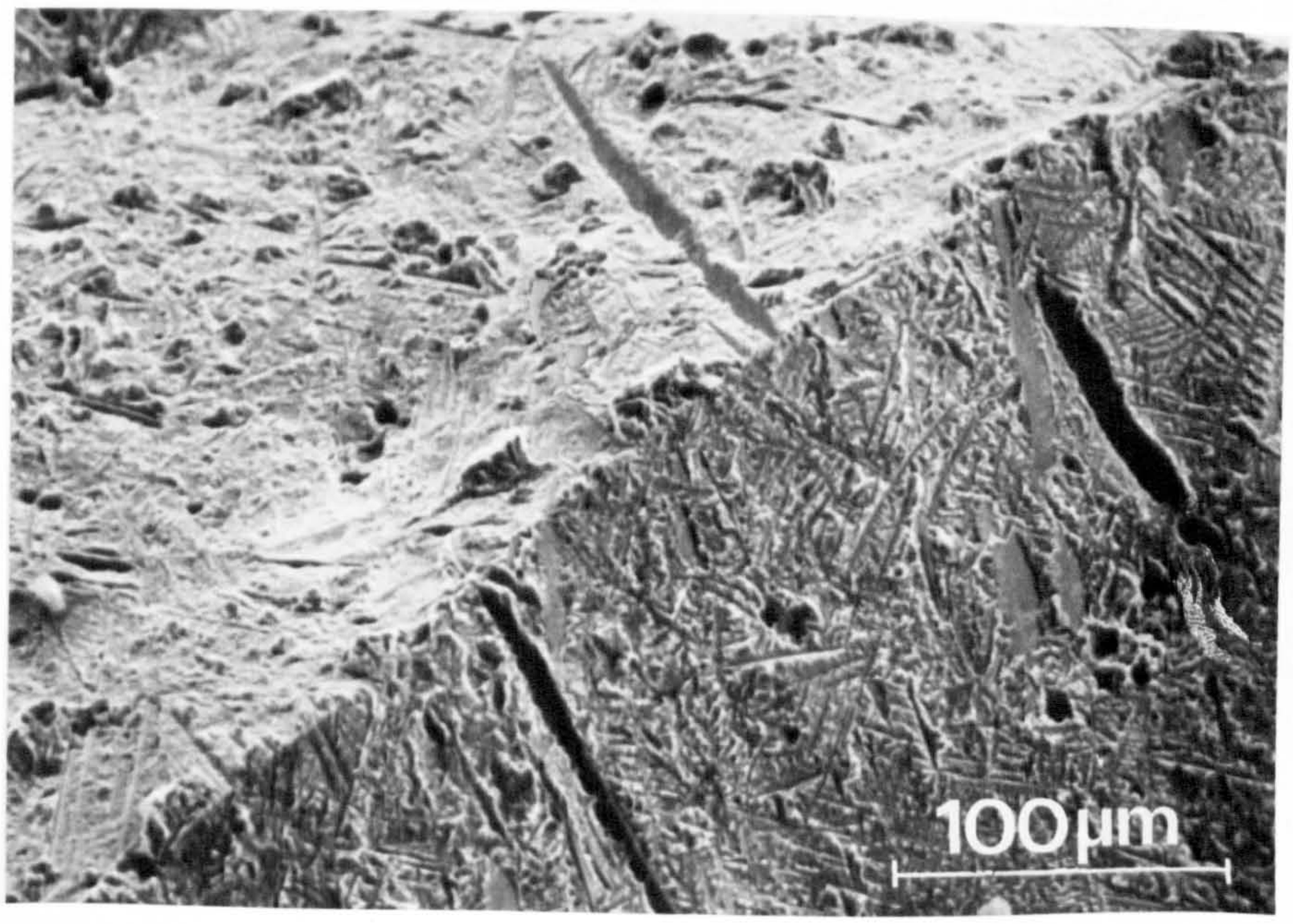

Fig. 6.21 As Fig. 6.20, but showing AlN plates terminating abruptly at the line of intersection of the three grains. This indicates that these plates have an orientation relationship with one of the two austenite grains on the mating half of the fracture surface.

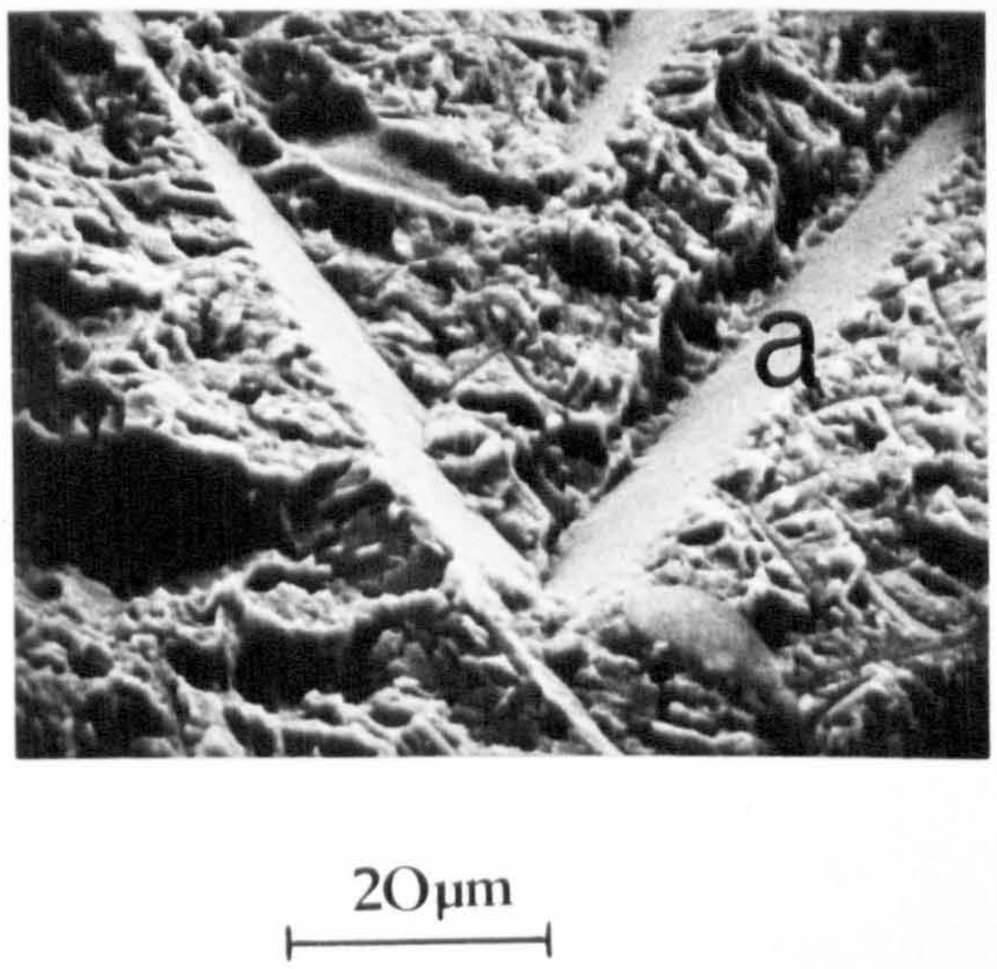

Fig. 6.22 Two intersecting plates on an intergranular fracture surface.

Fig. 6.23 The same plates as shown in Fig. 6.22, but tilted to the point of simultaneous extinction. The angle between the two normals to the plates is $71^{o} \pm 1^{o}$.

Fig. 6.24 Transmission electron micrograph of a thin foil taken from the prior austenite grain boundary of sample 4176/1. Plates of AlN have nucleated in the grain boundary and grown into the adjacent grains (now transformed to ferrite). (X85 000)

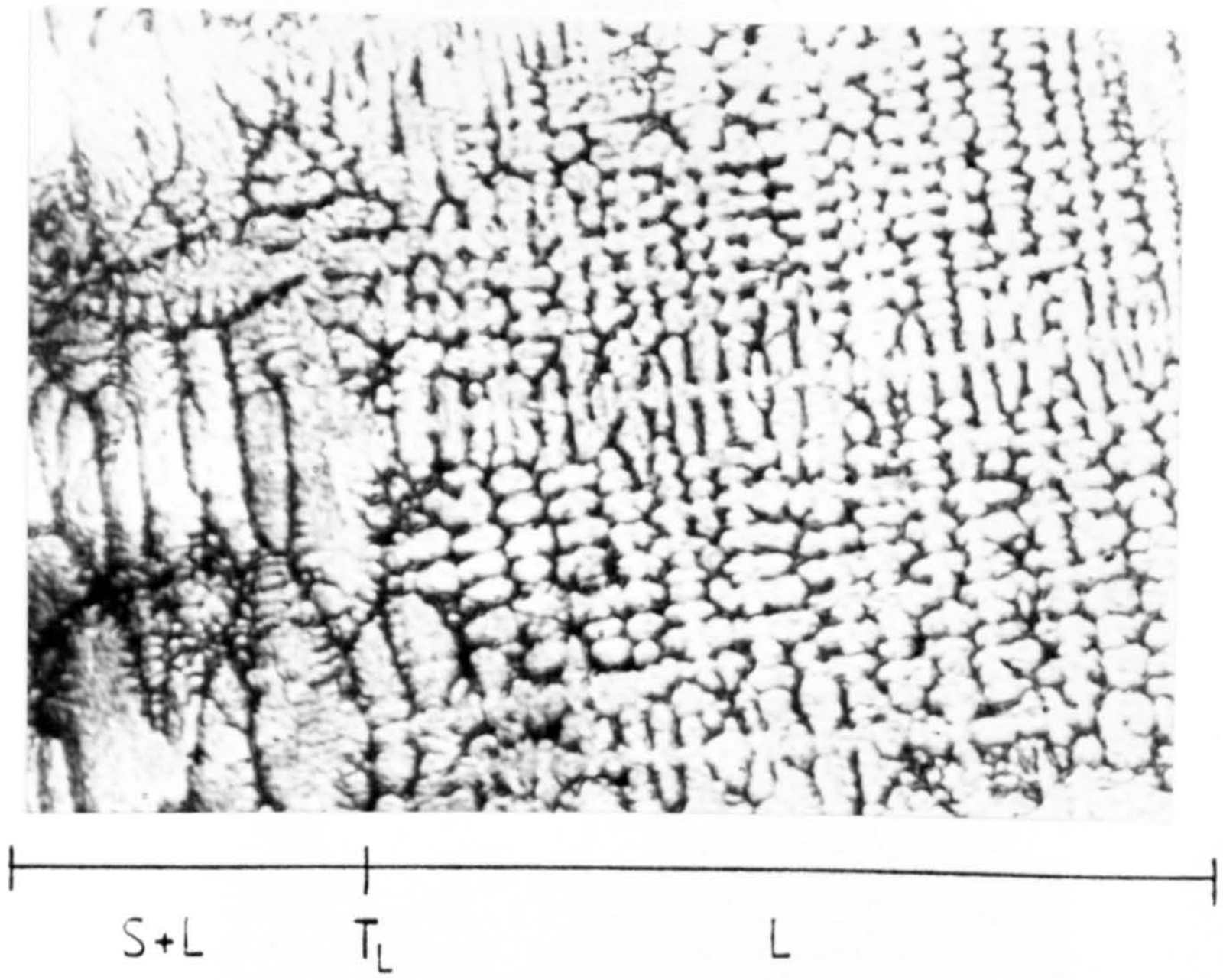

Fig. 6.25 Longitudinal section showing the position of the liquidus in a directionally solidified sample of cast 4383. Optical micrograph (X50). Etch: 4% picral.

Fig. 6.26 Fine dendritic structure of the as-quenched liquid region of the D.S. sample. (X35). Etch: 4% picral.

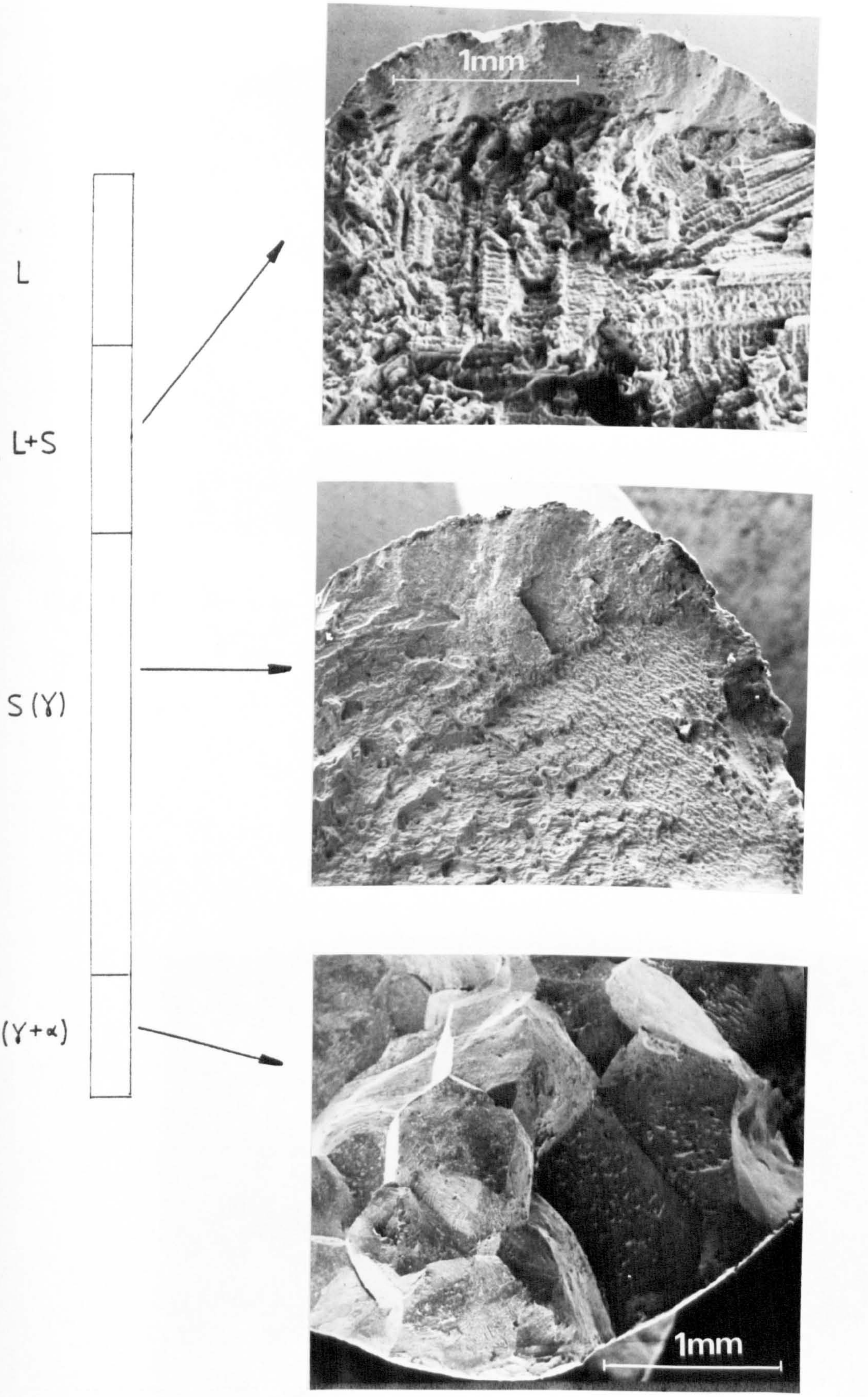

Fig. 6.27 The variation of fracture morphology with position along the directionally solidified castings. The macroscopic fracture morphology was the same for casts 4382 and 4383.

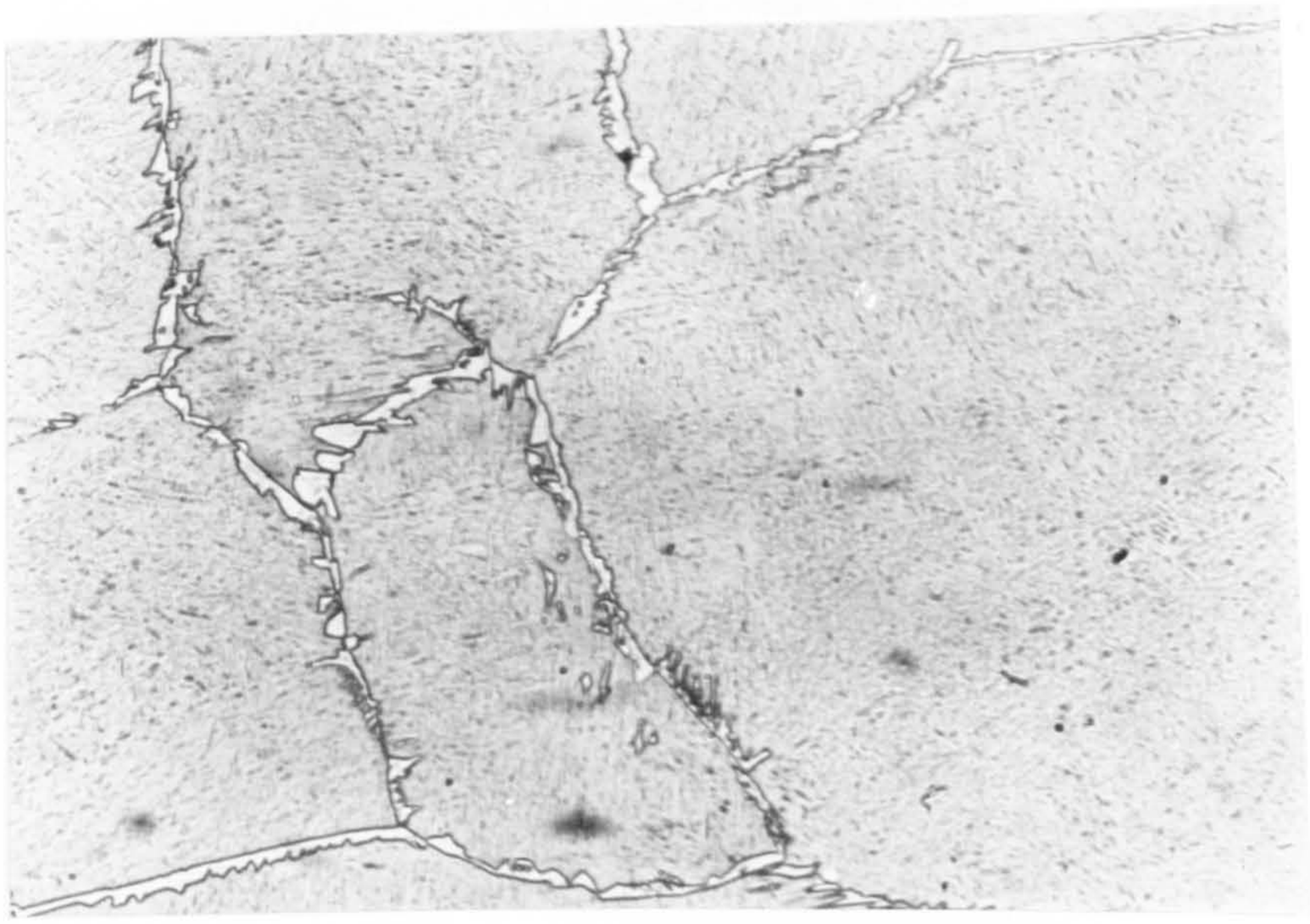

Fig. 6.28 Ferrite network responsible for the intergranular mode of failure seen in Fig. 6.27. The remainder of the microstructure is martensite (X50). Etch: 4% picral.

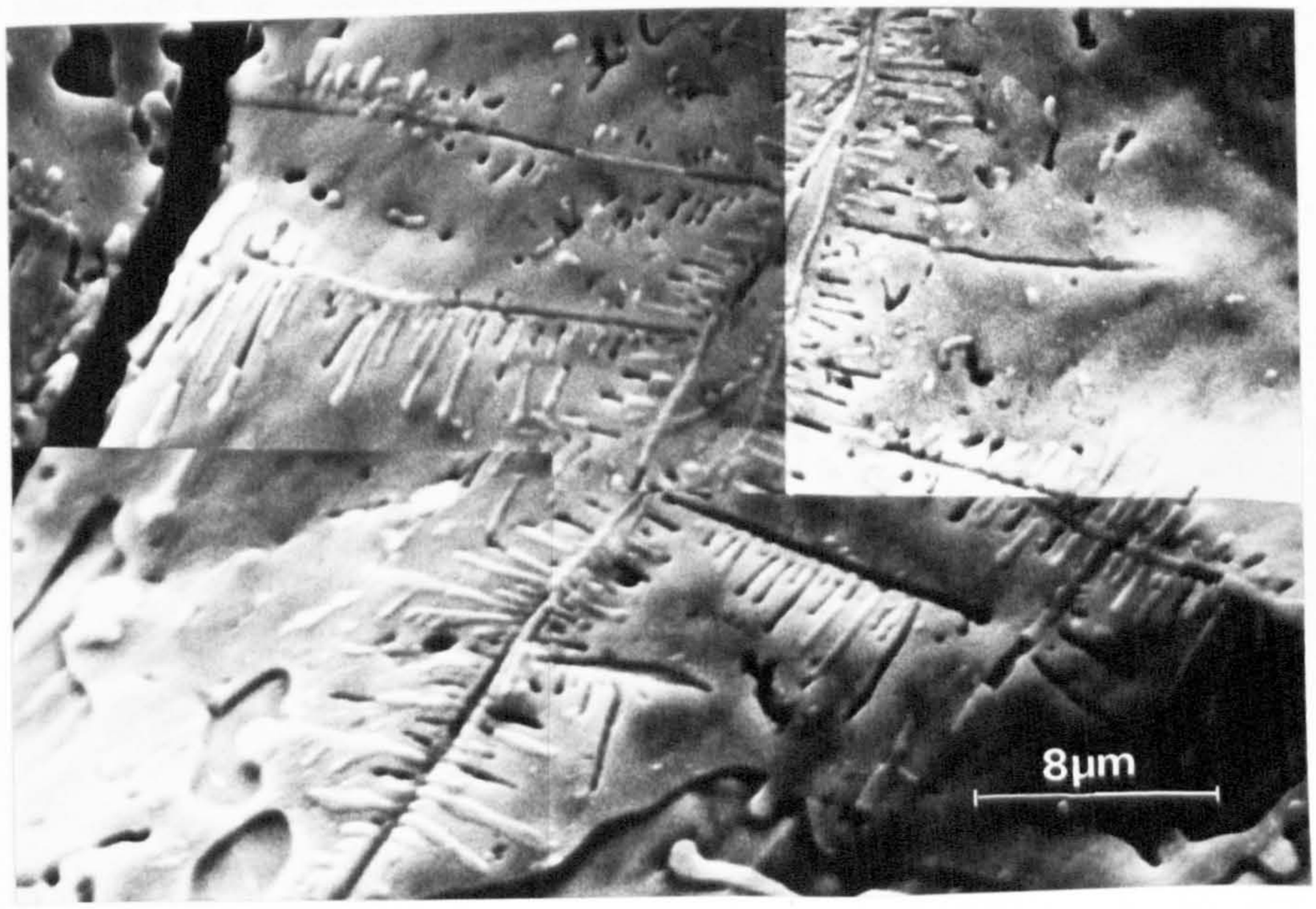

Fig. 6.29 Type II MnS inclusions on the interdendritic fracture surface of D.S. cast 4382.

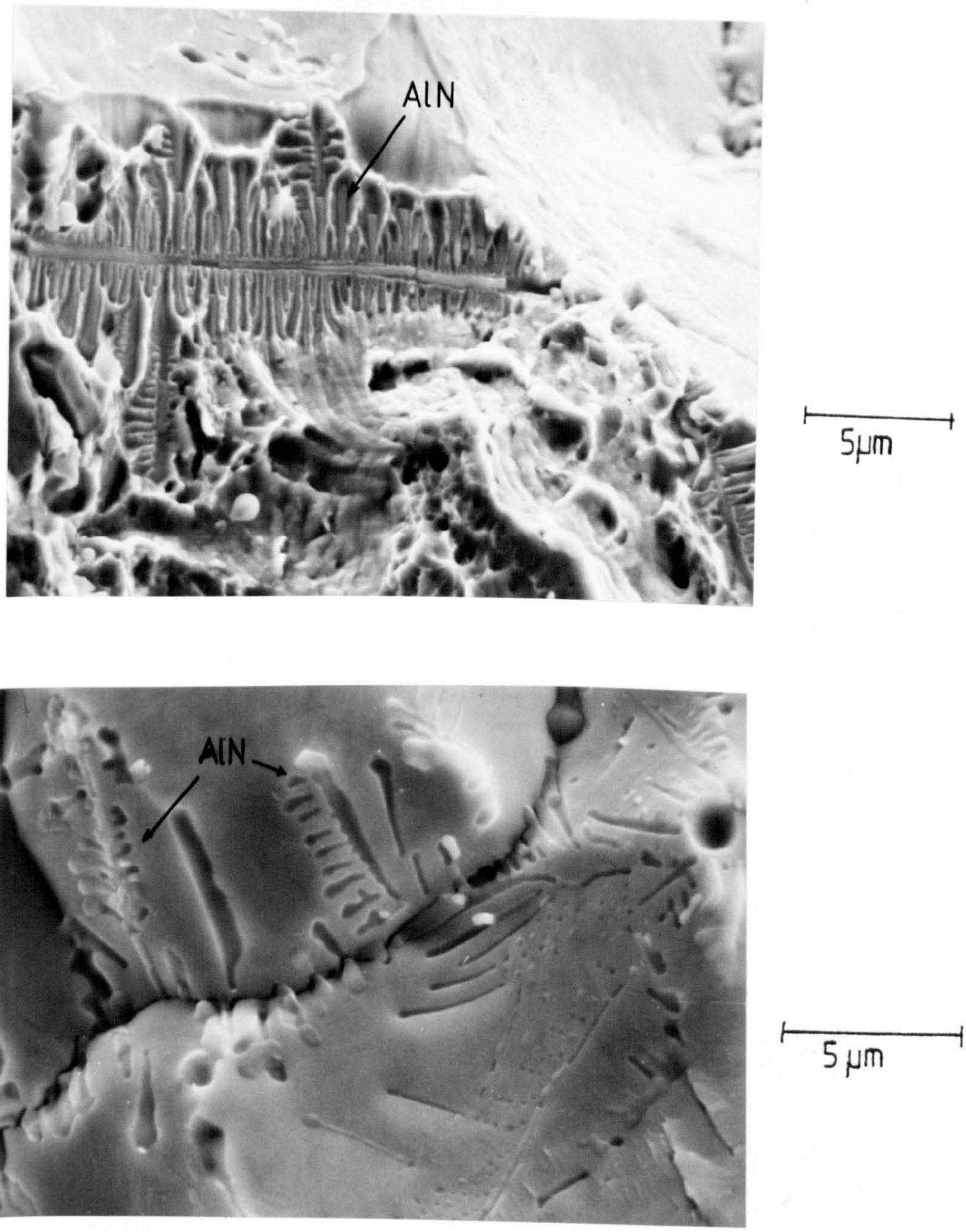

Fig. 6.30 Dendritic AlN precipitates on the interdendritic fracture surface of D.S. cast 4383.

(a)

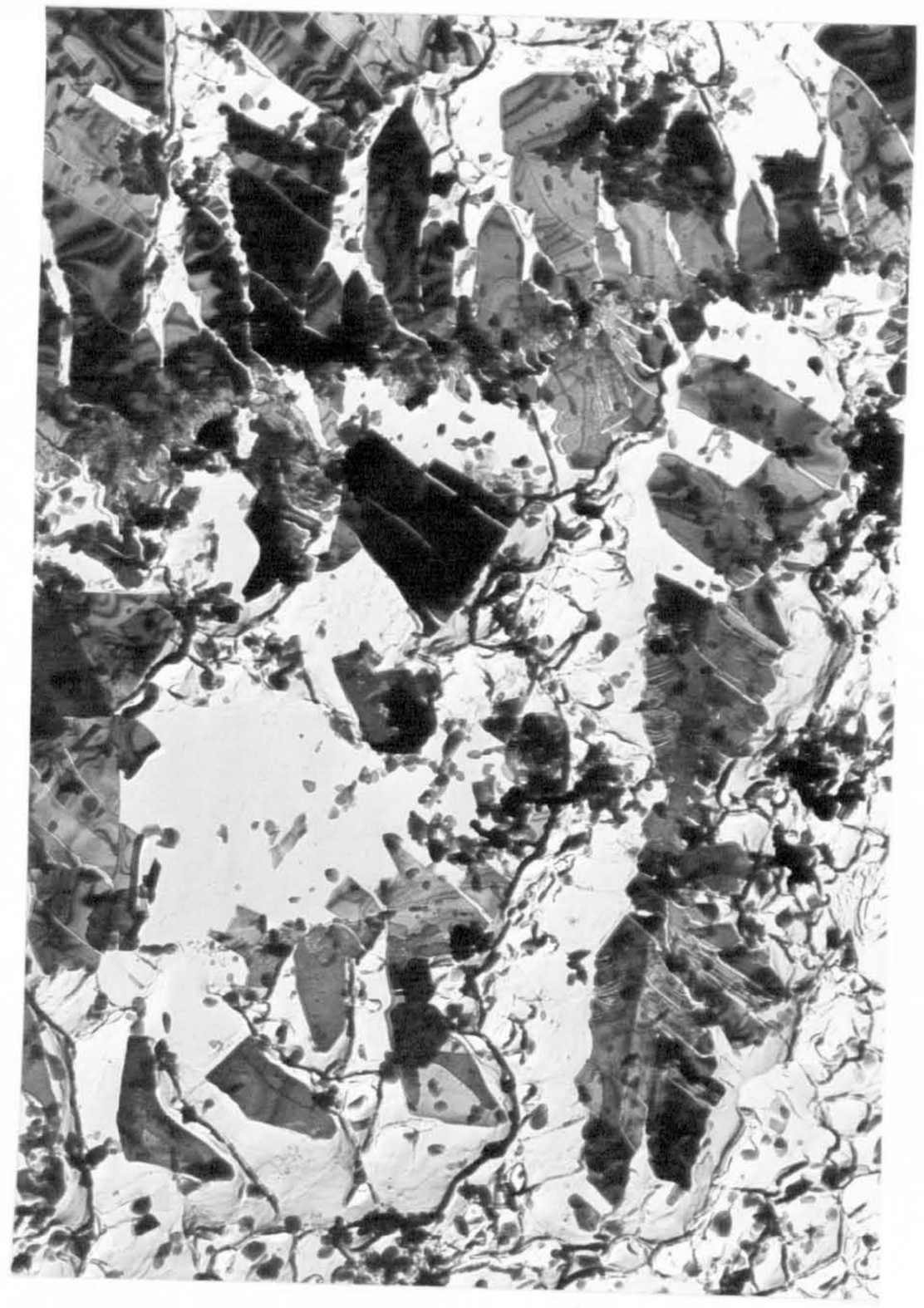

(b)

Fig. 6.31 Transmission electron micrographs showing areas where the dendritic and plate-like forms of AlN are continuous. Fig. 6.31a (X3500)
Fig. 6.31b (X8000)

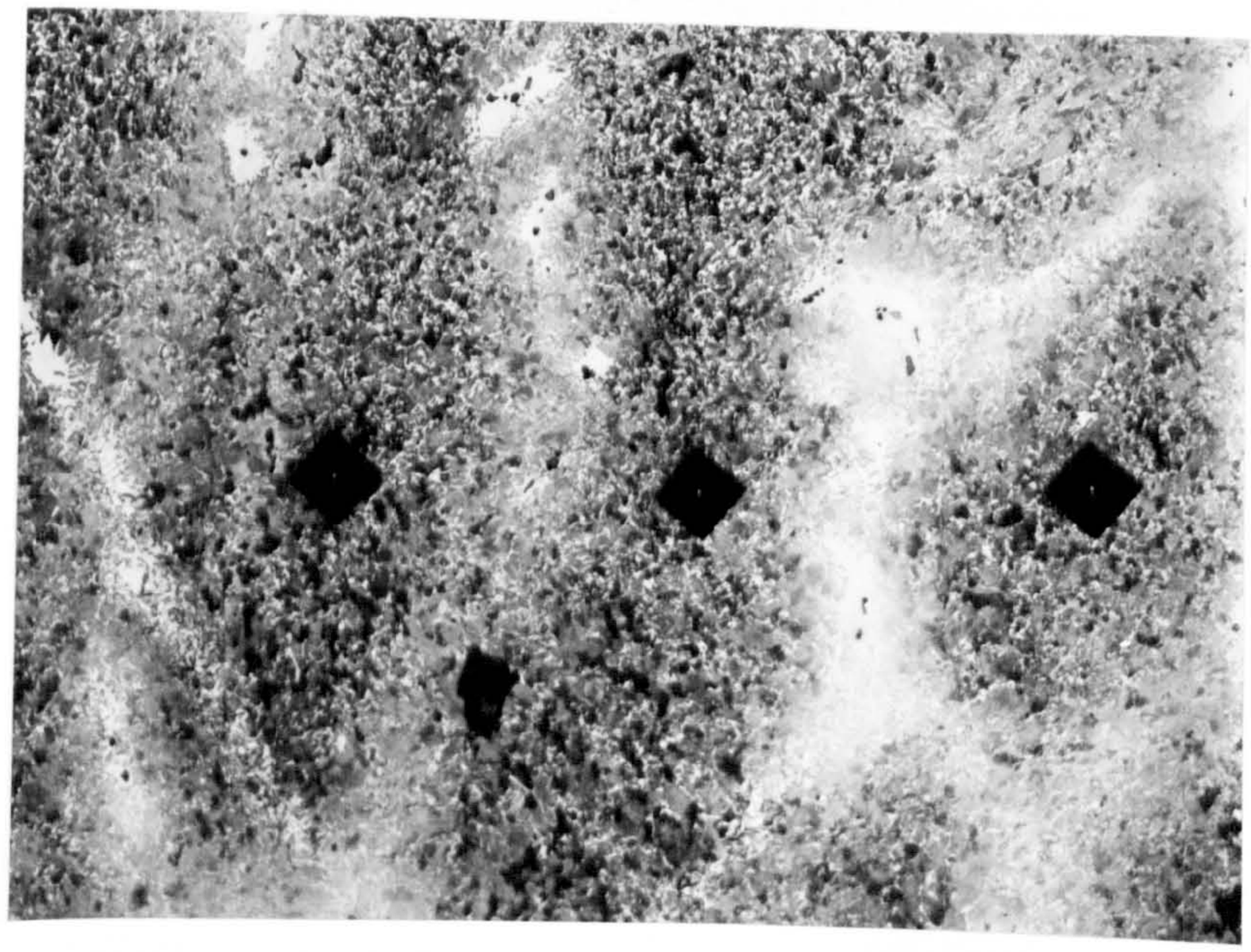

Fig. 6.32 Micro-hardness impressions used to identify the scan path for electron probe microanalysis of cast 4210. Etch: Marble's Reagent (X150)

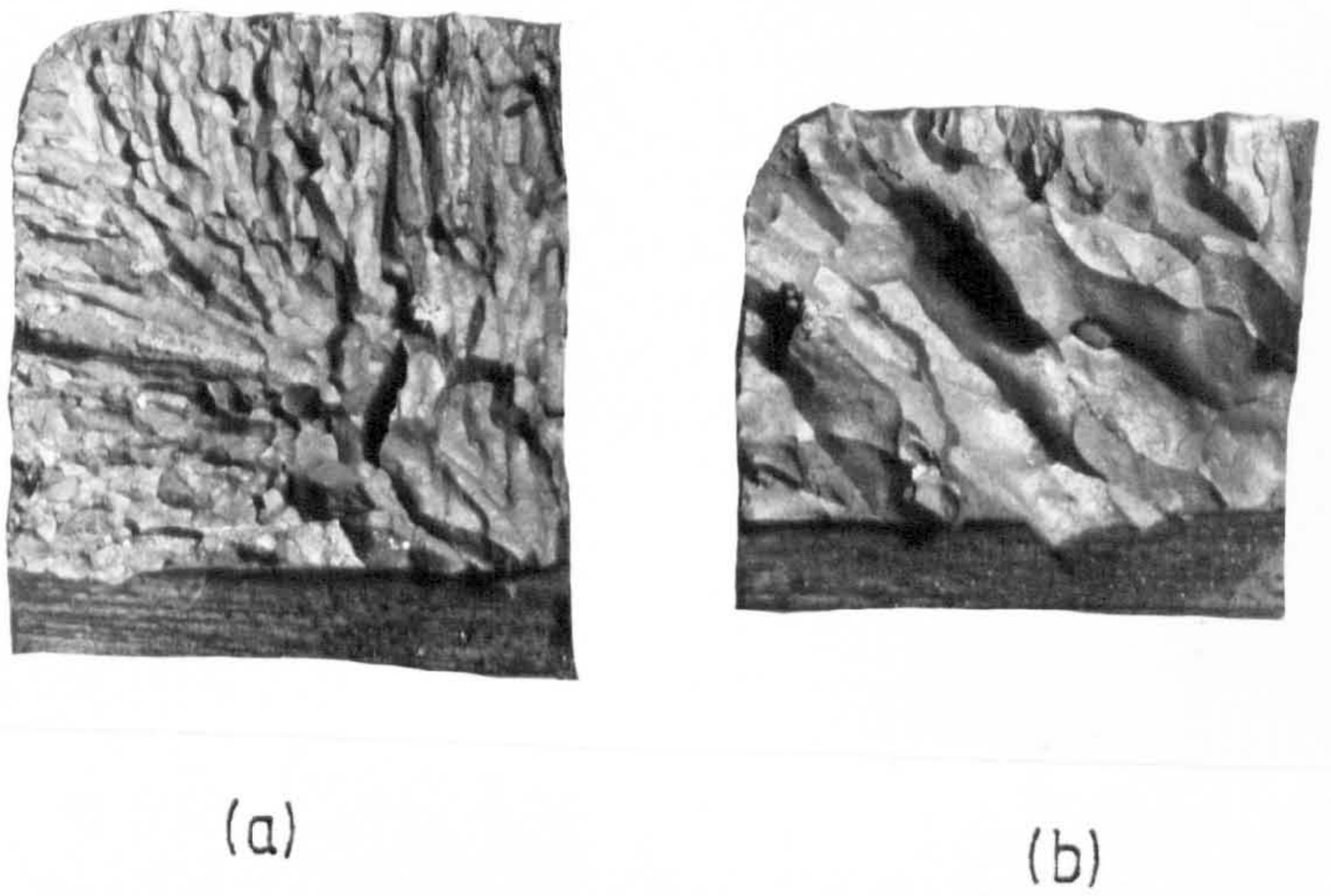

(a) (b)

Fig. 6.33 Fracture surfaces of three point bend specimens in the quenched and tempered condition taken from
a) Cast 4354 (0.56%C)
b) Cast 4353 (0.42%C).

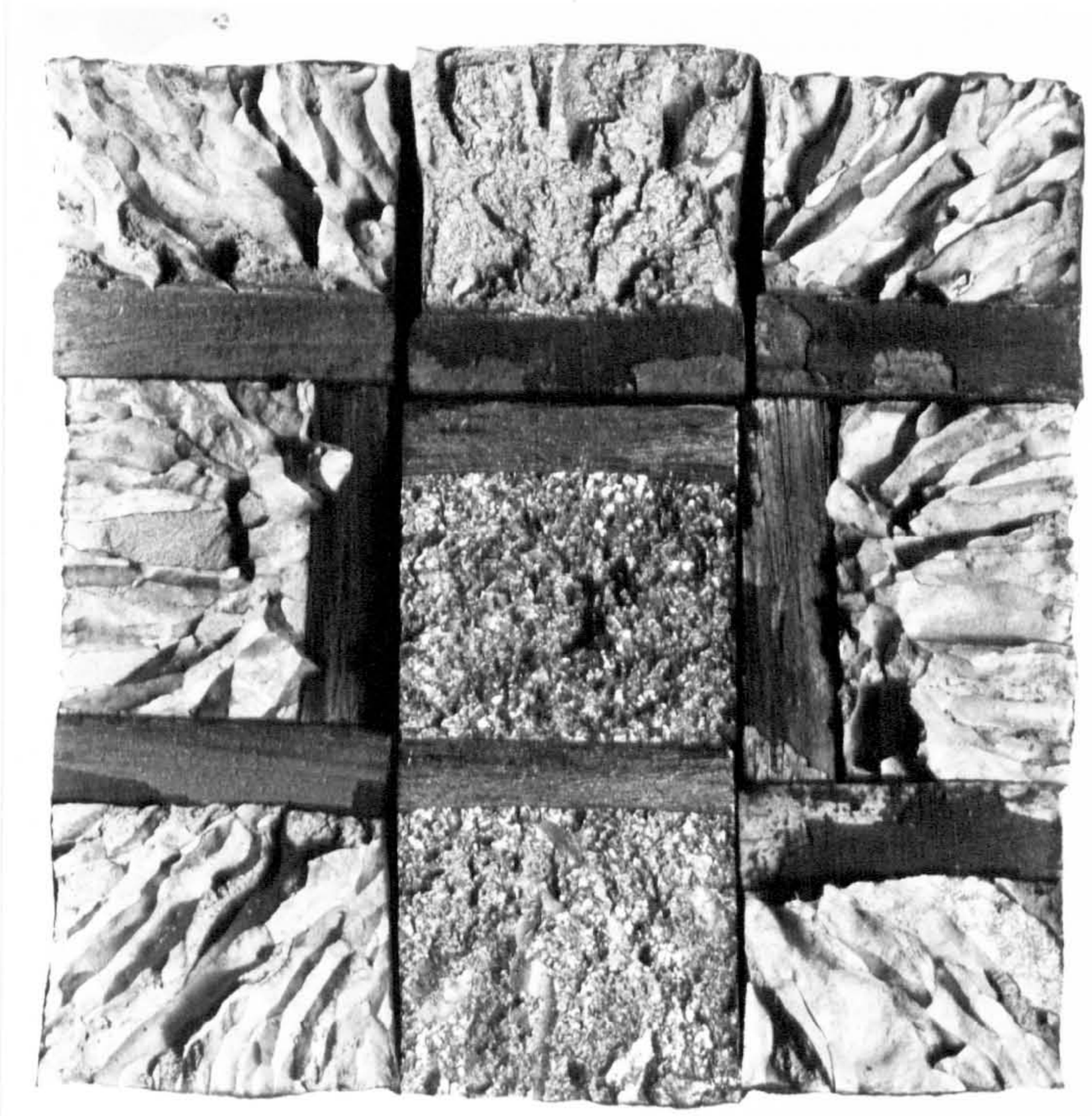

KEY:

900°C 1hr WQ	900°C 1hr Slow Cool	900°C 1hr WQ 650°C 1hr WQ
900°C 1hr Air Cool	As Cast	900°C 1hr WQ 650°C ½hr WQ
900°C 1hr OQ 650°C 1hr WQ	As Cast	900°C 1hr OQ 650°C ½hr WQ

Fig. 6.34 Fracture surfaces from cast 4176 after various heat treatments. (Actual size).

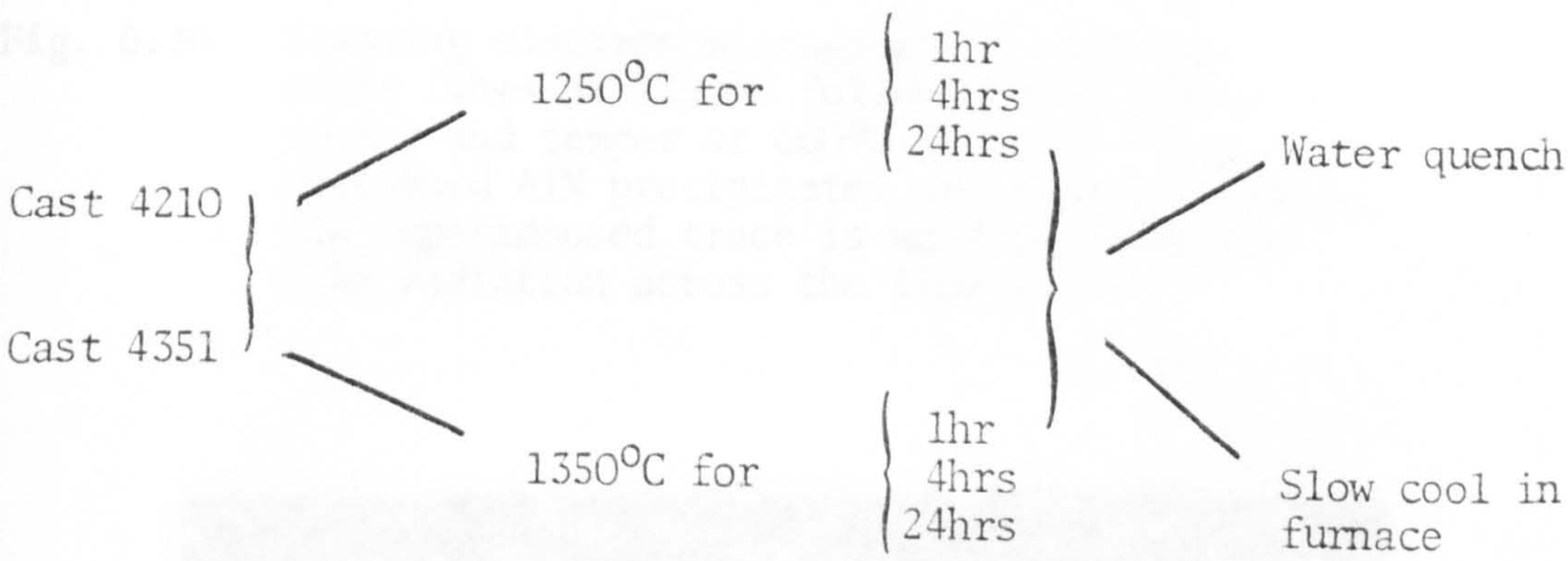

Fig. 6.35 High temperature heat treatment schedules for casts 4210 and 4351.

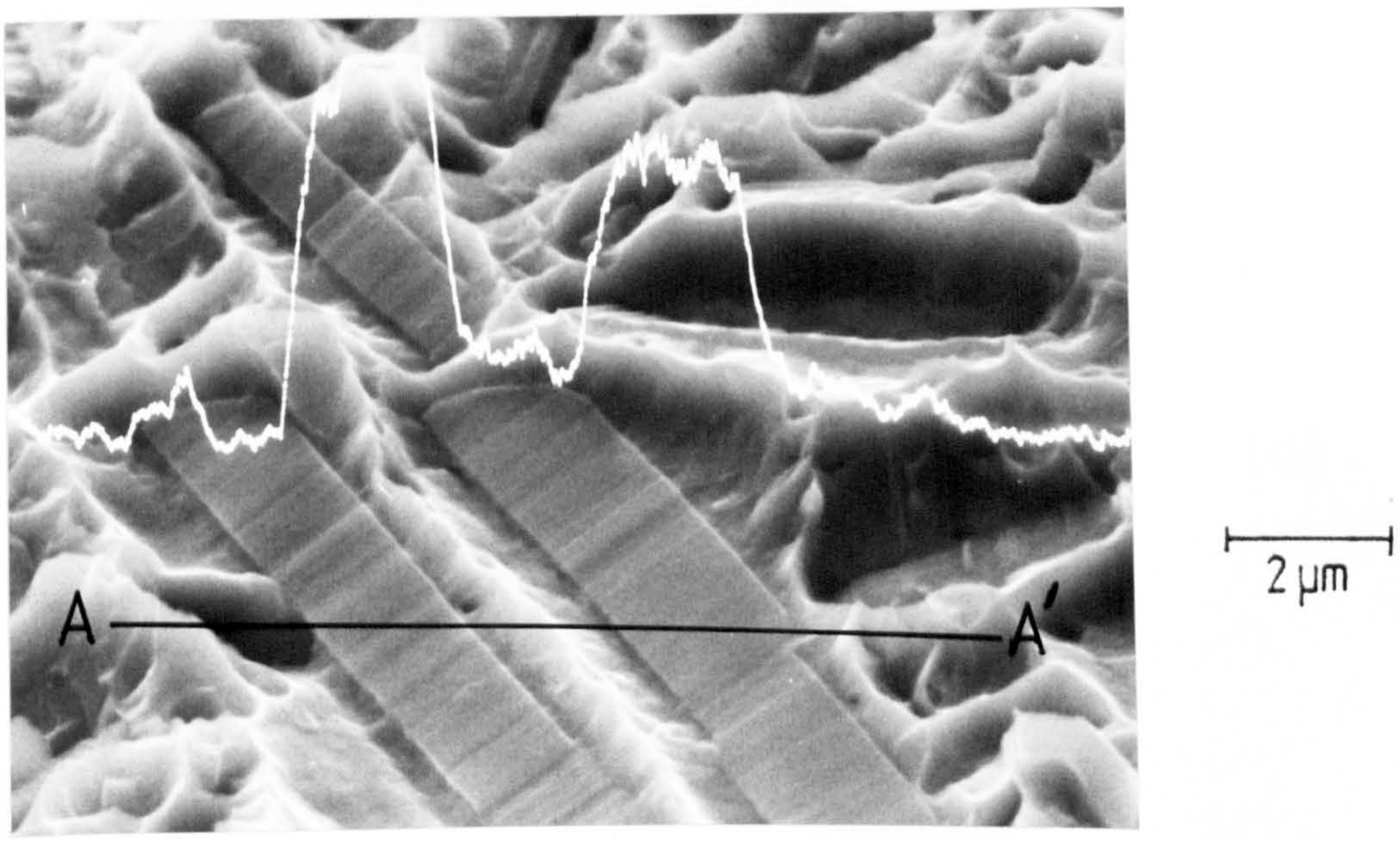

Fig. 6.36 Scanning electron micrograph of cast 4210 after 24hrs at 1250°C followed by a water quench and temper at 600°C for 1hr. The coarsened AlN precipitates are clearly visible. The superimposed trace is an X-ray scan for AlKα radiation across the line AA'.

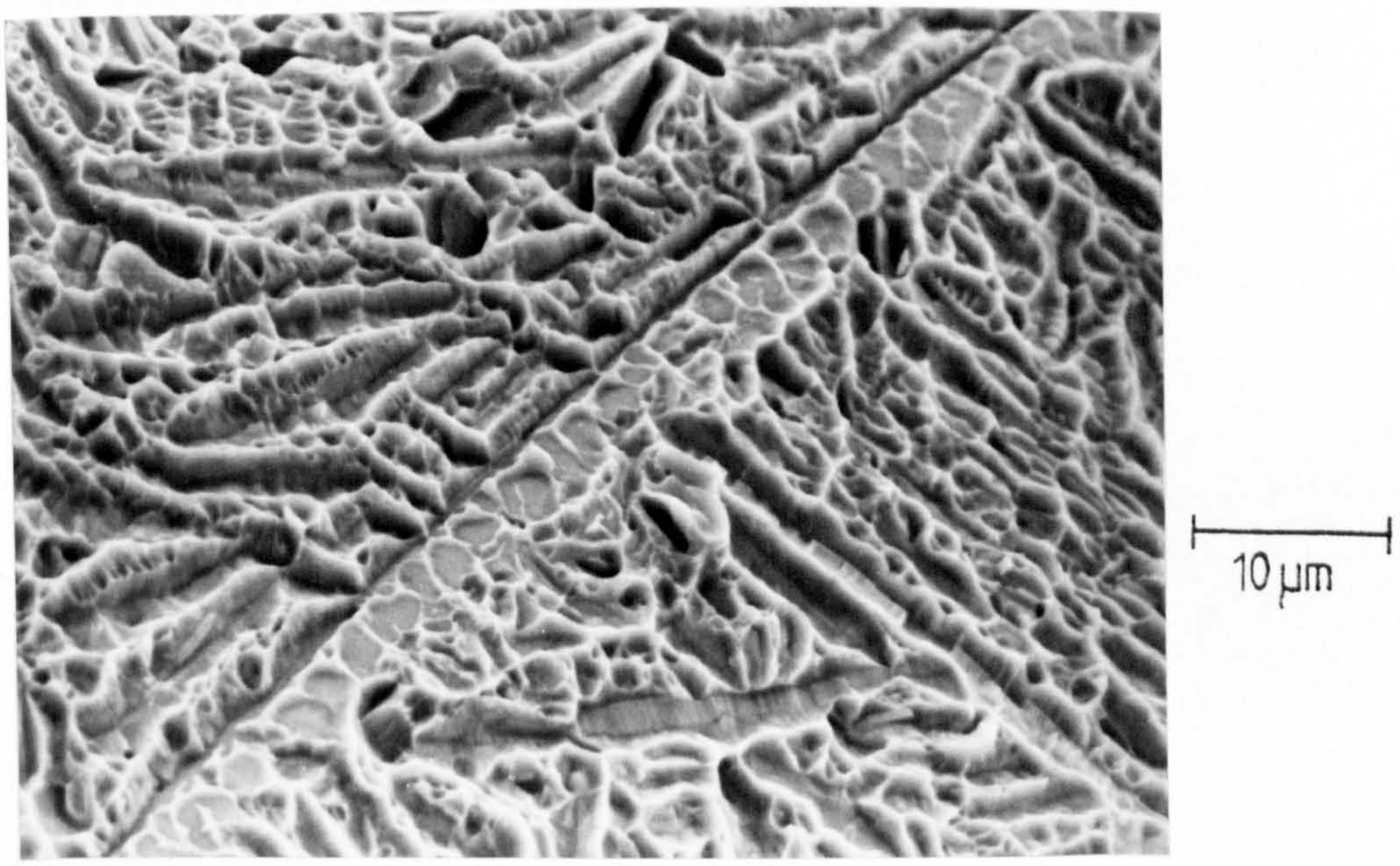

Fig. 6.37 As Fig. 6.36, showing the plate-like form of AlN which has begun to spheroidise and exhibits some microductility.

(a)

(b)

Fig. 6.38 Optical micrographs (unetched) of cast 4210 after high temperature heat treatment showing
(a) the plate-like form of the AlN and
(b) the coarsened dendrites.
Fig. 6.38a (X700)
Fig. 6.38b (X1200)

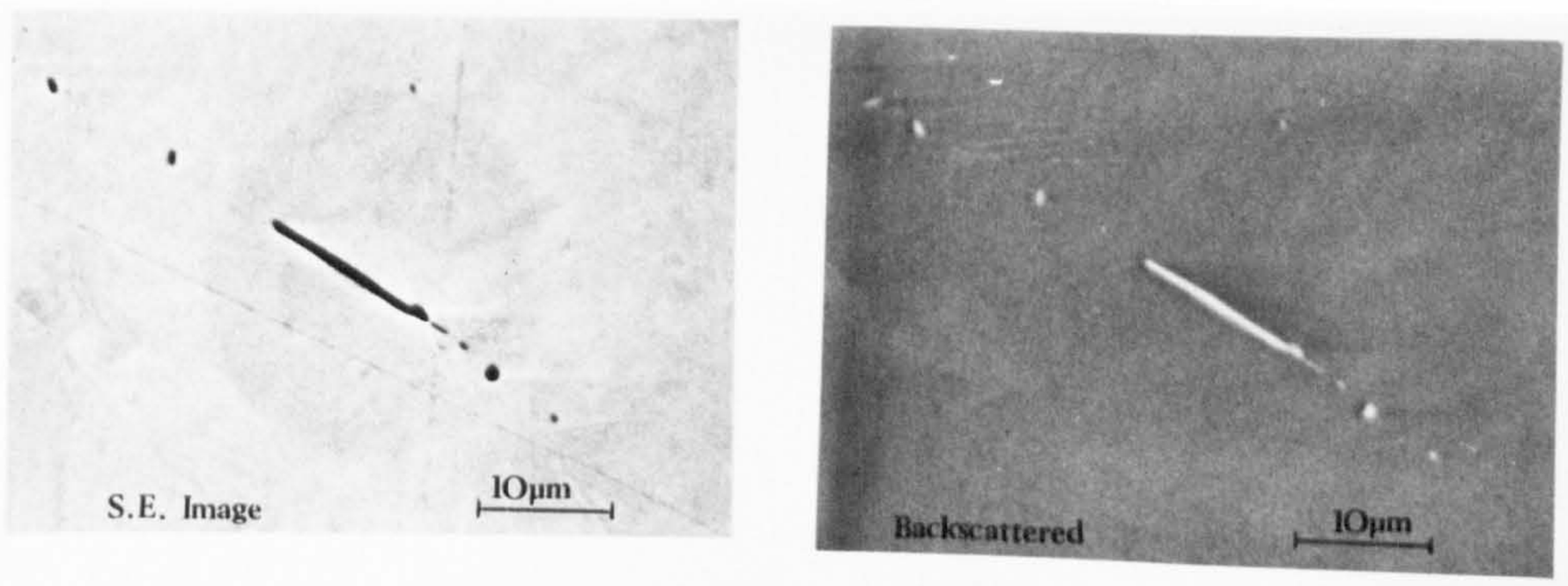

Fig. 6.39 Scanning electron micrographs of the coarsened AlN in a polished section, using secondary and backscattered electron imaging, and energy dispersive analysis.

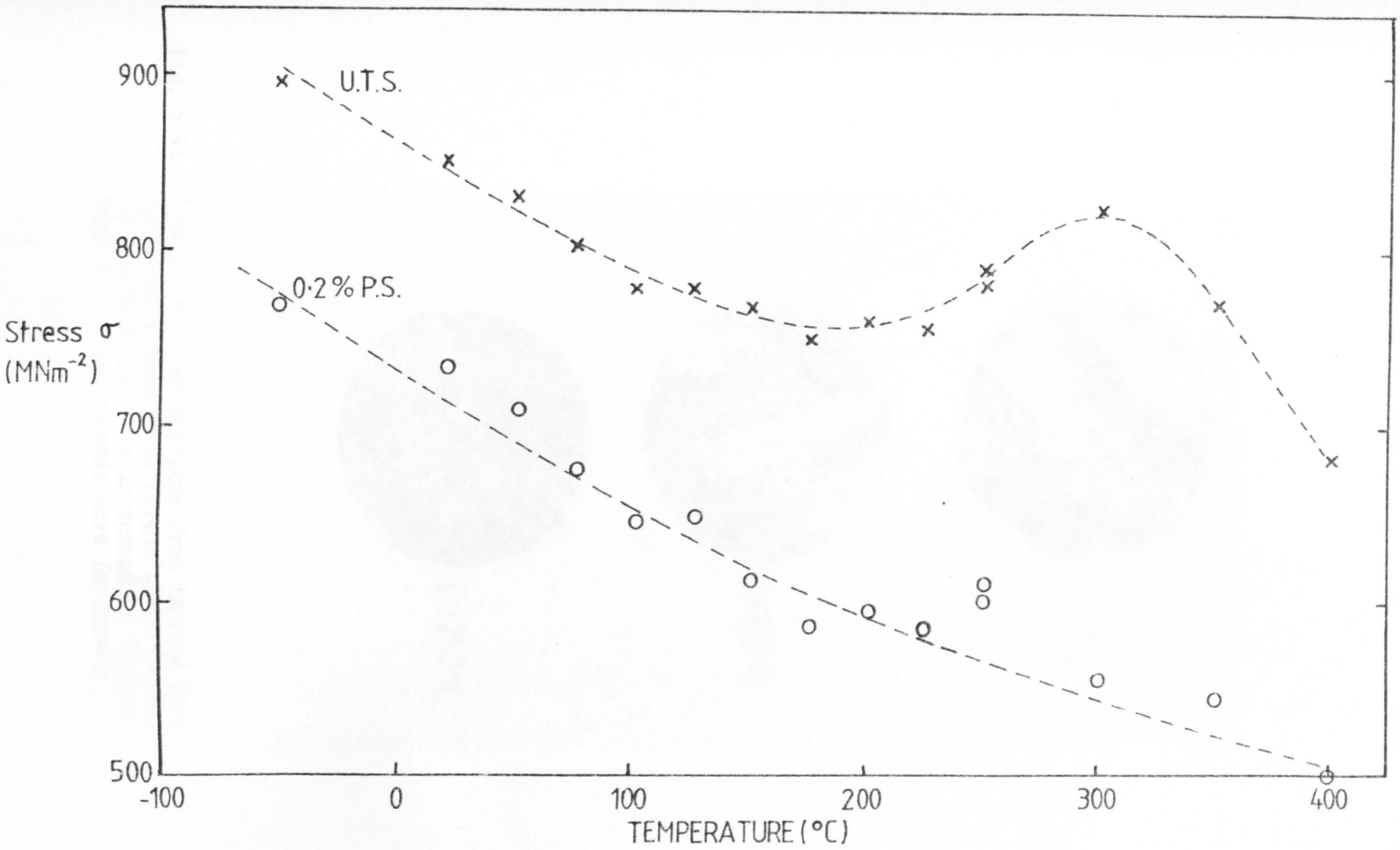

Fig. 6.40 The variation in intergranular tensile properties with temperature for cast 46/89.

(a) 20°C

(b) 125 °C

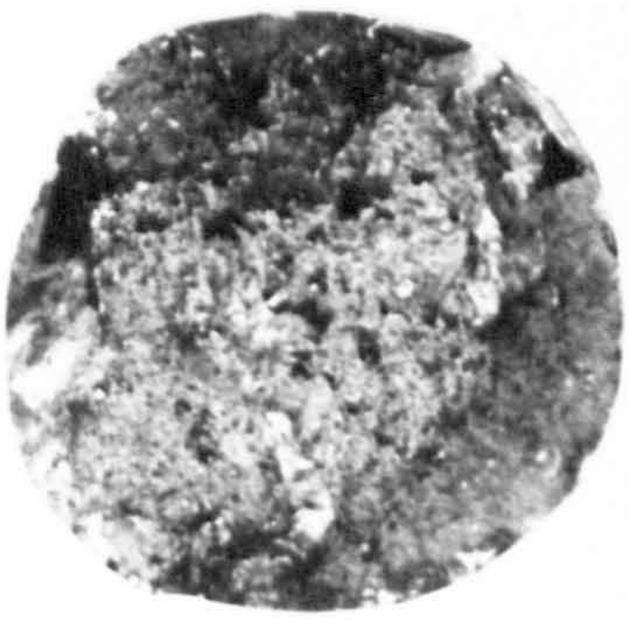

(c) 250 °C

Fig. 6.41 Typical fracture surfaces from tensile test specimens broken at different temperatures. As the temperature is increased, a fibrous mode of failure becomes more favourable.

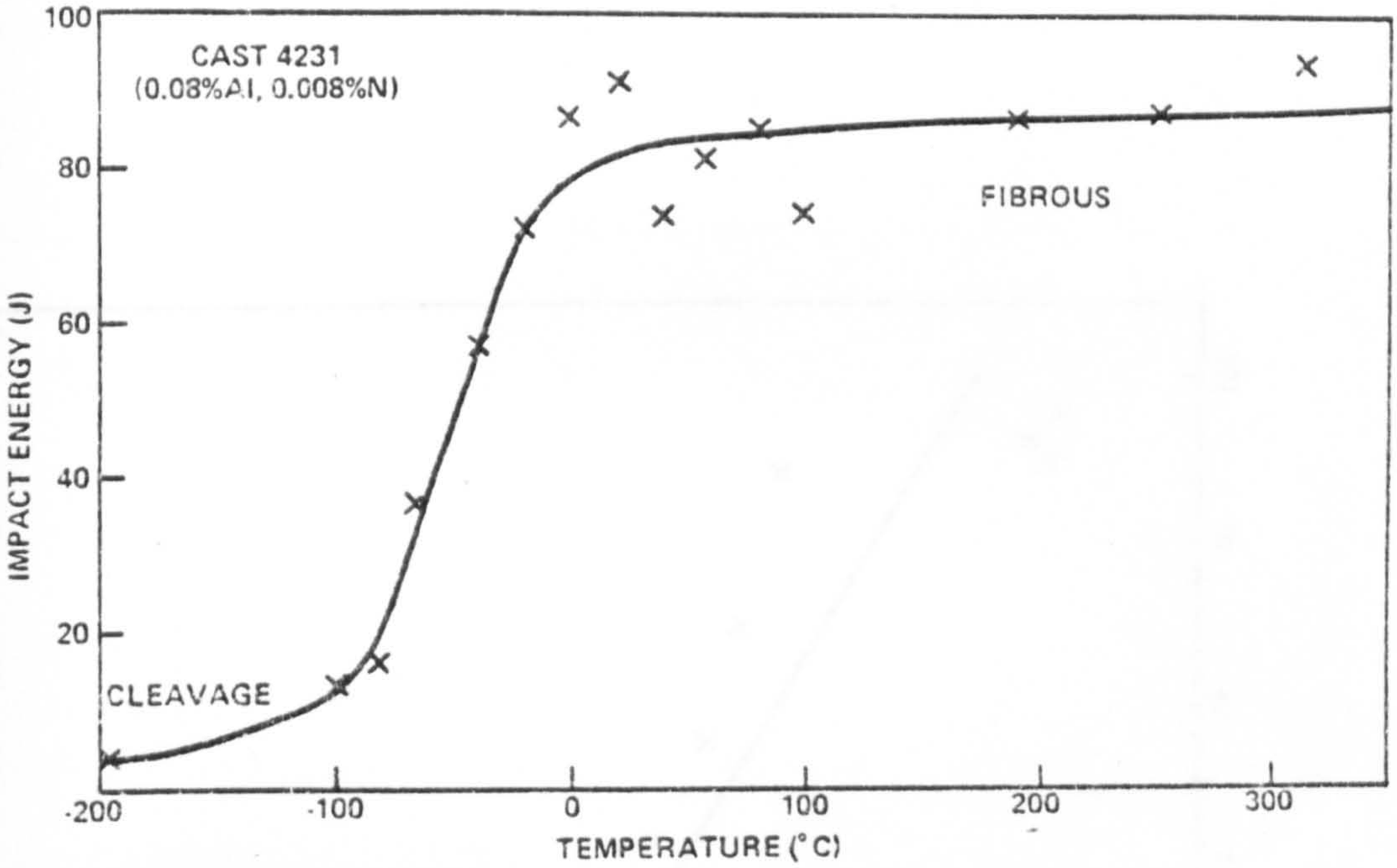

Fig. 6.42 Impact transition curve for cast 4231, containing 0.08%Al and 0.008%N. Quenched from 950°C and tempered for 1hr at 600°C.

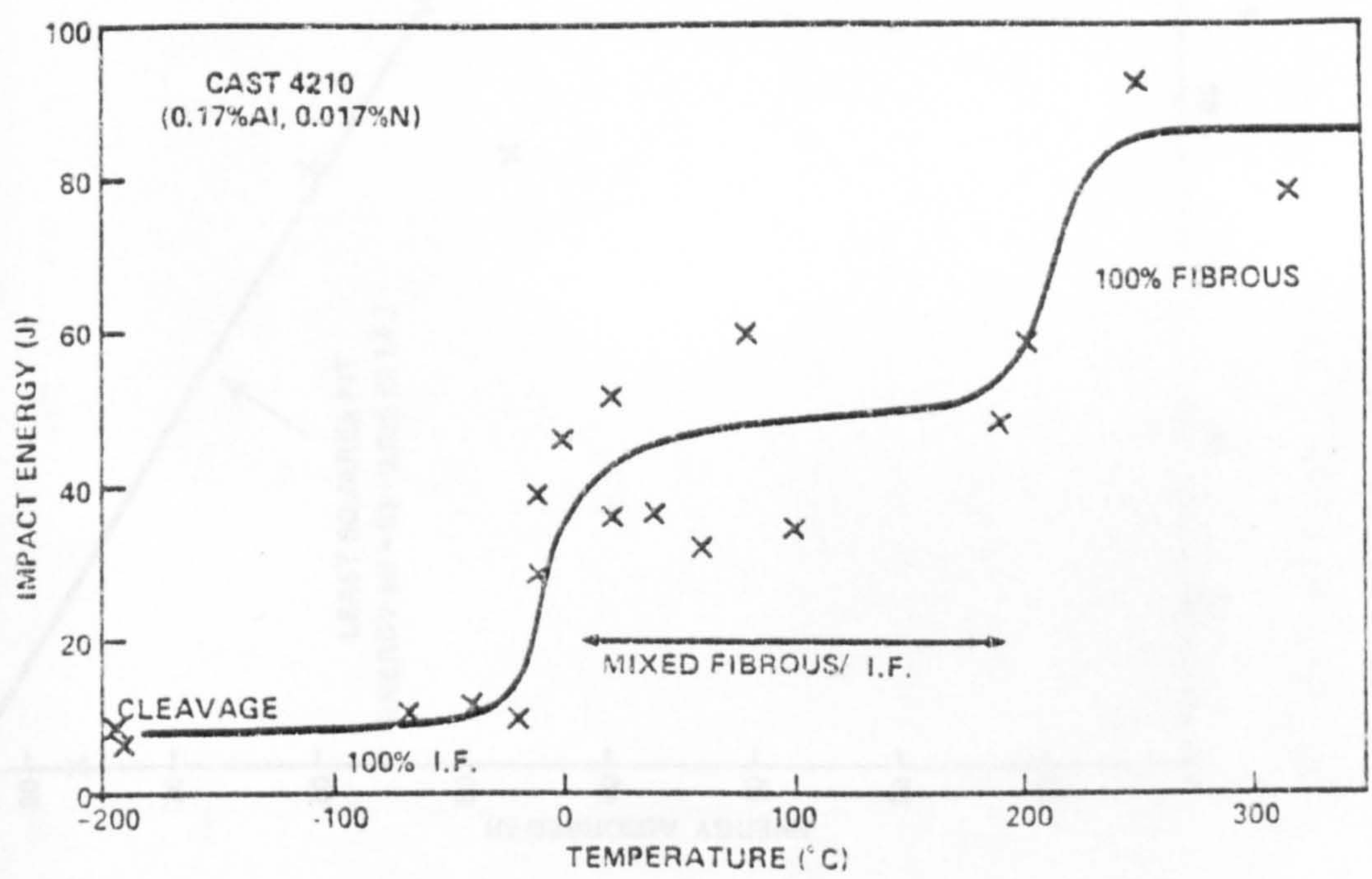

Fig. 6.43 Impact transition curve for cast 4210, containing 0.17%Al and 0.017%N. Quenched from 950°C and tempered for 1hr at 600°C. Note that the true upper shelf energy is not attained until temperatures in excess of 200°C because of the intergranular fracture regime.

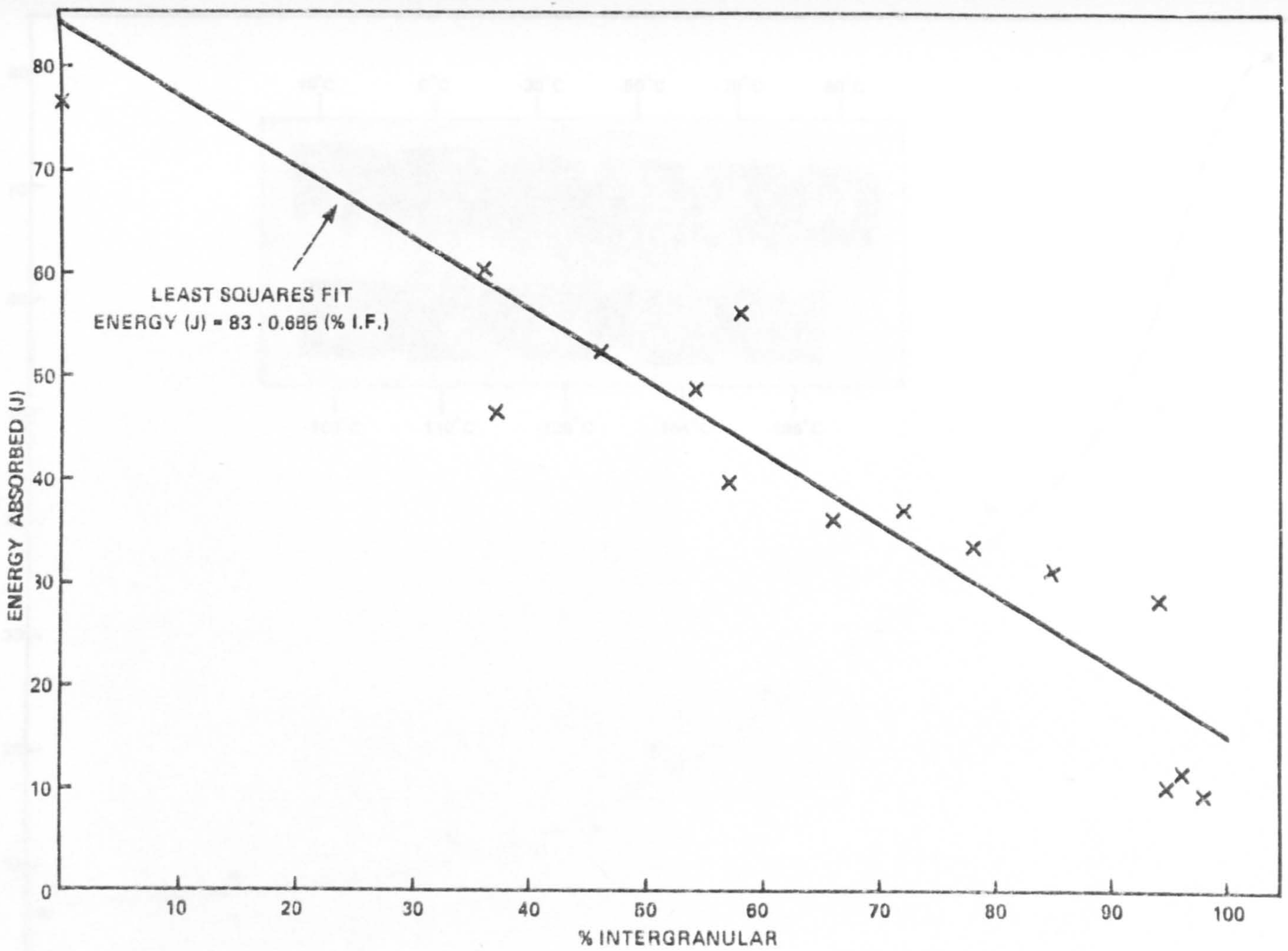

Fig. 6.44 Variation in impact energy with %I.F. for cast 4210.

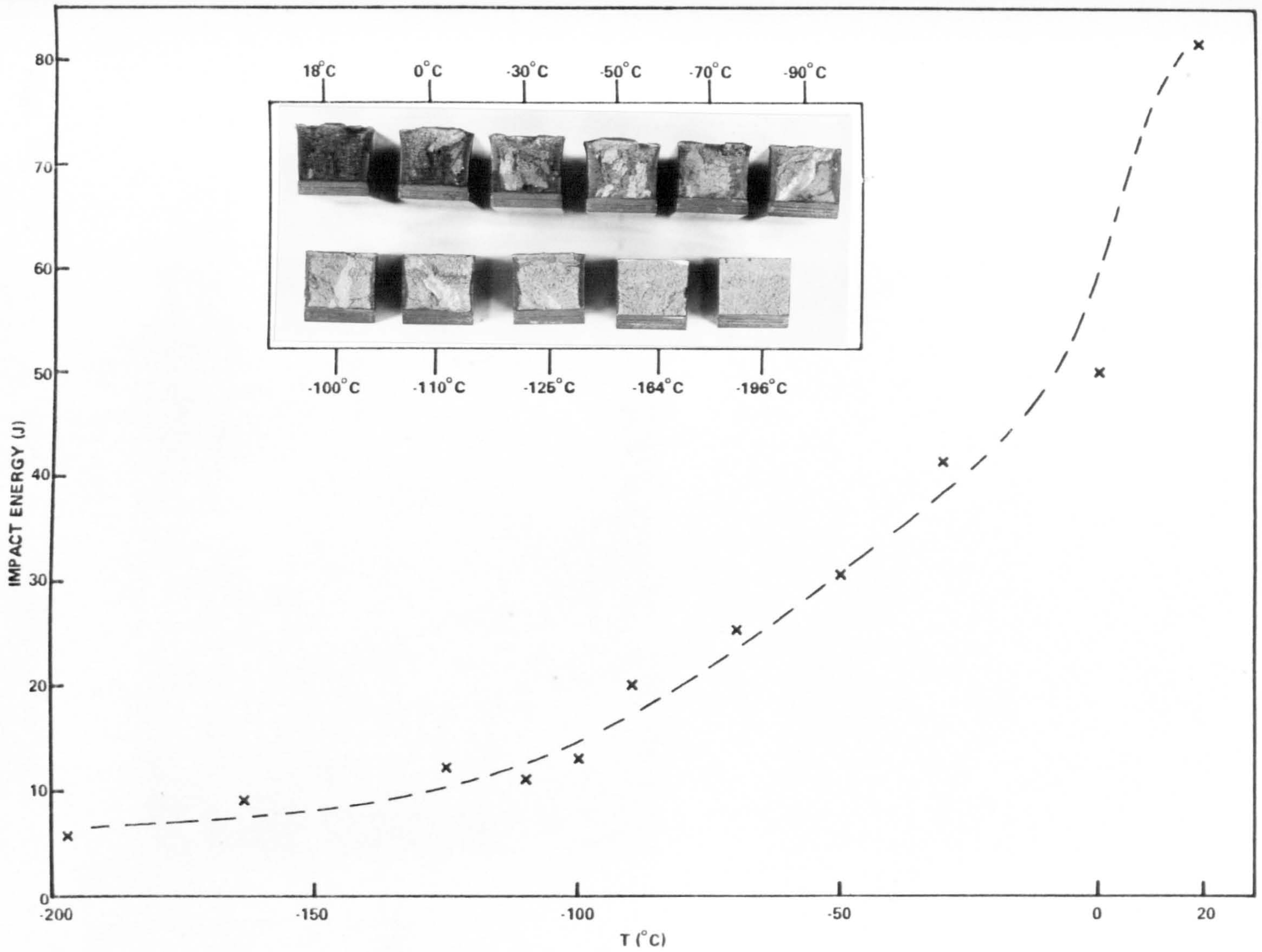

Fig. 6.45 Impact transition curve for cast 4351, containing 0.12%Al and 0.014%N. The variation in fracture morphology with temperature is also shown.

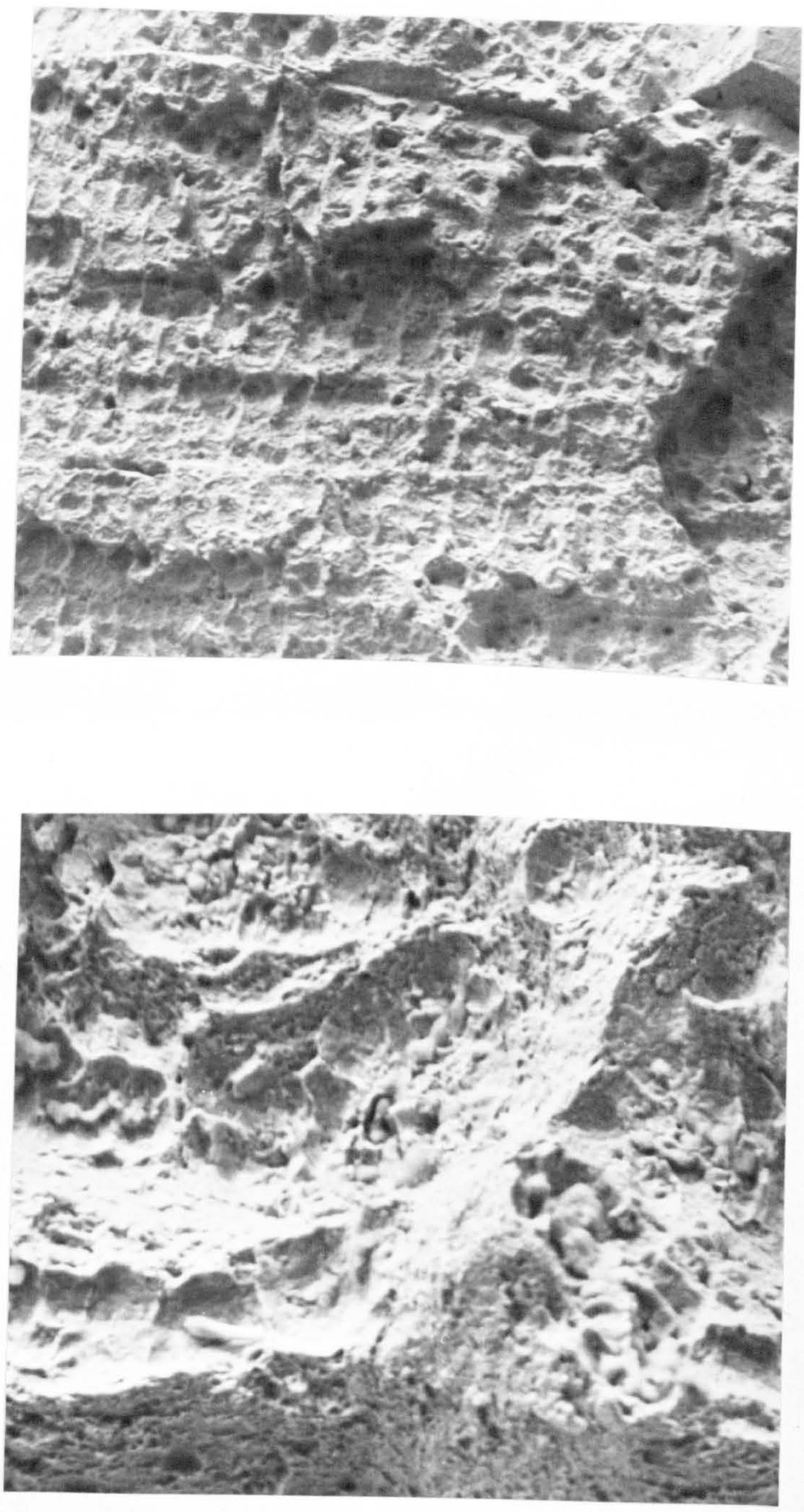

(a)

(b)

Fig. 6.46(a) Scanning electron micrograph showing coarse dendritic features on the fibrous fracture surface of cast 4351. (X80)

(b) A dendritic feature in more detail showing that fracture has been initiated in the normal way, by void nucleation at MnS inclusions. (X540)

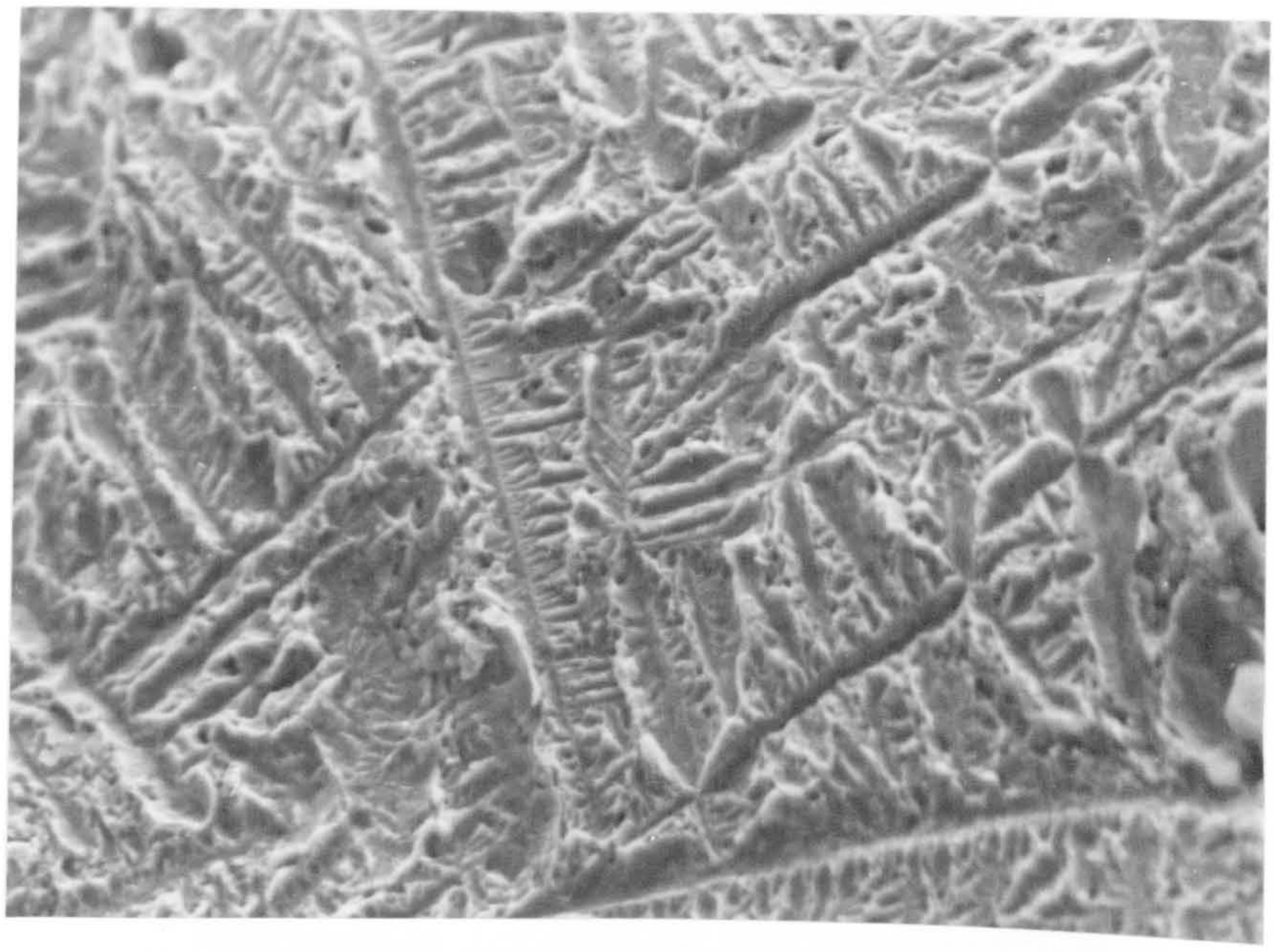

(a)

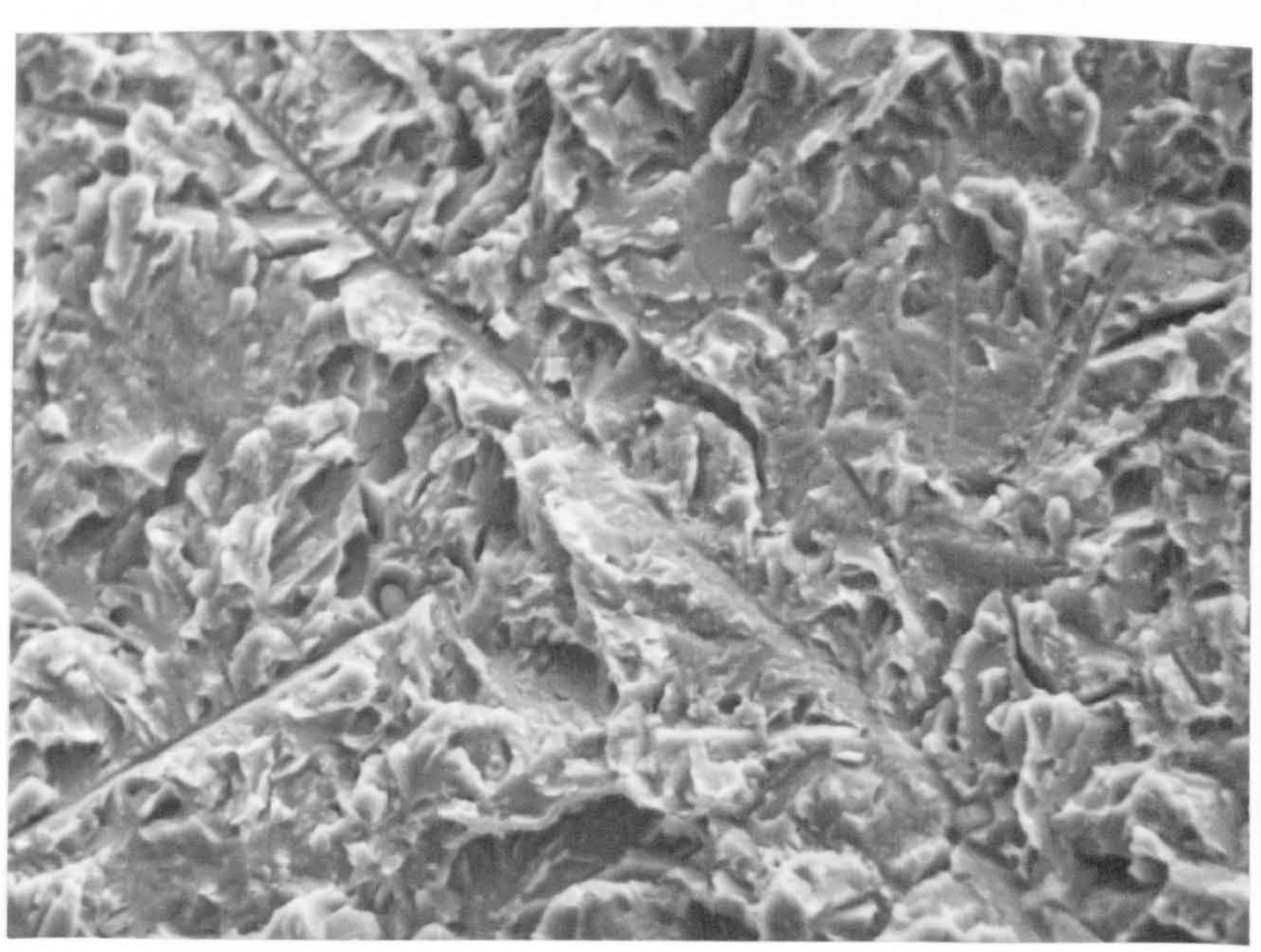

(b)

Fig. 6.47 Scanning electron micrographs showing the change in fracture morphology with decreasing testing temperature. Intergranular facets on Charpy impact specimens taken from cast 4351, fractured at (a) -30°C and (b) -125°C. (X640)

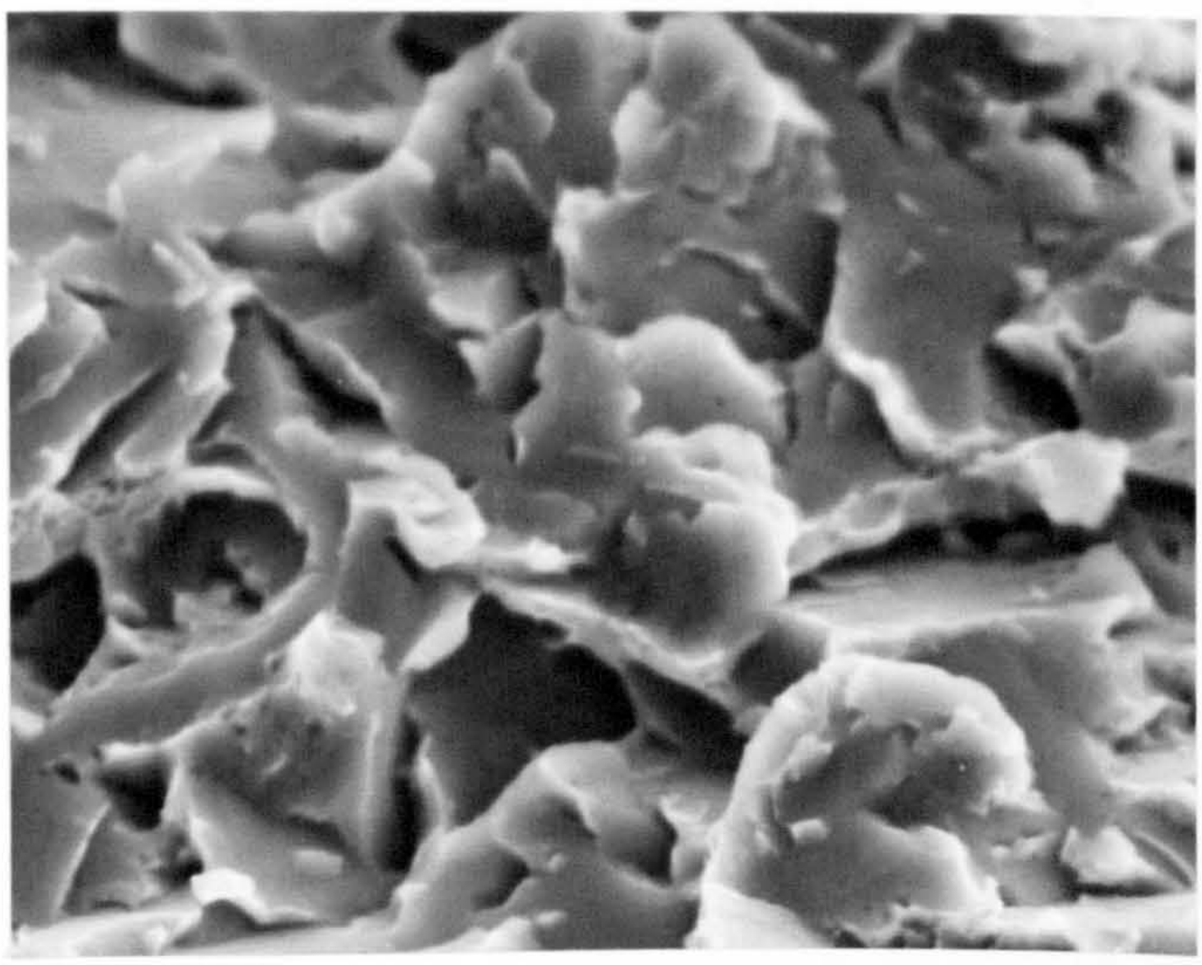

Fig. 6.48 Scanning electron micrograph showing cleavage, the typical low temperature fracture mechanism for all the Charpy samples. (X320)

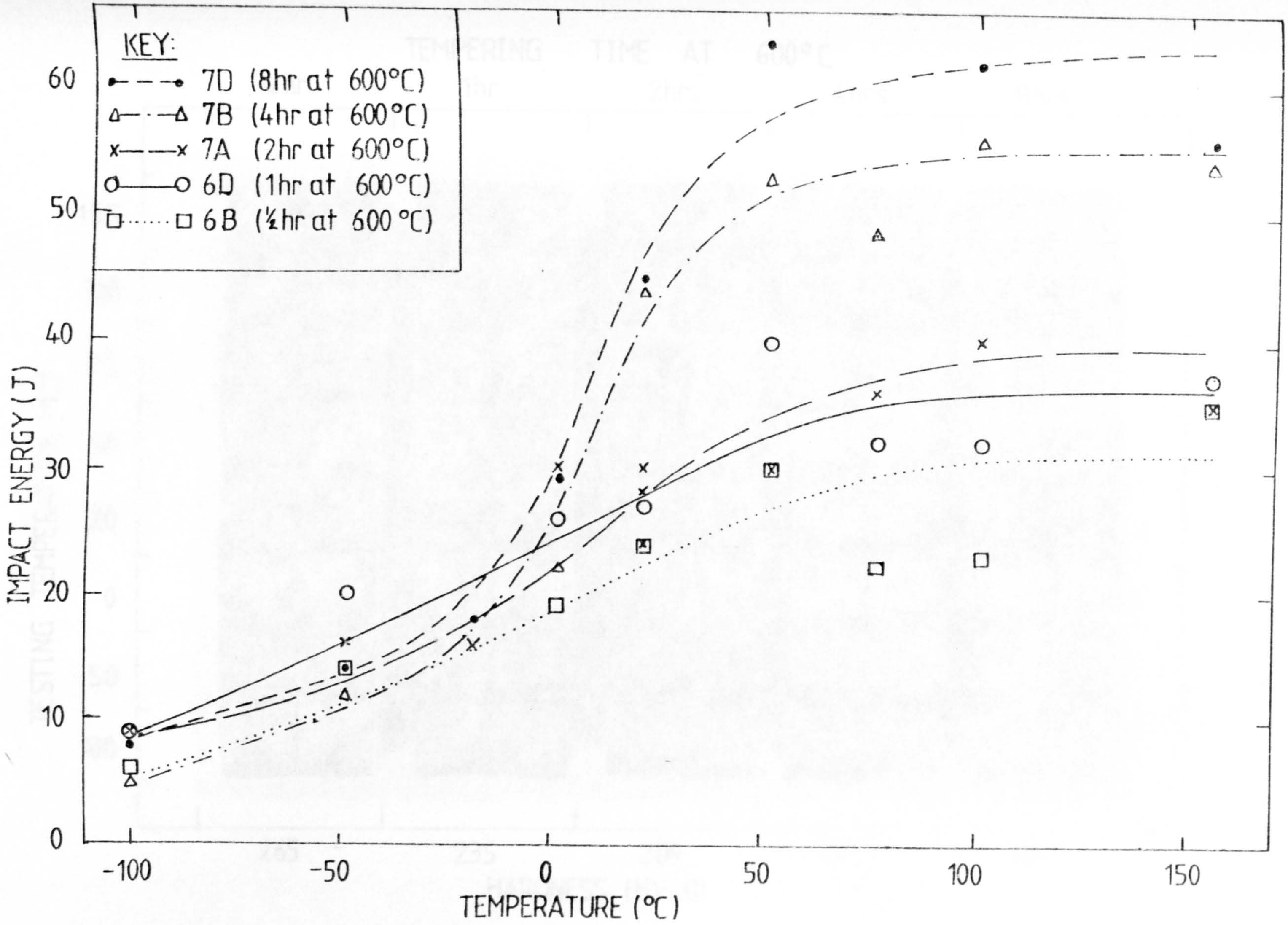

Fig. 6.49 Impact transition curves for casts 46/6 and 46/7, tempered to different hardness levels.

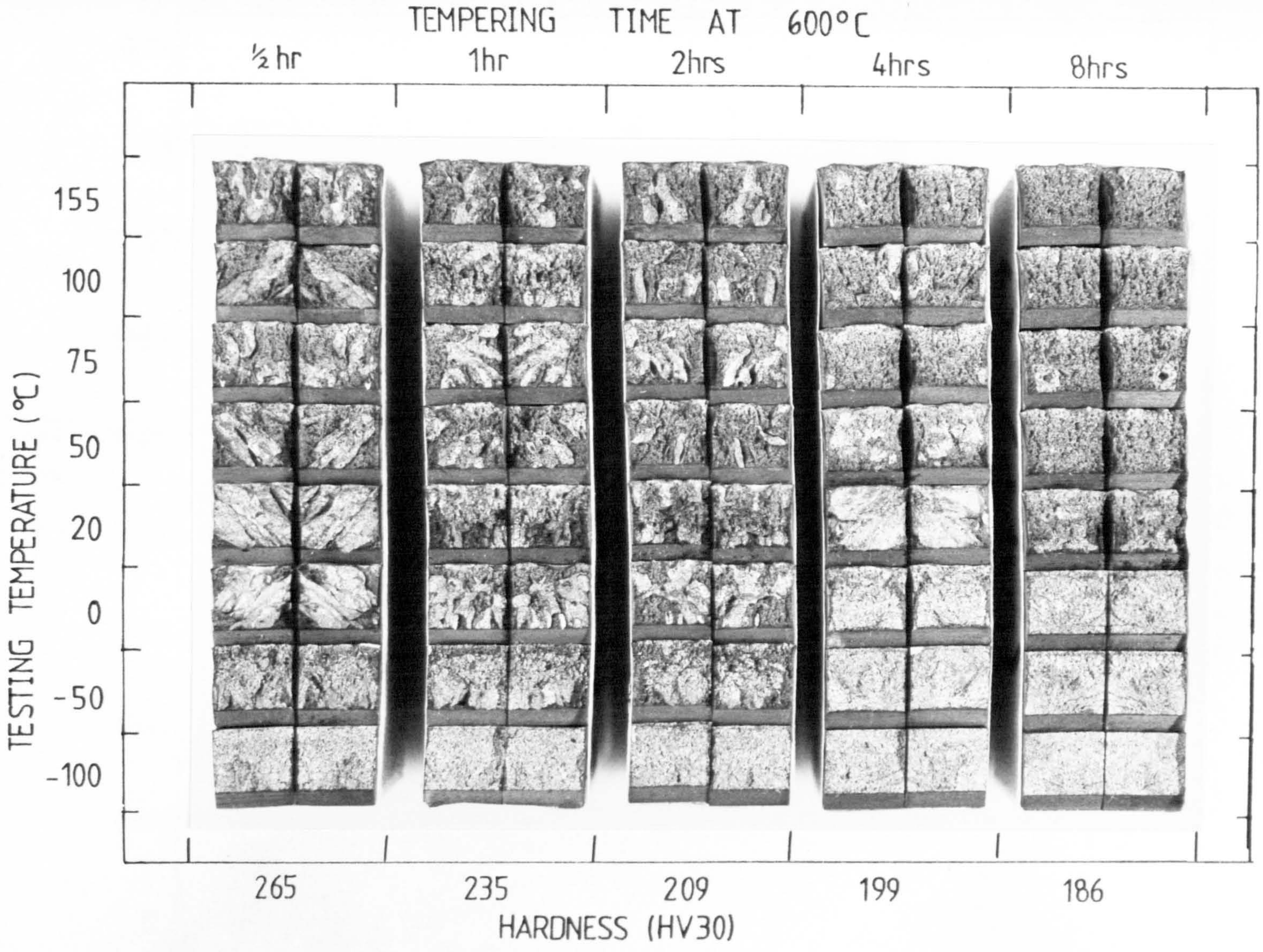

Fig. 6.50 The fracture characteristics of Charpy samples as a function of testing temperature for a range of hardness levels.

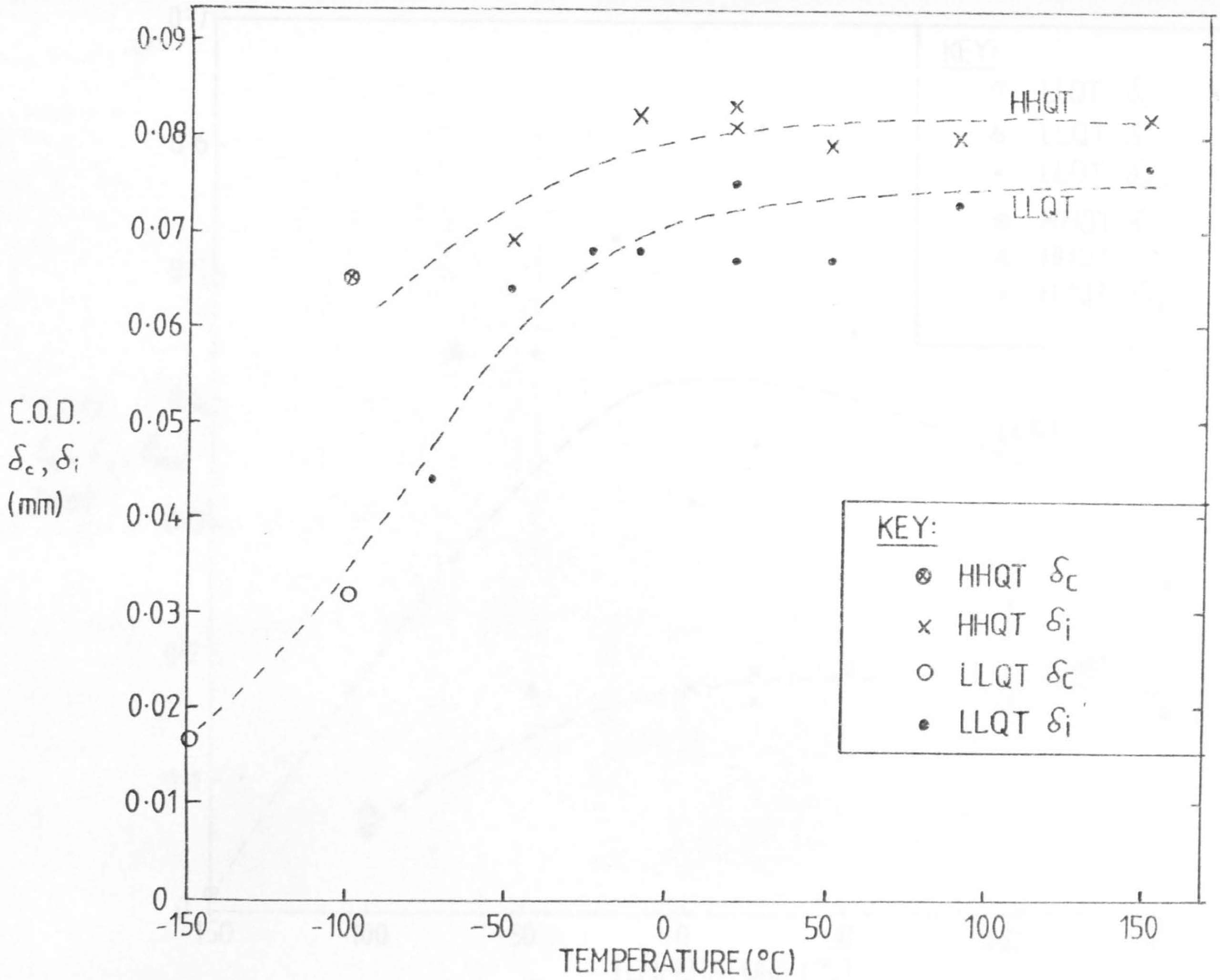

Fig. 6.51 COD transition curve for quenched and tempered casts based on δ_c and δ_i as 'critical' values.

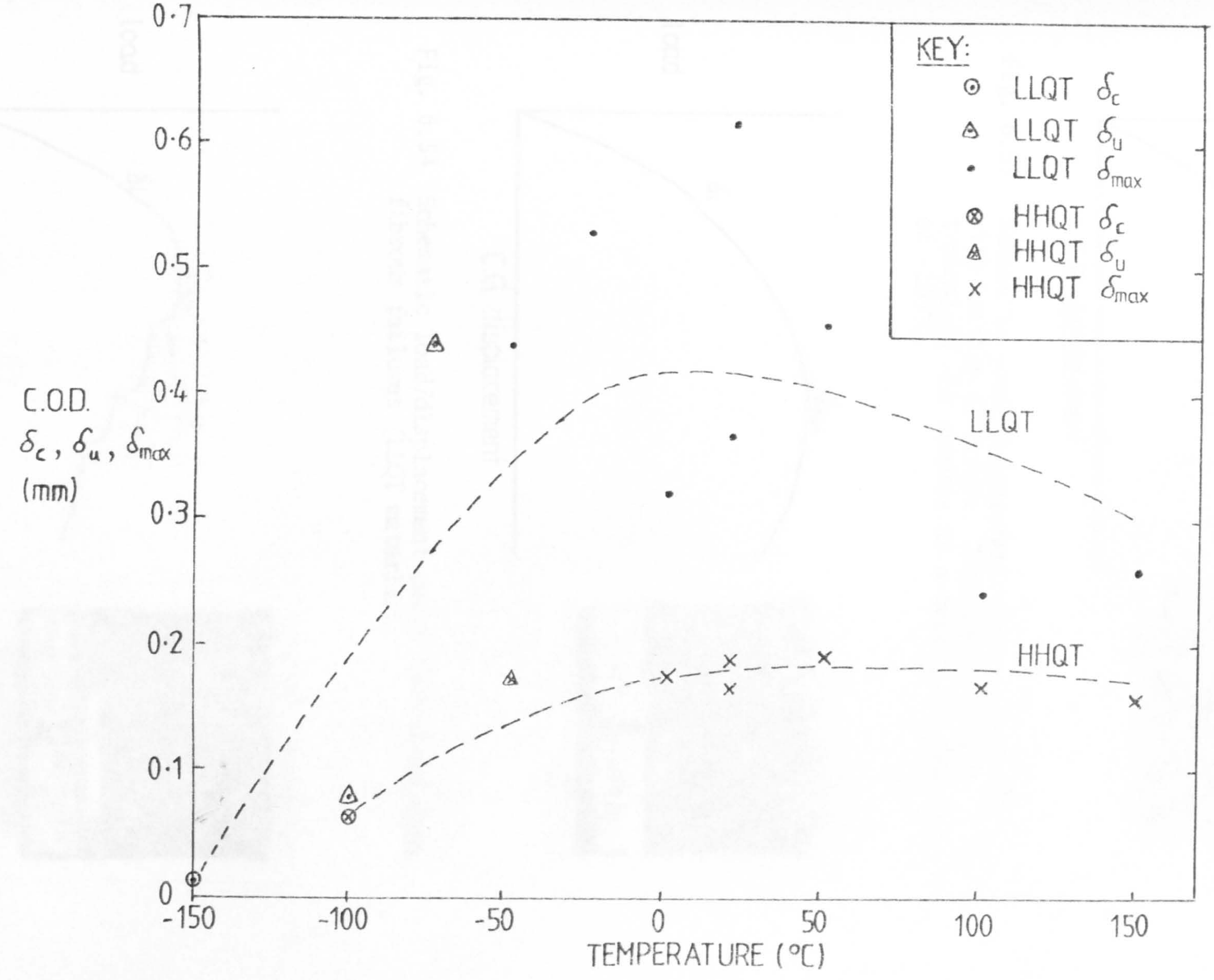

Fig. 6.52 COD transition curve for quenched and tempered casts based on δ_c, δ_u and δ_{max} as 'critical' values.

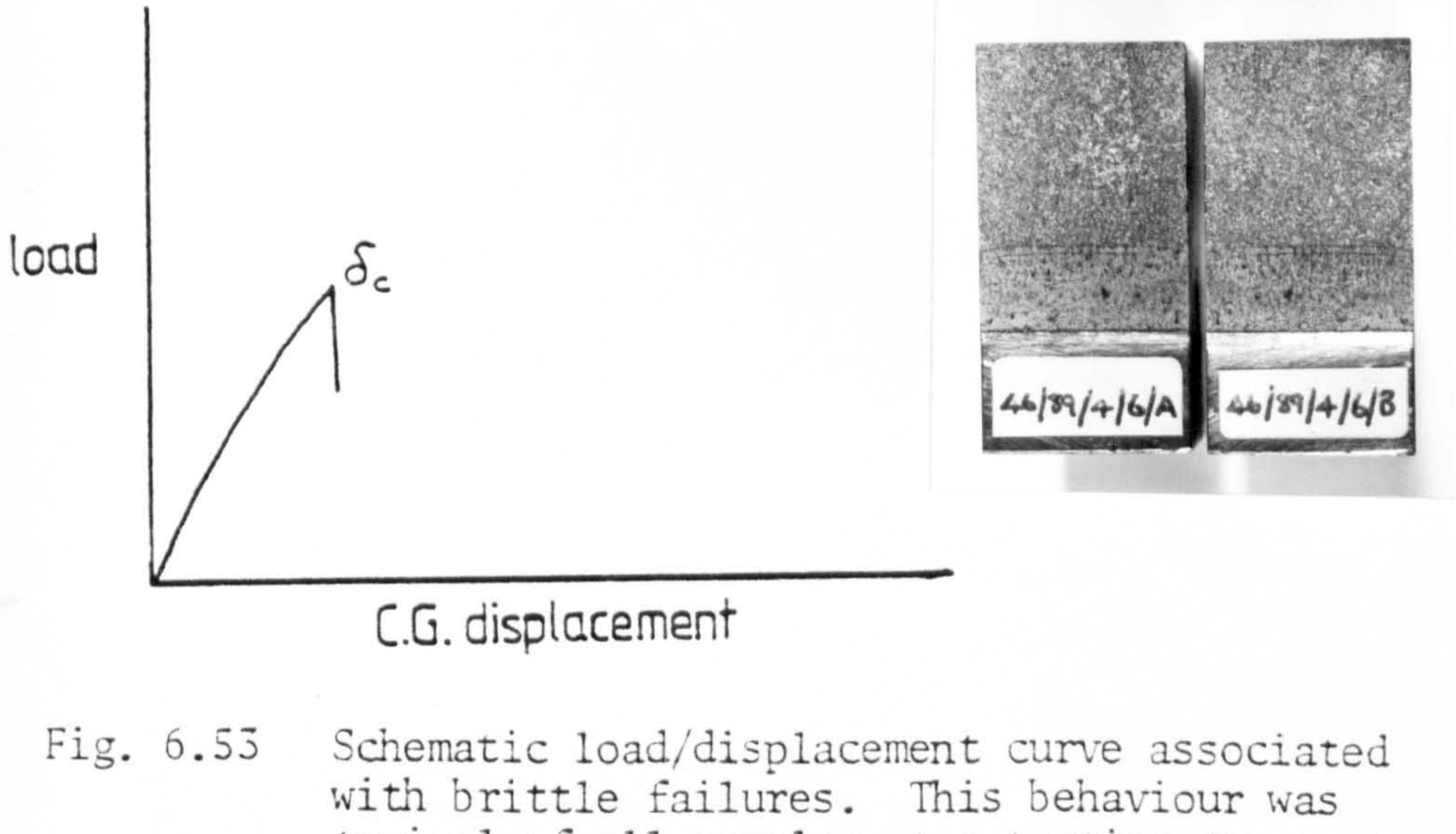

Fig. 6.53 Schematic load/displacement curve associated with brittle failures. This behaviour was typical of all samples at a testing temperature of -100°C.

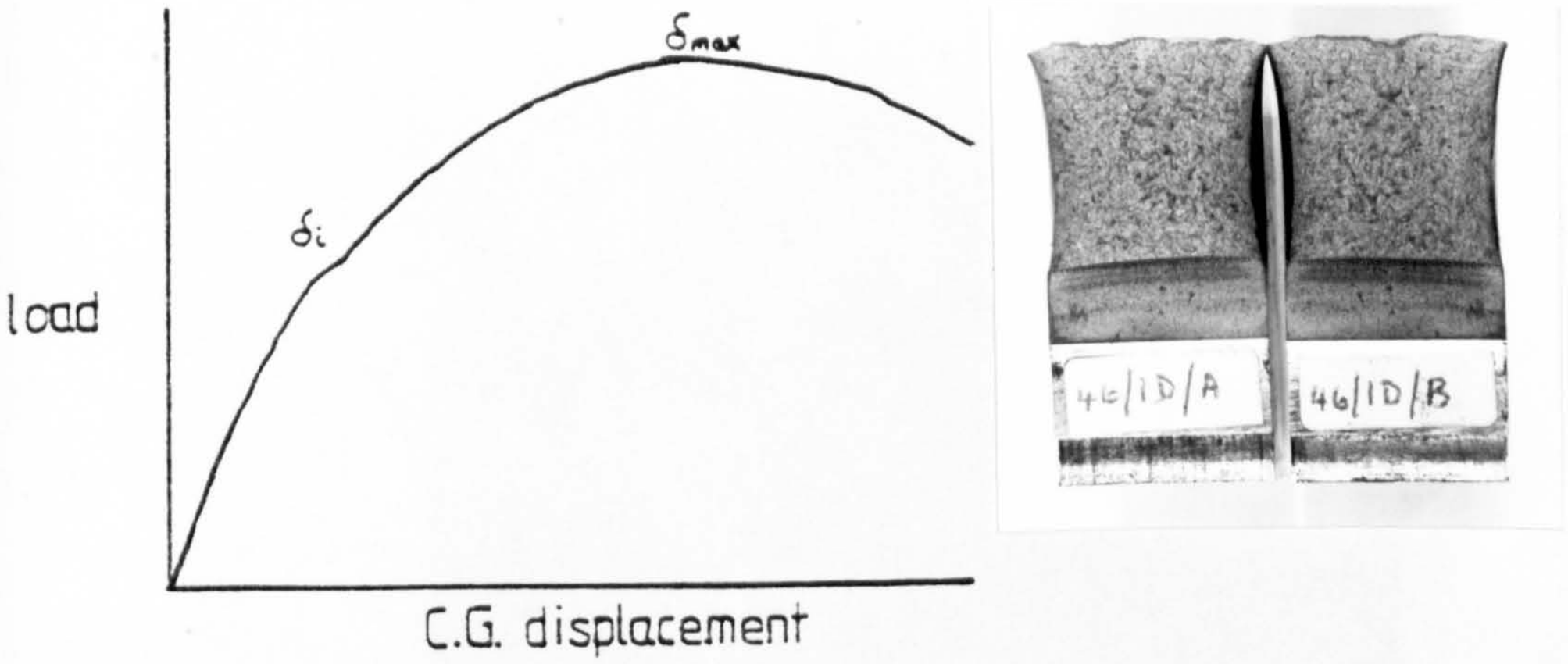

Fig. 6.54 Schematic load/displacement curve associated with fibrous failures (LLQT material).

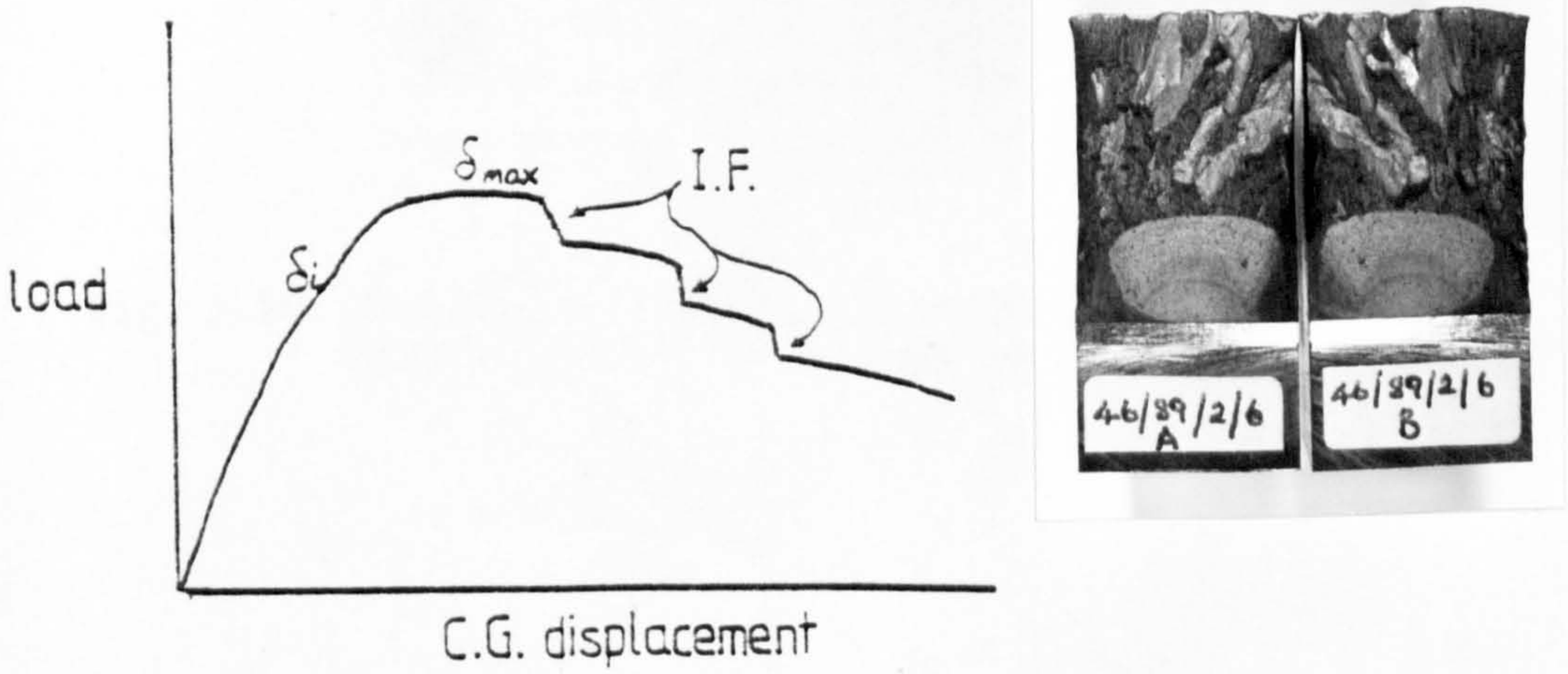

Fig. 6.55 Schematic load/displacement curve associated with mixed I.F./fibrous failures (HHQT material). Note the discontinuous steps after the attainment of maximum load.

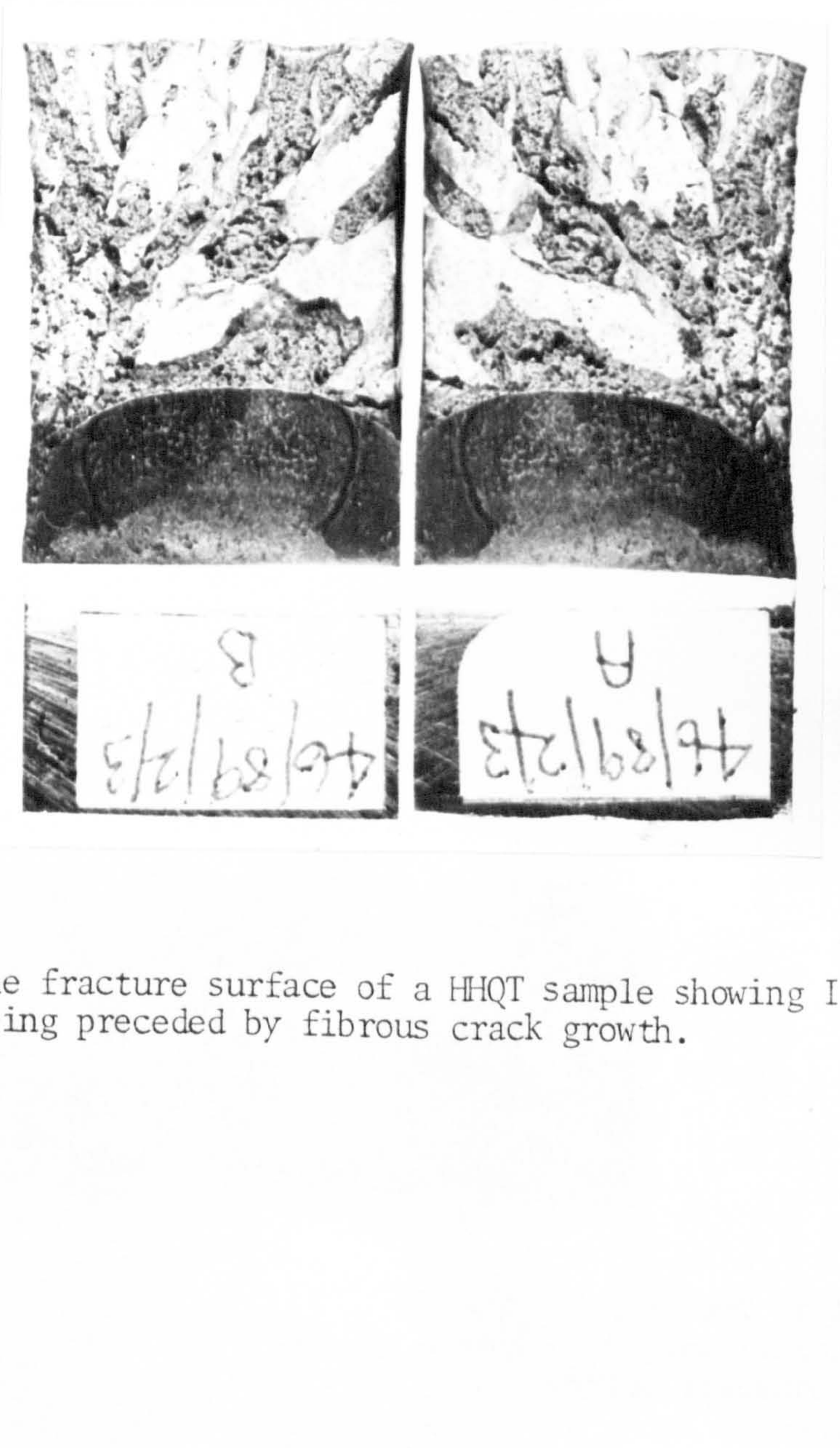

Fig. 6.56 The fracture surface of a HHQT sample showing I.F. being preceded by fibrous crack growth.

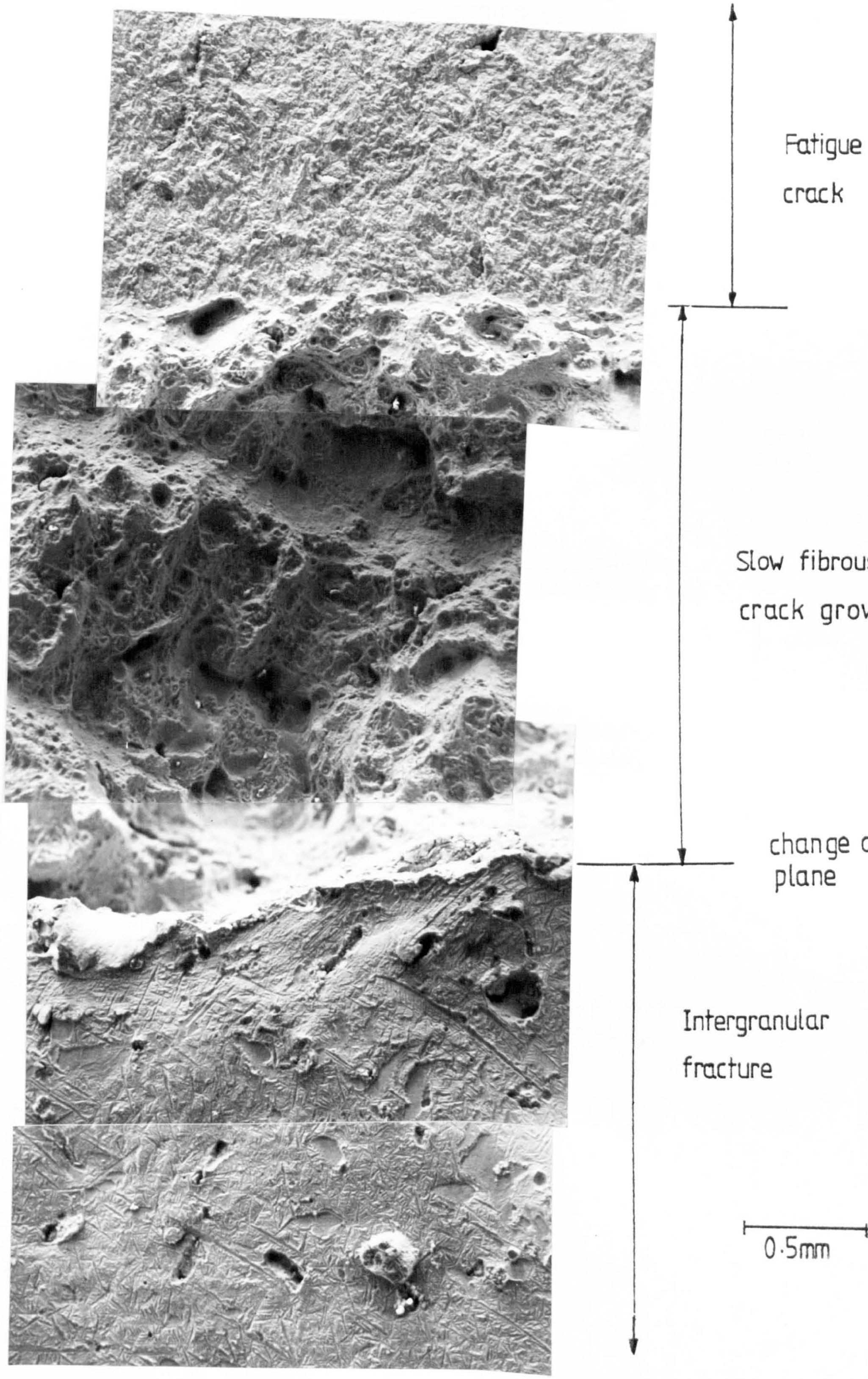

Fig. 6.57 Scanning electron micrograph at the root of a fatigue crack showing a region of slow fibrous crack growth prior to intergranular fracture. In order to propagate along the grain boundary, the crack had to deviate from its original plane by 1.3mm.

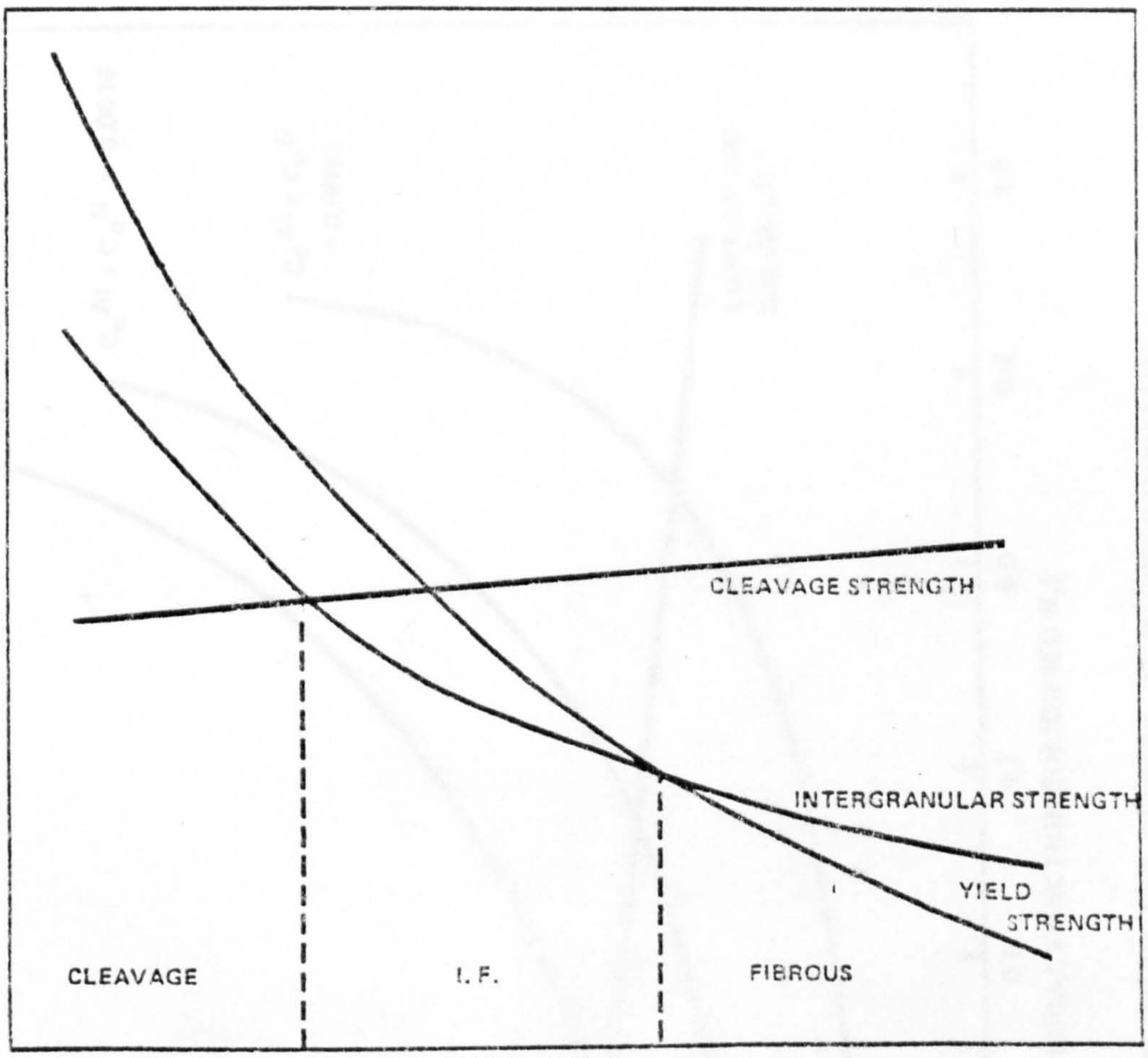

Fig. 7.1 Schematic diagram showing the variation of cleavage, intergranular and yield strengths with temperature. At a given temperature, fracture is likely to follow the weakest path.

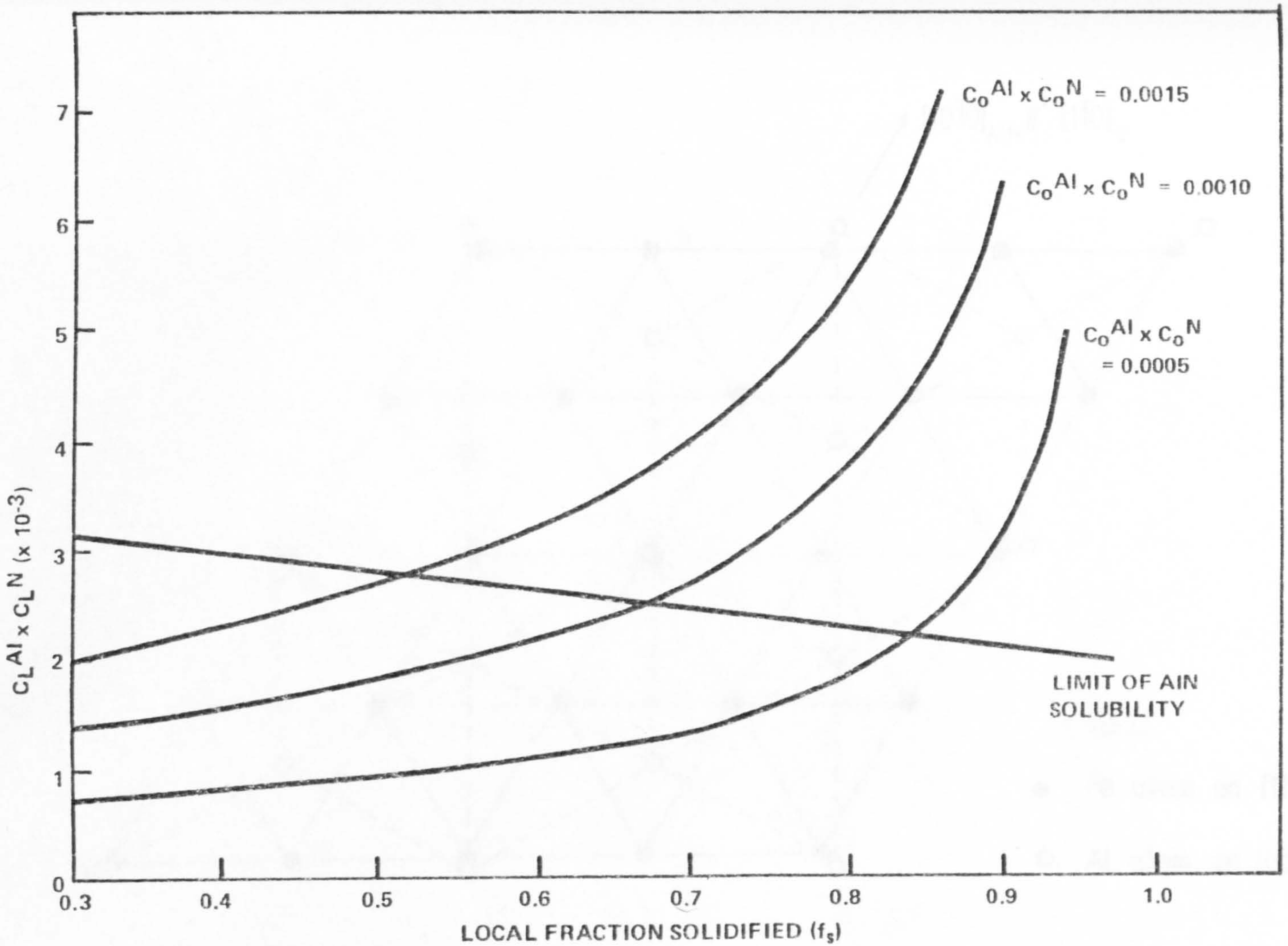

Fig. 7.2 Graph showing the effects of microsegregation of Al and N on the precipitation of AlN in the liquid state. For a given bulk liquid composition, (C_o^{Al} and C_o^N), precipitation can begin when the local concentrations of Al and N in the residual liquid, (C_L^{Al} and C_L^N), exceed the solubility product.

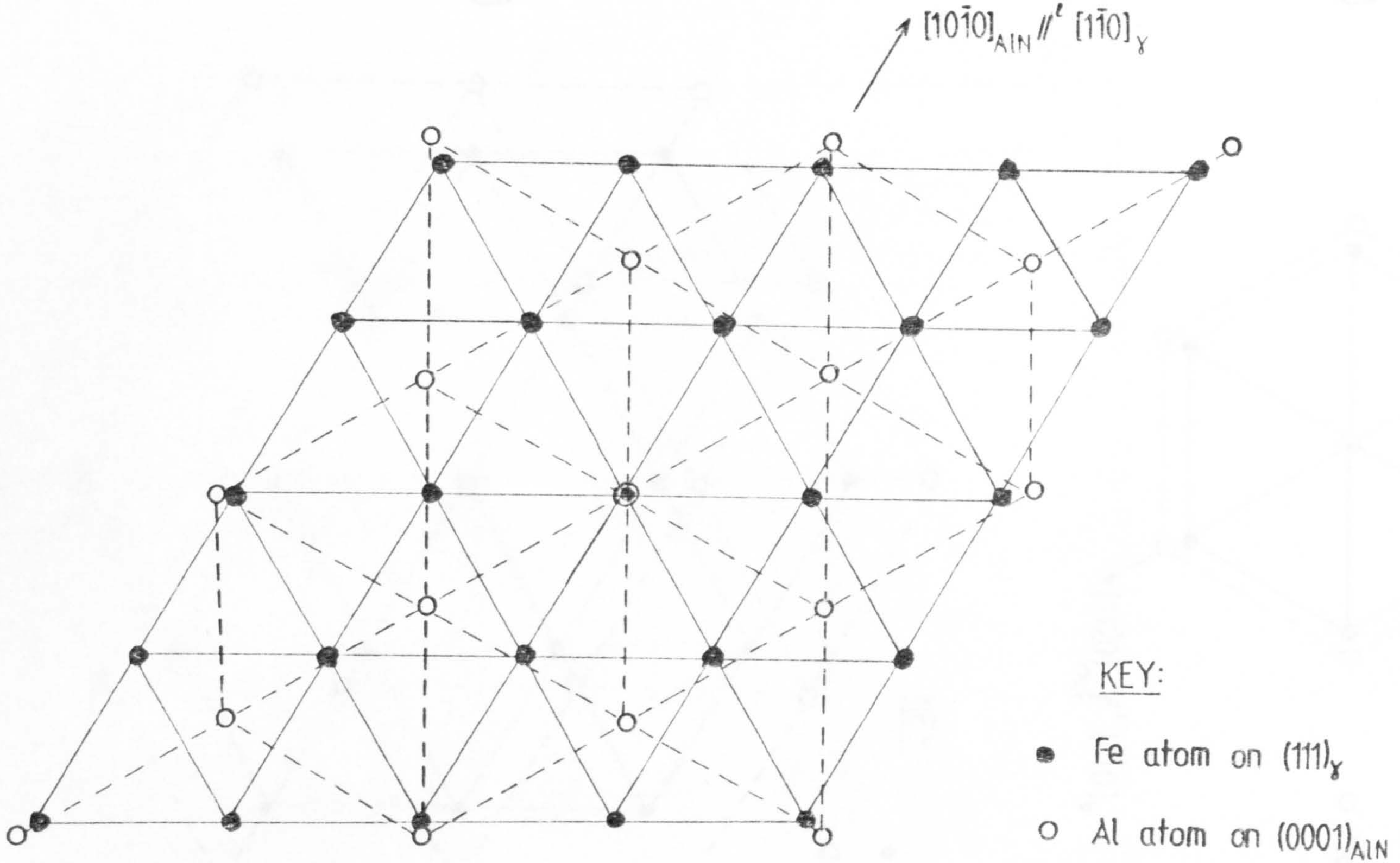

Fig. 7.3 The arrangement of aluminium and iron atoms on the $(0001)_{AlN}$ // $(111)_{\gamma}$ planes, with $[10\bar{1}0]_{AlN}$ // $[1\bar{1}0]_{\gamma}$

(a)

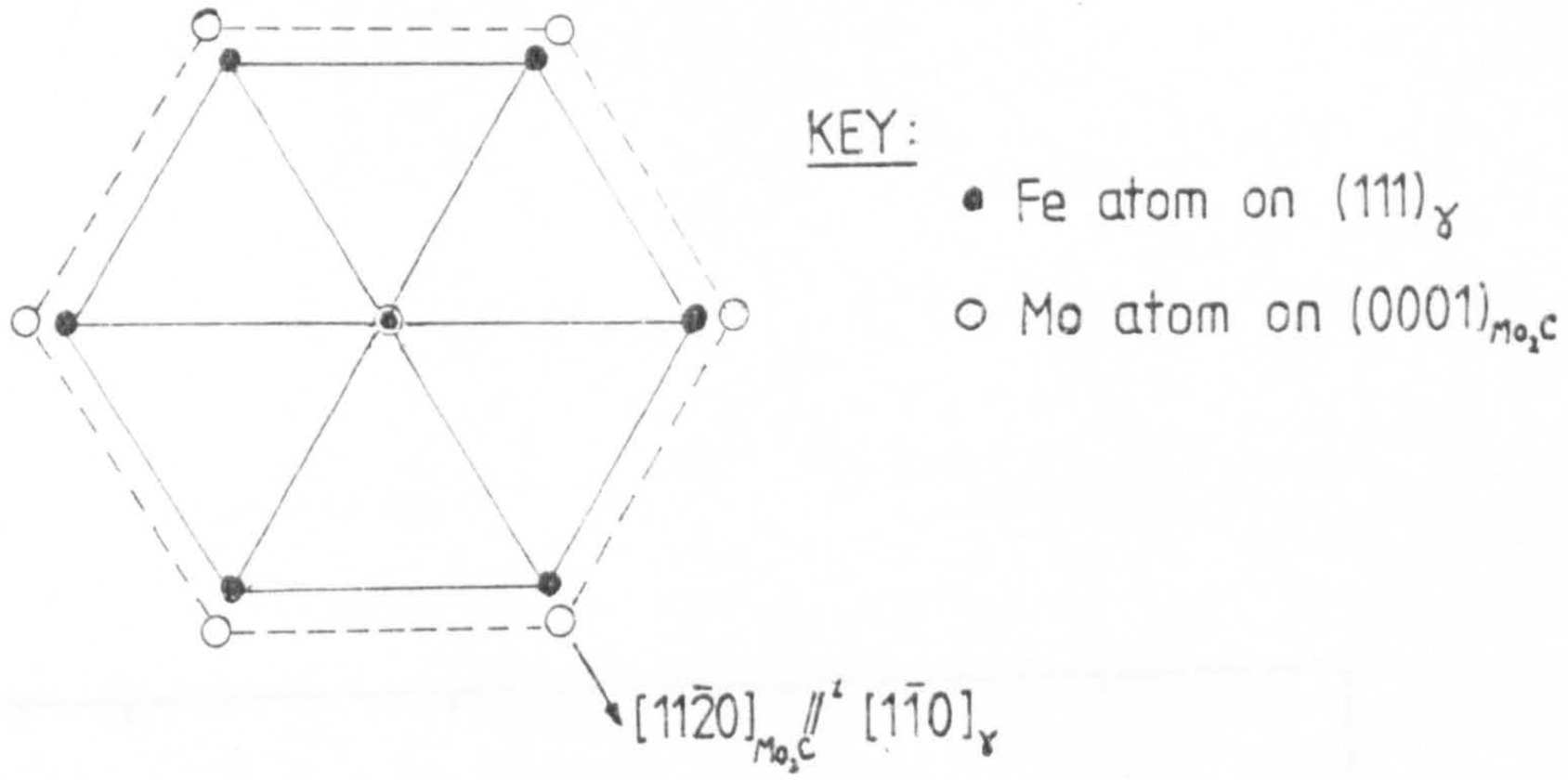

(b)

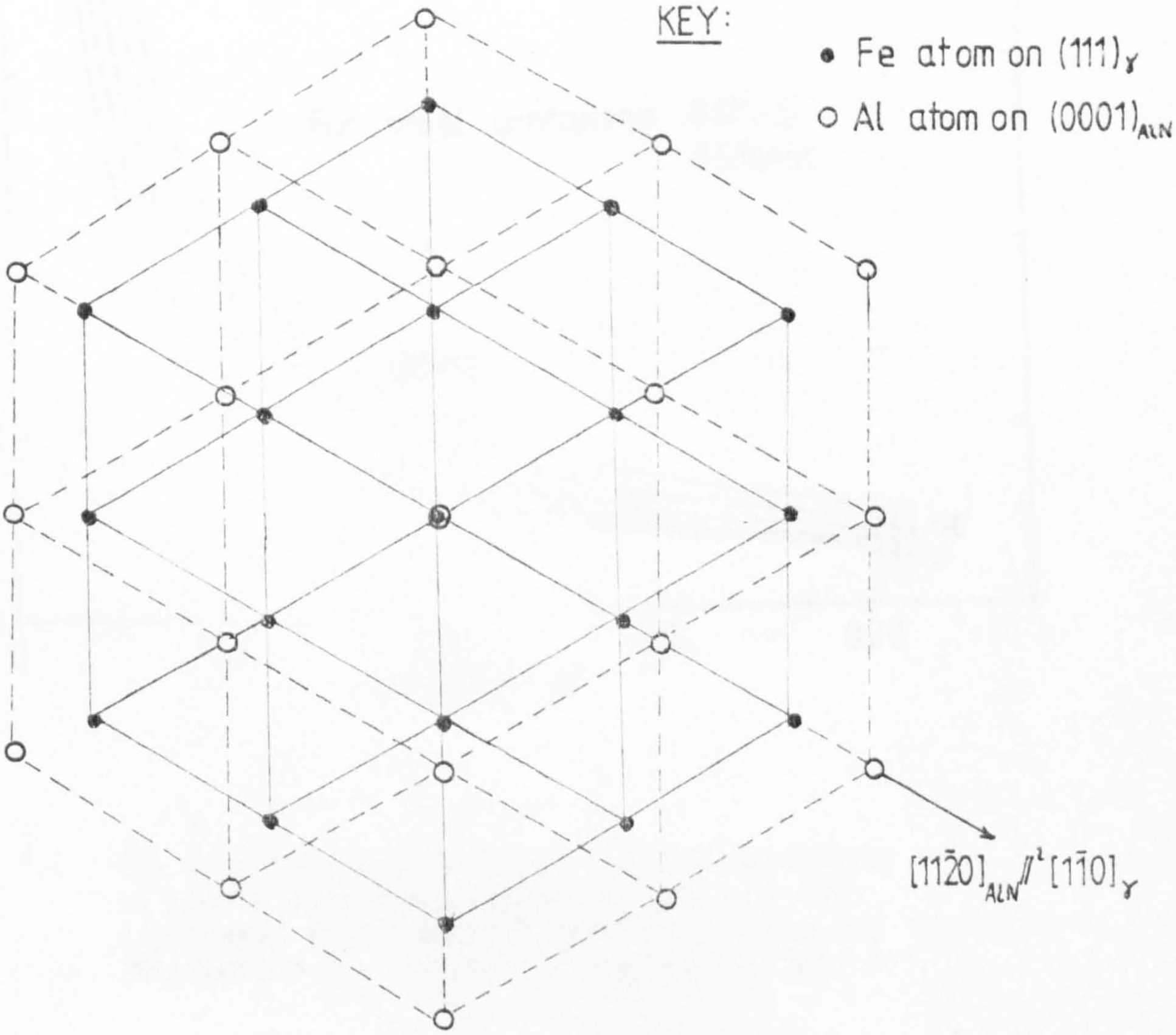

Fig. 7.4 a) The orientation relationship determined by Raynor et al (1966) for h.c.p. Mo_2C with austenite, with $\langle 11\bar{2}0\rangle_{Mo_2C}$ // $\langle 1\bar{1}0\rangle_\gamma$

b) The arrangement of Al and Fe atoms for AlN in the same orientation (i.e. with $\langle 11\bar{2}0\rangle_{AlN}$ // $\langle 1\bar{1}0\rangle_\gamma$). Note the large misfit in the $\langle 11\bar{2}0\rangle_{AlN}$ directions.

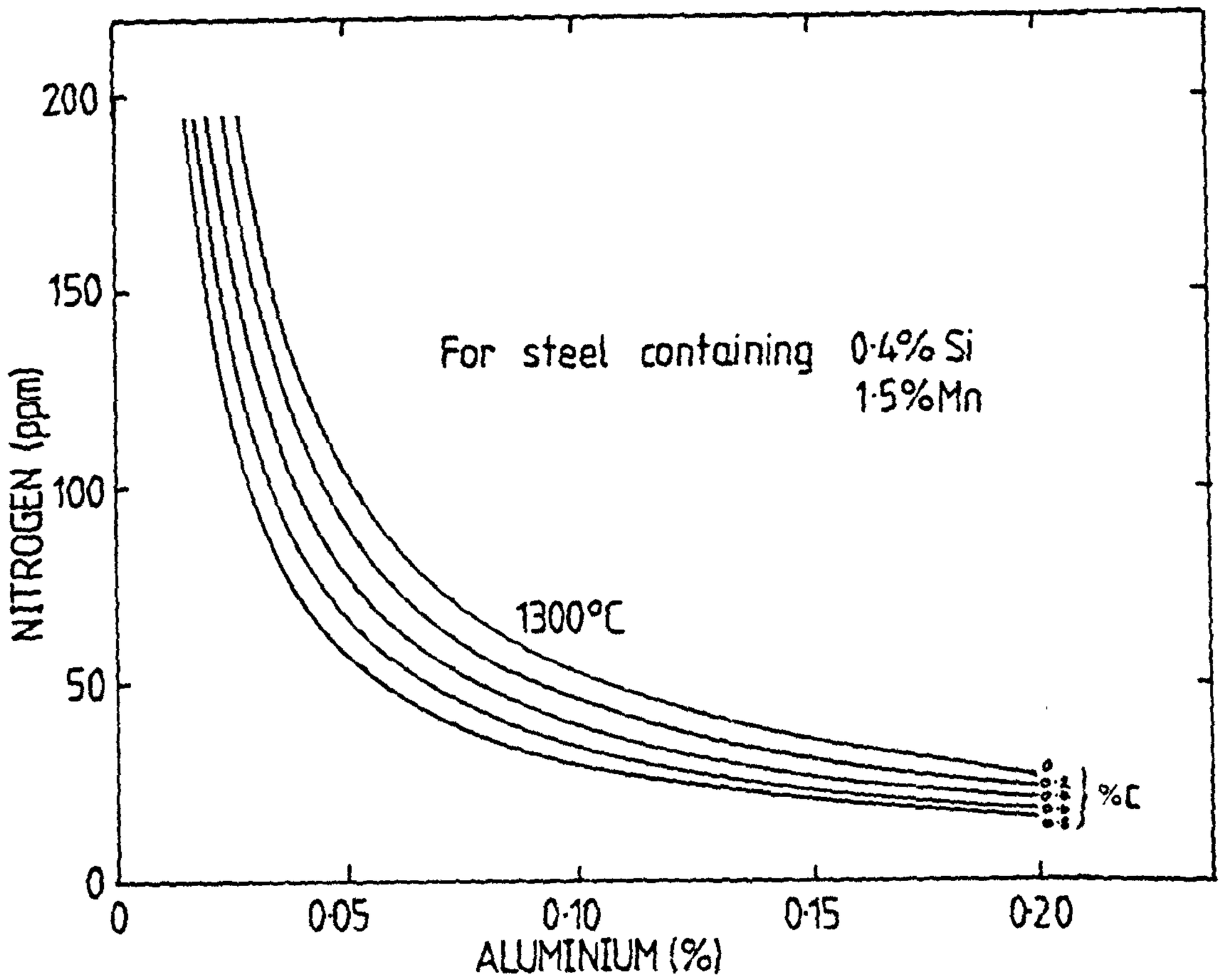

Fig. 7.5 The effect of carbon content on the solubility of AlN in austenite. Plotted using the data of Gladman and Pickering (1967) and using the interaction coefficients presented in Table 4.3.

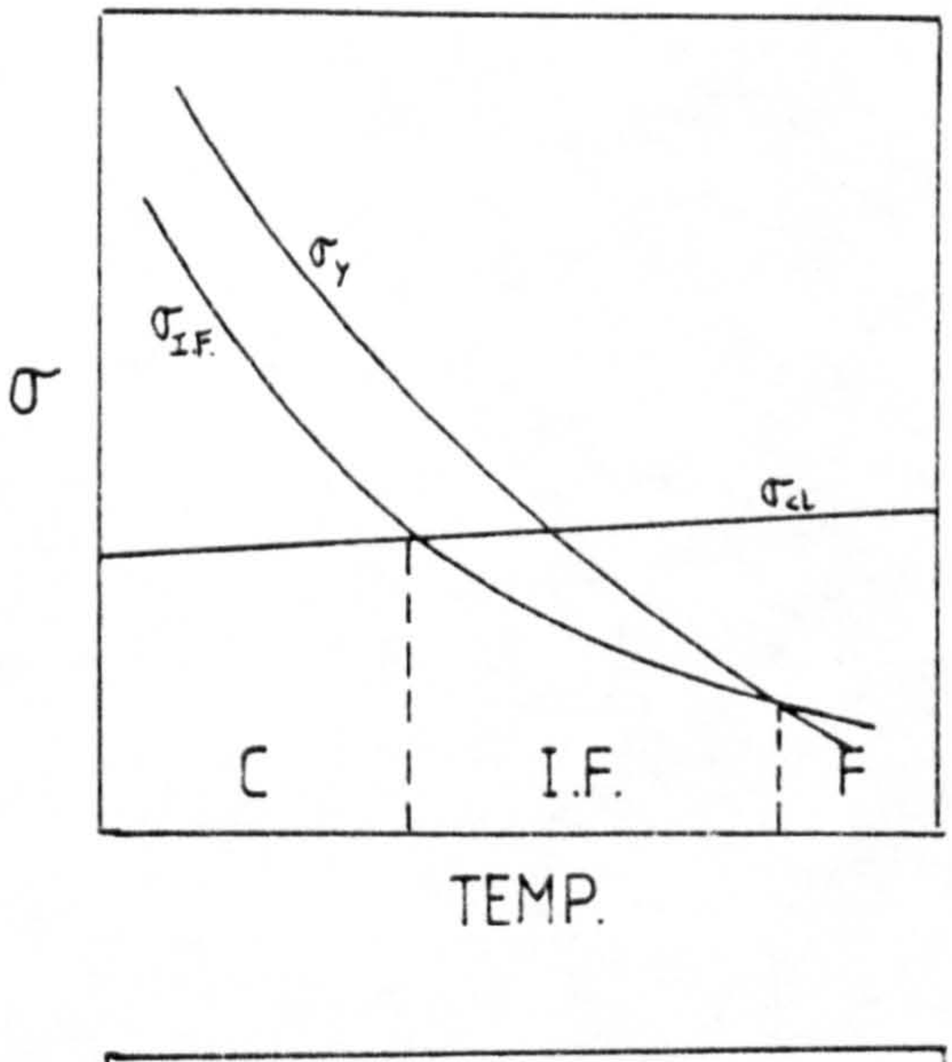

(a) high matrix strength

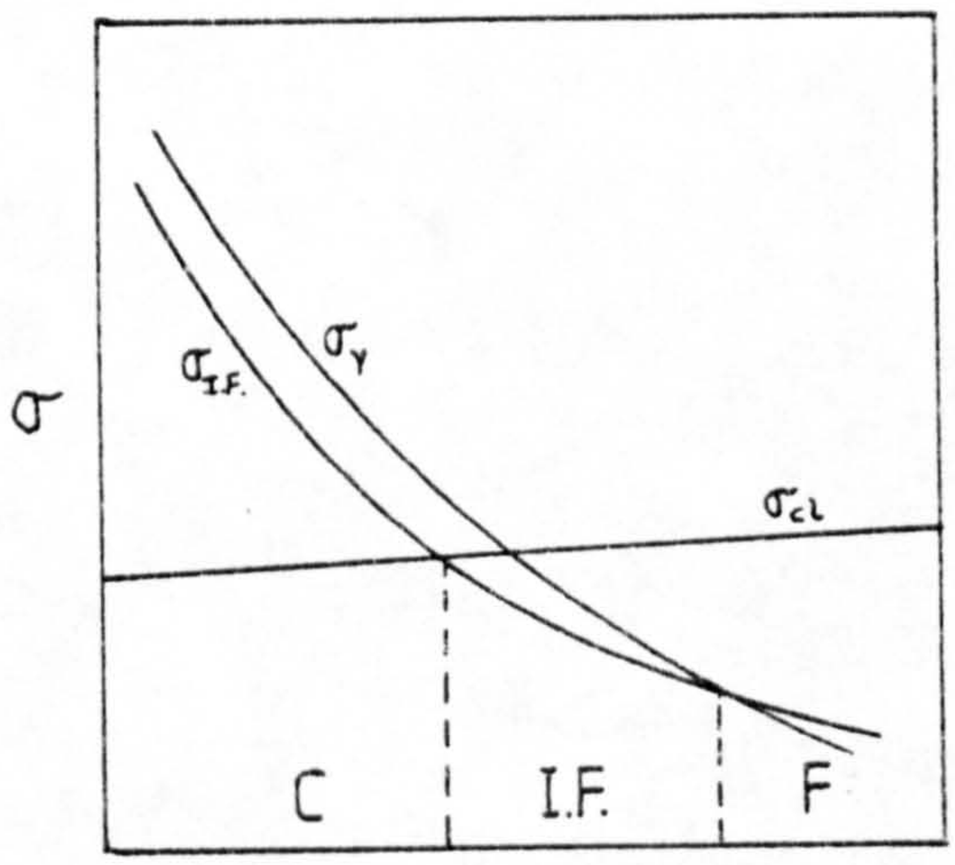

C = cleavage

F = fibrous

(b) intermediate matrix strength

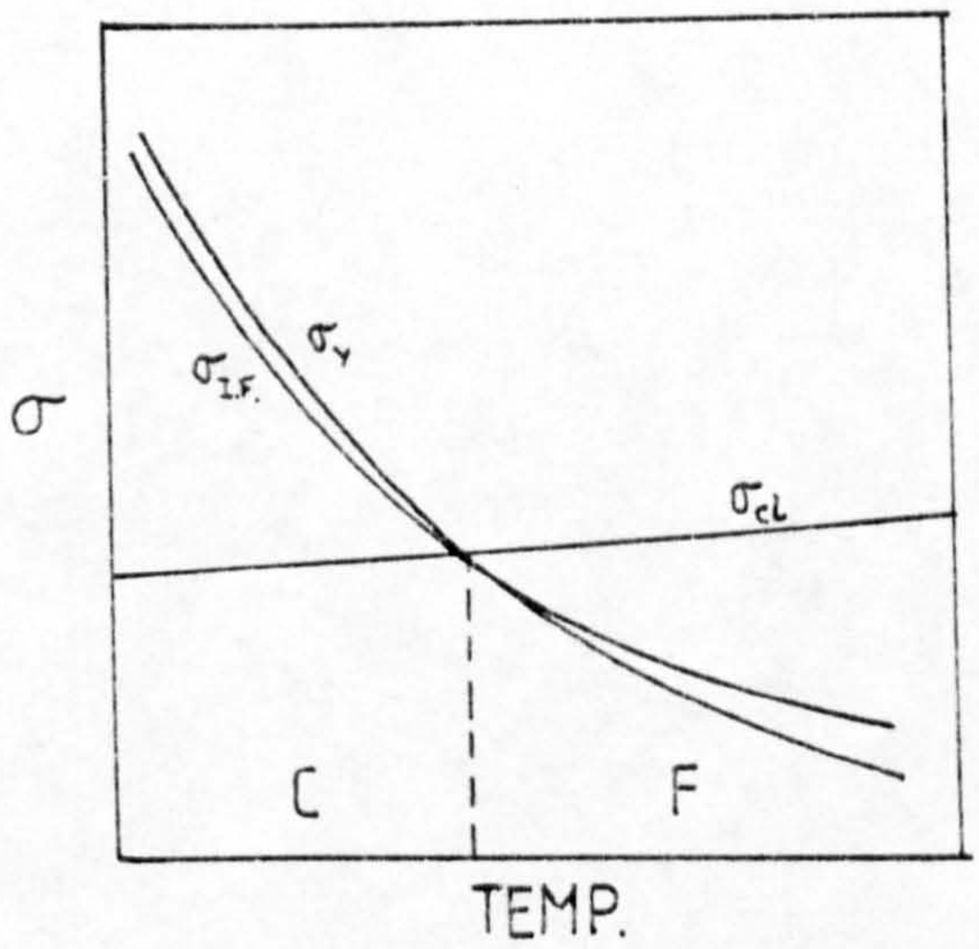

(c) low matrix strength

Fig. 7.6 Schematic strength/temperature diagrams showing the effects of matrix strength (σ_y) on intergranular fracture behaviour.